Master's thesis

NTNU
Norwegian University of Science and Technology
Faculty of Engineering
Department of Geoscience and Petroleum

Jørgen Sakariassen

The Upper Layered Series of the Reinfjord Ultramafic Complex

A Closer Look at the Magmatic and Structural Evolution of Dykes and Host Rocks

Master's thesis in Bedrock and Resource Geology
Supervisor: Bjørn Eske Sørensen
Co-supervisors: Rune E. Larsen & Kristian Drivenes
July 2020

NTNU
Norwegian University of
Science and Technology

Jørgen Sakariassen

The Upper Layered Series of the Reinfjord Ultramafic Complex

A Closer Look at the Magmatic and Structural Evolution of Dykes and Host Rocks

Master's thesis in Bedrock and Resource Geology
Supervisor: Bjørn Eske Sørensen
Co-supervisors: Rune E. Larsen & Kristian Drivenes
July 2020

Norwegian University of Science and Technology
Faculty of Engineering
Department of Geoscience and Petroleum

NTNU
Norwegian University of
Science and Technology

Summary

Reinfjord Ultramafic Complex (RUC) is a large ultramafic intrusion located in Northern Troms county in Norway. Reinfjord is one of four other ultramafic complexes in the Seiland Igneous Province (SIP), and these ultramafic complexes are believed to be the conduits for melt from the upper mantle through the crust, feeding SIP with primitive magma. Because of the deep seated and well-preserved nature of this ultramafic complex, RUC provides insight into mantle processes, and large melt transfers which are rarely preserved in these ultramafic rocks during their uplift. Primary magmatic structures and deformation processes which can be observed in RUC has been studied and described in this thesis.

In order to study the intrusion in detail samples have been collected and prepared in order to get quantitative analyses like XRD, major, minor and trace element analyses. Thin sections were also prepared from the samples to study the dykes and host rock features texturally and mineralogically. These thin sections were also used for SEM analyses and EPMA analyses.

Upper Layered Series (ULS) is a magmatic series in RUC which hosts a large variety of dykes as well as large serpentinization zones believed to relate to replacive dunite migration from Central Series (CS). The dykes themselves host features like diffuse infiltration of plag rich melt, strain localization and pseudotachylytes. ULS has been studied in order to better understand the temporal relationship with CS, as well as understand which deformation mechanisms and systems were active during the deformation of RUC and ULS. In addition to this, a new ore forming process has been identified in ULS, which may apply for all of RUC.

Earlier, large 1-5 metre replacive dunites have been believed to protrude from CS during its emplacement, into ULS. This thesis provides proof that these zones are simply serpentinization zones, and are most likely not related to any form of replacement textures. The serpentinization zones relate to a large normal fault east of the Southern Plateau of RUC, and are believed to be Caledonian serpentinization processes.

The earlies dyke generations are ultramafic lhz dykes, and have intruded into ULS via ductile fracturing. This dyke type also has a temporal relationship with a potential ore forming, plag and carbonate dominated infiltrating phase, believed to originate from partial melting of the surrounding Langstrand gabbro. The melt forming the plag domains seems to create a free sulphide liquid, capable of forming emulsion textured Fe-Ni-Cu-sulphides.

The phenocrystic hbl dyke has been described as a lamprophyre. This dyke type was compared to other known lamprophyre dykes around the world, and based on the findings, this dyke type does not seem to fit the chemical profiles of lamprophyres.

One of the dyke types most closely associated with deformation is the hbl gabbronorite found throughout ULS. This dyke is believed to have softened the surrounding wehrlite via fractionation of a H_2O and CO_2 phase out of the dyke, which has reacted with the wehrlite. This reaction has created large weakness planes in the reaction zones surrounding the hbl gabbronorite.

In addition to the textural, structural and chemical study of the many lithologies in RUC, a pressure and temperature estimate for ULS has also been calculated. This study provides a minimum emplacement depth and temperature for ULS at a pressure of 9,42 ± 0,87 kbar, and a temperature of 1037 ± 22 ^{O}C. This translates to an emplacement depth of ~32,5 km.

Sammendrag

Reinfjord Ultramafiske Kompleks (RUK) er en stor ultramafisk intrusjon i Nord-Troms i Norge. Reinfjord er en av fire ultramafiske komplekser i Seiland Magmatiske Provins (SMP) som man antar var transportpassasjen for primitiv magma fra den øvre mantelen gjennom skorpen, og har gjennom dette forsørget SMP med magma. På grunn av at RUK har så velbevarte teksturer og strukturer fra et stort dyp gir denne intrusjonen et unikt innblikk i mantelprosesser og andre dype magmaførende mekanismer som sjeldent bevares i slike ultramafiske intrusjoner når de kommer til overflaten. Primære magmatiske strukturer og deformasjonsprosesser som har blitt observert i RUK har blitt studert og beskrevet i dette arbeidet.

For å kunne studere intrusjonen i nok detalj ble det samlet steinprøver som videre ble preparert til kvantitative analyser som XRD, hovedelement, delelement og sporelement analyse. Det ble også preparert tynnslip for bruk i optisk mikroskop for mineralogisk og tekstuell analyse i kombinasjon med elektronmikroskopanalyse og mikrosondeanalyse.

Øvre lagdelte serie (ØLS) er en av de tre store magmatiske seriene i RUK. I denne magmatiske serien finnes flere gangbergarter samt store serpentiniseringssoner som tidligere ble trodd relaterte til emplasseringen av sentral serien (SS). Gangbergartene har bevart teksturer som infiltrasjon av en plagioklas og karbonatdannende smelte, lokalisering av deformasjon og pseudotakylitter. ØLS har blitt studert for å få en bedre forståelse av hvordan den relaterer til SS, i tillegg til hvordan deformasjon har preget denne magmatiske serien, samt hvilke deformasjonsmekanismer som har vært aktiv. I tillegg til dette har en ny malmdannende prosess blitt oppdaget, som kan ha en innvirkning på forståelsen av det malmdannende potensiale til RUK.

De 1-5 meter replasserende dunittene som tidligere var antatte utstikkere fra SS har blitt studert, og konklusjonen er at de ikke relaterer til en replasserende prosess, men heller senere Kaledonsk omvandling av bergartene.

Den eldste gangbergartstypen er en lhz gang, som er antatt å ha intrudert ØLS via duktil oppsprekking. Denne gangbergarten har i tillegg et temporalt forhold til den potensielle malmdannende plagioklasdannende smelten. På grunn av mineralogi og kjemi er det antatt at denne smelten stammer fra delvis oppsmelting av den omkringliggende Langstrand gabbroen. Det ser ut til at denne plagioklasdannende smelten skaper en fritt flytende sulfidsmelte i reaksjon med wehrlitten som kan danne emulsjonsteksturer av Fe-Ni-Cu-sulfider.

Den phenokrystiske hbl gangen har ofte blitt beskrevet som en lamprofyr. I dette studiet har denne gangtypen blitt sammenliknet med kjente lamprofyrer rundt i verden. Basert på kjemisk signatur ser ikke denne gangen ut til å relatere til tradisjonelle lamprofyrer, og dannelsesmodeller for lamprofyrer kan dermed ikke brukes for denne gangtypen.

Hbl gabbronoritten er den gangtypen som assosieres mest med deformasjon i ØLS. Denne gangen er ofte omsluttet av et gult deformasjonsmateriale. Dette er dannet av en reaksjon mellom wehrlitten og CO_2 og vann som er fraksjonert ut av den krystalliserende gabbroen. Denne reaksjonen har ført til at den omkringliggende wehrlitten har blitt mykere og svakere, og har dermed lettere tatt opp deformasjon.

Ett minimums emplasseringstrykk og temperatur har også blitt beregnet. Dette er på 9,42 ± 0,87 kbar og 1037 ± 22 ^{O}C, som er en ca. emplaceringsdybde på 32,5 km.

Acnowledgements

When I first contacted Bjørn Sørensen regarding a potential project for a thesis in June of 2018 he immediately proposed a project in the Reinfjord Ultramafic Complex. The combination of field work in a remote location, helicopter flights and living in a tent for several weeks sounded very appealing to me. Bjørn was very helpful in helping me tailor a project which involved both geochemistry, structural geology and petrology. I ended up working with a project I was very passionate about, in one of the most spectacular locations I have ever had the pleasure of visiting.

In addition to my main supervisor, Bjørn, I had great help from both of my co-supervisors Rune E. Larsen, and Kristian Drivenes. Rune is well acquainted with RUC, and assisted me with field work and tips along the way. Kristian was very helpful with anything EM-Lab related, from the optical microscopes to the EPMA. Along with my supervisors, I also found great help in Alf Orvik and Eric Ryan. They always had good tips and suggestions for my work, and also assisted me with sample preparation and field work in Reinfjord.

This work would also have been near impossible without the help of Oddmund Hansen, a local resident in Reinfjord. He helped us with setting up equipment and making sure we were prepared for the field work up on the plateau. He also provided us with food and shelter when we stayed in Reinfjord. His hospitality and problem solving attitude is unmatched.

A thanks must also be appointed to the Dept. of Petroleum and Geoscience for providing financial backing for this project. Field work, chemical analyses and hours using the different analytical instruments were all supported by the Dept. of Petroleum and Geoscience at NTNU.

The supporting staff at NTNU have been very helpful and accommodating. The Mineral Analysis lab and Thin Section lab have been a pleasure to work with, as they have always been supportive and helpful when asked for assistance.

Table of Content

List of figures

List of tables

List of abbreviations

Ab = Albite

An = Anorthite

Ccp = Chalcopyrite

Cpx = Clinopyroxene

CS = Central Series

Di = Diopside

Dol = Dolomite

En = Enstatite

EPMA = Electron Probe Microanalysis

Fo = Forsterite

Hbl = Hornblende

Km = kilometre

Lhz = Lherzolite

LSRD = Large Scale Replacive Dunite

M.A.S.L = Metres above sea level

Ol = olivine

Opx = Orthopyroxene

Peg = Pegmatite

Plag = Plagioclase

Pn = Pentlandite

Ppl = Plane polarized light

Px = Pyroxene

Pyh = Pyhrrotite

ULS = Upper Layered Series

Xpl = Cross polarized light

XRD = X-Ray diffraction

1 Introduction

1.1 Motivation and introduction

Reinfjord Ultramafic Complex is an ultramafic complex in the Seiland Igneous Province in Northern Troms county in Northern Norway. The unique aspect of this ultramafic intrusion is that it is believed to have acted as the conduits of melt from the upper mantle through the asthenosphere (Larsen, et al., 2018). Another unique aspect of RUC is the low degree of alteration seen in the complex. Deep ultramafic complexes are often so heavily overprinted by alteration during uplift that the primary magmatic textures and mineralogy is not preserved. This is not the case in RUC.

The well-preserved nature of the intrusion allows for studying of these primary magmatic processes and textures to an extremely high detail. This allows us to investigate the processes which happen beneath large igneous provinces, and what processes take place in magma chambers which are responsible for some of the largest igneous provinces in the world. This has implications for better understanding of hot spots, large primitive volcanoes, large ore forming intrusions, and simply provides a better understanding for the processes which take place in the upper mantle.

The complex has been studied by several geologists from the mid 19-hundreds up until today. It has been the focus of articles, Master theses, and PhD research. The separate pulses of magma have been researched, but a lot of focus has been turned towards the intrusion as a whole and the contact to the surrounding Langstrand gabbro. Voll (2019) and Anker-Rach (2013) both studied the ore forming potential of the complex, and Orvik (2019) focused on the dyke swarm of the Central Series magmatic pulse. Grant et al. (2016) published an article providing a good overview of RUC as a whole. Little attention has however been turned to the Southern plateu, as it was originally mapped as a protrusion of CS. This thesis aims at providing more detailed observations and interpretations to a less studied part of ULS.

Emplacement processes, fractionation processes and chemical evolution of ULS have been studied and described. Features found in ULS which are previously described (Grant et al. 2016; Larsen et al. 2018) as replacive dunites have been investigated to determine the origin and process responsible for these features. The different dykes found in ULS have been studied in combination with deformation. A potential ore forming mechanism has been investigated to further understand the ore forming potential of this intrusion. A pressure and temperature estimate was also found for one of the plag and hbl bearing dykes.

1.2 Geological setting and background

1.2.1 Seiland Igneous Province

The Seiland Igneous province (SIP) is a large igneous province (LIP) located in Northern Norway. The intrusion spans an area of >5000 km^2, containing > 25,000 km^3 (Griffin, Stuart, O'Neill, Kirkland, & O'Reilly, 2013) of igneous rocks. These rocks are primarily mafic and ultramafic rocks, with minor intrusions hosting alkaline, carbonatite and felsic rocks (Larsen, et al., 2018). SIP shares resemblance to other LIP's of similar age on Greenland and in North America, which are believed to relate to the opening of the Iapetus Ocean. These LIP's are therefore often referred to as Central Iapetus Magmatic Provinces (CIMP).

When compared to other CIMP's, SIP exposes a deeper window into the lower, more primitive parts of a LIP. With pressure estimates from the surrounding metasediments corresponding to lower crustal settings at 6-10 kb (Grant, et al., 2016). Other CIMP usually show the most evolved products, like flood basalts, and related sheeted dyke complexes, while SIP provides great insight into the conduit chambers, feeding melt up through the lithosphere. (Larsen, et al., 2018)

The age of SIP is believed to be similar to the other CIMP and formed in a narrow time frame <10Ma between 570-560 Ma. (Higgins & van Breemen, 1998). The earliest dates from SIP are obtained from the Øksfjord metagabbro and monzonite with dates of 829 ± 18 Ma. These are however most likely inaccurate dates as the Sm-Nd system used is vulnerable to resetting. (Krogh & Elvevold, 1990). The more recent geochronological studies by Roberts et al., (2010) have provided ages for the oldest alkaline and carbonatite rocks at 580-560 Ma with data showing a closer spread around 580 Ma. The mafic plutons dated by Roberts et al., (2006) give ages in a narrow range between 570-560 Ma.

During intrusion of the ultramafic suites, the surrounding gabbro experienced large-scale partial melting and assimilation into the ultramafic intrusion. Griffin et al., (2013), amongst others, reported that the intrusion of the layered gabbros must have closely preceded the intrusion of the ultramafic suites, as the gabbros had to be close to their solidus temperature during the time of ultramafic intrusion. The ultramafic complexes nor dykes have been dated directly but based on these relations it is approximated that the dates are only slightly younger than the gabbroic bodies.

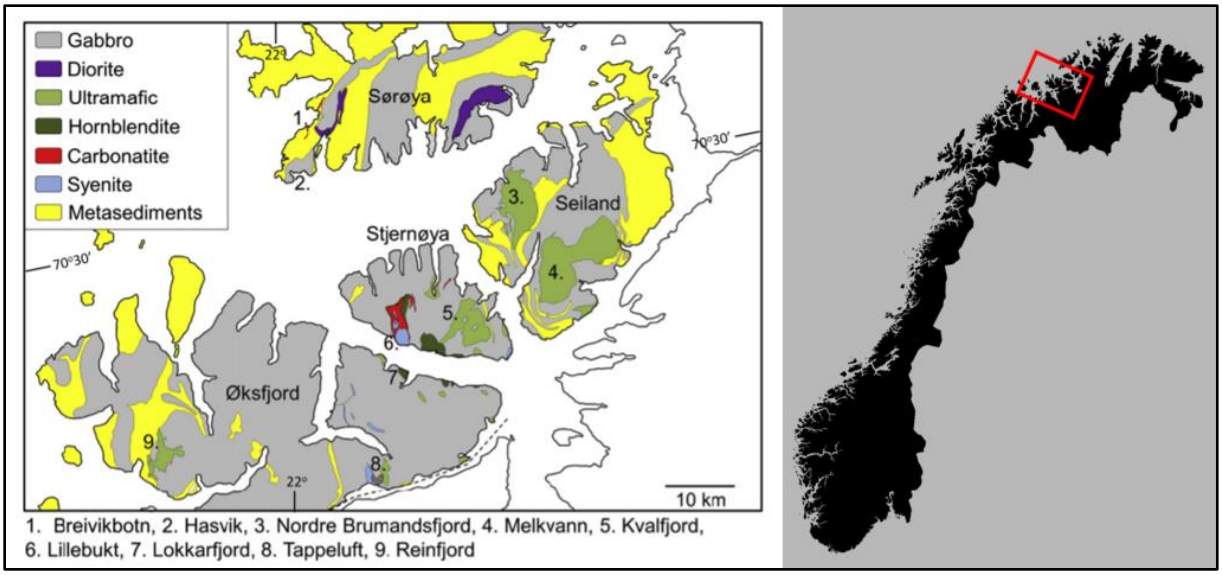

Figure 1.1. ***(Left): Geological map overviewing SIP. The map shows the area covered with gabbroic lithologies, as well as the other minor intrusive suites like diorite, hornblendite, carbonatite, syenite and ultramafic. The metasediments, metamorphosed by the intrusion are shown in yellow here. (Right): This map is a map of Norway, with the location of the left map marked out by the red square. Left map is form Larsen, et al., 2017.***

SIP is related to one of the strongest onshore gravitational anomalies in Northern Scandinavia (Larsen, et al., 2018), with some local, smaller positive anomalies being related to outcrops of ultramafic rocks. The larges anomaly however does not have a surface exposure of ultramafic rocks. These anomalies were investigated by Pastore et al., (2016) using gravimetric data and 3D forward modelling to generate a density model for the SIP and the ultramafic bodies. Some of the results of which can be seen in Figure 1.2.

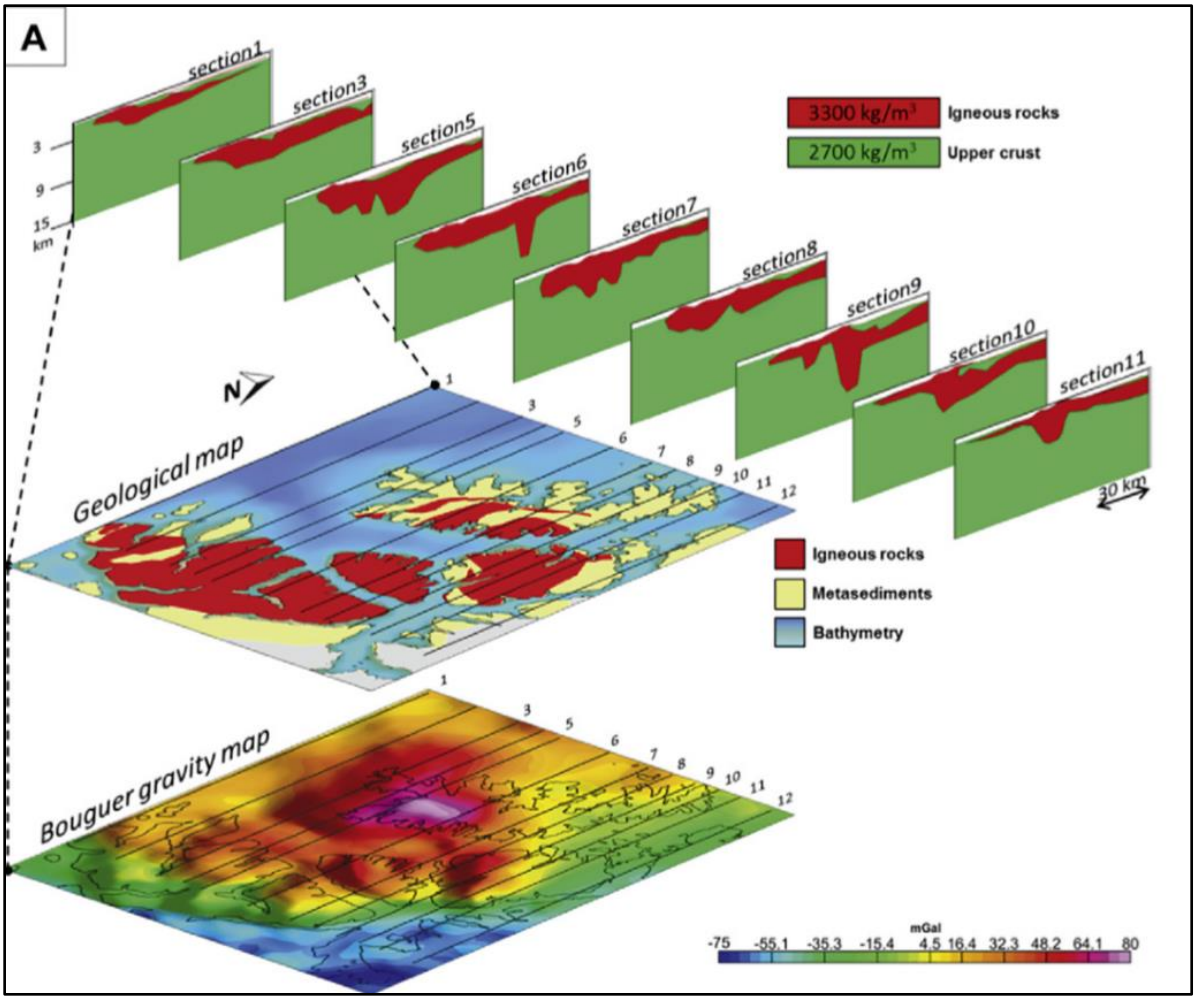

Figure 1.2. ***From Pastore et al., (2016). A Bouger gravity map and a simple geological map combined with 11 sections of modelled geometries of crustal and igneous rocks. The 2D cross sections are overlain the gravity and geological map to show the modelled sub surface geometries onto the map surface.***

Pastore et al. used an average value for intrusive rocks of 3300 kg/m^3, and an average crustal value of 2700 kg/m^3. These values do not account for density differences between mafic and ultramafic rocks, like gabbro and wehrlite, respectively. The values measured by Pastore et al., (2016) gave an estimate of 2752 ± 52 kg/m^3 for meta-sediments, 3042 ± 126 kg/m^3 for gabbros, and 3112 ± 94 kg/m^3 for ultramafic rocks.

The geometries of the modelled intrusive bodies show complex structures, with two distinct root structures as seen in Figure 1.2 Section 6 and 9. These roots are modelled ultramafic rocks which extend down to a depth of 9 km. This is however a minimum estimate, as the resolution of gravimetric modelling of small scale structures is poor (Larsen, et al., 2018). The subsurface extent of these bodies could therefore be greater than the modelled depth.

The map from Larsen et al., (2018) seen in Figure 1.1 show the extent of the intrusion, with the ultramafic centres numbered. The intrusion mainly covers the Øksfjord peninsula, Stjernøya, Sørøya and Seiland. As seen from the map, the most widespread lithology of the intrusion is a gabbroic lithology making up ~85% of the surface area of the intrusion shown in grey. The gabbroic rocks range from ol gabbro, px gabbro, syeno gabbro, pegmatitic gabbro and metagabbro. The gabbro shows rhythmic modal layering, cumulate textures, phase layering and cryptic layering. (Larsen, et al., 2018)

The ultramafic rocks in SIP are shown on the map in Figure 1.1 as isolated green bodies, and all of them are numbered and labelled. The ultramafic bodies make up 4 different ultramafic complexes and make up 8-10% of the total intrusion area. These are Nordre Bumandsfjord, Melkvann, Kvalfjord and Reinfjord Ultramafic Complex and are believed to be the main conduits of primitive melt feeding the larger intrusion.

1.2.2 Reinfjord Ultramafic Complex

Reinfjord Ultramafic Complex is the southwestern most ultramafic complex in SIP and is located on the southern end of the Øksfjord peninsula, seen as number 9 on Figure 1.1. The intrusion is emplaced in the Langstrand gabbronorite, with contacts to meta-sediments in the NW and SW corners, with steep contacts to both lithologies (Larsen, et al., 2018). Besides being the most well-preserved of the complexes, RUC also represents the deepest parts of any of the ultramafic complexes.

The intrusion itself is comprised of four separate magmatic series and the gabbronorite which the ultramafic magmas were intruded through, as well as marginal and roof zones. The ultramafic series consist of separate pulses of magma and are distinguishable from each other. These series are

- Marginal Series (MS)
- Lower Layered Series (LLS)
- Upper Layered Series (ULS)
- Central Series (CS)

as well as the Langstrand Gabbronorite.

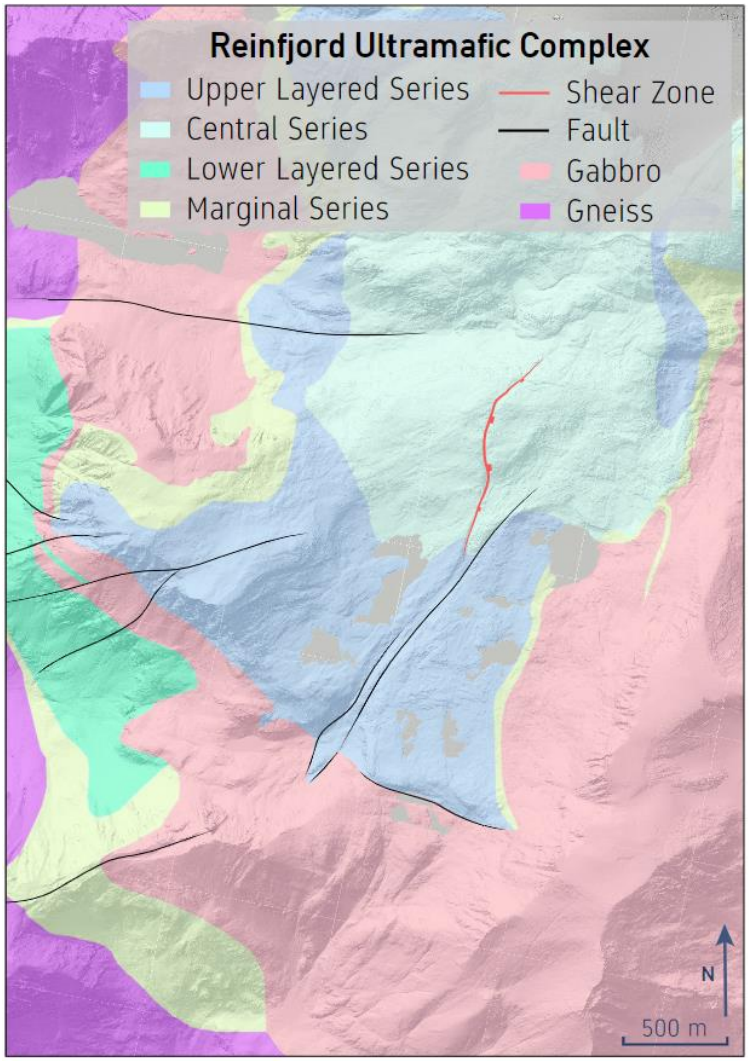

Figure 1.3. ***This is a revised geological map for RUC. The map includes the major magmatic series, LLS (green), ULS (blue), CS (pale blue), marginal series (yellow), as well as gabbro (pink), and the surrounding gneiss (purple). The major normal fault lines in black, as well as the major normal shear zone in red. (Ryan et al., in the process of publishing)***

The **Langstrand gabbronorite** is a layered gabbronorite dipping 10°-30° towards NNE enveloping most of the southern parts of the ultramafic magmatic series in Reinfjord. It is intruded into the surrounding psamittic to semipelitic garnet-bearing paragneiss with steep contacts creating a large high temperature contact metamorphic aureole. The paragneiss also occur as large rafts of xenoliths in the Langstrand gabbronorite (Bennet, 1974). The gabbronorite is a large, mafic pluton, with phase layering of plag, cpx and ol cumulates and a sub alkaline affinity possibly because of country rock contamination (Bennet et al., 1986).

Marginal zones are found along the contacts between the ultramafic series intrude the gabbro or the paragneiss. These zones are <150 m in thick hybrid zones containing several different lithologies like ol-melagabbro, pegmatitic gabbro, coarse grained websterites, and assimilated, partially recrystallized xenoliths of both gabbro and gneiss (Grant, et al., 2016). The ultramafic rocks also form metre thick apophyses protruding from the ultramafic intrusion into the surrounding gabbro, sub parallel to its magmatic layering. (Larsen, et al., 2018)

The **Lower Layered Series** is a magmatic series which outcrops on the SW part of the plateau on a steep cliff face. It consists of 4 cyclic events of rhythmically and modally layered ol and px dominated cumulates, where the bottom of each unit is marked by a layer of ol rich lherzolites with oikocrystic

opx (Figure 3.6) and poikilitic wehrlites. As the cyclic unit progresses upwards, the layers become increasingly cpx rich, forming wehrlites and ol clinopyroxenites. (Bennet et al., 1986)

Upper Layered Series is spatially separated from LLS by a 50 metre gabbro screen, and may be formed at the same time as LLS, this is however unclear (Emblin, 1985). ULS outcrops above LLS, on the SW hilltop, as well as on the southern plateau of RUC and eastern side of the plateau. It forms at most a 300-metre-thick layered unit starting at ~500 m.a.s.l. ULS is similarly to LLS comprised of 7 cyclic events of modally layered ol and cpx- cumulates, with the base of each layer comprising wehrlitic and dunitic layers (sometimes with poikilitic spinel), increasing in cpx as the layeres progress upward. (Larsen, et al., 2018)

Layering thickness varies from cm to dm to m scale and dips gently (10°-20°) towards ENE. Primary magmatic structures like slumping, cross bedding and current ripples can be found in the layers, and between layers of ULS. Two of these structures can be observed in Figure 1.4. Replacive dunitic processes are also common in ULS and can be observed in Figure 3.4. Lastly, the magmatic series is cut by several generations and types of dykes in a NNE-SSW trend.

Figure 1.4. ***(Left) Slumping texture seen in the contact between a px rich wehrlitic layer at the top, and an ol dominated dunitic layer at the bottom. (Right) Current ripples exposed in a wehrlitic layer, showing flow in the magma chamber. From Grant, et al., 2016.***

Central Series is intruded into ULS and is located in central parts of the intrusion. This intrusive relationship is established by large offshoots of dunitic melt, 1-5-metre-wide dykes protruding from CS into ULS. This relationship indicated that melt originating from CS is intruding into ULS. CS is rich with smaller replacive dunites, where dunitic melts mingle with px rich melt. This indicates that during the time of intrusion, ULS was not fully solidified. (Grant, et al., 2016)

The main lithology found in CS is dunite, making up ~70 vol% of the intrusive series, with the remaining being poikilitic wehrlites. Olivine is the only cumulus phase in this series but shows some degree of modal layering, but not to the same degree as ULS or LLS. It is however observed that the bottom of these units have interstitial cpx and spinel, while interstitial hbl is observed at the top of each unit. CS also contains Ni-Cu-PGE reefs which were discovered through the RUC drilling program.

A large dyke swarm is also hosted in CS, with a wide spread in both dyke thickness and lithology. The thickness varies from mm to dm, and the dykes themselves range from dunitic, wehrlitic, lherzolitic, gabbroic and hornblende bearing plag dykes.

Late deformation

Ubiquitous in RUC there are shear zones found in different parts of the magmatic series. These shear zones have been studied by Sørensen et al., (2019). Some of these shear zones can be seen in *0*

Olivine dominated shear zones. These shear zones have a different modal mineralogy to the host rock, with minerals like dol and opx making up the interstitial component in the shear zone where they sometimes form interconnected networks parallel to the SPO defined by ol. Different types of shear zones have also been identified, where the wider shear zones have different mineralogy and SPO than the narrow shear zones.

Based on thermodynamic modelling indicates high P and high T shearing at a minimum of 8 kb and 775 ^{o}C, indicating that these shear zones are most likely to be pre-Caledonian, and possibly related to the cooling and settling of the intrusion. The P-T estimates are based on the reaction between ol + cpx ⇌ en + dol. The modal difference from host rock to shear zone indicates a presence of a CO_2 rich fluid driving the metasomatism and deformation found in these shear zones.

1.3 Igneous petrology and geochemical theory

In order to understand how igneous rocks are formed, it is important to understand how geochemical and petrological processes form melts, and how processes like fractionation and differentiation affects melts, and in return allows for different rocks and mineral assemblages to form from a melt. In the early 20th century, N. L. Bowen and Alfred Harker started working with the genetic relationship between igneous rocks, and by this laid the foundation for the understanding of magmatic processes and differentiation (Cox, Bell, & Pankhurst, 1979). In this chapter the theory behind melt formation, petrogenesis, petrological and geochemical variations of igneous rocks will be presented.

1.3.1 Whole rock geochemistry

Major elements

In geochemistry, a major element is an element which comprises more than 1,0 wt% of the rocks total mass. This means major elements are crucial constituents in the rock forming minerals and are greatly affected by the melts which they crystallize from. These elements are often presented as oxides in whole rock analyses. Common major elements found in igneous rocks are SiO, Al_2O_3, FeO_{tot}, MgO, CaO, Na_2O, K_2O (Winter, 2001).

Major elements are useful as they can help with classifying rock types quantitatively based on chemical analyses and often assist in understanding minor variations in chemical concentrations across different rock types. These variations can indicate both the origin and evolution of magmatic systems (Winter, 2001). Classifications based on whole rock chemistry are commonly combined with optical microscopy in order to understand which phases incorporate the different major elements.

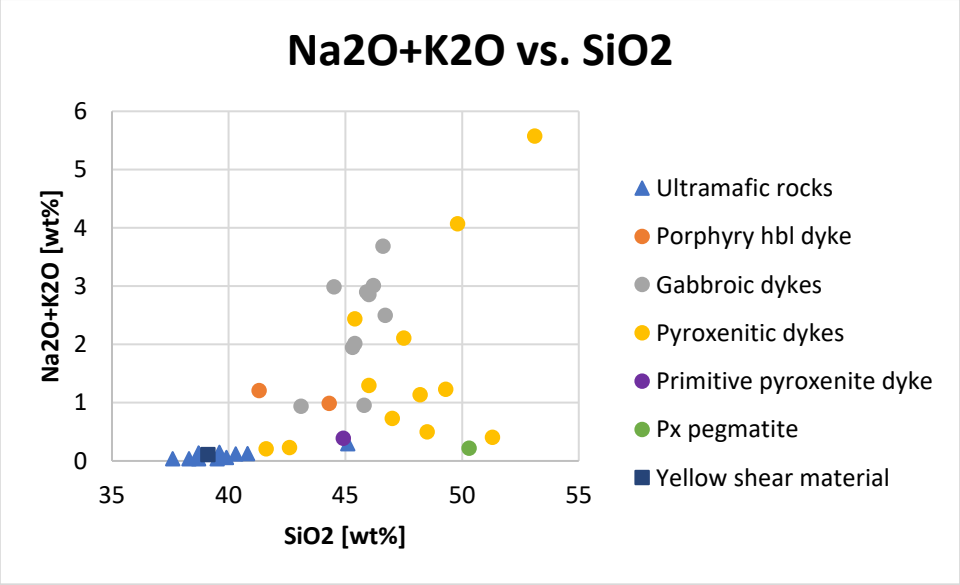

Figure 1.5 ***An exemplary plot of total alkalis vs silica (TAS) from several rock types form Reinfjord. This plot contains both dykes and host rock samples and help see systematic difference in alkalis across the different rock types.***

Minor elements

The *minor elements* are defined as elements making up 1,0-0,1 wt% of the rocks total mass. These minor elements may either be present in small concentrations as substitutions in a rock forming phase, like Ni in olivine. However, if the concentration is high enough the minor elements may form an accessory mineral phase, like pentlandite, a Ni-Fe sulphide. The minor elements are also presented as an oxide. Common minor elements in ultramafic systems are MnO, TiO_2, P_2O_5 and Cr_2O_3 (Winter, 2001, Best, 2003).

Trace elements

The trace elements are elements with concentrations less than 0,1 wt% of the rocks total mass. Trace elements are often reported as parts per million (ppm) and as an element itself rather than as an oxide. Since these elements occur in such low concentrations, it is rare for trace elements to stabilize mineral phases exclusive to the trace elements itself. Trace elements are more commonly found as substitutions in common mineral phases. A common example of this is Eu in plag, where Eu^{2+} can substitute for Ca (Winter, 2001, Cox, Bell, & Pankhurst, 1979).

Trace elements are useful to petrologists as they fractionate differently from the major, mineral forming elements, and can therefore be used to study the evolution of a magma (Winter, 2001). The trace elements are often more sensitive to processes like magma differentiation than major elements, and changes in concentrations of trace elements is hence often a result of a differentiation process. This makes them useful as indicators of magma source and degree of fractionation.

The trace elements are often divided into high field strength elements (HFSE) and large ion lithophile elements (LILE), sometimes referred to as low field strength elements (LFSE). Trace elements are separated into these two groups based on their ionic potential, which is defined as an ions charge (*Z*) divided by and ions atomic radius (*Å*)(Winter, 2001, Best, 2003). This affects how the element behaves in a crystal lattice as well as in a melt, and therefore affects which minerals and melts LILE and HFSE are compatible and incompatible in.

LILE are typically large ions with low atomic charge. This means the alkali metals and alkaline earth elements are included in this category as their atomic radii is relatively large and their valence numbers (# of electrons in outermost shell) are relatively low, as compared to HFSE like U, Ti, Hf, or Zr which have a smaller radii and higher valence numbers. Other typical and highly useful trace elements are the transition metals, like Sc, Ti, V, Cr, Mn, Co, Ni, Cu and Zn, as well as rare earth elements (REE), sometimes referred to as lanthanides (Winter, 2001). It is noteworthy that the REE with the lowest atomic number (La) has an atomic radius of 1,16 Å compared to the REE with the largest atomic number (Lu) with a radius of 0,93 Å. The REE are therefore also subdivided into light rare earth elements, and heavy rare earth elements.

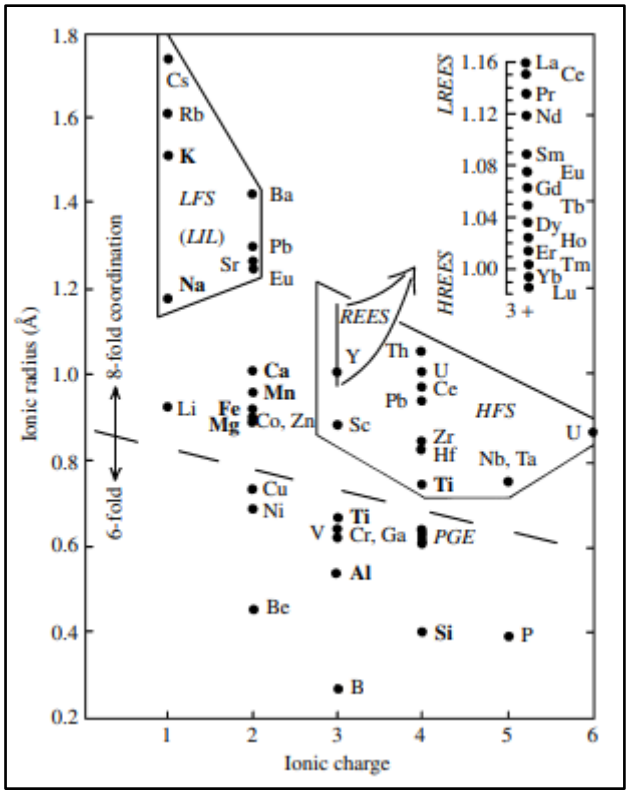

Figure 1.6 ***This figure shows the relationship between selected elements ionic charge and ionic radius. The ionic radius is separated into 8-fold coordination in the top part of the diagram and 6-fold in the bottom part of the diagram. The REE plot in the HFSE polygon, but are shown in the top right for clarity. From*** *(Best, 2003).*

What makes the trace elements useful is their ability to substitute for major elements in some crystal lattices, which can be used to study and understand the composition and evolution of the melt from which the minerals crystallized. Goldschmidt in his article (Goldschmidt, 1937) proposed some simple rules of elemental substitution in minerals and described how ions substitute in minerals.

1. The first rule of substitution is that ions of similar charge and similar size (±15%) may substitute for each other. This style of substitution is called **simple substitution**. Examples of simple substitution is substitution of Ni for Mg in forsterite, or Rb for K in K-feldspar. These ion pairs are similar in charge and size and are therefore expected to behave similarly in melts and minerals. These substitutions allow for solid solutions in minerals, and the concentrations of the end members is proportional to the concentration of the element from the melt. (Goldschmidt, 1937; Winter, 2001)
2. The second rule of substitution is that if two ions have a similar radius and the same valence, the smaller of the two ions will preferentially partition into the solid phase, and the larger ion will therefore enter the melt phase. This explains the trend of forsterite crystallizing prior to fayalite, as the Mg^{2+} ion is smaller than the Fe^{2+} ion, resulting in early peridotite cumulates being relatively enriched in forsterite, having a higher Mg/Fe ratio than the later forming cumulates. (Goldschmidt, 1937; Winter, 2001)

3. Lastly, if two ions have similar ionic radii, the higher valence ion like Zr, Cr^{3+} and V^{3+} will preferentially partition into the solid phase, leaving the melt depleted in these ions and relatively enriched in lower valence ions. (Winter, 2001)

These three rules are however simplifications of real magmatic systems and serve as a general guide rather than strict rules which apply to every system as there are many exlusions, and these rules do

not directly take electronegativity into account. Using these rules however provides a good starting point in understanding large scale magmatic trends.

In addition to dividing elements into categories based on their ionic potential it is also common to divide elements based of their affinity to different phases. The thee common categories are

1. **Chalcophile** elements are elements with an affinity for sulphide phases
2. **Siderophile** elements are elements with an affinity for iron
3. **Lithophile** elements are elements with an affinity for oxygen

1.3.2 Partition coefficients and element compatibility

One of the driving forces behind processes like magma evolution, fractionation or partial melting is elemental partitioning. Different elements have different partition coefficients into different materials. This partition coefficient is related to the ionic properties of an element as discussed in the previous subchapter.

An elements compatibility, or incompatibility is relative to which melt the element exists in as well as which mineral phases or crystal lattice the element can enter. The reaction happening when a rock undergoes partial melting at equilibrium can be expressed by the equation

$$i_{(Liquid)} \rightleftharpoons i_{(Solid)}$$

Equation 1.1

with $i_{(liquid)}$ representing the melt component and $i_{(solid)}$ representing a mineral phase component. (Best, 2003; Winter, 2001)

Using the fact that this reaction is an equilibrium reaction we can extrapolate an equilibrium coefficient to explain the distribution of an element between the two phases. This can be expressed as an empirical distribution constant

$$K_D = \frac{X_i^{Solid}}{X_i^{Liquid}}$$

Equation 1.2

where X_i is the molar fraction of an element in each phase. $K_D$is then a measure of the ratio between the mol fraction of a chemical component i in the solid phase and the liquid phase. This ratio then gives an indication of an element's compatibility in the melt/solid reaction. This is applicable for major elements with large concentrations, but trace elements are far more dilute in a melt, and the expression can be written as

$$K_D = \frac{C_S}{C_L}$$

Equation 1.3

If $K_D < 1$ when the system is in equilibrium the concentration of the element is higher in the liquid phase than the solid phase. The element preferentially partitions into the liquid phase, and the element would be described as incompatible in this system. Fractional crystallization will lead to the residual melt being enriched in the element.

If $K_D > 1$ the opposite occurs. The concentration of the element in equilibrium is higher in the solid phase than in the liquid phase. This means that the element is compatible in this system, and preferentially partitions into the mineral phase. If an element is compatible in a mineral, fractional crystallization would then cause the element to concentrate in the mineral, leaving the melt depleted of this respective element.

If $K_D = 1$ there is no change in the system, the element partitions equally into both the melt and mineral phase. Fractional crystallization or partial melting will not affect the elements concentration in either phases. (Cox, Bell, & Pankhurst, 1979; Winter, 2001; Best, 2003)

Another distribution coefficient commonly used is for whole rocks rather than just minerals. This coefficient is called bulk distribution coefficient ($\overline{D_i}$) (Winter, 2001) and is a sum of the contributions for a spesific component i in a mineral A and can be expressed as

$$\overline{D_i} = \sum W_A \, D_i^A$$

Equation 1.4

where W_A is the weight percent of the mineral in the rock, and D_i^A is the partition coefficient in component i in the mineral A. By viewing the system in terms of the whole rock instead of a single mineral we get a better understanding of both the relative amounts of elements fractionating, but also in which minerals fractionation is most predominant.

1.3.3 Melt generation from mantle rocks

Usually when melts generate in a geological setting it is the result of either an increase in volatiles, and increase in temperature, or a decrease in pressure. An introduction of volatiles (X) into a system can lower the solidus of the rock to intersect the geothermal gradient, causing melting of the rock. An increase in temperature (T) to a point of intersecting a rocks solidus will also cause the rock to melt. Similarly, a decrease in pressure (P) can also cause the rock to melt, as seen in Figure 1.7, or reversely, an increase in pressure can cause a melt to crystallize (Winter, 2001; Best, 2003; Gill, 2010).

As seen from Clapeyron equation, labled Equation 1.5, together with Figure 1.7 a decrease in P will by applying LeChatelier's principle cause an increase in volume to compensate for the reduction in order to minimize the effect of the reduction in pressure.

$$\frac{dP}{dT} = \frac{\Delta S}{\Delta V}$$

Equation 1.5

As $V_c < V_l$ a sufficient reduction in pressure may allow melting to happen. The same principle applies for a change in T. If T increases it will cause the system to limit the effects and the entropy of the system will increase, and as $S_c < S_l$ this may also promote melting. (Best, 2003)

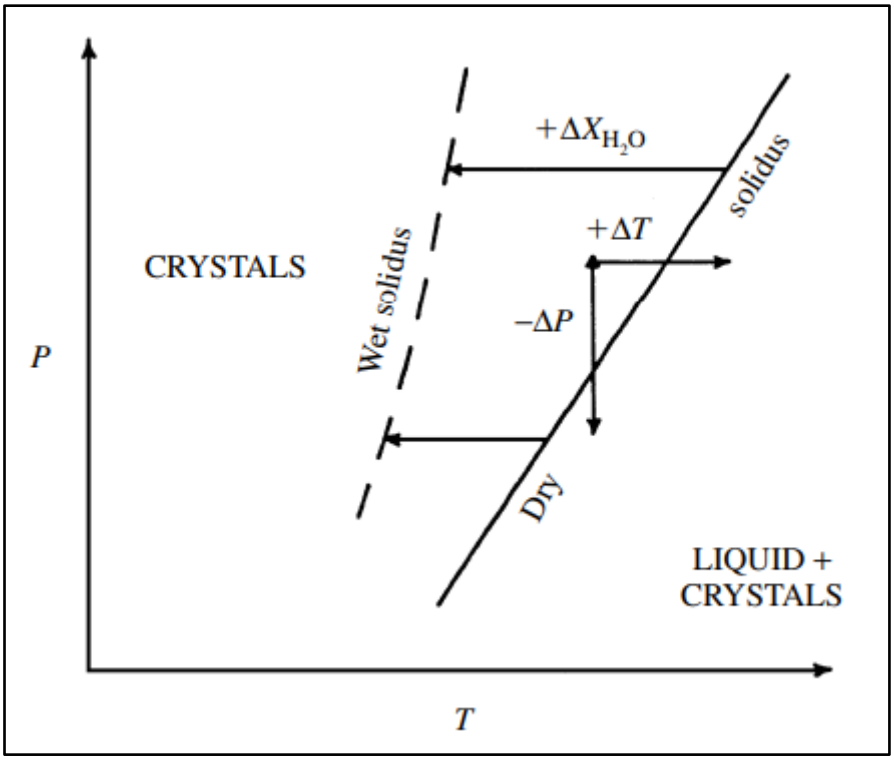

Figure 1.7 ***The figure shows how a theoretical rock sample may be melted either by decreasing pressure, increasing temperature, or adding volatiles which shift the solidus of the rock material. Figure from Best, 2003***

Figure 1.7 shows a theoretical example of how a rock can be brought to melting. A rock residing on the "crystals" field would be stable as a solid until an external force changed the P-T-X conditions. When the conditions change, the rock may cross its solidus placing it in the "liquid+crystals" field. Parts of the rock will start to melt at this point.

When a rock is heated to above its solidus the rock will start to melt. Where the first droplets of melt form will be a function of the mineralogy of the rock. A typical mantle rock may as an example, contain major ol, opx and cpx. When heatin this rock the first droplets of melt will form in the grain boundaries between the three, as these grain boundaries are the most unstable (Gill, 2010; Best, 2003; Winter, 2001; Yoder, 1976).

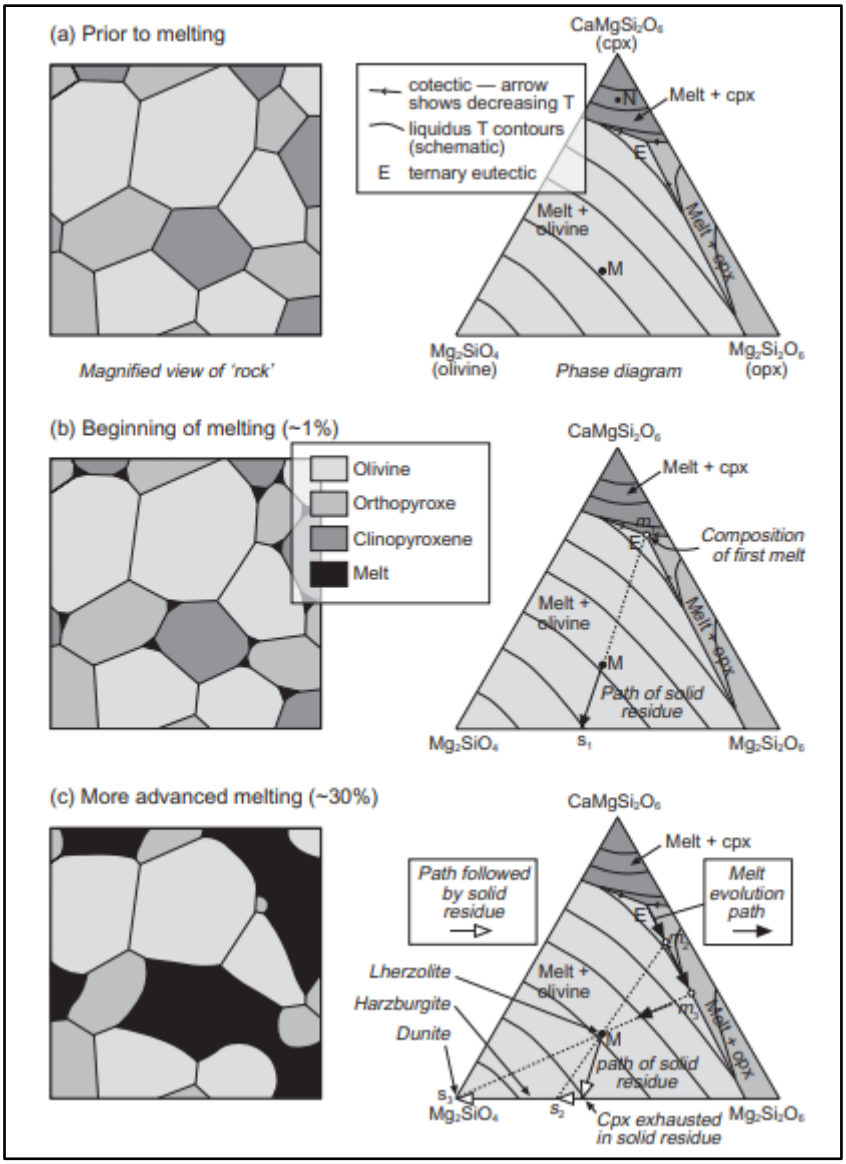

Figure 1.8. ***This figure shows how a mantle rock might melt. The figures on the left side show where melt droplets might originate, and the ternary phase diagram to the right shows the melting path of of a diopside-enstatite-forsterite system with composition shown by M*** *(Yoder, 1976)****. Ternary phase diagram shown evolution of melt and solid residue, first droplet of melt forms in the eutectic point labelled E. Figure from Gill, 2010.***

When melting any rock, the most thermodynamically unstable elements will be the first to melt, the first melt will generate in the point called the eutectic point, regardless of composition (Winter, 2001). Mantle rocks usually contain an aluminous phase like spinel, garnet or plagioclase depending on pressure (Best, 2003), these phases are however often minor compared to the FeMg silicates. In a simplified mantle rock containing forsterite, enstatite and diopside, diopside is usually the first phase to melt as seen in Figure 1.8.

When the cpx starts melting the solid residue will be depleted with respect to cpx. As seen from the left side melting illustration in Figure 1.8 the cpx is not the only mineral to melt, but it will dominate the melting phase, as minor opx and ol is melted. Once the cpx is all melted, the solid residue will only comprise opx and ol, therefore opx will start melting, and olivine will be the last mineral to enter the melt. In a closed system this will be what is often referred to as **equilibrium melting** (Best, 2003), where the melt and minerals are in equilibrium.

Opposite to equilibrium melting is **fractional partial melting**. This is a type of melting where the melt is removed from the crystalline residue as soon as it is generated, not allowing any time for exchange reactions between the melt and minerals. If this type of melting were to occur in a typical mantle rock like a lherzolite in an open system, the rock could end up depleted in Ca and other trace elements. The newly generated melt will then be rich in the elements dominating in cpx. This melt can be referred to as a fertile melt, as it is often rich in important trace elements, and ore forming phases (Robb, 2005).

As the cpx has mostly melted and subsequently been removed from crystalline residue, the remaining rock has now transitioned from a lherzolite to a harzburgite, and with further melting will transition into a pure dunite, a rock with >90% ol. These rocks are depleted with respect to many incompatible elements and are therefore often referred to as **depleted mantle.** As the upper mantle has experienced more cycles of decompressive melting the upper mantle often shown a more depleted chemical signature when compared to the lower mantle.

1.3.4 Partial Melting and Fractional Crystallization

When partially melting a mantle rock the newly formed melt will depend on the degree of melting, the minerals present in the rock and the elements present in the minerals, as well as temperature and pressure. The partition coefficient largely controls the concentration of trace elements in a newly formed melt, this is particularly important with regards to trace elements as they fractionate more than major elements.

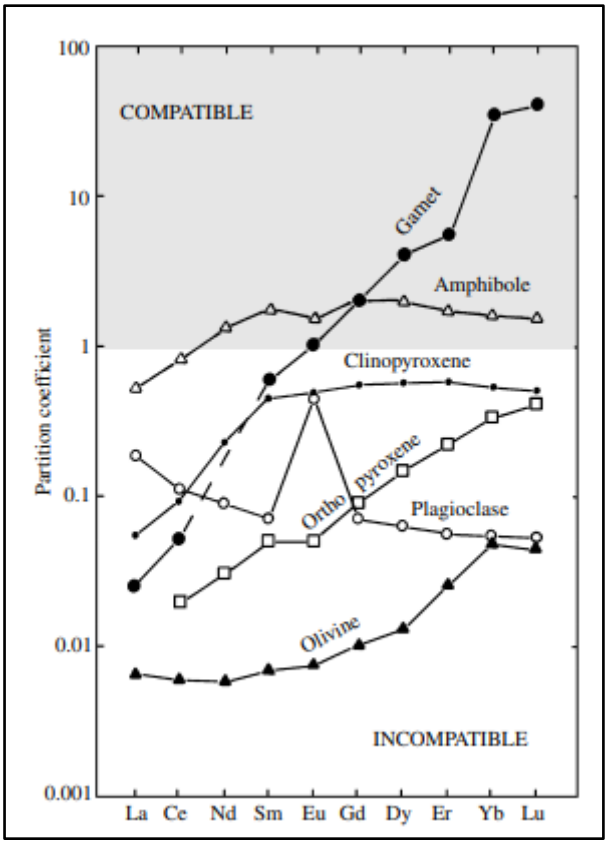

Figure 1.9. ***This figure shows the relationship between partition coefficients in REE in different minerals typically found in mafic and ultramafic rocks. This gives an illustration of which elements would preferentially partition into which minerals. Notably here is garnets affinity for HREE, and the positive Eu anomaly in plagioclase. From*** *(Best, 2003)*

As seen in Figure 1.9 the HREE have a higher affinity for minerals like garnet and amphibole with a partition coefficient > 1. During partial melting of a garnet dominated rock the melt would be enriched in LREE like La, Ce, Nd, and Sm since these elements are incompatible in garnet. The garnet rich rock itself would then be depleted in these minerals, but relatively enriched in HREE like Gd, Dy, Er, Yb and Lu. As seen from the figure, Eu plots close to 1, meaning the element in insensitive to either partial melting or fractional crystallization. These processes are ineffective for mobilization of Eu. (Cox, Bell, & Pankhurst, 1979; Gill, 2010; Winter, 2001)

Other minerals like olivine have a lower degree of compatibility for REE as well as other trace elements (Grant & Wood, 2009; Best, 2003; Gill, 2010). This makes dunitic rocks poor in these elements, as they are less able to find suitable cation spots in olivine as compared to other elements. Trace element concentration in in peridotite rocks often comes from cpx, as HREE are almost 100 times more compatible in cpx than in olivine. (Best, 2003)

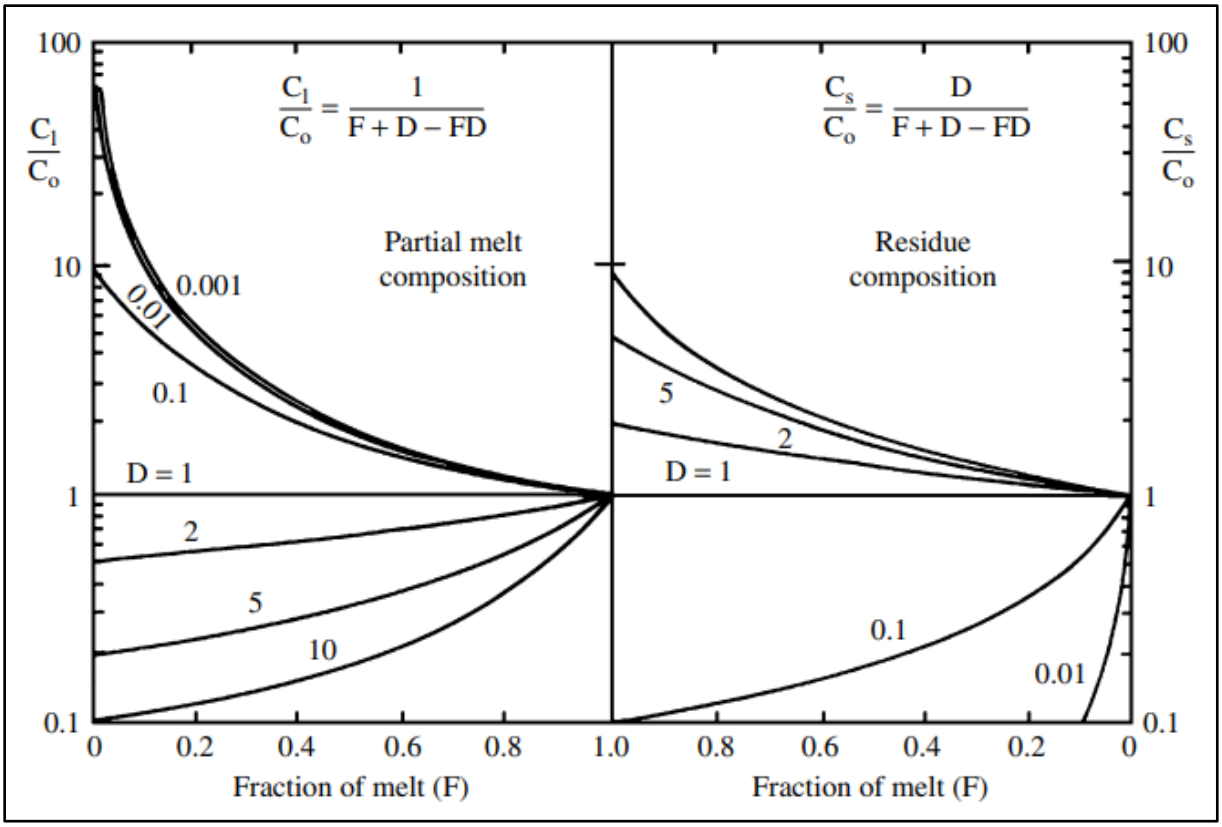

Figure 1.10. ***This figure shows the calculated concentration of trace elements in a partial melt composition, and a residue composition. The graph on the left side shows partial melting from left to right, and represents a batch melting scenario, as the partition coefficient curves end at C_l/C_o=1. The graph indicates elements with low compatibility will concentrate in newly formed melts relative to elements with high compatibility. Similarly, the graph to the right shows that during crystallization from a melt, the incompatible elements will have very low concentrations in newly formed crystals forming in a melt. The compatible elements will dominate in the earliest formed crystals. From*** *(Best, 2003)*

When melting a rock, the degree of melting plays a large role in the chemical composition of the newly formed melt. The graphs in Figure 1.10 shows the theoretical concentration of elements with different partition coefficients (D), over different degrees of melting (F). Both graphs represent a closed system since complete melting results in a melt having the same composition as the rock being melted.

For an open system small amounts of melt can escape, leaving a crystalline residue. When this happens the most incompatible elements will readily partition into the melt. For an ultramafic rock, this means any LILE naturally occurring in the rock will partition into the melt, as these elements struggle to incorporate into the minerals making up the rock. If the degree of melting is extremely low, the melt will then in theory be extremely enriched in these elements, which can then crystallize to form very enriched rocks. (Best, 2003; Winter, 2001; Cox, Bell, & Pankhurst, 1979)

Even though a newly formed melt during a low degree of melting will be strongly enriched in incompatible elements (D>>>1) the melt will still include a small portion of compatible elements. When concidering the formula from the left graph in Figure 1.10 explaining distribution of elements in the melt versus solid based on partition coefficient and degree of melting,

$$\frac{C_l}{C_o} = \frac{1}{F + D - FD}$$

Equation 1.6

it shows that low degrees of melting of compatible elements will still give a concentration ratio inversely proportional to the partition coefficient (Best, 2003). This means with infinitely low degrees of melting, an element with $D = 0{,}001$ will have ${C_l}/{C_o} = 1000$, while an element with $D = 5$ will have ${C_l}/{C_o} = 0{,}2$.

Like the partial melting affecting the chemical evolution of a melt, the fractional crystallization will also affect this. With progressive crystallization of the melt, the most incompatible elements will relative to the compatible elements be extremely concentrated in the melt, and stay in the melt until the system is almost completely crystallized.

1.3.5 Melt migration and dyking

As melts form in the mantle the melt will usually have a density much lower than the surrounding rock, making it buoyant. For the melt to mobilize it needs to mobilize either through self-generated hydraulic fracturing, or by obtaining porous flow. Hydraulic fracturing occurs when the fluid pore pressure σ_p exceeds the tensile strength σ_t of the material in question as well as the lowest principal stress σ_3. For hydraulic fracturing to occur, the system must be in the brittle regime, as ductile materials do not fracture in this manner. Porous flow would therefore be the dominating process of flow through the mantle.

Porous flow is obtained by creating an interconnected network of melt along grain boundaries between minerals through the rock. This relies on the principle of minimal surface energy and is a function of the crystal-crystal interfacial energy γ_{CC}, and the liquid-crystal interfacial energy γ_{LC}. These melt-crystal and crystal-crystal interfaces will form an angle known as a **dihedral angle,** θ. The dihedral angle is given by the formula from Best, 2003.

$$\theta = 2\ arc\cos\left(\frac{\gamma_{CC}}{2\gamma_{LC}}\right)$$

Equation 1.7

If $\gamma_{CC} = 2\gamma_{LC}$, then $\theta = 0^o$, meaning the entire surface of the grain will be coated in liquid as the theoretical contact surfaces are parallel. There are however no known geological materials in which this can happen. When $0^o < \theta \leq 60^o$ it is possible for the melt to form an interconnected web, and then migrate through the mineral aggregate. If $\theta \geq 60^o$, the melt will initially form as isolated pockets of melt at multigrain boundaries, and not form interconnected networks.

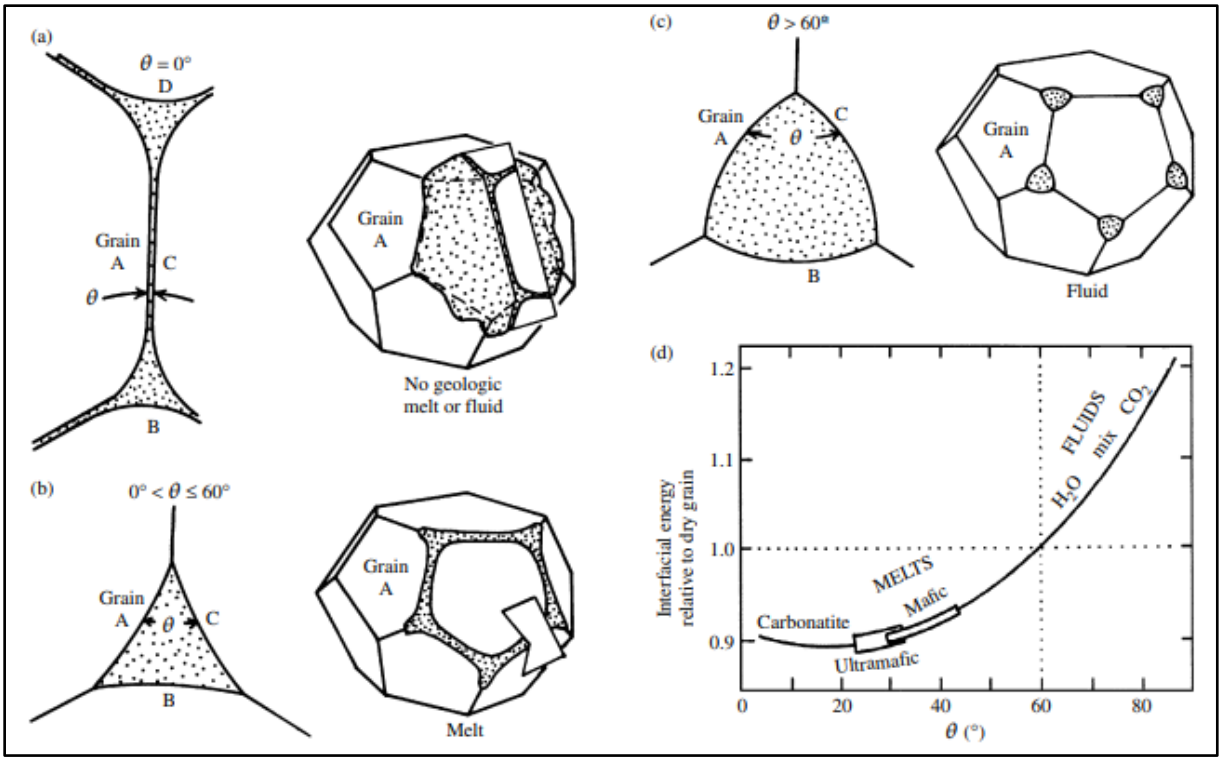

Figure 1.11. ***An illustration of how melt coats a grain with different θ.***

For the melt to properly migrate, there must be a sufficient melt volume in the system, so that the melt can form an interconnected network, as well as a volume great enough that the melt is not retained by surface tension from the rock. If θ is low, the amount of melt needed to form a network can be as low as ~1%. This means that for ultramafic systems as seen in Figure 1.11, the degree of melting needed to mobilize a melt is very low, as these systems often have $\theta \sim 20^o - 35^o$, and has also been reported by Laporte et al. (1997) to be less than 50^o for mafic systems.

When the dihedral angle increases to more than 60^o the degree of melting also needs to increase in order to create a network of melt (Beere, 1975). As seen in Figure 1.11, once $\theta > 60^o$ the melt starts forming as individual droplets in multigrain junctions. for these droplets to interconnect they need to increase their outreach to a critical size, where the droplets overlap. This then requires a higher degree of melting than a system with lower differences in γ_{LC} and γ_{CC}, and therefore lower dihedral angles.

According to Wickham (1987), there is a critical melt fraction for each melt system which he refers to as the **rheological critical melt percentage** (RCMP), and is the percentage of melt where the system moves from a rigid crystalline material towards being a crystal mush. The RCMP in a theoretical system of equally sized spheres is stated to be 26%, but with more viscous melt and variable sizes and shapes can vary from 30%-50%. As these areas of melt generation are usually in regions of high pressure, melt can be segregated through a process known as filter pressing, which is a pressure driven squeezing of melt from the crystal mush.

Despite RCMP being a theoretically sound idea, the principles were criticized by Rushmer (1996), who through experiments pointed out dihedral angles in relation to melt formation and mobility are of limited use in rocks. Rushmer also pointed out the limits of RCMP as it does not take necessary variables into account. Variables like depth of melting, melt reactions, melt driven volume change, tectonic setting (creating anisotropy in stress field), viscosity, composition and volatile content are not considered in the RCMP theory. Based on Rushmers estimates RCMP may be 1-7% for basalts/peridotites, and much higher for more viscous magmas.

Once these melts have formed, they can readily migrate through the crystal mush. Once a certain volume of melt is reached, and as the melt migrates into colder, more brittle parts of the crust dykes may begin to form as the pressure of the liquid exceeds the tensile strength of the rock. Once the fracture has formed, the fluid pressure only needs to exceed the minor principal stress. In this case the dykes open parallel to the minor principal stress axis σ_3, and propagates parallel to the major principal stress axis σ_1. According to Rubin (1995) dykes are the most effective way of transporting melt from the source region through cold lithosphere.

Since dykes are relativley small intrusive bodies, their ablility to carry heat is very limited. Heat convection to the wall rock will therefore not be sufficient to greatly affect the wall rock, but will in many cases lead to rapid cooling of the dyke (Best, 2003). Primary magmatic textures from the intrusive event can therefore easlily be preserved in both wall rock and dyke, making dykes a useful tool in interpreting intrusive conditions.

Dykes propagate differently depending on tectonic setting, temperature, pressure and melt composition amongst other factors. Propagation velocities for some mantle derived dykes can be as high as 0,01 to 10 m/s as recorded by Spera (1984) based on computed settling rates of xenoliths suspended in the dykes and depressurizing reactions.

Three different zones are often described in tensile fracture propagation, the crack itself, the intact host rock, and the **process zone** which is the immediate zone surrounding the fracture tip. (Rubin, 1995). Griffith (1920) proposed that if the released potential energy of the dyke was sufficient to provide energy for fracturing to happen, the crack will propagate. The potential energy of a dyke comes from elastic strain energy combined with any work done on the host rock by the magma or host rock.

Once the crack has been formed magma can flow through the crack. The pressure forcing the magma through the crack can come from three main sources (Rushmer, 1996)

1. Magma pressure at source of origin
2. Magma buoyancy
3. Tectonic and gravitative pressure

These pressures will be the driving forces for both crack initiation, maintaining crack opening, and allow for migration further up through the lithosphere, until the pressure either is insufficient to allow for further migration, or until the magma reaches the surface.

1.4 Structural geology and microtectonics

Magmatic processes control the initial formation of a rock in terms of texture, mineralogy and grain size. Structural processes can however overprint these processes, producing new fabrics and mineralogy. This chapter will focus on a few of the deformation mechanisms which play a role in the deformation of rocks. This information is gathered from Passchier & Trouw (2005).

1.4.1 Deformation in minerals

Feldspars

As both K-feldspars and plagioclase deform in a similar way, the deformation of the two mineral phases is often described together. The deformation of feldspars is strongly dependent on temperature and pressure.

At lower temperatures, below 400 ^{o}C, brittle fracturing and cataclastic flow is the main deformation mechanism. The result of this brittle deformation is often angular grain fragments and a large spread in grain sizes. The grains may show grain scale faults, bent cleavage and twinning with patchy undulose extinction.

For low to medium grade conditions (400-500 ^{o}C) internal microfracturing is still the dominating deformation mechanism, with some minor dislocation glide. Under these conditions features like tapering deformation twins, bent twins, undulose extinction and sharp boundary kink bands. Core-mantle structures are absent at these temperatures. A texture called bookshelf microfracturing can also be observed at this facies, by fracturing larger grains into book shaped fragments which then may be imbricated.

At medium grade conditions (450-600 ^{o}C) dislocation climb and dynamic recrystallization along grain edges starts to play an important role. This is mainly done in the bulging recrystallization (BLG) with nucleation and growth of new grains. Core-mantle structures are common at these temperatures, where the core of old grains is surrounded by a sharp contact with a mantle of new grains. Micro shear zones of recrystallized material may also develop inside the core grains.

When considering high grade conditions (600 ^{o}C) dislocation climb and recovery are more easily achieved in feldspars, and both sub grain rotation (SGR) and BLG recrystallization can happen, especially at higher strain rates. Core-mantle structures, like the ones seen in lower T regimes still happen, but the contact between core and mantle is less pronounced at these temperatures. Myrmekites in feldspars are common along foliation planes.

Lastly, for ultra-high temperatures (>850 ^{o}C) grain boundary migration (GBM) has been observed in plagioclase in the presence of a melt phase. The melt phase was determined by the occurrence of strain free interlobate grains in the presence of the deformed plagioclase.

Olivine

The controlling slip system of olivine is determined by the temperature of the system. Old olivine grains tend to show strong undulose extinction and subgrain boundaries. It has been reported by Suhr (1993) that olivine recrystallizes and fine grained concentrates in shear zones throug the process of flow partitioning. As temperatures increase, the controlling slip plane of olivine changes. At above 1250 ^{o}C a polygonal granoblastic fabric develops, consiting of strain free, recovered crystals. These grains are usually 0,4-1 mm, as flow stress may controll grain size, and mantle flow stresses are slow.

Pyroxenes

Some crystal dislocations in opx can be split into partial dislocations separated by stacking faults, where the crystal lattice may transform into the lattice of cpx. Exsolution lamellae of cpx may form along these dislocations, forming deformational exsolution lamellae of cpx in opx. At temperatures recorded in upper mantle conditions, opx can form ribbon grains with aspect ratios of 100:1. If the orientation of the opx grain is unsuitable for slip it may also form equidimensjonal porphyroclasts. Core mantle textures can be found in grains like these.

Cpx unit cells have shorter Burger vector lengths compared to opx as the unit cell in cpx in a-direction is half the length of the opx unit cell in a-direction. Because of this difference in unit cell length, and accompanying Burger vector length, the activation energy for slip in cpx is lower. Cpx therefore experiences more active slip than opx does. When cpx experiences diffusion creep this may be assisted by dynamic recrystallization and diffussive mass transfer.

Amphiboles

Amphiboles have unit cells more than twice the length of pyroxenes in the b-direction, making its Burger vectors longer. Similar to opx having longer Burger vectors than cpx, and therefore being more rigid than cpx, the same behaviour would be expected from amphiboles. This is however not the observed behaviour of amphiboles.

At temperatures 650-700 ^{o}C the dominating deformation mechanism in hbl is brittle fracturing and dissolution precipitation. Aggregates of fine grained hbl are more likely to be the product of fracturing instead of dynamic recrystallization. Below 650-700 ^{o}C core mantle structures can also be found in hbl, but are likely the product of fracturing in combination with recrystallization. The recrystallization here is believed to relate more to differences in chemical composition, and equilibrium reactions more so than strain energy. The suspected reason for the preference for fracturing and brittle behaviour is the well-developed cleavage in {110}.

At temperatures above 700 ^{o}C in dry rocks, hbl has been observed deform crystalloplastically, and dynamic recrysrallization has been observed to be driven by strain energy. Several slip systems can be active at the same time in hbl. When there is subgrain formation in hbl these grains are usually oriented and elongated parallel to the minerals c-axis.

1.4.2 Recrystallization

Grain boundary mobility is a method in which a crystal with high dislocation density may separate out new grains along its grain edge in order to decrease the internal energy of the crystal. The formation of new grains is associated with a growth in grain boundary length, which increases the grain boundary energy, but because of the removal of the dislocations, the total free energy of the system is lowered. The formation of these new grains surrounding the old grains are therefore recrystallized grains forming from the old grain. In some solid solution minerals these new grains may vary compositionally from the old grains.

Depending on the temperature and strain rate, different recrystallization mechanisms may control the formation of these new grains. These are bulging (BLG), subgrain rotation (SGR) and high temperature grain boundary migration. These recrystallization textures can be seen in Figure 1.12.

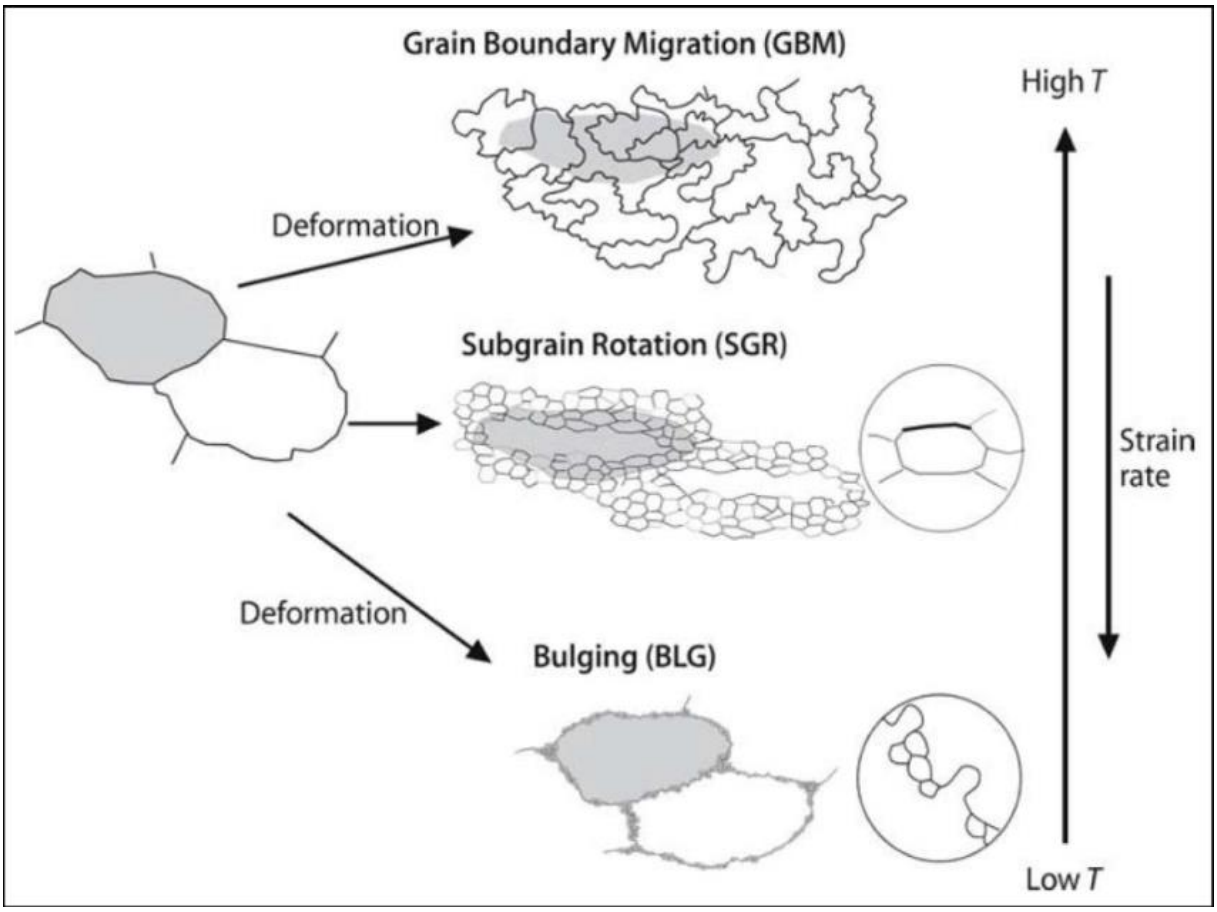

Figure 1.12. ***This figure is from Passchier & Trouw (2005). It shows texturally how different recrystallization mechanisms may look, and how they relate to eachother in terms of temperature and strain rate.***

Bulging recrystallization is the dominant mechanism at low temperatures. Crystals with high dislocation densities may experience grain boundaries bulging into the grain, forming a new separate grain from the original high dislocation density grain. This process may generate many small grains along the grain boundaries of grains with high dislocation density, as seen in Figure 1.12. These new grains may start off as bulges which form subgrain boundaries which then transition to grain boundaries, or simply by migration of grain boundaries. The cores of old grains can be surrounded by a rim of new grains, which is referred to as a core-mantle structure.

Subgrain rotation recrystallization is the next step up from BLG in terms of temperature. This form of recrystallization happens when dislocations keep being added to the crystals subgrain boundaries when dislocations can climb between lattice planes through the process of climb accommodated dislocation creep. The crystal lattice will keep rotating in relation to the subgrains surrounding, until the angle between lattices varies so much that the subgrain can no longer be considered as part of the old grain. A new grain is then formed through the process of subgrain rotation by progressive misorientation of subgrains.

Old grains in this regime tend to be deformed in a ductile manner, core-mantle textures may be present, but generally at lower strain rates. For SGR the sub and new grains tend to form sheets between old, remnant grains. Old grains may also be completely recrystallized, and turned into new or subgrains. The subgrains tend to be elongated.

High temperature grain boundary migration operates at higher temperature regimes than SGR. At these temperatures, the grain boundary mobility is so high that the grain boundaries can move through

entire crystals, removing dislocations and subgrains. Subgrains still form in this regime, but as temperatures are high and grain boundaries are mobile they may migrate away. The grain boundaries are lobate as seen in Figure 1.12, and grain sizes vary. At very temperatures the grain boundaries become even more loboid, and the grains may become strain free, as dislocations are removed.

2 Methods

2.1 Field methods

The locality for the field work in this project is in the mountains west of Reinfjord, located in Kværnangen municipality of Northern Troms. The field work was carried out over two field seasons, with the first season being in August of 2018, and the second being in August of 2019. The field seasons lasted 7 and 14 days respectively.

The mapping was done using a 4th generation *Apple iPad* with the FIELDMOVE software from *Midland Valley*. This application allowed for easy, all-weather mapping of outcrops, as well as allowing the user to take notes, describe and photograph textures, structures, and localities in the field. The information gathered is all georeferenced onto a digital map with satellite photos which was uploaded to the iPad itself. The structural measurements taken were all taken with a *Brunton Geo Pocket Transit* compass, as the iPads compass was not reliable enough for structural measurements. The measurements were therefore manually typed into the geological map.

The mapping itself was divided into a few focus points. The first objective was to get a good overview of the general geological variations in the host rock. The second objective was to map out zones believed to be related to replacive dunites. Lastly, a lot of time was spent observing and describing the different types and generations of dykes found in the ULS. One of the unique features of the RUC is the lack of vegetation, meaning the degree of exposure is high, with outcrops only being covered by snow, sand, or gravel, which makes for easier, more detailed mapping.

The sampling was done systematically throughout the field work to get a representative sample set for the southern plateau of the intrusion in terms of structures, textures and chemistry. All distinct dyke types were sampled to get chemical analyses and thin sections to see primary magmatic structures and textures together with deformation textures.

2.2 Lab work

2.2.1 Sample preparation for petrographic analysis

Cutting

After the field season in 2018 a set of 21 rock samples, both dyke and host rock, were brought back to NTNU for analyses. These samples were analysed and prepared over the academic year of 2018/2019. For the 2019 field season 22 additional samples were brought back for selection and preparation over the fall of 2019 and spring of 2020. The dyke samples were divided into different groups of dykes based on lithological and structural observations made in the field. The host rock samples were divided into groups based on where the samples were taken, and where the samples were sitting in relation to magmatic structures and serpentinization zones.

The samples relevant for petrographic analysis were cut with a rock saw in order to get a better impression of what textures and structures were present in the rock. Because of the *mm* thick weathering surface on most of the ultramafic samples, and some of the mafic dykes, cutting the rocks open was necessary to observe the smaller structures and textures. After cutting the relevant rock

samples into 1*cm* thick slabs the part of the rock sample relevant for petrographic analysis was marked out and submitted to the thin section lab for further preparation.

The thin section lab prepared 24 polished thin sections in total. The standard thin section from the lab is 46 mm long, 27 mm wide, and 30 µm thick. The primary focus of the study was magmatic processes, and late features, therefore, alteration veins, serpentinization and weakness zones were avoided. Doing this allowed for easier preparation of the thin section as well as providing a better impression of what the primary textures and structures looks like, rather than late alteration products.

2.2.2 Sample preparation for chemical analysis

All sample preparation was performed at the Dept. of Geoscience and Petroleum. The rock samples selected for thin section preparation were also relevant samples for chemical analysis to allow for correlation of the petrology of the samples to the chemistry of the samples. Therefore, during the cutting of slabs for thin sections, other parts of the sample were set aside for further crushing. The samples need to be crushed to work with the different analytical methods like X-Ray Diffraction (XRD) or ionic coupled plasma mass spectrometry (ICP-MS). To get a representative analysis, the grain size should be as similar as possible across the different minerals present in the sample. The whole process of preparing the samples can be seen as a flow chart in Figure 2.1.

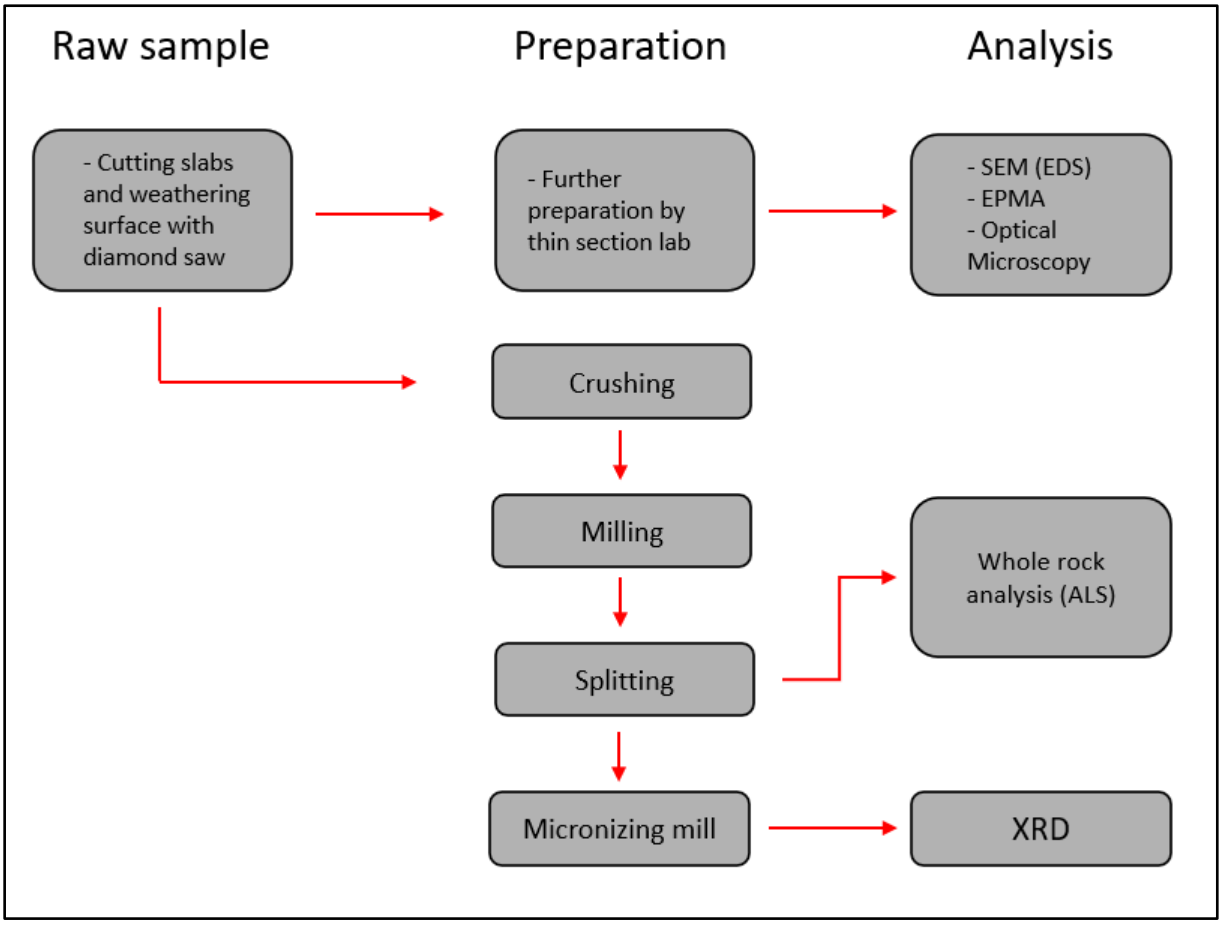

Figure 2.1. ***A flow chart over sample preparations prior to the sample analysis.***

Primary crushing

Once the relevant samples for chemical analysis were cut into a manageable size, and the weathering surface was removed the samples were crushed down to a size of <0,5 cm with the *fly press rock crusher*. The rock press is easy to clean, and mechanically simple, making the contamination risk lower than for other crushers. However, because of prolonged wear the skull crusher started shedding metallic particles into some of the samples. The samples suspected of containing metal shavings were all inspected, and no shavings were found. This could however mean ΣFe_{tot} in some samples is recorded as being higher than what is geologically correct.

Milling

After crushing the samples with the rock press, the crushed material was placed in a *Siebtechnik TS250 vibratory disk mill* for further grain size reduction. This mill, like the rock press, is a very simple mechanical mill. This translates to easy cleaning of the mill between samples, and therefore there is a minimal risk of cross contamination. The mill works by adding the crushed sample, 50g per cycle, into the chamber, between the centre plug and the outer ring as seen in Figure 2.2. The mill then gyrates the sample, meaning the grains will be crushed and grinded by the chamber rings and the chamber wall. After running cycles of 3 minutes for the hardest samples and 2 minutes for the weaker samples, the sample material was transferred back into the sample bag.

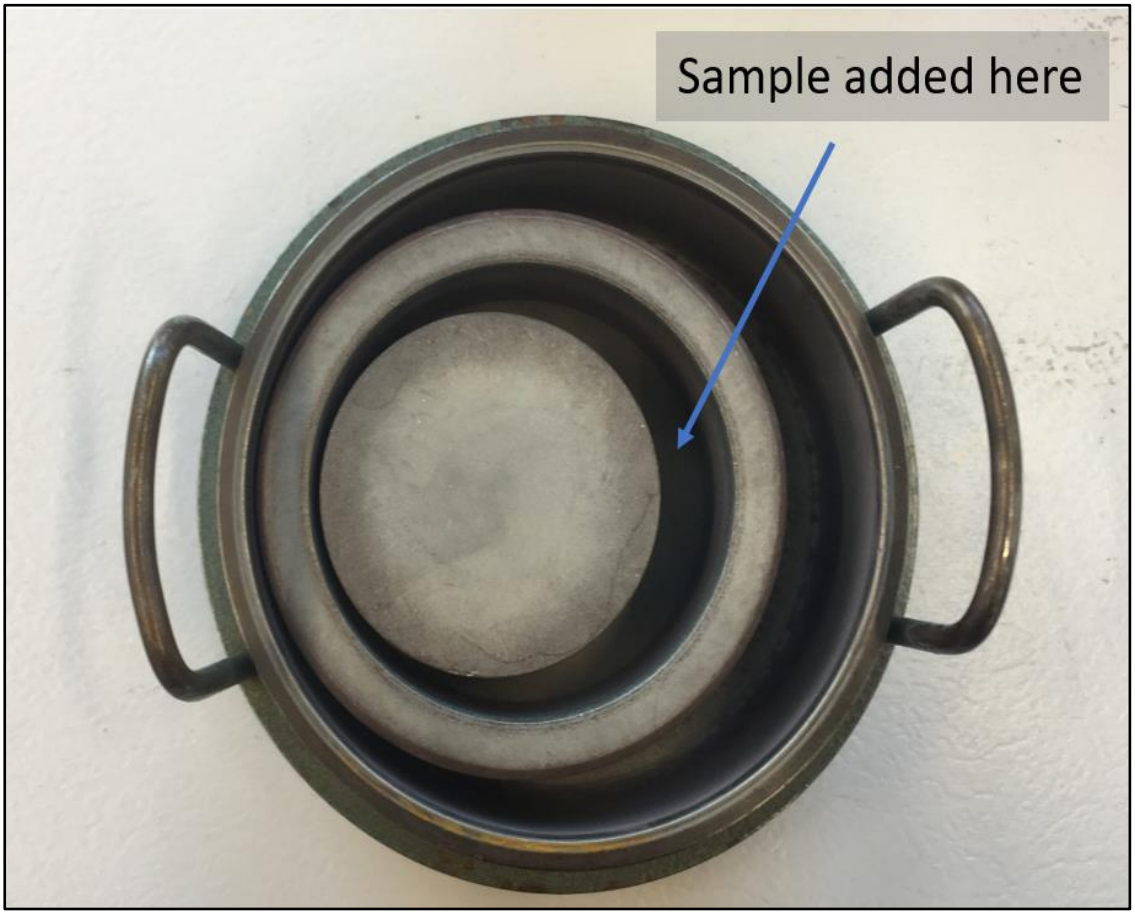

Figure 2.2. ***This image illustrates the type of milling chamber used in the Siebtechnik TS250 vibratory disk mill. This chamber is made of steel, while the one used to mill the samples form Reinfjord was a tungsten carbide milling chamber, as the steel chamber was too soft.***

Splitting

After the samples were milled to ~10µm the samples were ready to be split. The purpose of the splitter is to create statistically representative samples for chemical analysis. As some minerals, like micas and carbonates are mechanically weaker than minerals like feldspars or pyroxenes, the weaker minerals will often accumulate in the fine-grained portion of the sample. It is therefore important to have a homogenous sample set, where the sample being analysed represents the rock itself.

The splitter used for these samples is called a rotary splitter. It works by slowly adding the sample to a vibrating tray, which feeds a rotating dividing head with 8 collectors attached. After the splitting is finished, the result should be 8 separate glass containers filled with an equal amount of sample in them, as well as equal proportions of the different grain sizes. In order to obtain samples large enough for a complete chemical analysis (>100g), the contents of the glasses were mixed for some of the smaller samples.

After the samples were cut, crushed, milled and split they were sent to ALS Laboratory Group in Sweden to be analysed for whole rock (ME-ICP06), platinum group element (PGM-MS23) and trace element (ME-MS81 and ME-MS42) geochemistry. The list of all analysed elements can be found in the appendix.

Micronizing

The samples which had been crushed, milled, and split for chemical analysis had to be micronized and rounded even further before being the right size and shape for XRD analysis. The samples were micronized to a grain size <10 µm in a special plastic SAG-milling chamber filled with corundum plugs, ~1 g of rock sample and 10 ml of 96% ethanol for 2 minutes. After the sample was milled the ethanol and rock sample slurry was poured into a petri dish, which was put in a drying oven for the ethanol to vaporize away from the sample.

After the ethanol had vaporized, the sample was transferred over into an XRD quartz mount. The sample was compacted into the glass mount, making the surface of the micronized sample as smooth as possible using a small glass plate to avoid disturbance in the signal from topographic effects from the powder. When the samples were all prepared, they were inserted into the Bruker XRD, and programmed into the analytical series. The analysis then ran over night.

2.2.3 Optical microscopy

The thin sections prepared for this project were all scanned using an Olympus BX51 polarizing microscope fitted with a Märzhauzer automatic stage controlled by the Stream Motion software, in order to have a digital copy of the thin sections at the resolution of the 5x objective. The rest of the optical microscopy was done using a Nikon Eclipse E600 polarizing microscope, or a Nikon Eclipse *Ci Pol* microscope. All microscopes used in this project had both transmitted light and reflected light functions, necessary to determine both the translucent as well as opaque phases found in the samples.

Since some of the samples were going to be coated with carbon before being analysed in the SEM and EPMA, all reflected light microscopy was finished before coating, as the reflective properties of a mineral is affected when coated by carbon. The optical microscopes were also used to find and mark the areas of thin sections relevant for SEM and EPMA.

2.2.4 Scanning Electron Microscopy (SEM)

The SEM work done for this thesis was all done on a Hitachi SU6600 FEG SEM at the Dept. of Geoscience and Petroleum. Before the samples were inserted into the SEM, the samples were coated by a ca. 15 µm thick layer of carbon, using a Cressington 208 Carbon coater at the Electron Microscopy (EM) lab. This coating allows the user to run higher probe currents in high vacuum without getting charging effects on the sample, making the images captured with the SEM sharper, and more detailed. (Reed, 2005)

The SEM is a useful instrument for taking high magnification images of the sample. This is especially useful for fine-grained zones. The back-scatter detector in the SEM detects back-scattered electrons (BSE), which in return creates a brightness contrast in BSE images as a function of mean atomic number. The heavier atoms reflect more electrons compared to the lighter atoms, making minerals like ilmenite, containing Fe and Ti, brighter than minerals like plagioclase, containing Na, Ca, Al and Si. This difference in brightness is helpful in distinguishing between phases.

2.2.4.1 Energy Dispersive X-ray Spectroscopy (EDS)

The main motivation to use EDS in this project is that the grain size in the shear zones found in most of the dyke samples are to fine to observe in an optical microscope. In order to determine which phases and which elements partitioned into the different fine-grained phases EDS mapping was necessary. The EDS allows the user to quickly analyse a sample at high magnification for different elements over a designated area, with a spot size ~2µm. When doing larger scans and stitching each scan together, the covered area is usually around 200-1000µm. With the completed and stitched EDS map using the Espirit 1,9 EDS software it is possible to get an overview of chemical variations across the shear zones, and with a combination of EDS maps it is possible to determine which of the phases are present as well.

The EDS works by shooting a focused beam of electrons at the sample, which when making a map scans across the designated area. When the electron beam hits an element in the sample, an electron can be ejected from an orbital in the element, creating a vacancy in one of the electron orbitals. Since the element is unstable in this state an electron from an outer shell will make up for the instability by filling the vacancy. Since there is an energy difference between the electrons in the inner and outer shells, an X-ray is emitted, making up for the difference in energy. The X-ray is then detected by an X-ray detector, which converts the energy from the X-ray to an electric signal. (Goldstein, et al., 2012)

Each element has distinct X-ray energies for different electron shells. EDS uses this difference in energy levels to determine which elements are present, often by an element's Kα, but sometimes also the *Lα* signal depending on element. Based on the relative signal strength from the EDS it is possible to semi-quantitatively determine which mineral phases are present. Phases like amphibole, which is one of the few minerals which will give a potassium signal can be distinguished based on this. However, it is also possible to distinguish between enstatite, Mg-pyroxene, and forsterite, Mg-olivine, based on the relative signal strength from silica. This form of analysis is however not quantitative like EPMA, since there is no comparison to a known standard.

The samples were all analysed using an acceleration voltage of 15 KeV, extraction voltage of 2,20 kV and ~60 µA, with a working distance of ~15 mm. This set up was ideal for silicate analyses and also

some of the sulphides, without creating too much interference. When mapping sulphides like pn or ccp the acceleration voltage was adjusted to 20 KeV to excite the elements enough to get a signal. All EDS analysis were performed in a high vacuum <10^{-3} Pa. These settings provided the best resolution and most reliable signal strength for this type of analysis.

2.2.5 Electron Probe Microanalysis (EPMA)

Both major as well as some minor elements for the different mineral phases were analysed using the JEOL JXA-8530F Plus EPMA at the Norwegian Laboratory for Mineral and Materials Characterisation (MiMaC) at the Department of Geoscience and Petroleum. The EPMA was set with an acceleration voltage of 15 KeV, a probe current of 10 nA, and a variable spot size between 2-5 µm depending on what type of mineral and grain size was being analysed. All samples were coated before being analysed with the EPMA to avoid charging.

Compared to the EDS which detects the energy of the emitted X-rays, the EPMA uses five wavelength dispersive X-ray spectrometers (WDS). The EPMA is also equipped with an EDS allowing for fast phase determination through spot analysis, this greatly improved workflow as well as ensuring the correct minerals were analysed with the EPMA.

The instrument was set up and calibrated by Kristian Drivenes[1], who set up the analytical series for each element, which crystals to analyse with, which lines and which standards to analyse as well.

Amphibole

For amphibole measurements the elements Na, Mg, Al, Ca, K, Cr, Fe, Ni, Mn, Si, Ti, Zn, and Cl were measures. H was added as 2 wt% after the analysis was done. The standard used was a kaersutite crystal, and elemental analyses were compared to the known chemical composition of the kaersutite. The measuring time on peak T_P varied from 10-40 seconds depending on the element, with 5-20 seconds of measuring background T_B before peak, and 5-20 seconds T_B after peak. The standard deviation (SD) and limit of detection (LOD) for amphiboles is based on 106 amphibole spot analyses.

Element	Crystal	Standard	Line	S.D %	L.O.D (ppm)
Na	TAPH	Albite	K_α	1,76%	529
Mg	TAPH	Diopside	K_α	0,66%	620
Al	TAPH	Sanidine	K_α	0,36%	210
Ca	PETJ	Diopside	K_α	0,48%	212
K	PETJ	Sanidine	K_α	2,17%	205
Cr	LIF	Chromite	K_α	34,48%	168
Fe	LIF	Magnetite	K_α	1,06%	530
Ni	LIF	Pentlandite	K_α	93,8%	434
Mn	LIF	Rodonitt	K_α	23,6%	505
Si	PETH	Diopside	K_α	0,6%	475
Ti	PETH	Rutile	K_α	1,07%	458
Zn	LIFH	Zn	K_α	171,48%	317
Cl	PETJ	Tugtupite	K_α	82,39%	919

Table 2.1. ***This table shows the elements analysed in amphiboles, and which crystals, standards and lines were used to measure the signal. SD and LOD were provided in a sheet from the analysis provided in the appendix.***

[1] Postdoctoral at NTNU, and co-supervisor for this thesis

The minor elements like Cr, Ni, Mn Cl, and especially Zn have such high standard deviations, that an accurate quantification is unlikely. These elements generally occur in very small concentrations in amphiboles, which makes accurate measurements of them difficult. The major mineral forming elements occur in higher concentrations and therefore also provide more accurate measurements. Some of the minor elements are also below the LOD, meaning the signal may only come from static, and signal overlap.

Plagioclase

For the plag analyses a sanidine, diopside and albite standard were used to calibrate all measurements. These standards were from the sample set of standards used for amphibole. For some samples, particularly the samples with high water content, some of the total wt% results provided low values, some were as low as 89-90%, usually with a discrepancy in Si. This is probably due to fractures so small that they were not visible in the EDS images. These fractures could be the cause for low totals.

Element	Crystal	Standard	Line	SD%	LOD (ppm)
Na	TAPH	Albite	K_α	13,41	376
Mg	TAPH	Diopside	K_α	163,27%	183
Al	TAPL	Sanidine	K_α	9,74%	149
Ca	PETL	Diopside	K_α	2,96%	111
Ti	PETL	Rutile	K_α	8,77%	63
Sr	PETL	SrF_2	K_α	177,31%	88
Ba	PETL	Sanidine	K_α	72,54%	376
Fe	LIFL	Magnetite	K_α	182,30%	198
K	PETJ	Sanidine	K_α	18,77%	137,
Si	PETH	Diopside	K_α	-	600
Mn	LIFH	Rodonitt	K_α	-	300

Table 2.2. ***This table shows the elements analysed for the plagioclase composition, as well as which crystals, standards and lines were used. The standard deviation and limit of detection is also provided from the raw EPMA data sheet which is output from the analysis. This sheet did however not return SD values for Si and Mn. These values are therefore unknown in this analysis.***

Similar to the amphibole analysis, all spots were measured with around 10-40 second T_P, and a 5-20 second T_B. The first set of plagioclase spots which were analysed were analysed using the same setup as for px and ol. The three past analyses, where the most spots were analysed were set up using a designated plag setup. The setup used in these later analyses is the setup seen in Table 2.2. Ol and px were not analysed for Ba or Sr, as these elements would not be relevant for this type of analysis. In order to analyse all spots faster plag was therefore set up as an individual program.

Pyroxene and olivine

Px and ol were analysed using the same type of setup, where each spot was analysed for the same elements. Px grains were filled with µm scale exsolution lamellae of both Fe-Ti oxides as well as opx lamellae in cpx. These lamellae were avoided but may have been slightly incorporated in some of the analyses. The standards used for these analyses were an olivine standard, diopside standard, albite standard, and a garnet standard.

Element	Crystal	Standard	Line	SD (%)	LOD (ppm)
Na	TAPH	Albite	K_α	44,17%	746
Mg	TAPH	Diopside	K_α	7,39%	509
Al	TAPL	Sanidine	K_α	14,37%	216
Ca	PETL	Diopside	K_α	11,7%	206
K	PETL	Sanidine	K_α	560,86%	235
Cr	LIFL	Chromite	K_α	65,67%	526
Fe	LIFL	Magnetite	K_α	12,55%	432
Mn	LIFL	Rodonitt	K_α	76,07%	470
Ni	LIFL	Pentlandite	K_α	309,04%	502
Ti	PETH	Rutile	K_α	34,64%	316
Si	PETH	Diopside	K_α	-	500

Table 2.3. ***Table showing the analysed elements and which crystals were used to analyse the element. The K_α line was used for each element. The SD and LOD are also provided for each element except for Si, as the spread sheet did not include this value.***

The major mineral forming elements provide the lowest standard deviations as these values are most consistent. The minor elements such as Cr, K, Mn, Ti and Ni are often below the detection limit, and are therefore not usable for analytical purposes.

2.2.6 X-Ray diffraction (XRD)

As the different dyke lithologies vary in their mineral content it would be relevant to get quantitative mineralogy of the different lithologies using the Bruker X-Ray Diffractor D8 Advanced operated by the Chemical and Mineralogical lab at the Dept. of Geoscience and Petroleum. This XRD operated with 40 Kv acceleration voltage, 40 mA probe current, and *CuK_α* radiation of λ=1,5406 Å. This XRD analysis was performed and set up by Laurentius Tijhuis[2], and the results from the analysis were interpreted by Bjørn Eske Sørensen using the Bruker Eva software for identification and the Topas 4.2 Rietveld software for mineral mode quantification.

[2] Senior engineer at NTNU, IGP

3 Results

3.1 Field map and overview

During the field work the southern plateau and parts of the intrusion surrounding the southern lake district was mapped. The area was mapped with focus on the wehrlites, the large scale replacive dunites, and the major dyke types found on the plateau. The LSRD are seen on the map as large orange "arms" where the majority of the zones are trending NE-SW and a few minor zones are trending NW-SE. These zones are easily visible in the field due to their orange hue, and characteristic shape.

The major dyke types which were in focus are the dykes which present a large surface extent, and which are of high abundance. The dyke types are seen on the legend in the map, and are also presented in the results chapter. Rock classification diagrams are found in Appendix B.

The first dyke presented in the results chapter is the **phenocrystic hbl dyke**. This is mapped as a dark burgundy dyke trending slightly more N-S than the other NE-SW trending dykes. The dyke is a massive, 5-20 cm wide, steeply dipping dark dyke, characterised by 0,5-2 cm phenocrysts of hbl in a dark grey-green ground mass. This dyke is not as common as some of the other dykes, but still has a large horizontal extent. It outcrops on the southern side of the plateau, on the plateau itself, and also appears on the northern side of the southern lake.

The second dyke described is the **lherzolitic and composite dykes**. These dykes are found ubiquitous across the plateau, but the most massive and characteristic of theses dykes have been mapped. The lhz dykes are seen as bright green dykes on the map, and the composite dykes are seen as blue dykes. These dykes are mapped separately as they have different appearances in the field, but are described together as they relate temporally, texturally, and chemically. They are fine grained, primarily consisting of ol, px and some hbl. The composite factor is the plag veinlets/domains infiltrating these dykes, creating local pockets and enrichments of undeformed, equigranular plag, residing between the primary lherzolitic minerals.

The next dyke described is the **hornblende gabbronorite dyke**, which is believed to be one of the youngest dykes found in ULS. These dykes are mapped as two separate dyke types based on degree of deformation. The dyke changes appearance when the dykes are deformed, from a dark, relatively coarse (3-5mm) dyke with visible xenocrysts, to a very fine grained light grey dyke with distinct foliation like fabric. These dykes are often seen enveloped by a cryptocrystalline mass of ol, with a characteristic curry yellow colour, sometimes referred to as yellow shear zones, or fine grained ol rich shear zone. These zones seem to preferentially follow this hbl rich dyke type.

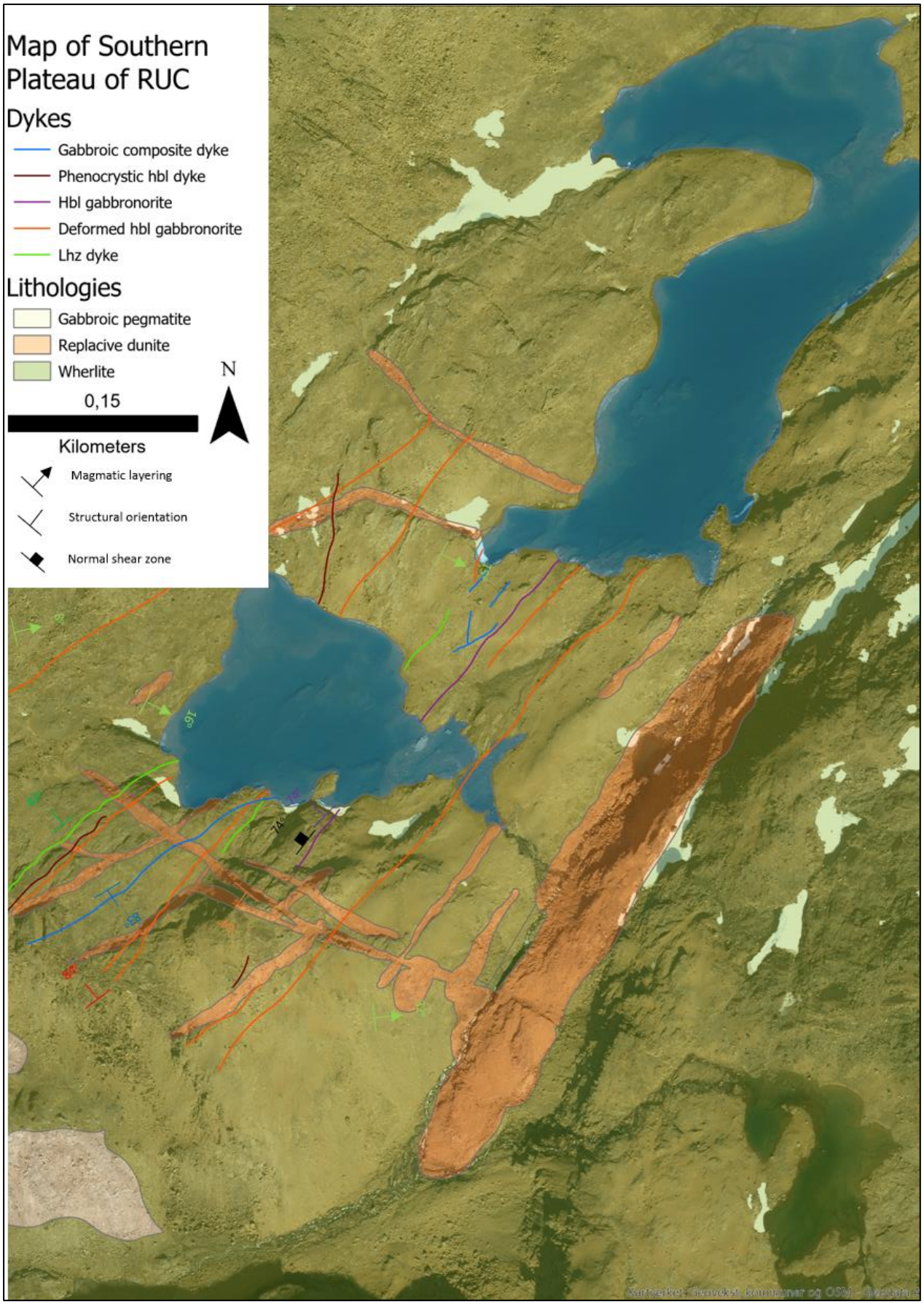

Figure 3.1. ***This figure shows the geological map of the southern plateau of RUC. The colour of measurements corresponds with the lithology from which it is taken.***

3.2 Wehrlites, and host rock features

3.2.1 Field observations

Wehrlites

The main lithology found on the Southern Plateau of the RUC, is a modally layered equigranular to porphyritic wehrlitic lithology. The rock can show a bimodal grain size distribution with respect to px and ol, with the px consequently being coarser grained than the ol. The rocks have a characteristic pale-yellow to pale green weathering colour, with dark green to black px, showing a metallic lustre and often a skeletal structure.

As ol has poor weathering resistance compared to px, the poikilitic and clustered texture of px can easily be observed in situ as the pyroxenes protrude from the weathered olivine groundmass. Because of the modal layering, the texture of the rocks also varies. The layers primarily vary with respect to px content and ol content, from ol dominated layers to px dominated layers, but accessory minerals like spinel, Fe-Ti oxides and sulphides vary within layers.

The transition between the layers of wehrlite, dunite and olivine px can sometimes be observed as sharp contacts as seen in Figure 3.2, or as a gradual transition between the two phases, where the content of px decreases proportionally with an increase of the ol content as seen in Figure 3.3. Some layers are poor in pyroxene, but rarely have a pyroxene content <10% in the primary layering, meaning the layers gradually vary from an olivine pyroxenite to an olivine rich wehrlite as seen in Figure 3.2. The px can vary form 1-2 mm in size to 1,5-2 cm aggregates of px crystals in the most coarse-grained parts of the intrusion varying in percentages, from ~15% up in cpx poor layers to ~45% in px rich layers.

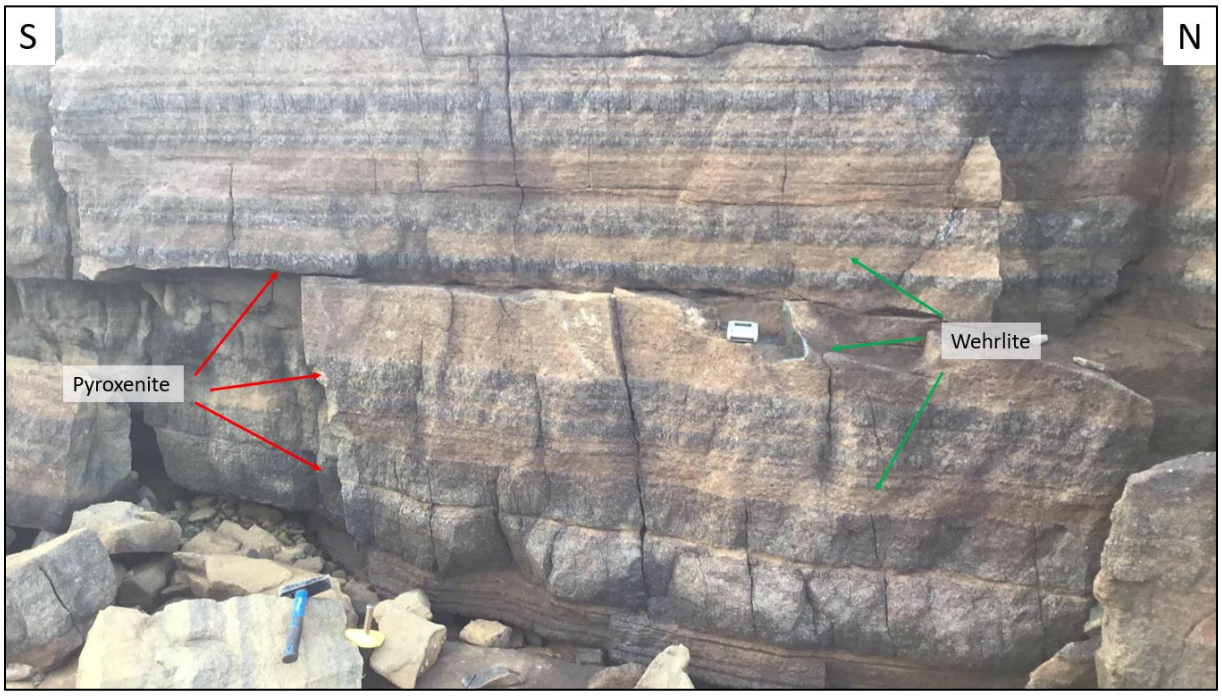

Figure 3.2. ***Modal layering in the wehrlite. Dark layers have higher px content than lighter, orange-yellow layers. The contacts seen here are sharp, layering contacts. Compass for scale.***

As the plateau is sub-parallel to the original magmatic layering of the intrusions it is difficult to observe the layering of the intrusion on the plateau itself. The general trend of layering for ULS is gently dipping (10-20°) towards east, making the variations in layering more difficult to observe on the sub-horizontal

plateau. The variation in layering is more easily observed in the western hillside of the plateau. These textural variations are, however, the same variations found in the vertical walls where the primary magmatic layering is more visible. This can explain some of the local variations in texture and px content across the plateau.

Figure 3.3. ***Picture showing one of the sampling localities from the second field season. The bottom of the outcrop consists of a metre-thick layer dominated by coarse, porphyritic, equigranular px, and medium grained olivine making up the ground mass. This layer is overlain by a 10 cm horizon of olivine clinopyroxenite, which grades up into cyclic variations of cm thick dunitic layers, and more massive metre scale wehrlitic layers.***

As can be seen in Figure 3.2 and Figure 3.3 the intrusion shows layering varying from sharp, distinct contacts, to more gradual grading contacts. These variations in layer lithologies imply some form of recharging mechanic must be in place in the magma chamber controlling the cyclical variations.

Smaller areas of “replacive dunite” (Larsen, et al., 2018) can be found throughout ULS. They migrate as irregular shapes through the wehrlite, often with undulating, sharp contacts, indicating a strong chemical gradient between infiltrating melt and the existing wehrlitic mush. These replacive dunites are considered to be one of the recharge pathways for melt throughout the magma chamber and are used to interpret intra-chamber flow and turbulence.

The px content of the dunite varies strongly throughout, and replacive dunite is often used as a field name, indicating an infiltration of melt depleted in px. The replacive dunite is however not a dunite sensu stricto, but rather an ol rich wehrlite. Cpx crystals are here seen as dark, often green crystals in the beige yellow weathered olivine matrix. Variations in the replacive dunite in the form of variable amounts of px can be seen in Figure 3.4.

Figure 3.4. ***Replacive dunite in the ULS wehrlite. The replacive dunite has a characteristic irregular shape, with flame like off-shoots into the wehrlite. Patches close to the dunitic zone vary in cpx content.***

The flame like pathch of dunitic material found in Figure 3.4 is an example of a primary magmatic structure ubitquitus throug both ULS and CS. As seen in the figure the dunitic melt appears to have opened up the wehrlitic mush, filling the opening with dinitic melt, assimilating parts of the wehrlite, seen as “ghost rafts” shown in Figure 3.5.

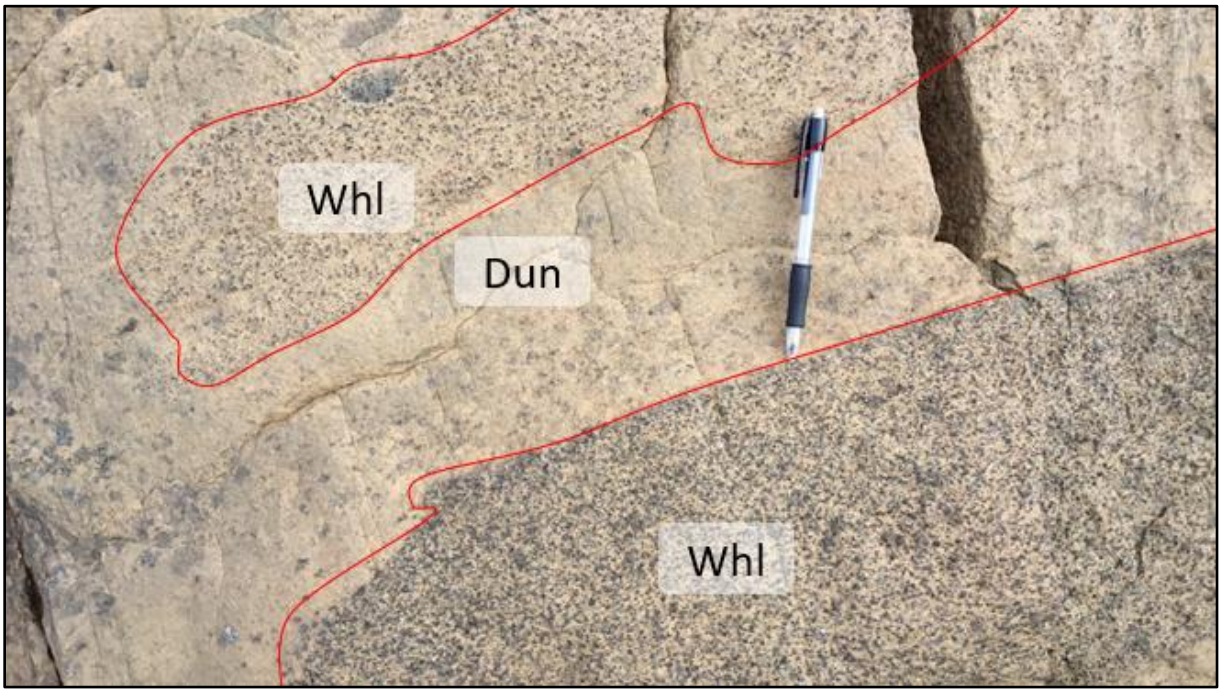

Figure 3.5. ***Contact between a px rich wehrlite and a px poor replacive dunite. The dunite contains a “ghost raft” of wehrlite, like a xenolith. Contacts between wehrlitic domains and dunitic domains marked in red.***

The contact between the wehrlite and replacive dunite varies between being a sharp contact as seen in the bottom part of Figure 3.5, to a more gradual, diffuse change towards a more px rich domain as seen in the ghost raft when moving from the dunitic domain into the wehrlitic domain as seen in the top of the image. The ghost raft is relatively depleted in px compared to the wall rock in the bottom right of the figure.

Structures like the infiltrating dunitic melt observed seen in Figure 3.5 are present in many localities. Varying degrees of melt mixing, melt reactions consuming px, and asimilation of wehrlitic material is common. This combined with varying textures of px is also a normal feature. Figure 3.6 shows a variety of px textures found in certain layers of ULS. Instead of having large, single solid crystals of px, they form spherical flower-like aggregates of px.

Figure 3.6. ***Poikilitic cpx found in ULS. Groundmass in this area is primarily ol, and px content appears as 2-3 cm, spherical, skeletal px crystals. These are 3D structures, which appear as circular flower-like poikilitic crystals where the cavities of the crystals are filled with ol groundmass.***

The poikilitic texture shown in Figure 3.6 is seen in local areas and constraint to certain layers. This seems to be one of the layering styles of ULS, and appears to be bound to primary magmatic layering rather than intruding melt like the infiltrations of replacive dunites.

Px Pegmatite

Recharges of px rich melts are also seen, and seem to intrude later than the dunitic, px poor melts. As seen in Figure 3.7, monomineralic coarse grained aggregates of px with crystals being as large as 5 cm,

referred to here as a px pegmatite can be found unsystematically scattered throughout ULS. Sometimes these pegmatites appear as dyke like bodies, with a near vertical dip. In other localities they appear as blobs, or isolated pockets of peg, cutting the primary layering of ULS.

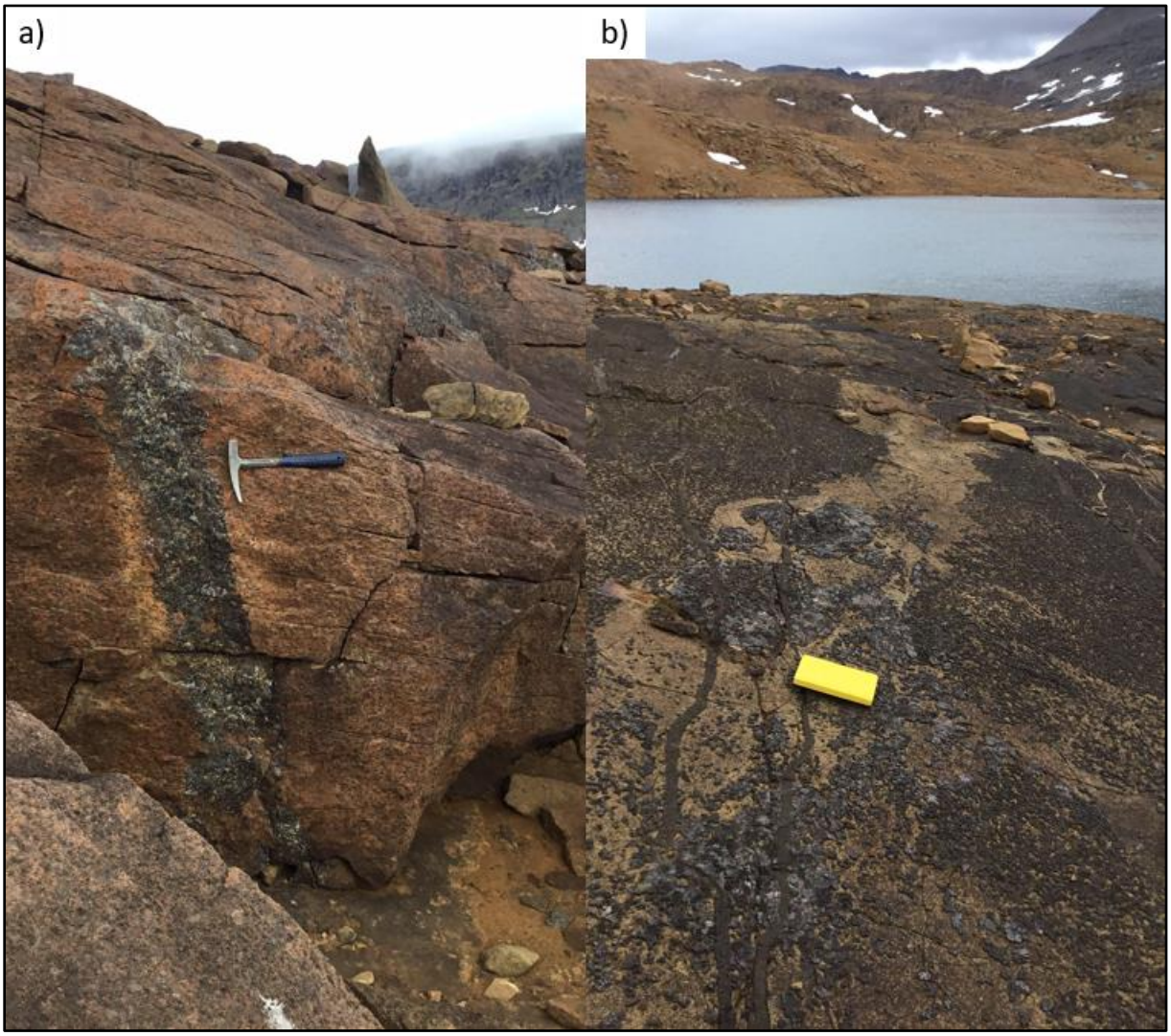

Figure 3.7. ***This figure shows infiltration of a coarse cpx pegmatite into ULS. a) shows a dyke like intrusive style, with a sharp straight contact, 20cm wide and with a large extent. b) shows a less connected style of intrusion, with isolated stocks and blobs of cpx pegmatite. The pegmatite seems to preferentially follow an existing path of replacive dunite as it intruded.***

The contacts between the pegmatite and surrounding wehrlite is highly irregular and undulating. The individual blobs are especially indicative of the pegmatite having intruded ULS while the wehrlite was still a mush. Creating such undulating geometries would be implausible under more brittle conditions. The px pegmatites are therefore considered primary magmatic infiltrations of px rich melt into ULS.

The melt creating the px pegmatites must be fundamentally different from the infiltrating dunitic melt seen in Figure 3.4, as the chemistry, mineralogy and grain size is vastly different. In order to create a grainsize this large diffusion rates must be high, with substantially lower diffusion rates than what is seen in the dunites.

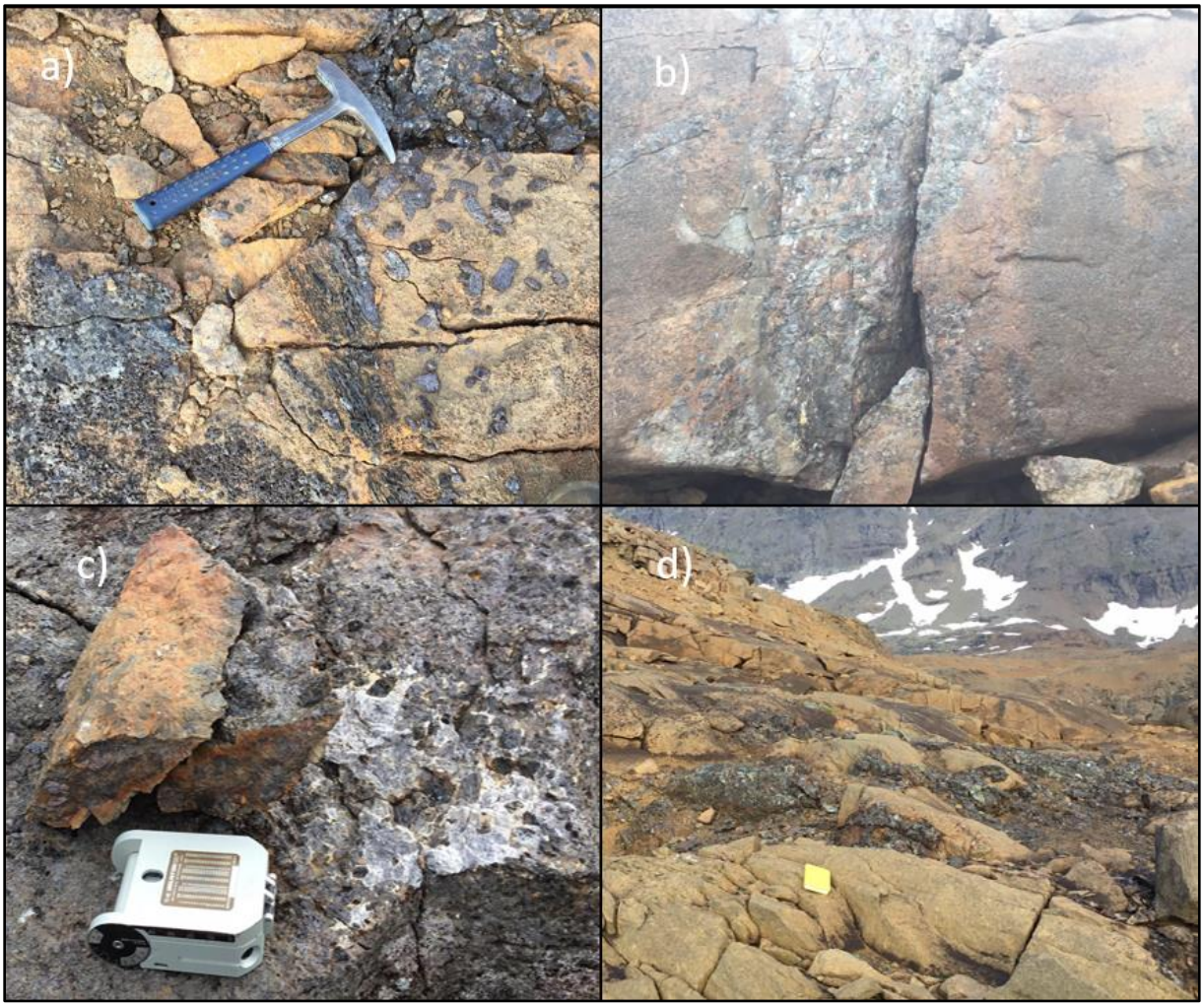

Figure 3.8. ***This figure contains four images showing features observed in the pegmatite. a) This image is showing individual grains of px in a wehrlitic groundmass close to a 15 cm body of pegmatite located above the hammer head. The px grains are also smeared out in a sinestral fashion by one of the shear zones. These grains show a surface covered in small cavities ~1-2 mm wide, where mineral inclusions like ol could have been weathered away, exposing a cavity. b) shows a plug of px pegmatite in a north west facing wall on the plateau. The peg has similarly to Figure 3.7a) a steep dyke like emplacement style. The plug here however has less of a sharp contact, and it seems like there are settling processes taking place, as some px grains show an SPO, indicating some degree of flow in the chamber. The pegmatite intrudes more irregularly into the host rock, indicating intrusion into a less solid material. c) shows a different type of pegmatite, where instead of the pegmatite consisting only of coarse grained px the pegmatite consists of coarse 1-2 cm plagioclase, and possibly some px and nepheline seen as the leucocratic part of image c), right of the compass. d) is one of the pegmatite fields on the southern part of the plateau. This portion of the plateau has several irregular 1-2 m bodies of pegmatite scattered across a 100x50 m area. These bodies are possibly connected in a 3D structure.***

The intrusion of the pegmatites seems to follow the infiltration of the replacive dunite in certain parts of ULS, and similarly to the replacive dunite also seems to have infiltrated into a mushy wehrlite as the contacts are often irregular but sharp. The pegmatite can however also show more diffuse infiltration as seen in Figure 3.8a), where individual coarse grained px crystals sit in a wehrlitic groundmass, isolated from the typical metre scale bodies of pegmatite found throughout ULS.

Large Scale Replacive Dunites

In Larsen, et al. (2018) large scale replacive dunitic (LSRD) zones were identified. The zones discussed in this paper are different from the replacive dunite infiltrations found in the localities from Figure 3.4 and Figure 3.5 as these replacive dunites described are local infiltrations of dunitic melt, often on the scale of 10's of cm, and the contacts resemble mush infiltration with highly irregular contacts. The

replacive dunites described in Larsen, et al. (2018) are map scale, several metre-wide zones, which span out 100's of metres throughout CS and ULS. These zones can easily be identified on the geological map.

Figure 3.9. ***This image shows observed features in the larges scale replacive dunites. a) This photo is waken from one of the E-W trending replacive dunites. The rock is here seen heavily jointed with serpentine covering the jointing surface. b) A gradual transition from the large replacive dunite with its characteristic orange yellow weathering colour on the right side of the contact can be seen here. The wehrlite seen with a greenish grey weathering colour is seen on the left side.***

The replacive dunite zones are well mapped across the southern plateau of RUC. Figure 3.9 shows the transition between the replacive dunite and the host wehrlite. The contact between these two phases is always seen as a diffuse, gradual change where the rocks distinguished by their weathering colour. The orange yellow weathering colour of these zones are characteristic and can be followed in the field across the entire plateau.

The zones are cut by dykes, meaning if this is a true magmatic intrusive process it must predate the intrusion of dykes throughout the magmatic series. These zones are also associated with strong jointing features, where subvertical joints follow the strike of the replacive dunites. These joints are commonly filled with serpentine, and other late hydrous alteration minerals. Dykes found in these large replacive dunites are also jointed with serpentine filled joints.

The large scale replacive dunite has a characteristic jet-black colour in fresh surfaces and are softer when scraped with a hammer compared to the wehrlite. Primary magmatic layering does not seem to be well preserved in these zones, however, the amount of px does not seem to change drastically from wehrlite to replacive dunite.

3.2.2 Petrological and mineralogical results

3.2.2.1 Wehrlite

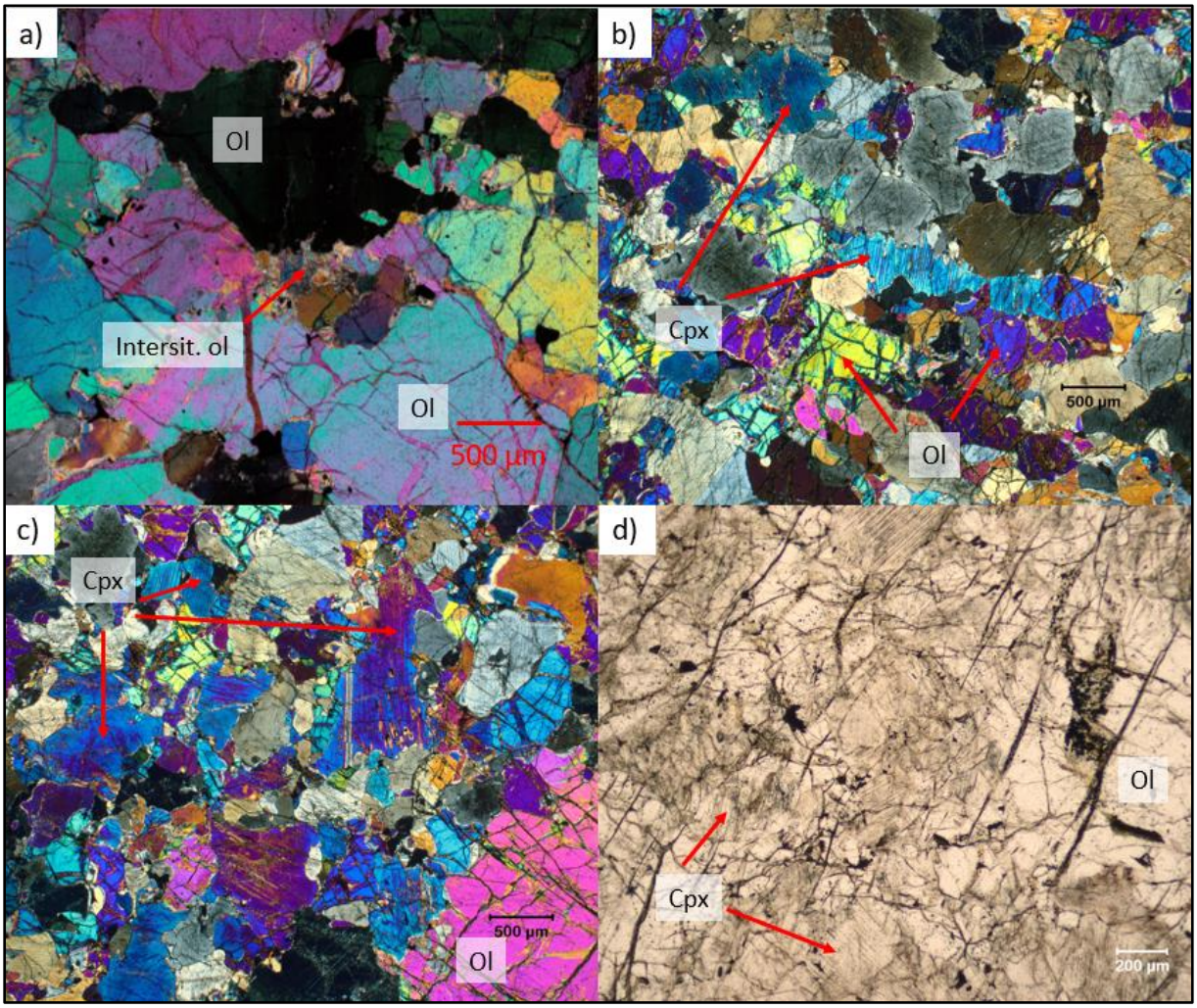

Figure 3.10. ***This figure shows four images taken using an optic microscope of wehrlite and dunite samples. a) This picture is take in one of the dunitic domains of the host rock in xpl. The sample is dominated by ~2mm subhedral ol grains with high 3rd order green and pink colours labelled ol in the image. These large grains are considered to be the cumulate phase in this sample, with a finer grained interstitial phase of ol labelled intersit. ol in the picture. This sample is poor in px, and is taken from one of the more dunitic layers in the intrusion. The interstitial grains occur locked between the larger ol grains, and are most likely to be crystallized after the large cumulus ol phase. Some of the ol grains display wavy extinction, where the extinction moves like a wave through the mineral upon stage rotation. This is an indication of kink banding in the mineral. b) This sample is taken from one of the pyroxenitic layers. There seems to be a slight layering fabric of the px grains, as some of these are elongated and oriented parallel to each other. The sample is dominated by cpx, where some grains are marked by arrows, often seen as anhedreal minerals with exsolution lamellae of opx or iron oxides and 2nd order blue to purple interference colours. The sample also contains some ol, seen as fractured crystals with 3rd order green, yellow and purple interference colours. There seems to be a bimodal distribution of grain size with some interstitial grains being smaller than the larger subhedral grains. c) This picture is taken from the same sample as seen in b). The main mineral in the sample is cpx and opx with some ol. The interstitial phases are often slightly edge rounded. The large subhedral 3rd order pink ol grain labelled as ol on the picture has minor fractures throughout the grain filled with iddingsite, a hydrous alteration mineral. Grain boundaries between the larger grains are interlocking, and appear to have crystallized under equilibrium conditions. d) This picture is taken using ppl to illustrate the optical difference in ppl between ol and px in the host rock. The px grains have a more cloudy appearance when compared to the ol grains. The iddingsite filled fractures are also more visible in ppl, as these veins have a brownish translucent colour in ppl. This picture is taken from the same sample as in picture b) and c).***

Based on the images in Figure 3.10, it is apparent that the mineralogy of the wehrlite changes with each individual layer. The image from Figure 3.10 a) is taken from a more dunitic domain, and contains much less px than the samples in b), c) and d). These cyclical variations observed in these images are also observed in the field, as seen in Figure 3.2.

The mineralogy of the host rock has been analysed using XRD. The samples analysed however are more dunitic than the sample observed in Figure 3.10 b), c) and d) as these have a px content close to a pyroxenite rather than a wehrlite.

The small interstitial ol and px grains are believed to be an intercumulus phase, crystallizing later than the larger cumulus phases. The smaller grain size and rounded shape indicate some form of equilibrium reaction has happened between the two phases.

The XRD results from the wehrlite samples are shown in Table 3.1. These samples are taken from dunitic domains in the host rock.

Sample	Rock type	Fo	Hbl	Di	En	Bt	Lz
JS18-3	**Wehrlite**	80,41	0	15,88	3,23	0	0,48
JS_2_4	**Wehrlite**	89	0	5,39	0,001	0	5,61
JS01-CR	**Wehrlite**	79,66	1,99	10,93	6,18	0,93	0,31
JS_2_5	**Wehrlite**	94,47	0	4,3	0	0	1,22
JS_2_6	**Repl dunite**	96,32	0	3,68	0	0	0
JS_2_13_3	**Repl dunite**	31,45	0	36,71	0	0	31,84
JS_2_13_4	**Wehrlite**	69,46	0	25,77	4,2	0	0,56
JS_2_13_5	**Wehrlite**	59,6	1,5	29,31	8,45	0	1,14
JS_2_15.G_2	**Wehrlite**	73,49	0	17,3	2,46	0	6,75
JS_2_15.G_3	**Wehrlite**	17,76	1,7	69,85	10,46	0	0,24
JS_2_16	**Wehrlite**	44,6	0	31,15	0	0	24,26
JS_2_19-B	**Wehrlite**	75,4	0	18,48	0	0	2,82

Table 3.1. ***Table showing average mineral composition for wehrlite samples. Results obtained from XRD analysis based on two samples.***

The wehrlite is dominated by olivine with an average of 73,56 ± 22,6% and has a diopside content of 21,98 ± 17,8%. This classifies the host rock as a wehrlite, with some samples classified as true dunites. The enstatite content varies as the serpentinized samples often have no enstatite. The content is however low with a maximum of 10,46% in a pyroxenite sample. The hbl content is relatively high in some samples, with an average value of 1,30 ± 0,89% for the hbl bearing samples. However, only 4 samples have a measured hbl content. One sample has a recorded bt content at 0,93%. This has not been confirmed optically and may be an erroneous analysis, or it may be a contamination from the dyke which is related to this sample.

There are also accessory opaque minerals identified optically as ilm, pyh, pn and ccp, these are however present in low volumes in the wehrlite. The iron oxides like ilm or mag often occur as lamellae in px crystals or as small interstitial grains between other silicate minerals. These inclusions are often on the scale of 5 by 25 µm and would be difficult to detect in an XRD analysis as seen in Figure 3.11.

Based on EPMA analyses done in the wehrlite have a cpx content as shown in Table 3.2

Element	Cpx mass%	Ol mass%
SiO_2	49,76%	39,16%
Al_2O_3	4,50%	0,0%
FeO	5,78%	18,42%
CaO	19,94%	0,09%
MgO	17,34%	43,17%
Na_2O	0,53%	0,04%
K_2O	0,0%	0,0%
Cr_2O_3	0,49%	0,01%
TiO_2	1,19%	0,03%
MnO	0,14%	0,26%
NiO	0,04%	0,21%

Table 3.2. ***Table showing EPMA results from ol and cpx analyses from JS_2_19-C, a wehrlite sample.***

The average mineral formulas for the analysed cpx in the wehrlite is

$$(Ca_{0,95}Na_{0,05})(Mg_{0,82}Fe_{0,14}Ti_{0,04})\ (Si_{1,83}Al_{0,17})O_6$$

while the average mineral formula of olivine based on the analysis is

$$\left(Mg_{0,81}Fe_{0,19}\right)SiO_4$$

Both the ol and cpx are dominated by Mg, making the minerals plot within the forsterite field and diopside field, respectively. The small contribution of Ni in olivine is not enough to make it a significant impact on the mineral formula and could possibly be caused by pentlandite inclusions. The Ti content in cpx can be an effect of exsolution lamellae found naturally in the cpx.

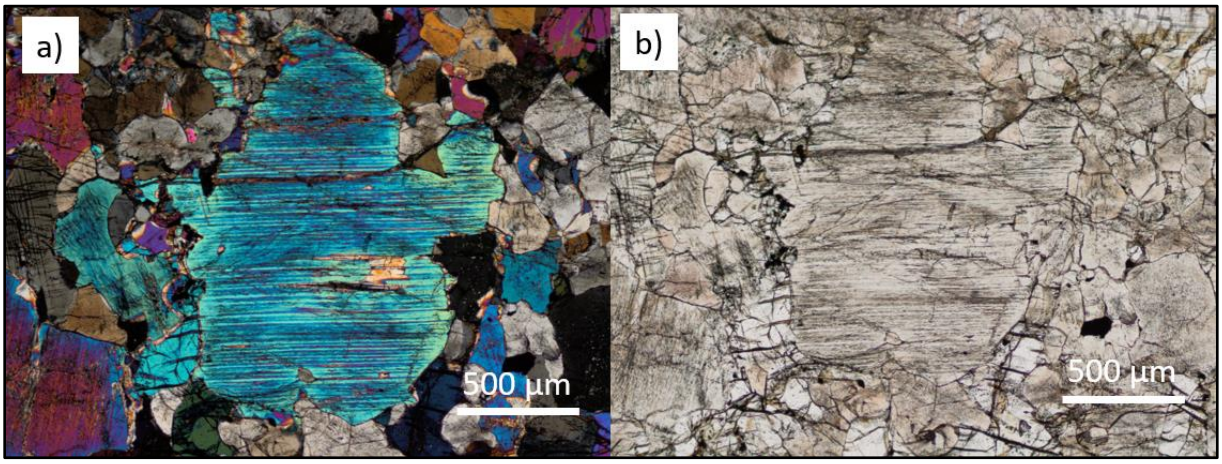

Figure 3.11. ***CPX grain from JS_2_19-C showing iron oxide filled lamellae. These exsolution lamellae consist of opx and ilmenite. Image a) is shown with XPL, image b) is in PPL. Primary magmatic pyroxene from a pyroxene rich layer in ULS.***

The cpx grain seen in Figure 3.11 shows primary magmatic interlocking grain boundaries with the surrounding px and ol grains. As this sample is taken from a pyroxene rich layer of the ULS, this sample is richer in px than the average wehrlite, and therefore also has some larger px grains. This grain is roughly 1 mm in size, surrounded by smaller grains of ol and px. The grain has a characteristic “dirty” look in PPL as the grain has a high density of exsolution lamellae.

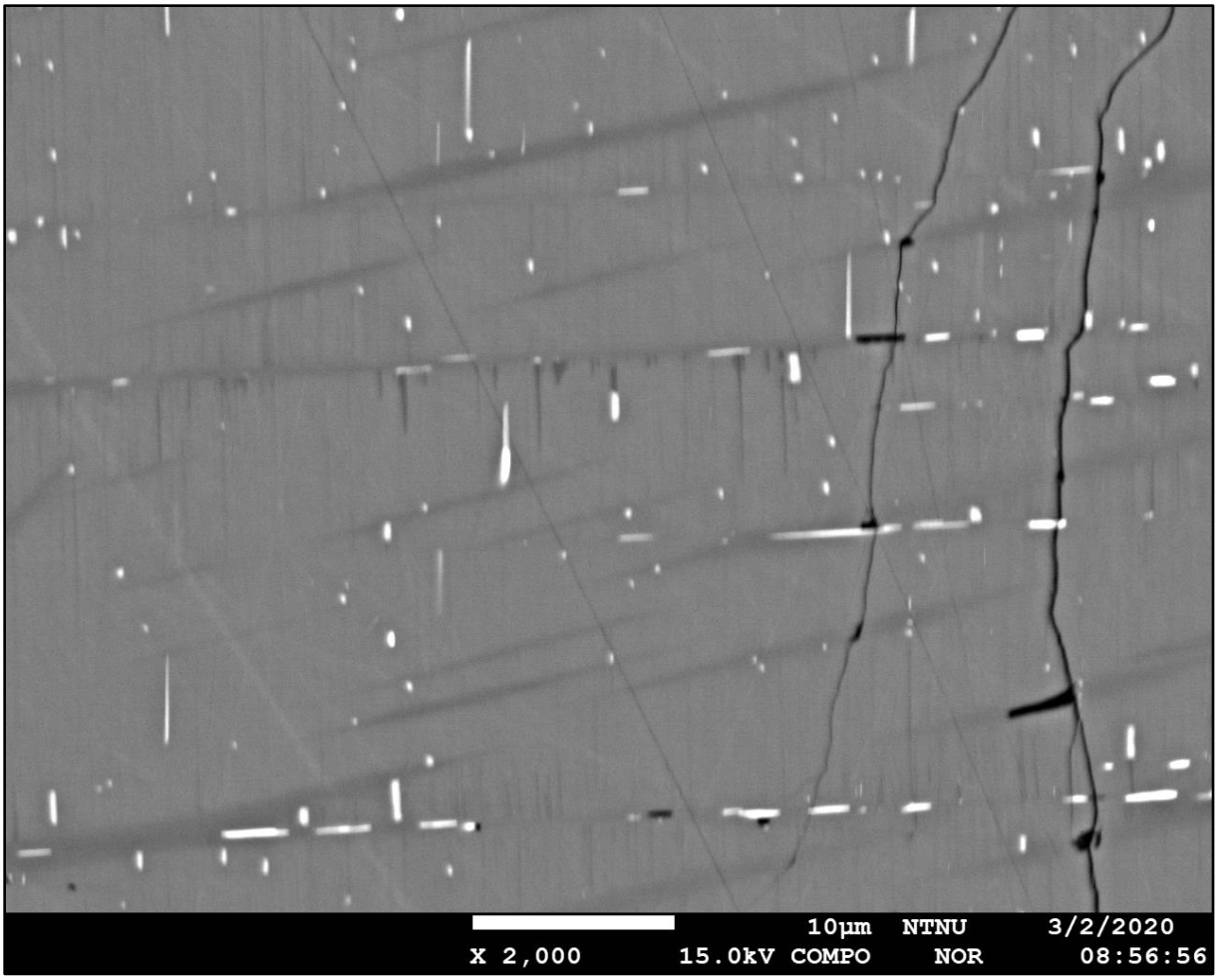

Figure 3.12. ***This image is a high magnification (2000x) BSE image taken from a px grain in a wehrlite sample. The bright laths seen here are ilmenite lamellae. These lamellae seem to closely follow the 90º cleavage of the cpx.***

The exsolution lamellae seen in Figure 3.12 are a common feature found in the cpx throughout the wehrlite and px rich dykes. As these lamellae are so closely packed, and sit imbedded in the mineral they might give falsely high Fe-Ti values for EPMA analyses. Since the laths systematically follows cleavage, it is more likely that these are in fact exsolution lamellae rather than inclusions found in the minerals.

The dunitic domains as seen in Figure 3.5 tend to be coarser grained than the wehrlitic domains. Figure 3.13 shows a microscope picture taken from of a sample from the dunitic domain. The grain size in this sample is ca. 2 mm and the rock is mainly comprised of ol with minor cpx and some oxides like ilmenite and magnetite, as well as some later alteration products such as serpentine and iddingsite filling fractures in the ol. The ol grains found in Figure 3.13 show ol grains which crystallized in equilibrium. The grains are interlocking and seem to have crystallized under static conditions. There is little to no fabric be found in these rock samples. There are no reaction zones between olivine grains either.

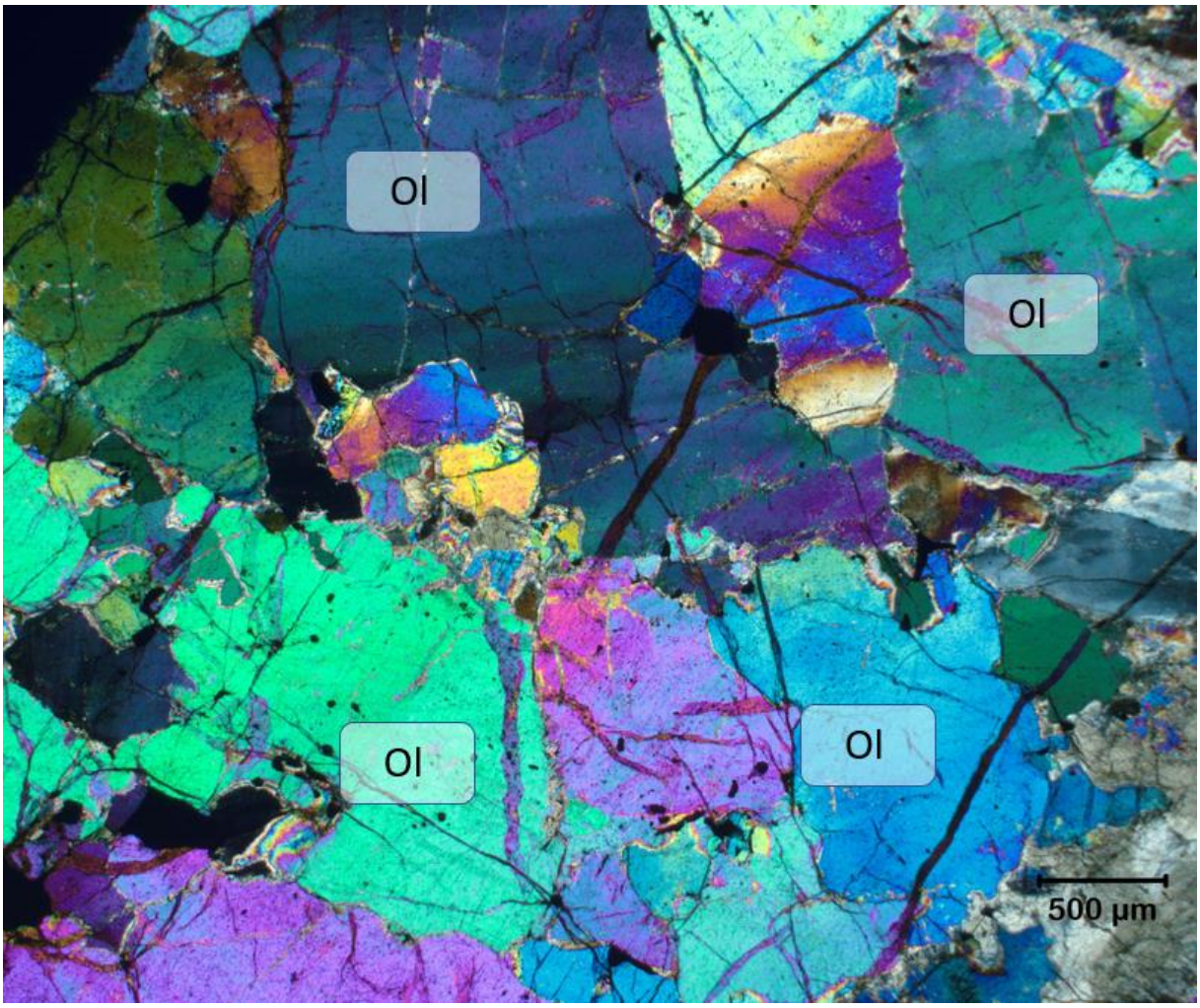

Figure 3.13 : ***A picture showing primary magmatic texture in a dunitic rock sample. Primarily olivine in sample. 2,5x magnification. Grain boundaries are interlocking, and somewhat irregular between coexisting ol grains***

The ol grains shown in Figure 3.13 are also rich in minor inclusions of minerals like ilm and spinel. Some of the ol grains also contain fluid inclusions <1 µm. The olivine grains also show a slight degree of undulating extinction in this sample, seen in the large, dark blue to dark purple ol grain at the top of the image. This indicates some degree of strain is accommodated in this sample. The sample is taken 1,5 cm from a dyke contact where a phenocrystic hbl dyke intruded.

3.2.2.2 Pyroxene pegmatite

The px pegmatite was also analysed using XRD. As the average grain size in this lithology is up towards 5 cm, getting a statistically representative sample was difficult, as this sample would be too large to transport in the field. The results from this single sample may therefore not be entirely representative of the px pegmatites throughout the ULS.

Mineral	Percentage
Forsterite	4,22%
Hornblende	3,10%
Diopside	29,42%
Enstatite	60,38%
Ilmenite	2,98%

Table 3.3. ***XRD results from px pegmatite sample JS16-3.***

The sample is dominated by enstatite and diopside, with pyroxenes making up 89,80% of the entire sample. The additional minerals like fo, hbl and ilm most likely sit as inclusions in the large px grains, as the sample appears to only contain px in hand specimen, with no apparent additional mineral phase existing between grain boundaries. On weathered surfaces the px grains often have cavities where minerals like ol used to reside.

There are local variations in the pegmatite as seen in Figure 3.8c), where the pegmatite locally is enriched in plagioclase. These pegmatites are often located closer to the southern gabbro bodies in the marginal zone.

3.2.2.3 Replacive dunite

In addition to the samples of wehrlite that were taken samples were also collected from the LSRD.

Sample	Rock type	Fo	Hbl	Di	Lz
JS17-2	**Repl dunite**	40,99%	0,26%	16,95%	41,8%
JS_2_13_3	**Repl dunite**	31,45%		36,71%	31,84%
JS_2_16	**Repl dunite**	44,6%		31,15%	24,26%

Table 3.4. ***This table shows XRD results from large scale replacive dunite samples.***

There is a significant mineralogical change from the wehrlite as seen in Table 3.1 to the LSRD as seen in the XRD results from Table 3.4.

The samples are strongly serpentinized compared to similar wehrlites as seen in the analysis in Table 3.1. The forsterite content for JS17-2 is reduced by ~40%, and the enstatite content is completely consumed according to the XRD analysis. The diopside content of 16,95% is comparable to other unserpentinized samples of wehrlite. There was no measured en in these samples, and a significant reduction in ol content.

When observing these zones in the field, there seems to be a change in mineralogy, namely a decrease in px content. This observation is confirmed by this XRD analysis, as the enstatite component is in fact absent in this sample.

3.2.3 Whole rock geochemical results

The geochemical results were plotted with measured known cpx and ol compositions from the intrusion. There is a systematic increase in CaO and Al_2O_3 with an increase in SiO_2, and a decrease in FeO and MgO with an increase in SiO_2. This implies ol is strongly controlling fractionation. As ol crystallizes it pulls MgO and FeO out of the melt. These results are observed in Figure 3.14. These trends are indicated by arrows and shows the relationship between these elements and the major rock forming minerals in these samples.

The whole rock chemical analyses for major elements is presented in Table 3.5

Label	Rock type	SiO2	Al2O3	FeO	CaO	MgO	Na2O	Cr2O3	TiO2	MnO
JS01-CR	Wehrlite	39,6	1,5	16,9	2,27	38	0,15	0,298	0,2	0,2
JS16-3	Px peg	50,3	3,51	13,7	7,47	23,1	0,21	0,199	0,84	0,22
JS17-2	Repl dunite	37,6	0,48	15,1	2,06	33,5	0,04	0,13	0,12	0,18
JS18-3	Wehrlite	39,9	0,62	16,25	3,39	37,1	0,06	0,162	0,14	0,2
JS_2_4	Dunite	38,7	0,19	17,6	0,67	41,5	0,04	0,066	0,04	0,2
JS_2_5	Repl dunite	38,3	0,22	16	0,56	42	0,04	0,075	0,04	0,18
JS_2_6	Wehrlite	39,5	0,24	17,3	0,5	43,5	0,04	0,088	0,04	0,19
JS_2_13_3	Repl dunite	38,7	1,15	14,35	3,93	31,8	0,12	0,216	0,29	0,17
JS_2_13_4	Wehrlite	40,6	1,07	15,8	4,65	35,2	0,15	0,246	0,27	0,19
JS_2_13_5	Wehrlite	41,6	1,85	15,85	6,78	31	0,22	0,228	0,49	0,19
JS_2_15.G_2	Wehrlite	39,9	0,62	16,25	3,3	36,8	0,1	0,204	0,13	0,19
JS_2_15.G_3	Wehrlite	48	2,76	9,16	15,65	21,8	0,38	0,78	0,56	0,15
JS_2_16	Repl dunite	38,7	0,9	14,15	4,27	33,1	0,13	0,307	0,2	0,17
JS_2_19-A	Wehrlite	40,3	0,84	20,3	3,29	36,2	0,11	0,096	0,21	0,22
JS_2_19-B	Wehrlite	40,8	1,03	18,3	4	36,2	0,13	0,123	0,27	0,21
JS_2_19-C	Wehrlite	45,1	2,62	13,3	10,8	26,4	0,3	0,336	0,68	0,18

Table 3.5. ***Major elements based on whole rock analyses are presented in this table. The table contains wehrlites, dunites, replacive dunites and px peg analyses.***

There is a large accumulation of wehrlitic compositions which fall close to the composition of ol, while some plot closer towards the cluster of cpx analyses. Most of the samples fall along the mixing line between ol and cpx, indicating that these two minerals have the main control on fractionation when looking at the wehrlites.

The LSRDs plot slightly away from the rest of the wehrlites, as they are poor in SiO_2 compared to the wehrlites. This is probably due to the serpentinization as seen by the XRD results in Table 3.4 as the relative SiO_2 is lower for lizardite than for minerals like ol and cpx.

The px pegmatite also plots away from the rest of the trends as this sample is poor in ol (<5%), with the major controlling mineral in this sample being enstatite. This makes the mixing line between cpx and ol non applicable for this specific sample since enstatite has different Fe/Si and Mg/Si ratios than ol and cpx.

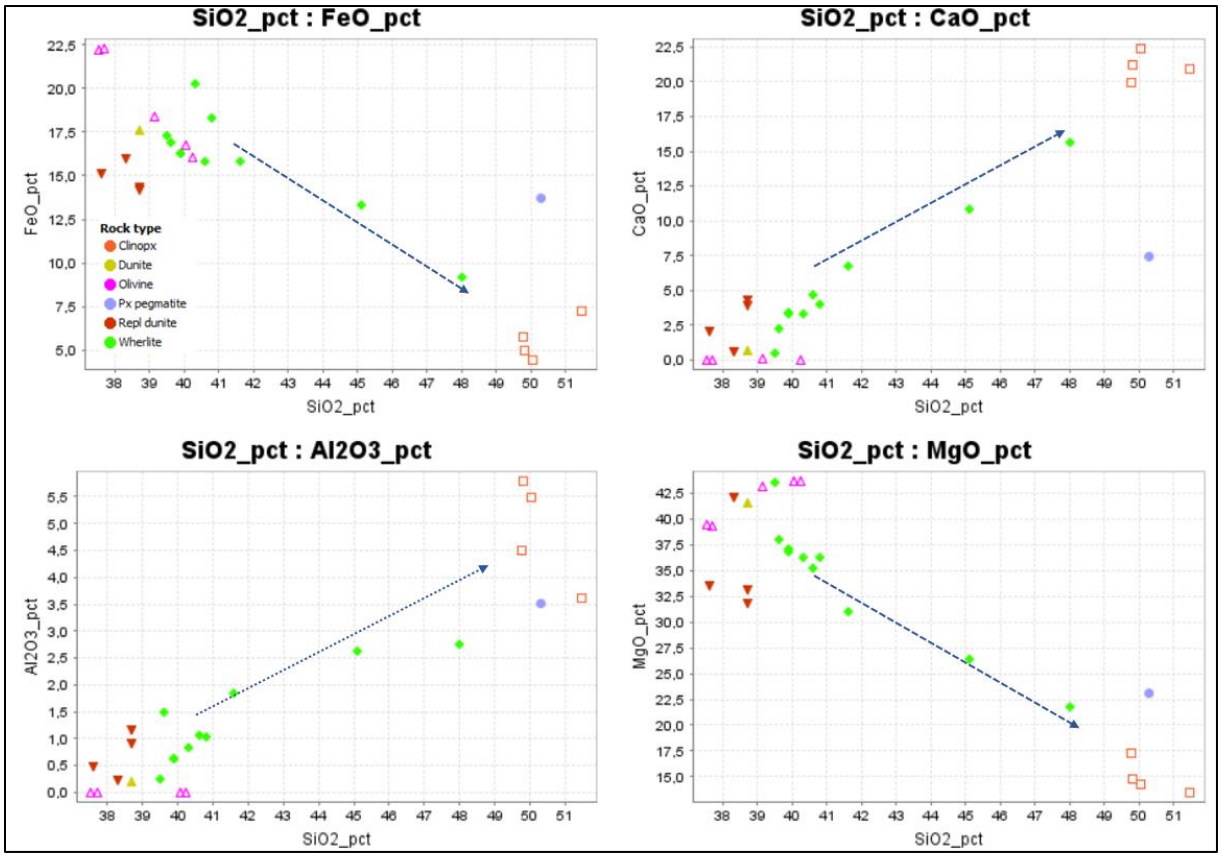

Figure 3.14. ***Major elements results from the wehrlites (green), large scale replacive dunites (red), px pegmatites (blue) and dunites (yellow) in ULS. Ol (pink open triangle) and cpx (red open square) are plotted in, and the fractionation trend is indicated by the blue stippled arrow. Al_2O_3, FeO, CaO and MgO are plotted against SiO_2. All measurements are in wt%.***

In Figure 3.15 the major elements SiO_2, Al_2O_3, CaO and FeO are plotted against MgO, as MgO often is a better indicator of fractionation in ultramafic systems than SiO_2. Similar trends are seen in Figure 3.15 and in Figure 3.14. For the MgO plot, the mixing trend between cpx and ol still prevails, and indicates that the evolution of the rocks is strongly controlled by the fractionation of ol and cpx. There is a negative trend between MgO and SiO_2, CaO and Al_2O_3, but a positive trend between MgO and FeO. This means that the wehrlites chemical change varies with the amount of ol and cpx, as these two are the main modal phases.

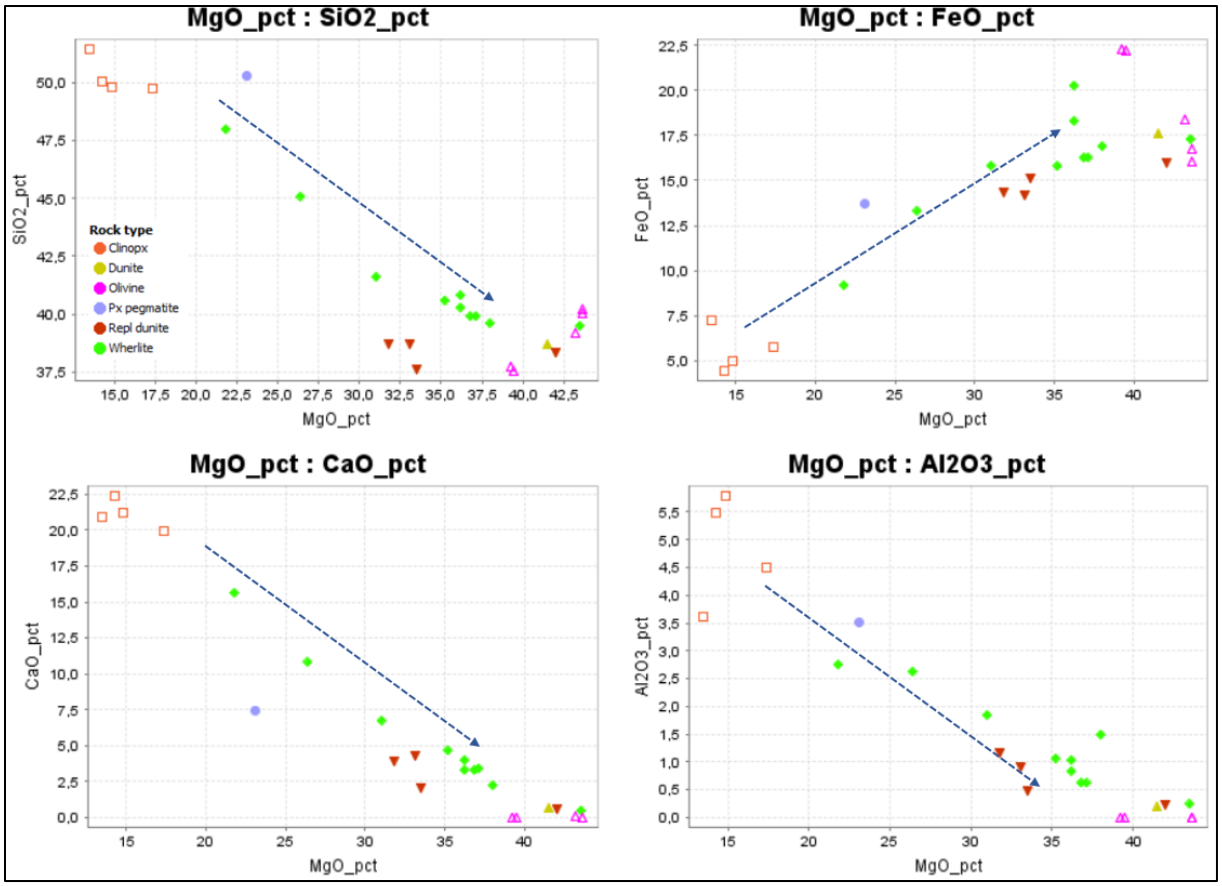

Figure 3.15. ***Major elements results from the wehrlites (green), large scale replacive dunites (red), px pegmatites (blue) and dunites (yellow) in ULS. Ol (pink open triangle) and cpx (red open square) are plotted in, and the fractionation trend is indicated by the blue stippled arrow. Al_2O_3, FeO, CaO and MgO are plotted against MgO.***

The geochemical REE results for the host rocks are presented in Figure 3.16.

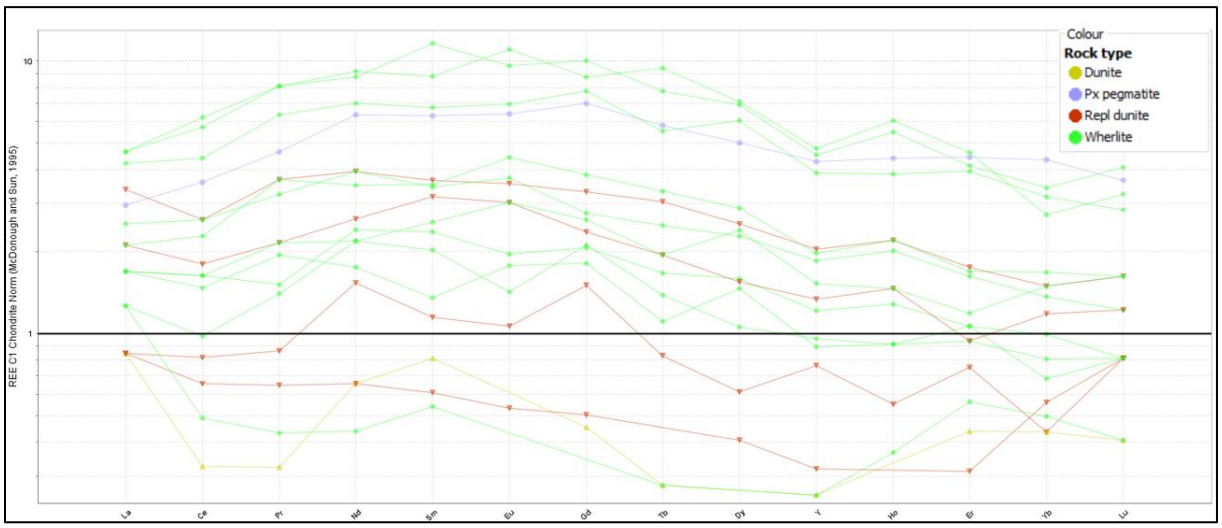

Figure 3.16. ***This graph shows REE results from the wehrlites (green), dunites (yellow), large scale replacive dunites (red) and the px pegmatite (blue), normalized to a chondrite and plotted across the REE, from La on the left to Lu on the right.***

The chondrite normalized bulk REE diagram shows a distinct concave shape for the wehrlites, with a low LREE increasing up to Sm and Eu, with a steady decrease towards HREE. The curves with the concave shape predominantly plot above 1. Notably in the wehrlites, there is a slight Y anomaly, where

the curve dips down below the expected value. The most enriched curves correspond with the high px wehrlites, where samples were taken from pyroxene rich layers.

The other emerging trend is found in the depleted samples, where the sample plots around or below 1. These are the more dunitic samples, rich in ol, and less dominated by px. The yellow curve from Figure 3.16 is a true primary magmatic replacive dunite, where the sample is >90% ol. This sample has a depletion in all REE when compared to the wehrlites, with a slight increase in La, Nd and Sm. However, none of these samples are especially enriched. The highest recorded chondrite normalized value of these samples is a Sm value 10,5 times higher than for a chondrite.

The LSRD show similar MREE and HREE trends to the wehrlites, as these samples still have a high cpx content. The most enriched LSRD samples seen as red curves in Figure 3.16 show a slight increase in La when compared to the wehrlites, meaning these samples have a relative enrichment in this element. There are samples from the wehrlite which have a similar increase in La, most of these samples are however taken close to the serpentinization zone, meaning the samples might have been contaminated by metasomatizing fluids.

While the most enriched LSRD samples are taken from px rich layers, the two most depleted samples are taken from more ol dominated layers. These samples are both depleted, with a very flat REE curve except for the Lu concentration which spikes for both samples unlike the two other more wehrlitic altered samples.

The px pegmatite follows a similar curve to the most enriched, cpx rich wehrlites. This is explained by the similar cpx content to the enriched wehrlites. The px peg is dominated by opx, which similarly to ol is incapable of incorporating high amounts of REE into its lattice. The px peg notably does not have the same Y anomaly as the wehrlites and dunites have. But overall has a very similar concave shape, with an inclination from LREE to MREE, and a decline towards HREE.

Two of the samples from the wehrlite were also rich in PGE. These two are the most mineralized samples found in the intrusion. Sample JS17-2 is taken from the LSRD, while JS18-3 is taken from the same magmatic layer 8 m away from the LSRD. The sampled have a Au and Pd content comparable to other wehrlites, but an anomalously high Pt value.

Element (ppm)	JS17-2	JS18-3
Au	0,004	0,006
Pt	0,0178	0,0263
Pd	0,031	0,013

Table 3.6. ***This table shows the most enriched PGE samples found in ULS.***

The enriched PGE results from the two host rock samples are presented in Table 3.6. The samples may have been sampled in an exposed reef.

3.3 Porphyritic hornblende dyke

3.3.1 Field observations

The porphyritic hornblende dykes are characteristic when observed in the field. The dykes have a dark groundmass with dark phenocrysts of hbl. These phenocrysts vary in size from 0,5-1,5 mm and often protrude from the ground mass of the dyke. They occur as straight dykes, which seem to follow a structural path without much deviation from this. The margins of the dykes seem to be similar to the core of the dyke with respect to grain size without the presence of a chilled margin.

The dykes vary in thickness from 5-15 cm in width and vary with respect to the size of the actual phenocrysts. The larger phenocrysts have been observed in narrower dykes, more towards the south eastern end of the plateau. This may however just be local variations in the dyke type. Some of the hbl phenocrysts show a slight SPO where the length of the hbl crystals align parallel with the dyke, indicating some degree of flow. Other than this, this dyke type shows little fabric, and does not seem to be deformed in a significant way.

The hbl phenocrysts found in these dykes are always rounded and contain chadacrysts. Despite the size of the phenocrysts varying across localities, the sizes are uniform and equigranular in a single outcrop, only varying with a few mm at most. The phenocrysts are most likely to originate from the same place, with similar crystallizing conditions. These textures can be seen in Figure 3.17.

Figure 3.17. ***Field observations from the porphyritic hornblende dykes. a) Three dark porphyritic hbl dykes cut the wehrlite on a vertical south facing wall. The dykes are sub vertical and dip towards west, with a NNE-SSW trend. These dykes had the largest observed phenocrysts, with the hbl phenocrysts being as large as 1,5 cm. This locality is where JS21, a porphyritic hbl dyke sample was collected. These dykes are also micro faulted, with no more than 2 cm displacement buy some of the shear zones described in chapter 3.2. b) close to the locality where picture a) was taken, this dyke was photographed. It is a dyke similar in width, but with smaller phenocrysts. The phenocrysts seen in this dyke are representative for the other dykes of this type with rounded, oval shapes, and equigranular size. c) This picture is taken from the central southern plateau. This dyke is similar to the dykes in a) and b), but the dyke has a higher concentration of hbl phenocrysts, as well as having smaller phenocrysts than the other two dykes. The image makes it appear as if the this dyke has a different ground mass colour than the two other dykes, but this is related to the light conditions when the photo was taken. When the phenocrysts protrude as they do in this image it is possible to observe the 3D spherical shape of the phenocrysts. They are "egg shaped" when observed in a 3D view, with an elongated oval shape.***

The dykes on the plateau seem to follow a relatively straight path, with occasional jumps, where the dyke shifts laterally without shearing. The dyke disappears and reappears laterally from where it disappeared. This shift can partially be seen in Figure 3.18c).

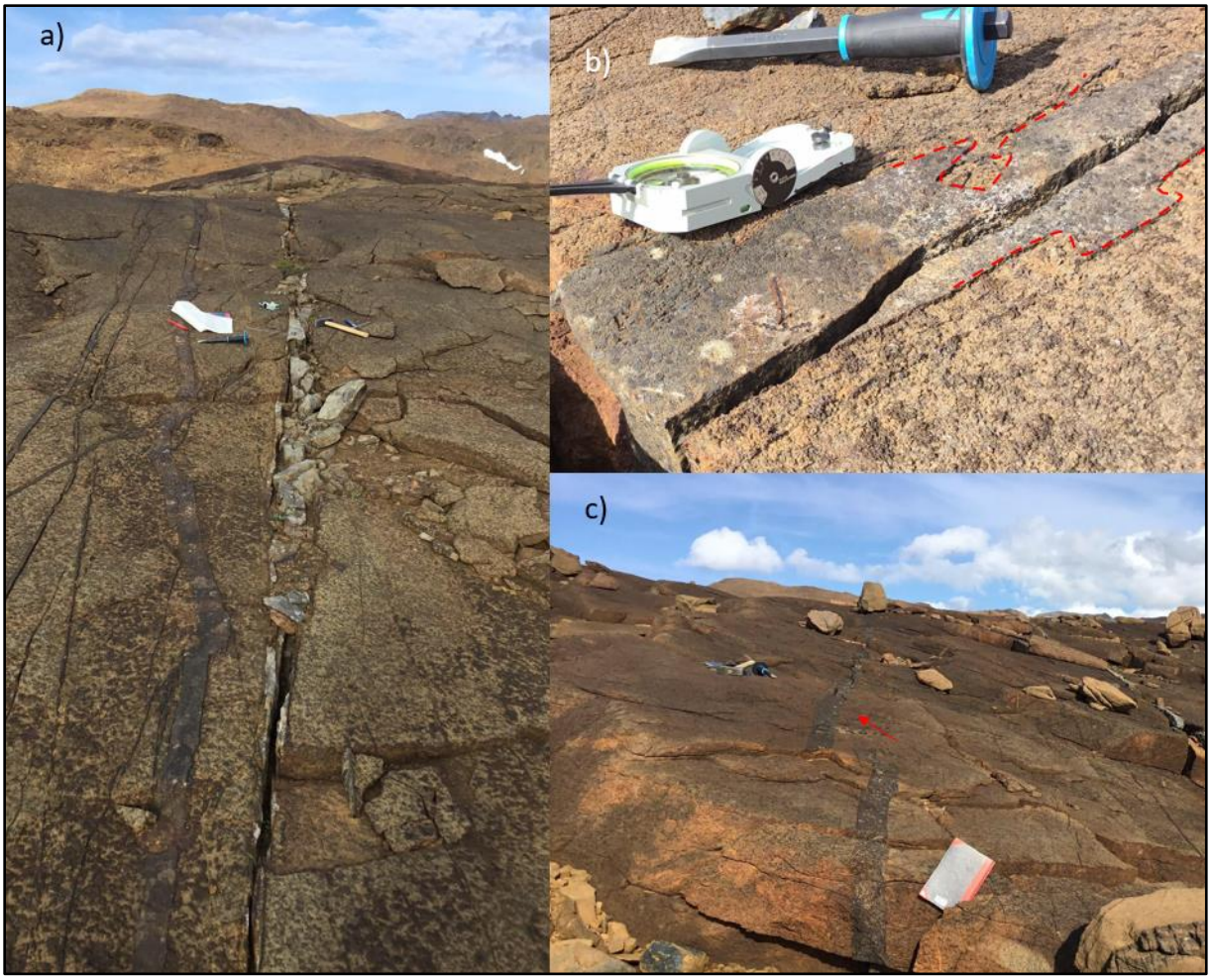

Figure 3.18. ***These images are all from the same dyke, only in different localities along the strike of the dyke. a) One of the porphyritic hbl dykes (left side) parallel to a gabbroic dyke (right side) on the plateau. The dyke is structurally more integral and solid than the parallel gabbro dyke. The porphyritic dyke follows kinks, and generally follows an undulating path. The dyke also splits up into more narrow offshoots which often reconnect with the original dyke. This may indicate intrusion into a less brittle wehrlite. b) This locality is the sampling locality of JS03. The dyke is here seen with two irregularities marked by red stippled lines. The bottom line outlines a square protrusion from the dyke, which protrudes perpendicular to the strike of the dyke. The protrusion is ~2cm wide, and ~5 cm along. The stippled line at the top shows a pocket of wehrlite, trapped within the intruding dyke. These features, combined with the lack of a chilled margin indicate intrusion into a relatively hot wehrlite, as it would not be possible to create these structures in a brittle, cold host rock. c) The dyke will occasionally disappear, and reappear further away along the strike, often laterally displaced. These shifts are regular, and do not seem to be related to shearing, as the characteristic shear zone colour would be visible if this was the case. This seems like a primary intrusive structure, where the dyke migrated in 3D.***

This type of dyke is more often observed on the southern part of the plateau, well within ULS, by have also been seen to extend up towards CS in the north. The only dyke observed in the northern parts of ULS is a 3 cm wide dyke with phenocrysts <5mm.

3.3.2 Petrographic observations

The characteristic trait for these dykes is the abnormally large hbl phenocrysts. Phenocrysts are observed in several different dyke types, but none as large as the phenocrysts in the porphyritic hbl dykes. The sample seen in Figure 3.20 is taken from the locality seen in Figure 3.17a). There are 4 thin sections from this type of dyke. Two of them are from a dyke with large 1,5 cm phenocrysts, the other two are from a dyke with smaller phenocrysts 0,5 cm. Both sets have included the wall rock contact.

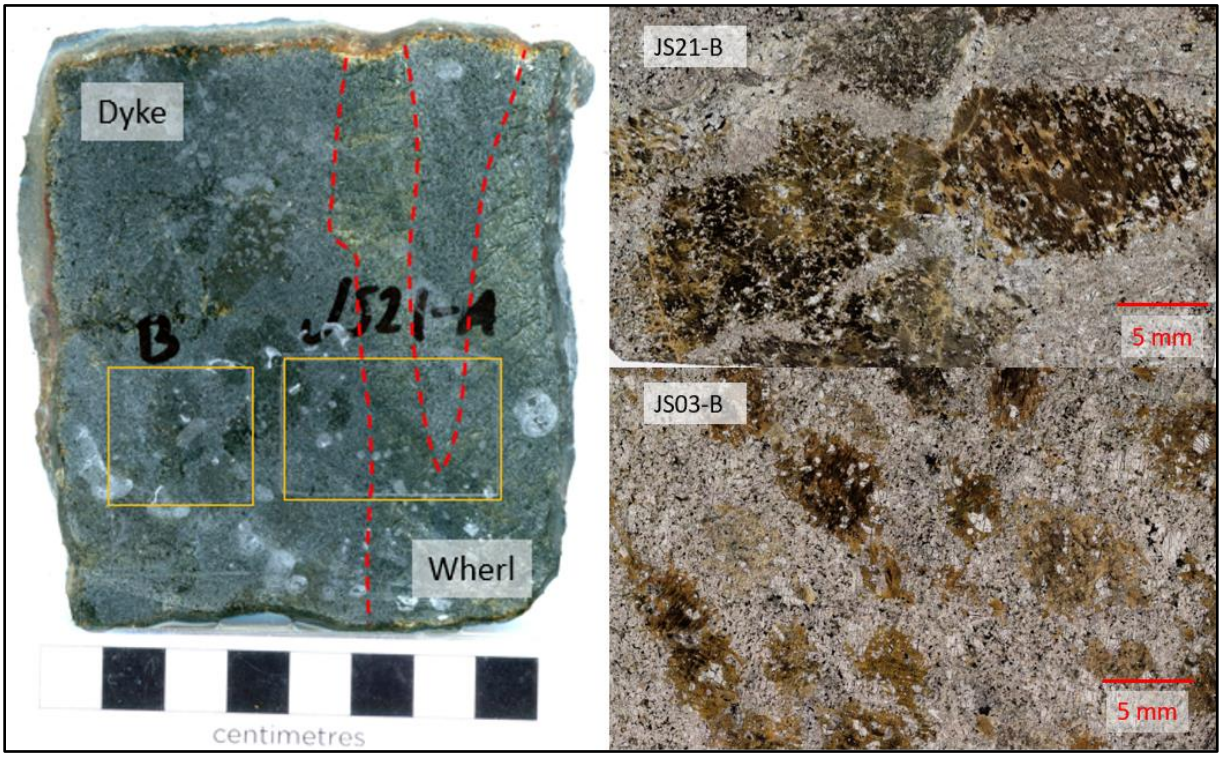

Figure 3.19. ***This figure shows the cut surface of the two JS21 thin sections which were prepared. The area where the thin sections come from are outlined with orange squares on the left image. The contact between dyke and wehrlite is outlined with red stippled lines. The tongue of dyke infiltrating to the right of the main dyke can be seen in Figure 3.20, with the same area stippled out in a red line. The ppl image to the top right is taken from the orange frame to the left, JS21-B, where large 1,5 cm, oriented hbl crystals are seen. The bottom right is a different thin section with smaller phenocrysts, JS03-B.***

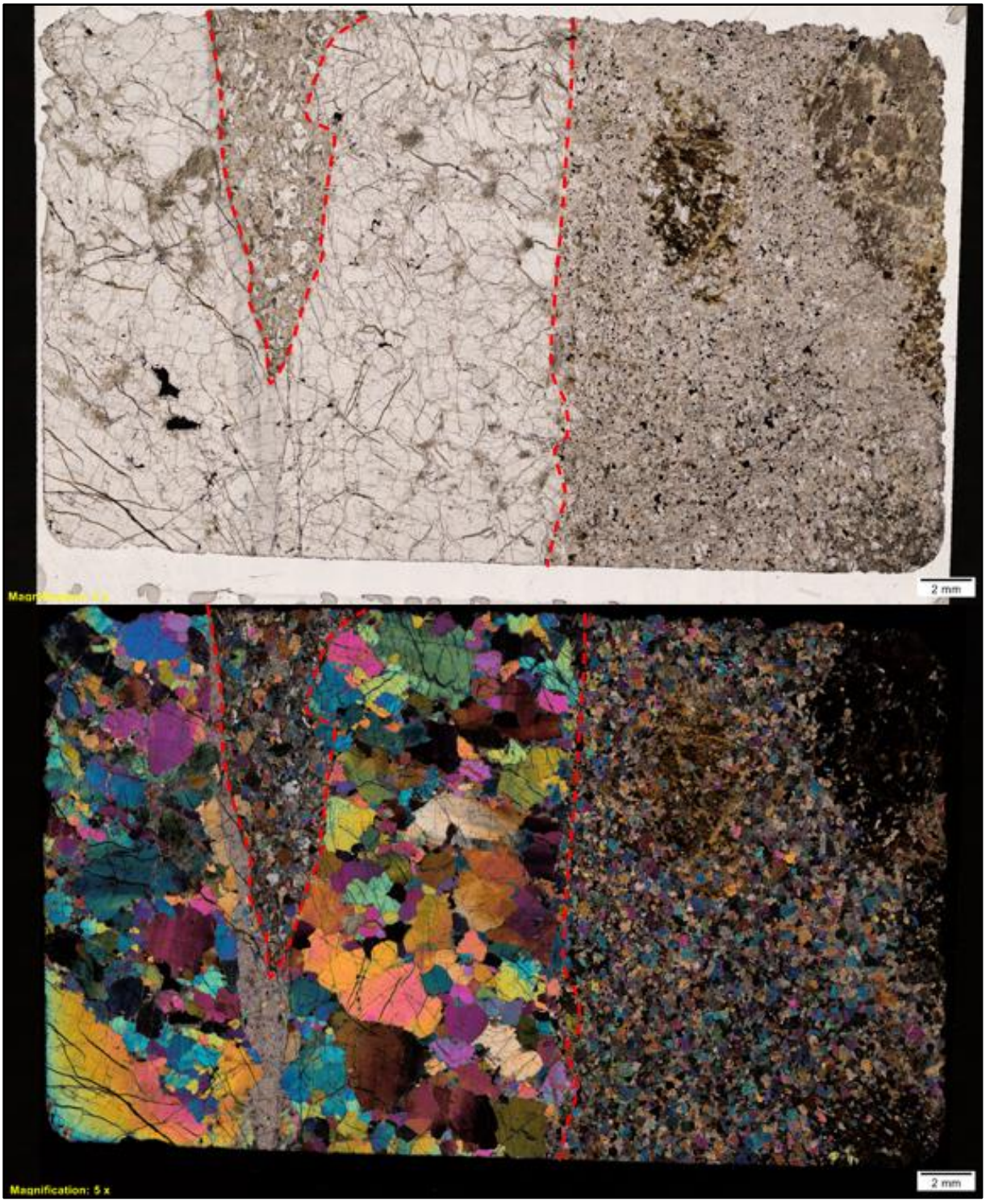

Figure 3.20. ***(Top) A ppl scan of thin section JS21-A. This thin section clearly shows the difference between the dark pyroxenitic, fine grained ground mass of the dyke and the coarse grained translucent mineralogy of the olivine dominated wehrlitic wall rock. The contact between the dyke and wall rock is more apparent in the ppl image, as the olivine and px provide good contrast. The hbl phenocrysts are also easily observed in the ppl image. The contact is marked out by the stippled red line, as well as a tongue of dyke intruding isolated from the dyke. This is marked out by the stippled red line to the left. (Bottom) An xpl image of the same thin section as seen on top. It is easier to distinguish the individual ol grains in the host rock as well as the individual grains in the dyke groundmass. The hbl phenocrysts however disappear slightly in the xpl image. The same red lines as can be seen on the top image are overlain on the bottom image.***

The dyke contact is as seen in Figure 3.20 straight and does seem to follow around individual grains of ol. The olivine grains along the contact seem relatively unaffected by the intruding dyke. The ol grains show little reaction textures in the contact, and are less fracture filled and altered than other host rocks associated with the nearby intrusion of a dyke. The host rock which this dyke has intruded into is an olivine dominated rock, with minor px.

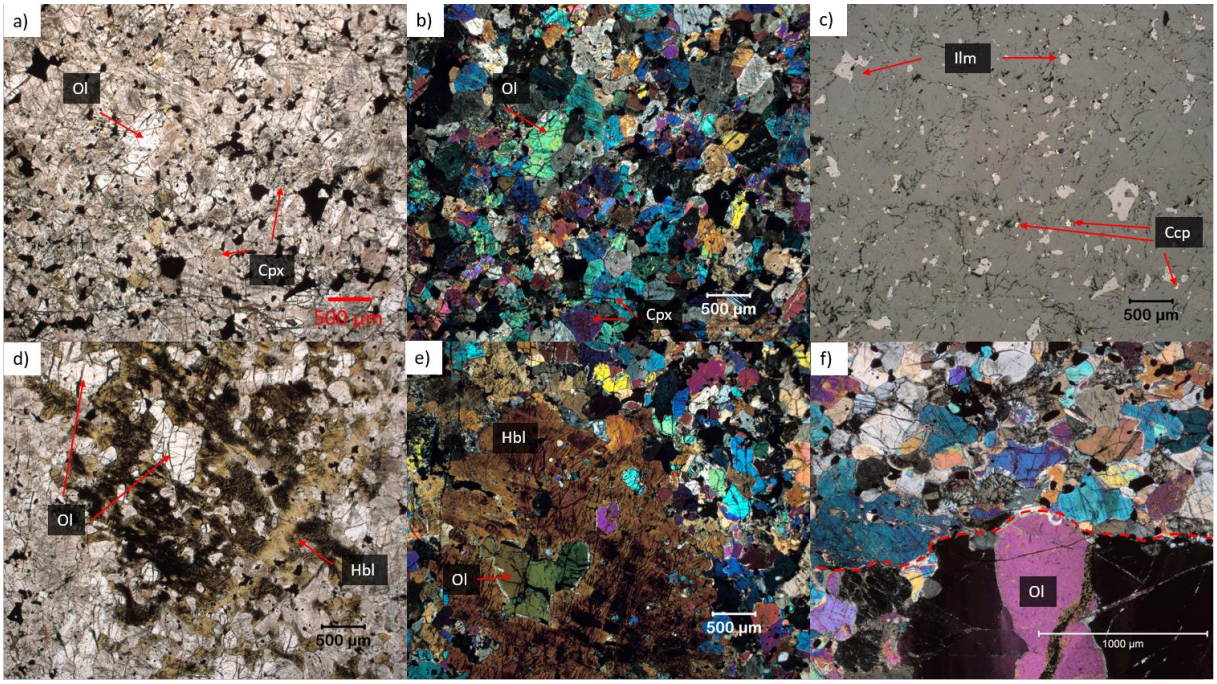

Figure 3.21. ***These six images are microscope images from the porphyritic hornblende dykes. The three first images (a-c) are taken in the same position, orientation, and magnification, changing from ppl to xpl to rfl respectively. a) This image shows the groundmass of this dyke type. The main component of the groundmass is an-subhedral equigranular cpx and opx, with some ol and accessory hbl and opaques. The average grain size in this groundmass is ~500 µm. A large ol grain is pointed out and labelled with a red arrow. The "dirty" pink tinted minerals are cpx and opx. b) This image is taken in xpl to better show the individual interlocking grains. The cpx grains are second order blue in interference colour, with exsolution lamellae of opx and some oxide minerals. The ol grain pointed out is the same grain as pointed out in a). c) This image was taken using reflected light in order to illustrate the composition of the opaque phases. The dominant opaque phase is interstitial ilm, as pointed out by the red arrows. There is also a minor sulphide phase where pyh and ccp are intergrown. These grains are however small ~25µm interstitial phases. d) The large hornblende grain seen in this image hosts several inclusions. The chadacrysts here are rounded grains of both ol and px. Compared to the similar grains in the groundmass, some of these grains are smaller, and significantly more rounded, tending towards spherical. This indicates an equilibrating reaction between the oikocrysts and chadacrysts. The hbl grain itself seems to be rounded at the edged as well. e) Similarly to image d), this image shows a large hbl grain with inclusions of smaller px and ol grains. The inclusions seem to get progressively smaller from the core of the oikocryst to the rim. These are also similarly rounded like the chadacrysts in d). f) Lastly, this image shows the contact between the dyke and the wehrlitic host rock. The olivine grains in the host rock are rounded in the contact, and some of the grains have also developed a symplectite corona texture.***

The dyke is a uniform dyke, with the groundmass being consistent both texturally and mineralogically. The only significant variation lies in the changing of phenocrysts size. The oikocrysts are similarly shaped and the chadacrysts are of similar shape and size across the different sizes of oikocrysts. This is also a dyke rich in iron oxides like ilm, as well as some minor sulphide grains. When ccp is observed in this dyke it is usually closely associated with another iron sulphide like pn or pyh. This is probably a result of exsolution from a singular iron sulphide melt droplet.

Since the chadacrysts are rounded as seen in Figure 3.21 d) and e), this would indicate some reaction has taken place to round out the edges of the grains. The contact with the host rock also shows a similar texture, as existing angular ol grains are rounded and often have a corona texture along the

infiltrating dyke. The presence of these textures indicates there has been sufficient heat in the system for these equilibrium reactions between dyke and host rock to take place.

The observed mineralogy from optical microscope is supported by XRD analyses seen in Table 3.7. Based on the XRD results, the groundmass of the dyke, excluding the phenocrysts are px dominated, with more cpx than opx, meaning a higher Ca content in this dyke. The dyke itself plots as a hornblende phenocryst bearing olivine websterite.

Mineral	JS03	JS21
Fo	19,68	11,98
Hbl	29,17	22,65
Di	28,81	33,78
En	15,21	27,39
Bt	1,01	0
And	0,86	0
Spl	1,92	0
Ilm	3,34	4,21

Table 3.7. ***This table provides XRD results from analysis from two different localities of the same type of dyke. JS03 is the dyke sample with 5mm phenocrysts, while JS21 is the sample with larger 15mm phenocrysts.***

Both dykes have similar mineralogy with some variations. The hbl content and fo content is higher for JS03. JS03 also has more accessory phases like bt, and and spinel. The sampling locality where this sample is taken from is stratigraphically lower than JS21, and the host wehrlite in this sample has a higher spinel content than seen in other wehrlites in ULS. The extra spl content in this dyke could therefore be assimilated from the host rock, but texturally looks like it is primary in the dyke at this locality.

The dykes are also rich in ilm as confirmed by rfl microscopy. These ilm grains often occur as interstitial small grains but can also be seen as larger grains with inclusions of silicates. The ilm content of ~4% for this sample is higher than what is observed in other dyke types and is a distinguishing mineralogical difference when looking at the ground mass compared to other dykes. This dyke type is also lacking plagioclase, with the content being 0,86% in the sample richest in plag. These grains are randomly distributed, and often associated with re-equilibrium reactions between the ultramafic minerals and plagioclase.

3.3.3 Geochemistry

The whole rock ICP-MS analyses from the porphyritic hornblende olivine websterite are provided in Table 3.8.

Element oxide	JS03	JS21
SiO2	41,3	44,3
Al2O3	7,02	5,66
FeO	16,25	13,7
CaO	10,5	11
MgO	19,3	20
Na2O	1,05	0,85
K2O	0,16	0,14
Cr2O3	0,126	0,174
TiO2	2,59	3,18
MnO	0,2	0,18
P2O5	0,03	0,02
SrO	0,03	0,01
BaO	<0.01	<0.01
LOI	0,04	0,07

Table 3.8. ***Whole rock analysis of major elements from the two porphyritic hornblende dykes. All oxides are in wt%.***

The chemical analyses show small variances in chemistry related to variations in mineralogy. JS21 is a sample richer in SiO_2 which may be attributed to the increased amount of px. JS03 has more FeO, which may be a result of more ol inclusions and primary ol in the dyke. The observed spinel in JS03 may cause the slight increase in Al_2O_3 when compared to JS21. Other than this the two dykes are very similar in chemistry.

As the late alteration products like serpentine are hydrous phases, LOI is a good indicator of how altered a sample is. Either of these samples look altered when viewed optically, which is supported by low LOI. The LOI in this sample may come from the hornblende content.

The high Ti content of this dyke type is related to the high concentration of ilm in the sample, as Ti is one of the main constituents of this mineral. Cpx can also incorporate some Ti in its Y-site in the crystal lattice, which is the smaller octahedral site (Chenriak & Liang, 2012). This is however not sufficient to explain the ~3wt% TiO_2 found in this sample.

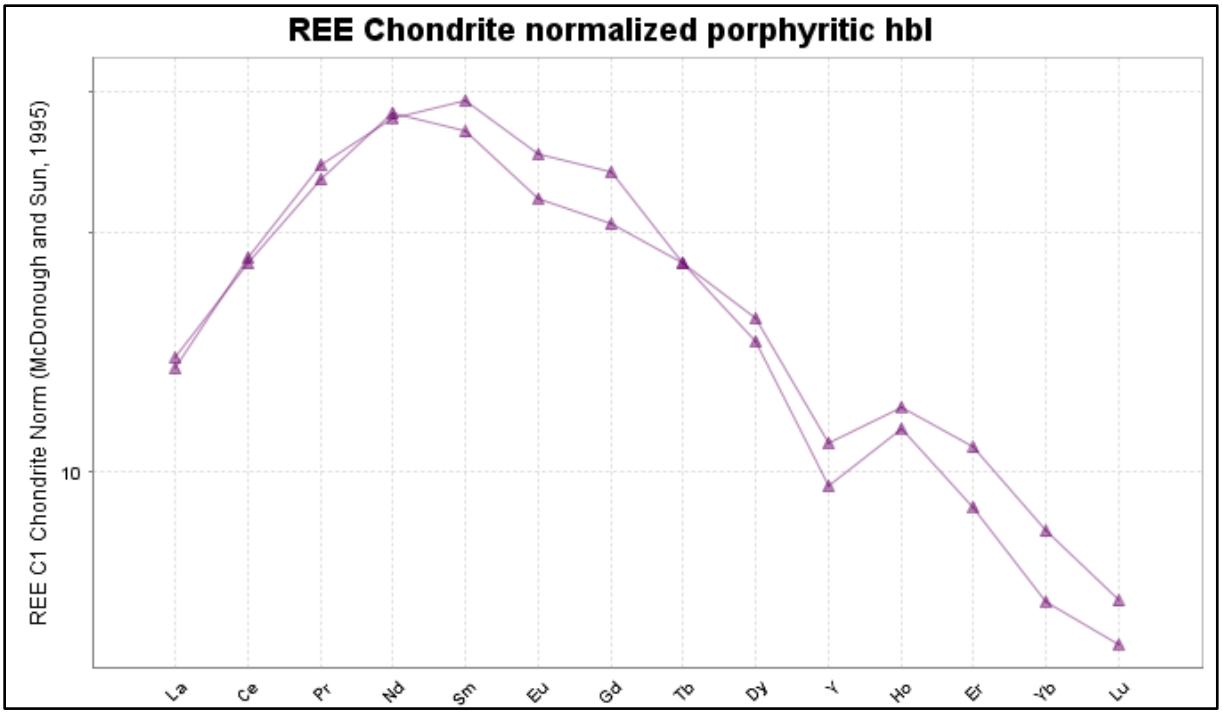

Figure 3.22. ***This graph shows the two porphyritic hornblende samples normalized to a chondrite (McDonough and Sun, 1995) and plotted against REE and Yttrium. The REEs range from LREE from the left side to HREE to the right side.***

When observing the chondrite normalised samples in Figure 3.22 the two dykes are very well correlated and adhere to similar trends. The graph has a characteristic shape with a depletion in LREE, with an increase from La to Nd, with a downwards trend from Sm to Lu, being relatively depleted in HREE, while remaining above the HREE chondrite values. The notable anomaly in this graph is a slight depletion in Y, with values plotting below the expected curve of descent.

.

3.4 Lherzolitic and composite dykes

3.4.1 Field observations

The lherzolitic dykes (lhz dykes) is a common dyke type found throughout the plateau of ULS. It is a dark, medium grained dyke, often observed with plagioclase rich domains in the dyke itself. The dykes are mapped and described as lhz dykes and composite dykes (comp dykes), as this dyke type is often found with these additional plag domains. This dyke similarly, to the other dykes which have intruded ULS has a NNE-SSW strike direction, with a steep, subvertical dip. Based on cross cutting relationships this dyke generation also seem to be one of the older dyke types, predated by a few pyroxenitic dykes.

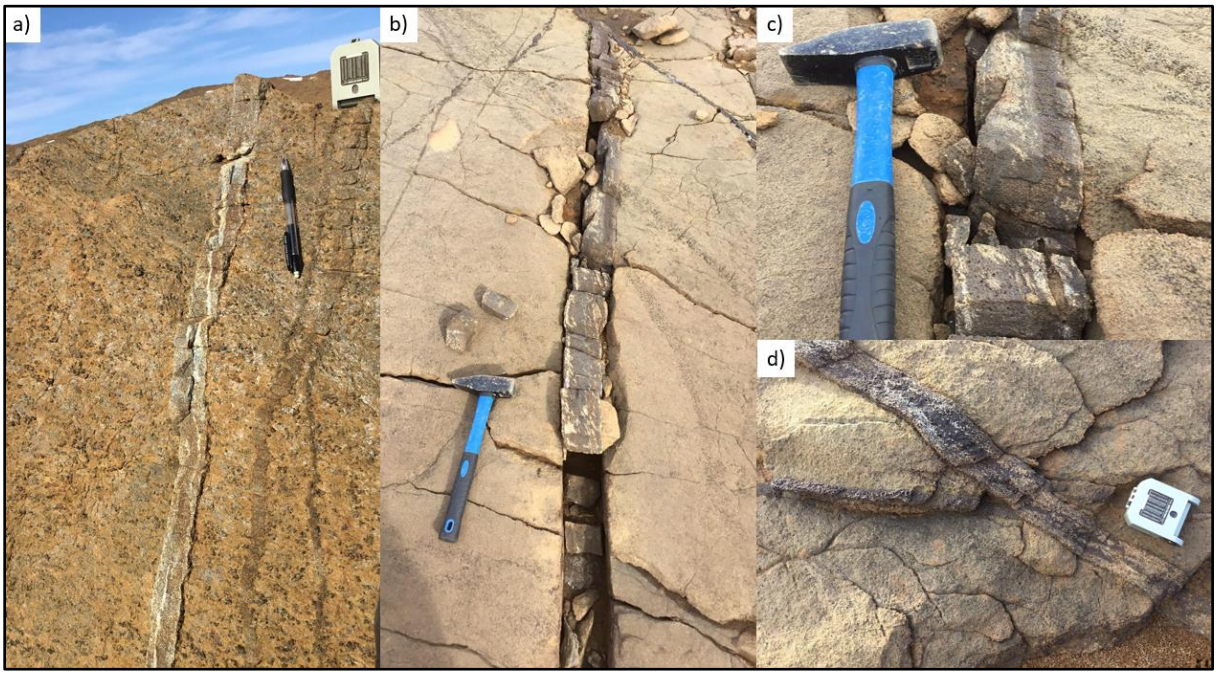

Figure 3.23. ***This figure shows pictures from four different localities in ULS of the same dyke type. a) This dyke has one of the largest observed plag domains found in a dyke of this type. The plag domain is seen as cm wide leucocratic "vein" following parallel to the dyke, and is located in the middle of the dyke in this locality. In this locality the plag domain is almost monomineralic. The groundmass of the dyke is predominantly cpx and ol, with some opx and hbl as well. This dyke is relatively fine grained, with grain size being ~1mm. This is the sampling locality of JS_2_8. The dyke is relatively straight with a somewhat undulating contact as seen in this locality. The dyke does not follow a perfect fracture, but rather kinks and bends slightly. b) This locality shows the same dyke type, also with leucocratic zones enriched in plag. The dyke cuts local layering in the wehrlite, and similarly to the dyke in a) this dyke is relatively straight, with a sharp but slightly undulating contact with the wehrlite. c) This photo is taken from the same locality as the dyke in locality b). The dyke has very local zones of plag, and the domains seem to follow along the sides of the dyke. This dyke however seems to be a composite of three different types of dyke, and might include both a pyroxenitic dyke, as well as a lhz dyke with plag infiltration. d) This photo shows one of the lhz plag composite dykes cutting one of the older px rich dyke types found in ULS. The dyke resembles the dyke in locality b) and c) as the plag domains are diffuse and along the edges, while the plag in a) is strongly centred and monomineralic.***

From the localities seen in Figure 3.23 the dykes of this type usually has a dark brown weathering surface, which can progress towards a lighter, more leucocratic surface as the plag content increases sufficiently. The dykes usually appear as thin 5-10 cm rough dykes, which protrude up from the surrounding wehrlite. They are easily identifiable because of the plag domains found in them. This is the only dyke type where this process has been so readily observed. It can be observed in other dyke types as well, but the fine grained lhz dyke type is the most common for this.

The dyke also varies with respect to ol content. The ol is usually observed as larger, 2-3 mm ol grains. This can be seen in Figure 3.23 c), as the one part of the dyke has small holes covering the surface

where the ol xenocrysts have been weathered away. Some of the dykes of this type however, lack ol xenocrysts all together. Without the plag domains, these dykes then appear like dark, ultramafic dykes.

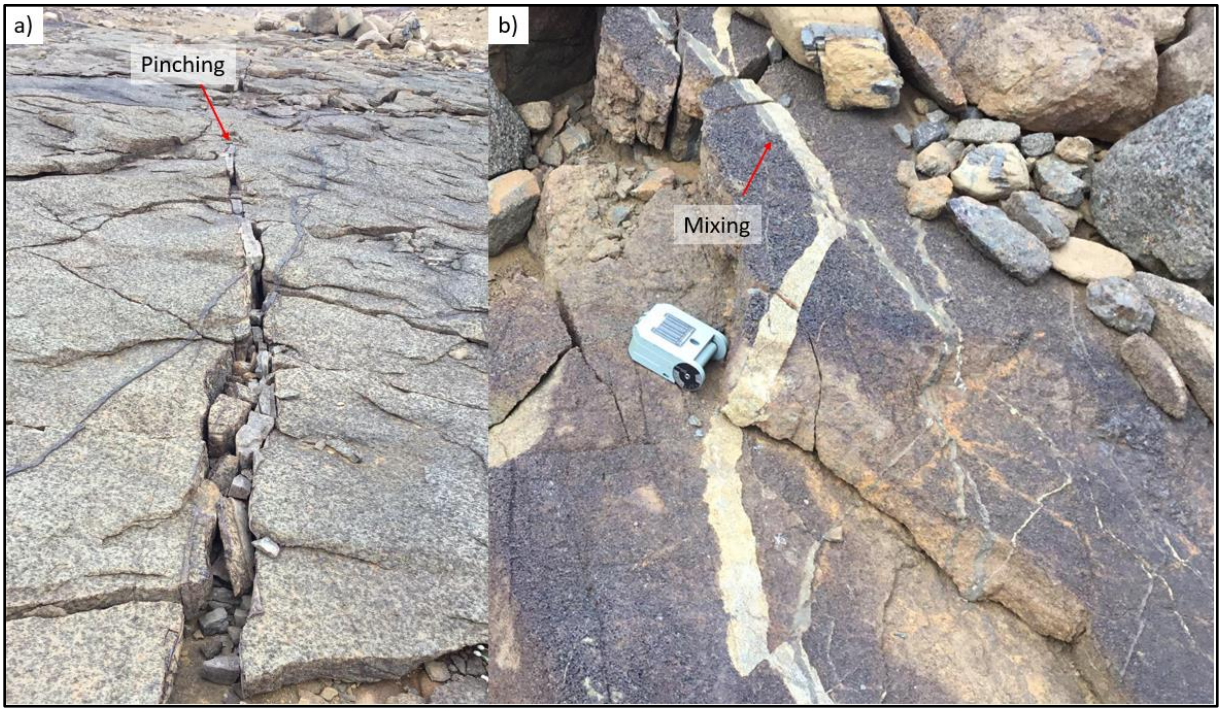

Figure 3.24. ***These two localities show observed structures in the lhz and comp dykes. a) This is the sampling locality of JS11, a sample rich in px and ol, with a few infiltrations of plag. The dyke protrudes straight, and pinches where the arrow indicates pinching. The dyke reappears 15-20 m away from where it pinched, with the same orientation. b) This locality shows a similar dyke, only much more dominated by plag. The leucocratic dyke is seen mixing and mingling with a darker lhz dyke where the arrow indicates mixing. The dyke here is more randomly oriented, than previously shown. The small veinlets in the bottom right of the image are close to monomineralic veinlets of plagioclase which mix with the darker lhz dyke. The dyke here is believed to have intruded into the wehrlite while the wehrlite was still close to solidus and malleable.***

Figure 3.24 shows differences in orientation from similar dykes from different localities. The weathering colour of these dykes are strongly affected by the modal percentage of plag present in the dyke. Once the dyke has a network of plag formed, and the amount of plag is sufficient the weathering surface becomes leucocratic as seen in Figure 3.24 b).

3.4.2 Petrographic observations

Samples were taken from a wide range of these dykes. Some were lacking plag, while others were very rich in plag, and some only had plag in localized domains.

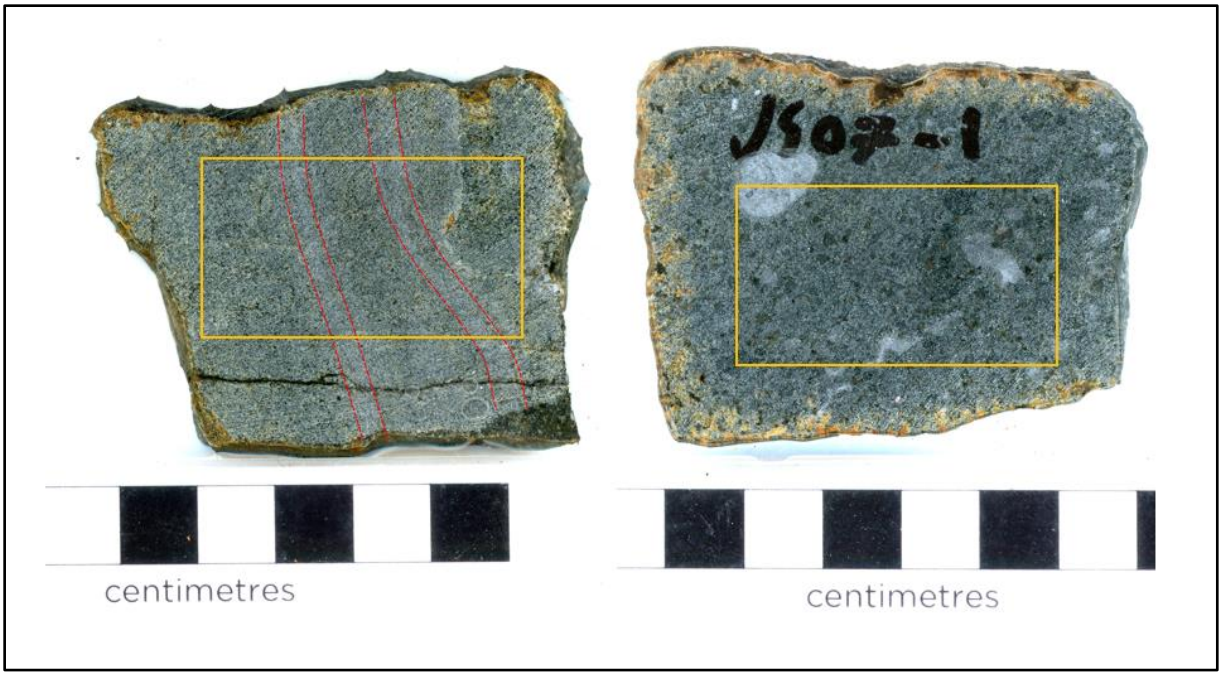

Figure 3.25. ***This image shows two of the samples collected for thin section preparation. The left sample is JS11, the right sample is JS07. These are mineralogically similar, whit the exception of sample JS11 not having the same amount of ol xenocrysts as JS07. The areas where thin sections were prepared are marked out with orange squares. The left sample also hosts two plag domains marked out by red stippled lines.***

As seen in the samples in Figure 3.25 they both have a dark green to grey fine-grained groundmass. Both dyke samples are ~6cm in width, with a 0,5 cm weathering surface covering the samples. There is little evidence of a chilled margin in these dykes, and apart from the plag domains the dykes show little to no fabric. The left and right sides of the sample are representative of the contacts with the wehrlite, as these samples were taken without a host rock contact. The wavy and undulating contact is observable in these samples.

Texturally this lithology is homogenous, with interlocking grain boundaries, which for the most part crystallized under equilibrium conditions. The plag domains sometimes cause coronas to form, and the ol xenocrysts also seem to have re-equilibrated with the dyke itself. The hbl as seen in Figure 3.26 seems to be interstitial, and may have been one of the later phases to have crystallized in these particular dykes. The px and primary ol however seem to have crystallized together.

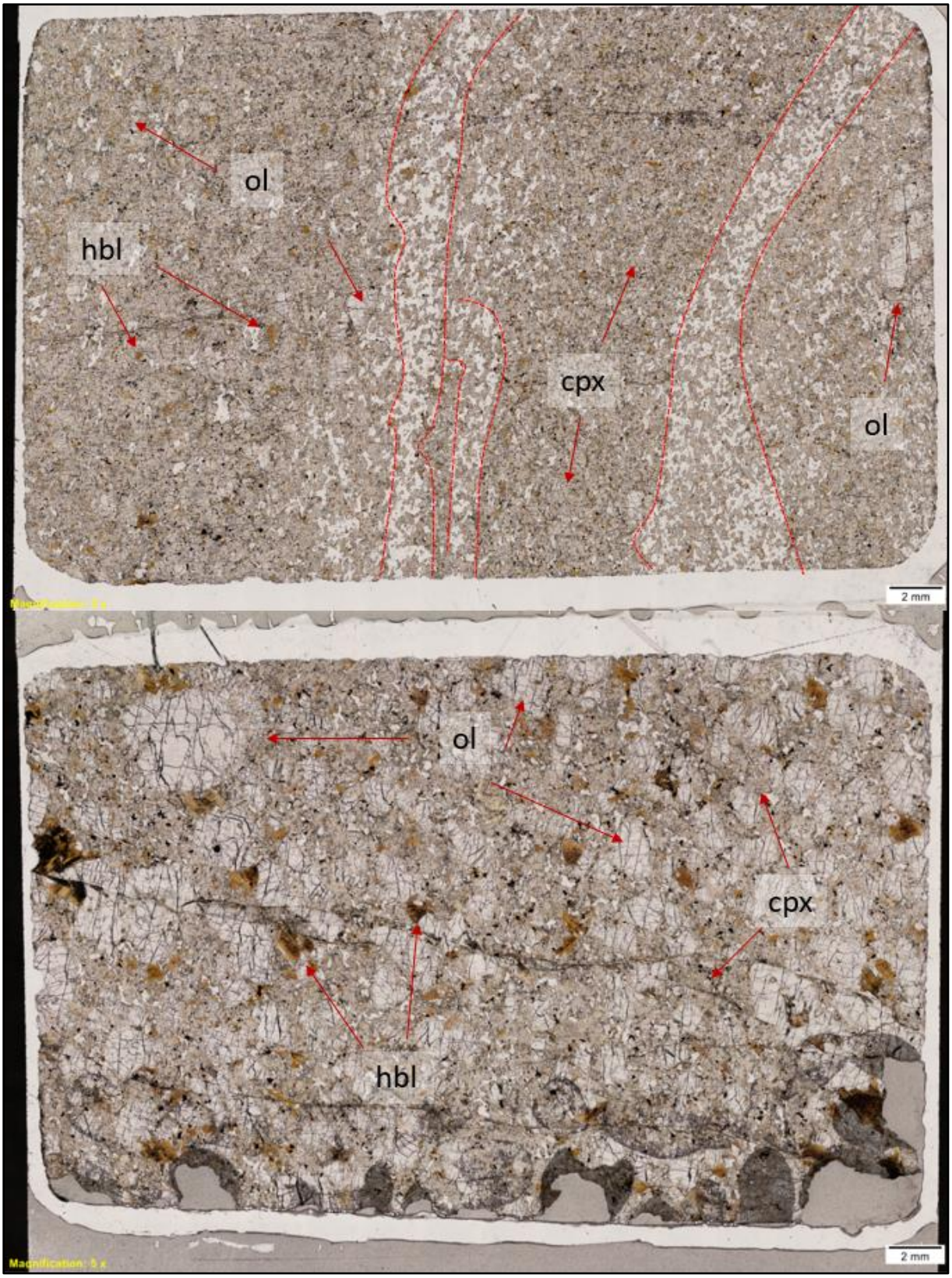

Figure 3.26. ***In this figure the thin sections from Figure 3.25 are presented. Both pictures are taken in ppl. (Top) The top thin section is from JS11, the lhz dyke with two veins of plag infiltrating through the sample. The plag domains are marked out by red stippled lines, and the contrast between the grey cpx and clear plag makes the plag easy to observe. There are isolated grains of plag throughout the sample, but the majority of the plag is localized to the two veins cutting through the sample. Minerals like hbl and cpx which make up the majority of the groundmass have been indicated. The sample also has some xenocrystic ol, but not as much as JS07, the bottom thin section. (Bottom) The bottom thin section is mineralogically similar to the top thin section, but texturally different. This sample is coarser grained, with larger 1-2mm***

hbl grains, and coarse ol xenocrysts, which are roughly the same size as the cumulate ol found in the wehrlites at 2-4mm. The ol phenocrysts all have a rounded shape, which indicate equilibrium reactions may have occurred. The sample does contain some plag, but similarly to the sample above, it seems to migrate through the sample, rather than being a primary magmatic mineral.

The observed leucocratic domains found when observing this dyke type in the field (Figure 3.23 b) and c)) appear as the interconnected networks of plag as seen marked by red stippled lines in Figure 3.26 (top). The plag in these dykes usually does not appear as isolated interstitial grains, but as a part of a larger 3D interconnected structure migrating through the dykes.

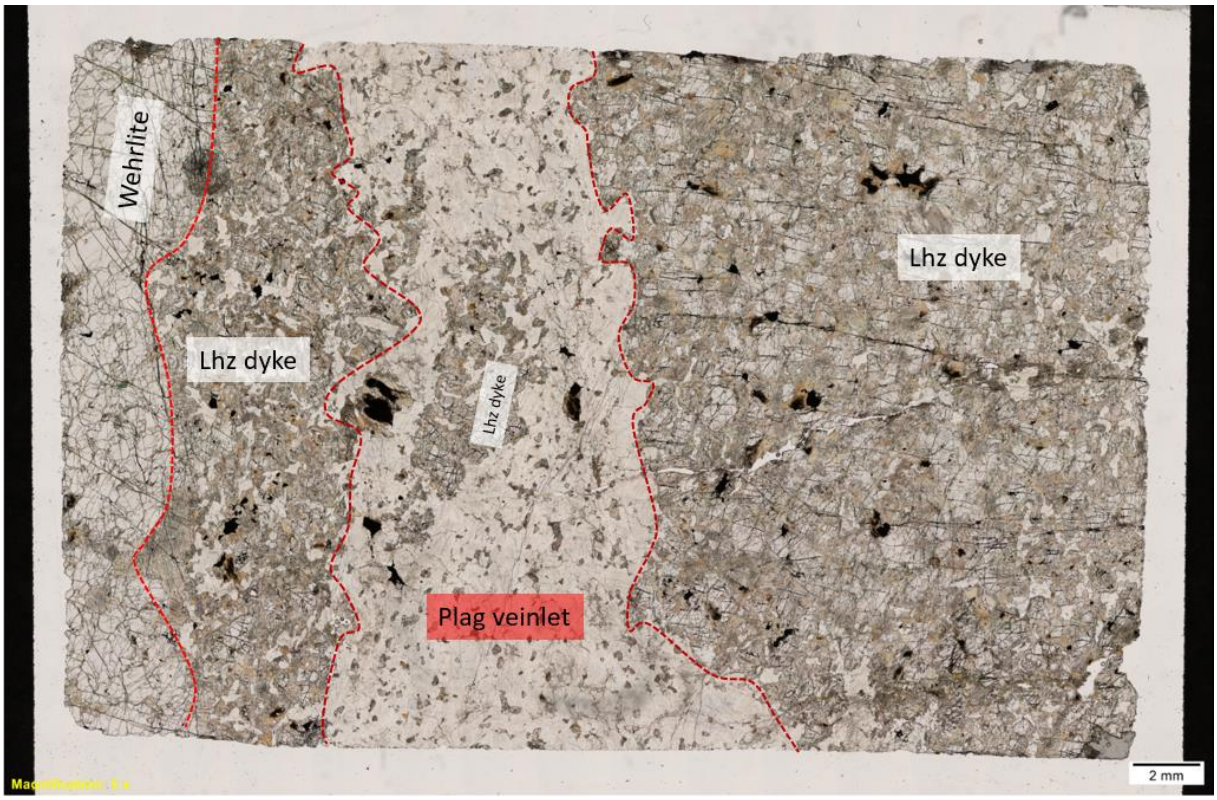

Figure 3.27. ***The lhz dyke is intruded by a larger, more massive plag veinlet. The contact to the dyke is highly irregular, with the veinlet following the grain boundaries of the lhz dyke closely. There is a 4x10 mm xenolith of the lhz dyke assimilated in the plag veinlet, as well as there being several px grains entrained in the plag and other fragments from the lhz dyke.***

The sample in Figure 3.27 is taken from the locality shown in Figure 3.23 a). This shows that the infiltrating material is similar, but it can infiltrate in different ways. The infiltration seen in Figure 3.27 is different when compared to the diffuse domains seen in Figure 3.26 (top), as this is a nearly monomineralic reopening of the existing dyke path, while the infiltration happening in Figure 3.26 happens more along grain boundaries.

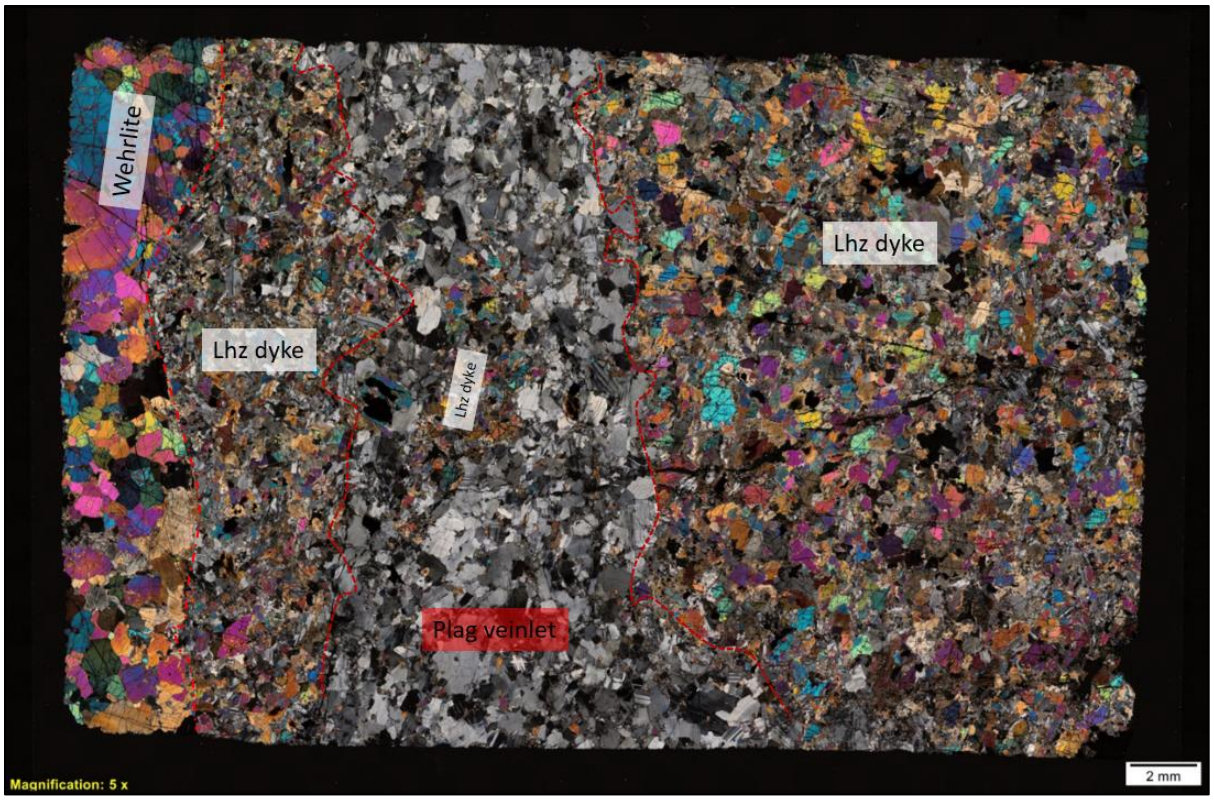

Figure 3.28. ***This sample is the same sample as presented in Figure 3.27, but here shown in xpl. The plag dominated zone is here seen as a monotone light to dark grey mass when compared to the mixed interference colours of the ol, px and hbl in the lhz dyke. The contact with the host rock is also seen to the left, labelled "Wehrlite". The host rock seems to be relatively unaffected by the emplacement of this dyke in terms of reactions, alteration and fractures.***

It can be seen in Figure 3.28 that the plag is for the most part localized in the main veinlet, but some plag is also observed in the lhz dyke, particularly in the segment of lhz dyke wedged between the wall rock (wehrlite) and the plag veinlet. This plag is believed to have originated in one of these plag domains, and are now infiltrating between grains like observed in Figure 3.26 (top).

The XRD analyses from the pure lhz dyke, and the associated comp dyke is presented in Table 3.9. When the primary groundmass excluding the plag domains, these dykes plot in the Di dominated wehrlite to and ol websterite. If the plag was included as a primary magmatic mineral in this dyke, and not a later infiltration, the composite dykes would be classified as an ol gabbronorite.

	JS11-03	**JS02-3**	**JS_2_18**	**JS09**	**JS07**	**JS09**
Type	Comp dyke	Comp dyke	Comp dyke	Lhz dyke	Lhz dyke	Lhz dyke
Fo	13,46	12,03	18,28	61,35	40,95	63,68
Hbl	14,83	7,42	5,71	2,86	11,09	2,4
Di	26,63	28,59	32,49	24,96	26,7	23,48
En	25,38	33,53	41,6	10,83	11,09	9,93
Lz	0	0	1,92	0	0	0
And	19,7	17,86	0	0	10,16	0,51
Ilm	0	0,57	0	0	0	0

Table 3.9. ***This table shows XRD results from samples classified as composite dykes, and lhz dykes.***

The most consistent mineral in these samples is Di with an average of 27,14% ± 3,14. The ol content varies strongly, as the degree of xenocryst assimilation varies across the sample set, with two JS09 samples both having ol content above 60%. JS07 is classified as a Lhz sample, primarily based on the

observed textures in this dyke. The XRD did however return a higher plag content than what was observed in the thin section in Figure 3.26 (bottom), of 10,16%. The same abnormality was observed in JS_2_18, which was sampled from Figure 3.23 c), which clearly has significant plag domains, but has an analysed plag content of 0%.

The as most of the plag content seems to be strongly localized, the sample analysed with XRD may not have contained one of these plag domains. This may have been the case for JS_2_18. As for JS07, the sample sent to be analysed may have contained a localized plag domain which did not appear in the sample from which the thin section was prepared.

Hbl is present in all samples, and is observed optically in the thin sections presented from this dyke type. The highest measured hbl content is in JS11-03 at 14,83% hbl, while the lowest concentration measured is JS09 at 2,4%. The hbl based on optical observation seems to be primary magmatic anhedreal hbl. For the most composite samples, the En content seems to be inversely correlated with the Fo content. When the Fo content is low, the En content seems to be higher.

3.4.3 Whole rock geochemistry

The whole rock, major geochemistry of these dykes are presented in Table 3.10. The massive plag rich domain seen in Figure 3.27 was cut way from the lhz dyke in order to analyse this material in an isolated sample, free of contamination. This is plotted as plag dyke.

Lables	Rock type	SiO2 (wt%)	Al2O3 (wt%)	FeO (wt%)	CaO (wt%)	MgO (wt%)	Na2O (wt%)	TiO2 (wt%)
JS01	Px comp	47	5,81	12,75	10,8	21,6	0,69	0,9
JS02-3	Px comp	49,3	9,4	11	10,4	18,85	1,18	0,73
JS11-3	Px comp	48,2	8,41	10,75	10,1	20,5	1,08	0,85
JS_2_2	Px comp	47,5	14,8	8,64	12,4	13,1	2,02	0,56
JS_2_18	Px comp	48,5	4,34	13,05	9	24,3	0,48	0,7
JS07-2	Lherzolite	43,1	6,85	14	8,66	24,7	0,9	1,22
JS09-1	Lherzolite	41,6	1,32	17,1	5,52	33,1	0,18	0,31
JS_2_8-B	Lherzolite	46	9,4	10,75	10,9	21,4	1,24	0,66
JS_2_9-O	Px dyke	51,3	3,88	10,4	12,9	20,8	0,4	0,71
JS_2_10	Px dyke	44,9	4,37	11,55	14,45	22,5	0,39	1,21
JS_2_8-A	Plag dyke	49,8	24,5	3,03	12,1	4,53	3,94	0,27

Table 3.10. ***This table shows the whole rock chemistry for this dyke type. The labels are presented with the rock types, and JS_2_10 is included as a wehrlite dyke, and JS_2_9-O is included as a webserite dyke.***

The SiO_2 content for the comp dykes is consistent, with an average of 48,1 ± 0,89 wt%. The Al_2O_3 content however varies more, with an average value of 8,55 ± 4,03 wt%. As Al is a mineral forming element in plag, an increase in plag would be expected to cause an increase in Al_2O_3 content. CaO content is also relatively consistent with an average value of 10,54 ± 1,24 wt%.

The chemistry for the lhz dykes shows a lower SiO_2 content, this is however expected because of the mineralogy of these dykes. The ol and en rich dykes have a lower SiO_2 content than plag rich dykes, as these minerals incorporate Si differently.

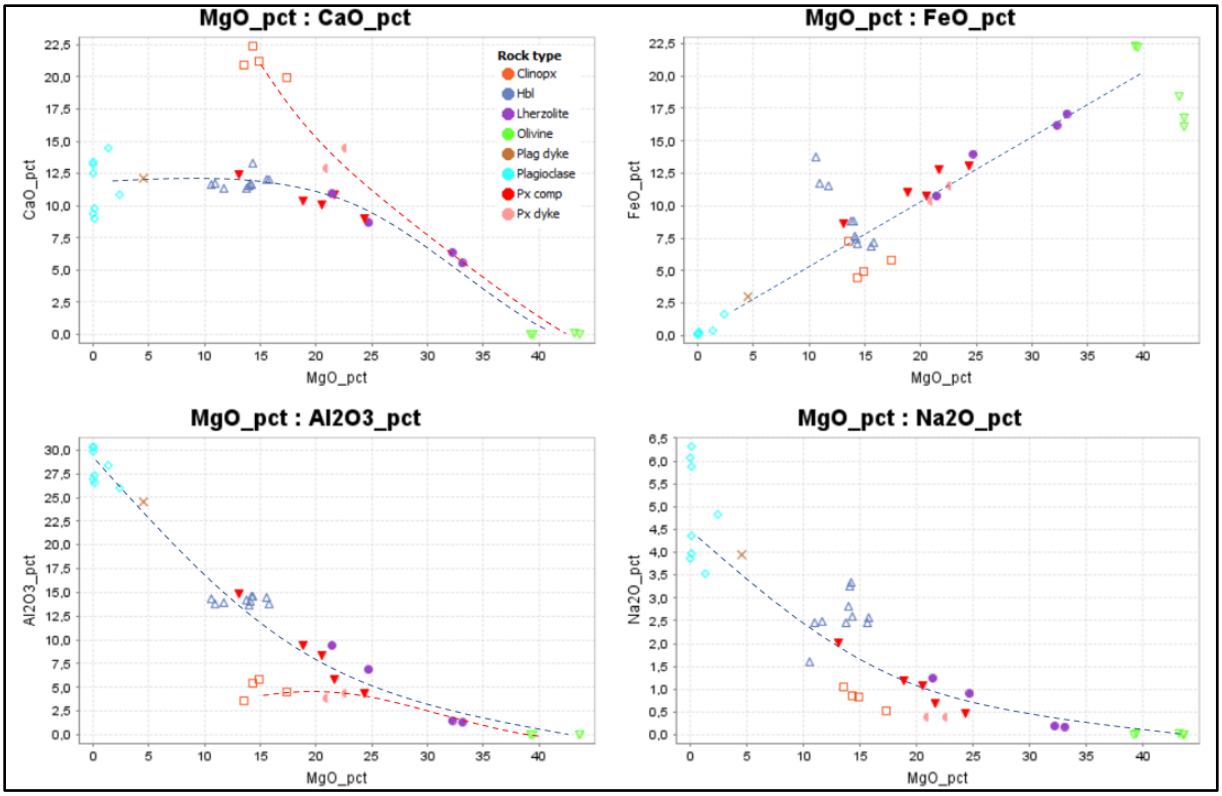

Figure 3.29. ***This figure shows the comp dyke (red triangle), lhz dykes (purple circles) and two px rich dykes (pink half-moon) plotted with the minerals plag (open turquoise square), hbl (blue open triangle), cpx (red open square), and ol (green open triangle). The blue stippled lines represent the mixing series between ol and plag, while the red stippled line seen in the MgO-CaO and MgO-Al_2O_3 plot represent the mixing line between cpx and ol. The elements are plotted against MgO as the Mg content between the samples varies significantly.***

As seen in Figure 3.29 the comp and lhz dykes seem to fall along the mixing line between ol and cpx, with the px dykes following the red line between ol and cpx. In the MgO-CaO plot the lhz samples rich in ol plot closer to ol analyses than the samples infiltrated by plag. The comp samples follow the curve between plag and ol indicating the increase and incorporation of plag. The monomineralic plag domain, here plotted as a brown cross, plots very close to the measured composition of plag. This then indicates that the increase in Ca is caused by the infiltration of plag in these samples, rather than from the cpx.

A similar trend is observed in MgO-Al_2O_3, as the dykes seem to evolve towards the plag dyke and plag measurements, rather than towards the cpx measurements. The measured plag material also falls between the hbl measurements and plag measurements, indicating that the phase might not be entirely monomineralic, and may contain some hbl in addition to plag.

The samples follow straight paths for both the Na_2O and FeO, and a similar trend to CaO and Al_2O_3 is observed, where the analyses for the dykes fall between the mixing lines of ol and plag.

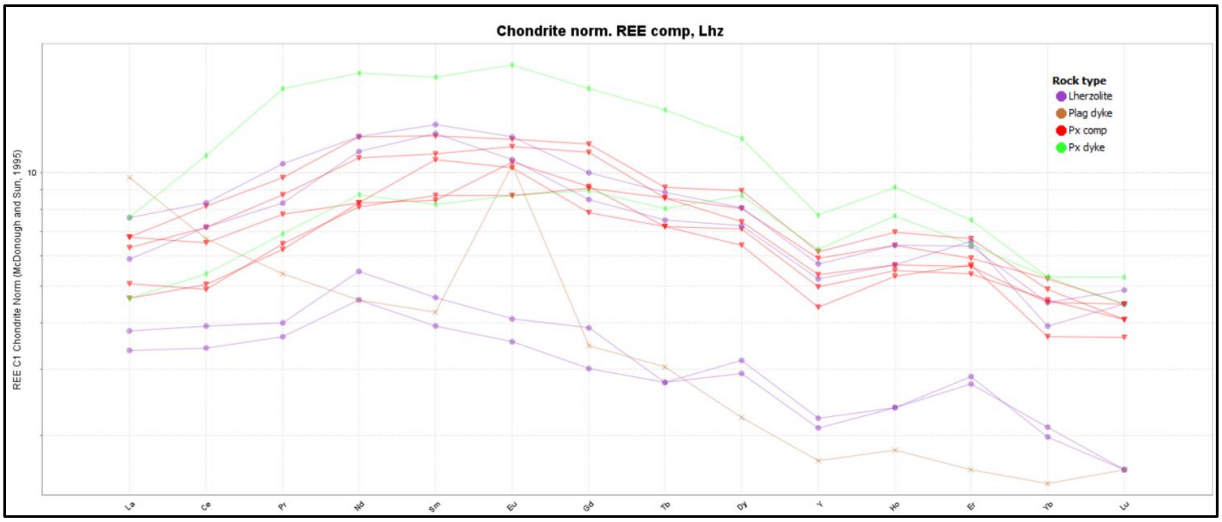

Figure 3.30. ***Chondrite normalized REE plot of the lhz dyke (purple), comp dyke (red), px dyke (green) and the plag dyke (brown).***

The chondrite normalized REE diagram seen in Figure 3.30 shows the REE as well as Y, and the values for the different samples are plotted. There are three main observed trends in this plot. The two most depleted lhz curves is relatively flat, slightly concave, with a peak around Nd, and a decline towards Lu. These two samples are rich in assimilated ol xenocrysts (~60%) which may affect the REE curve. The other lhz samples plot higher, but show a similar curve to the depleted curves. These dykes have a notable negative Y anomaly.

When looking at the curves of the comp dykes in Figure 3.30 the curves have a concave shape, with a peak around Nd, Sm. Despite varying mineralogy and whole rock geochemistry, the REE patterns are similar, with similar shapes and enrichments. These dykes, similarly to the lhz dykes have a significant negative Y anomaly. Some of the lhz dykes show a similar trend to the comp dykes, with similar REE trends. One of the px dykes also plots within this field, but has a slightly lower Sm and Nd peak than the comp dykes. The most enriched dyke is however JS_2_10, which has a Di content of 61,4%.

Lastly, the plag dyke has been plotted together with the other dykes. This is the only convex REE curve, with a maximum at LREE and a minimum at HREE. Of the samples plotted here, this is the most depleted samples with respect to HREE and the most enriched in La. It is also the only sample with a significant positive Eu anomaly. This is however to be expected of a material that is so enriched in plag, as plag can incorporate Eu more easily into its crystal lattice than other minerals.

3.4.4 Mineral chemistry

In addition to the whole rock chemistry a few samples were analysed using EPMA. This was only done on sample JS07 and JS_2_8 shown in Figure 3.26 and Figure 3.27.

Plagioclase	Na2O	Al2O3	CaO	K2O	SiO2	Total	An%
JS07	4,61	29,38	12,15	0,02	53,10	99,41	59,28
JS07	4,53	29,43	12,28	0,02	52,64	99,11	59,94
JS07	4,56	29,44	12,23	0,02	52,73	99,21	59,74
JS07	3,88	30,37	13,37	0,01	51,54	99,32	65,62
JS07	4,36	29,66	12,53	0,02	52,34	99,26	61,37
JS07	4,32	29,94	12,63	0,01	52,60	99,61	61,76
JS07	4,29	29,86	12,71	0,02	52,39	99,39	62,07
JS_2_8	4,06	30,37	13,16	0,02	52,34	100,04	64,18
JS_2_8	4,73	28,36	11,63	0,16	53,20	99,65	57,38

Table 3.11. ***This table shows the measured plag grains from sample JS07 and JS_2_8, with the calculated An content of each sample. All measurements are wt%.***

The plag analyses were all checked for zonation. Due to the irregular, and elongated shape of many of the grains, significant zonation was not observed. Some grains may be normally zoned, with a Ca rich core and a Na rich rim, but the zonation was subtle, if present at all.

Representative averages for EMPA analyses are presented in Table 3.11. The An content varies from $An_{57,38}$ – $An_{64,18}$. The analyses vary slightly from grain to grain, and some of the plag grains seem to have been re-equilibrated with very Na rich rims. This rim seems to be a sub solidus reaction, and does not represent the primary magmatic composition of the plag in this dyke type.

The calculated plagioclase formula for this dyke type is

$$(Ca_{0,65-0,57}Na_{0,34-0,42})(Al_{1,52-1,63}Si_{2,37-2,43})O_8$$

Some cpx grains were also analysed in the samples. These are presented in Table 3.12.

Clinopx	Na2O	MgO	Al2O3	CaO	Cr2O3	FeO	TiO2	SiO2	Total	Di%
JS07	0,78	14,37	5,23	22,41	0,36	4,55	1,44	50,04	99,34	84,9
JS07	0,76	14,70	4,82	22,96	0,29	4,18	1,24	50,46	99,58	86,2
JS07	0,90	14,15	5,70	22,29	0,38	4,40	1,45	49,97	99,38	85,1
JS_2_8	0,67	14,15	5,55	22,92	0,44	4,39	1,45	49,76	99,47	85,1
JS_2_8	0,63	15,15	4,48	21,60	0,37	5,07	1,22	50,78	99,48	84,4

Table 3.12. ***This table shows representative average values for the cpx grains analysed in JS07 and JS_2_8. Measurements are in wt%.***

The diopside content for the analysed cpx is Mg rich with the content varying from $Di_{84,4}$ – $Di_{86,2}$. The Cr content here is above LOD, but below quantification limit, meaning the measured amount only indicates the presence of Cr, rather than establishing the amount.

The calculated cpx formula for this dyke type is

$$(Ca_{0,85-0.91}Na_{0,05-0,06})(Mg_{0,77-0,83}Fe_{0,13-0,15}Al_{0,07-0,10}Ti_{0,03-0,04})(Si_{1,84-1,88}Al_{0,12-0,16})O_6$$

The plag rich domain seen in Figure 3.27 is also rich in carbonates. Some of these carbonate grains were analysed using the program set up for plag, cpx and ol. These results are presented in Table 3.13.

Carbonates	MgO	CaO	FeO	MnO	Total	Mg#
JS_2_8	19,8	28,88	2,85	0,1991	51,7688	0,512
JS_2_8	20	29,07	2,73	0,1274	51,988	0,511
JS_2_8	19,9	28,91	2,73	0,1475	51,7379	0,511
JS_2_8	19,62	28,96	2,81	0,1432	51,6158	0,515
JS_2_8	19,88	28,92	2,71	0,1421	51,7103	0,511
JS_2_8	19,92	28,93	2,7	0,1634	51,7317	0,511
JS_2_8	19,85	28,94	2,73	0,1633	51,706	0,512
JS_2_8	19,6	28,99	2,91	0,1778	51,7335	0,515

Table 3.13. ***This table shows the analyses for the carb grains found in the plag rich domain in JS_2_8. The totals for these analyses are very low (~51%) because the grains were analysed as silicate minerals, as a designated carbonate program was not set up. The cations however were analysed properly. Measurements are in wt%.***

The carbonate grains plot as dolomite grains, with the molar proportion Ca/Mg~1, with some additional Fe. The analyses are consistent, and despite the totals being low, they are consistently low. The analysis lacks a Carbon channel, meaning the additional C in the carbonates was not analysed.

The carbonate formula calculated for these carbonates are

$$(Ca_{0,98-0,99}Mg_{0,93-0,94}Fe_{0,07})CO_3$$

Amphibole was also analysed in these samples. The results are presented in Table 3.14.

Amph	SiO2	Al2O3	FeO	CaO	MgO	Na2O	K2O	Cr2O3	TiO2	Total	Class
JS07	41,57	13,97	7,70	11,73	14,07	3,17	0,68	0,41	4,23	99,72	Ti-parg
JS07	42,06	14,18	7,48	11,73	14,04	3,28	0,62	0,42	4,04	100,02	Ti-parg
JS07	42,45	14,07	7,62	11,68	14,02	3,24	0,61	0,36	3,94	100,13	Ti-parg
JS_2_8	43,04	13,99	8,91	11,45	13,76	2,39	1,01	0,27	3,02	100,02	Ti-parg

Table 3.14. ***This table shows the analysed amphiboles from JS07 and one sample from JS_2_8.***

The measured hbl in the samples all plots as Ti-rich pargasite (Hawthorne, et al., 2012). The JS_2_8 hbl has a slight enrichment in K compared to the other samples, and a decrease in Na.

The calculated hbl formulas from Hawthorne et al. (2012) are

$$(Na_{0,47-0,734}K_{0,11-0,19})(Ca_{1,77-1,83}Na_{1,73-2,05})(Mg_{2,97-3,05}Fe_{0,91-1,03}Al_{0,43-0,61}Ti_{0,43-0,46})$$

$$(Si_{6,04-6,22}Al_{1,78-1,96)}O_{22}(OH_2)$$

3.4.5 Plagioclase amphibole thermobarometry

Based on the EPMA analyses of a few select spots of amphibole and plagioclase a thermo-barometric measurement was calculated using the formulas developed by Ridolfi et al. (2009) and Molina et al. (2015). The analysis was based on primary magmatic amphibole and plagioclase from JS07, as these were believed to have crystallized under equilibrium conditions.

The temperature and pressure calculated based on the analyses in JS07 and JS_2_8 using the Amp-TB spreadsheet from Ridolfi et al. (2009) is presented in Table 3.15.

Sample	Temperature	Pressure
07_a1_amp8	1034 ± 22	602 ± 66
07_a1_amp9	1034 ± 22	588 ± 65
07_a1_amp10	1041 ± 22	602 ± 66
07_a1_amp11	1038 ± 22	544 ± 60
07_a1_amp12	1037 ± 22	578 ± 64
07_a1_amp13	1039 ± 22	604 ± 66
2_8_a2_amp1	960 ± 56	-
2_8_a2_amp2	988 ± 56	-
2_8_a2_amp3	973 ± 56	-
2_8_a2_amp4	981 ± 56	-
2_8_a2_amp5	1008 ± 56	-
2_8_a2_amp6	988 ± 56	-
2_8_a2_amp7	1002 ± 56	-
2_8_a2_amp17	965 ± 56	-
2_8_a2_amp18	988 ± 56	-

Table 3.15. ***Temperature and pressure estimate for the emplacement of the lhz dykes are presented in this table.***

Ridolfi et al. (2009) is bases its calculations on calcic amphiboles. If the amphibole analysed has a Ca content which is too low, the calculation is not valid. Similarly, if the Al content of an amphibole is too high the calculation is not valid. The analysed grains from JS07 have Ca and Al contents which are in range for the calculation, and both a temperature and pressure estimate can be calculated. The samples form JS_2_8 however, have Al values which are too high, making a pressure estimate invalid as it is based on the Al content in amphiboles.

The pressure results from Ridolfi et al. (2009) do not seem realistic, as the parameters which it is based on is sensitive to later alteration and sub-solidus reactions. An amphibole-plagioclase barometer is therefore used as well.

Using the temperature estimated from Ridolfi et al. (2009) with the Molina et al. (2015) plag-amph thermobarometer a pressure estimate was obtained. These results are presented in Table 3.16.

Plag spots	Hbl spots	Lower T (^{O}C)	Upper T (^{O}C)	Lower P (kbar)	Upper P (kbar)
07_a_1_plag20	**07_a1_amp8**	1012	1056	8,06	8,52
07_a_1_plag21	**07_a1_amp9**	1012	1056	9,83	10,51
07_a_1_plag22	**07_a1_amp10**	1019	1063	8,92	9,57
07_a_1_plag23	**07_a1_amp11**	1016	1060	8,20	8,86
07_a_1_plag24	**07_a1_amp12**	1015	1059	9,51	10,18
07_a_1_plag25	**07_a1_amp13**	1017	1061	10,09	10,80

Table 3.16. ***This table shows the temperature and pressure ranges from the six analyses of amph-plag pairs from JS07, using the Molina et al. (2015) calculation.***

The temperatures obtained from Ridolfi et al. (2009) presented in Table 3.15 were used to obtain a pressure estimate from each sample. The minimum and maximum temperatures from Table 3.15 were used, as well as the chemistry from the amph together with the associated plag analysis. The pressures do vary between the different samples, as the chemistry of the samples vary. An estimate of average pressures and temperatures were therefore made.

The temperature and pressure estimate for this dyke type is **1037 ± 22 ^{O}C** at **9,42 ± 0,87 kbar** (both estimates are given at σ_1).

The grains used for this analysis can be seen in Figure 3.31.

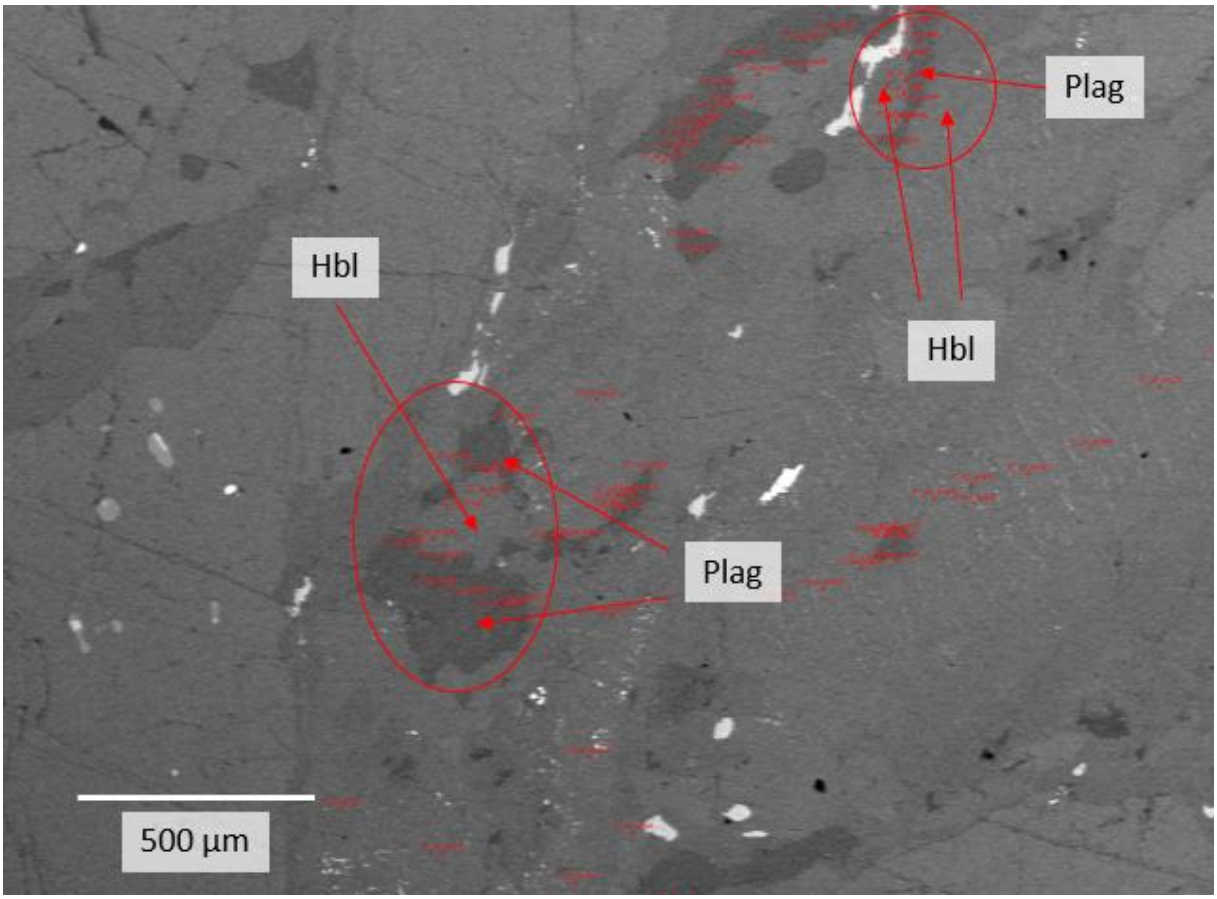

Figure 3.31. ***The spots used for the thermobarometry are shown in this sample. The dark grey grain is the plag grain used, and the surrounding lighter grain is a chemically homogenous hbl.***

This grain was selected, as the analyses form the grain were homogenous and robust analyses. The grain has no zonation, and is assumed to be in equilibrium with the hbl. These grains were not deformed either, meaning the analysis would depict the actual magmatic chemistry of the minerals. The grains from JS_2_8 were not used for the pressure estimates, as the temperature estimated from Ridolfi et al. (2009) were unreliable, which would carry over to the pressure estimates.

3.5 Hornblende gabbronorite dyke

3.5.1 Field observations

The hornblende gabbronorite (hbl gabbro) is one of the most massive dykes found in ULS, and has a large extent along strike, often continuously exposed for more than 100 m. It is steeply dipping (>75-80°), and trending NNE-SSW. The dyke can vary from 10-50 cm in width, and has a light grey to dark grey appearance when seen in the field. The dyke is medium to fine grained with 2-3 mm grains, sometimes including xenocrysts of ol and px up to 0,5 cm. The mineralogy of the dyke is dominated by plag and hbl, with opx and some cpx as part of its ground mass.

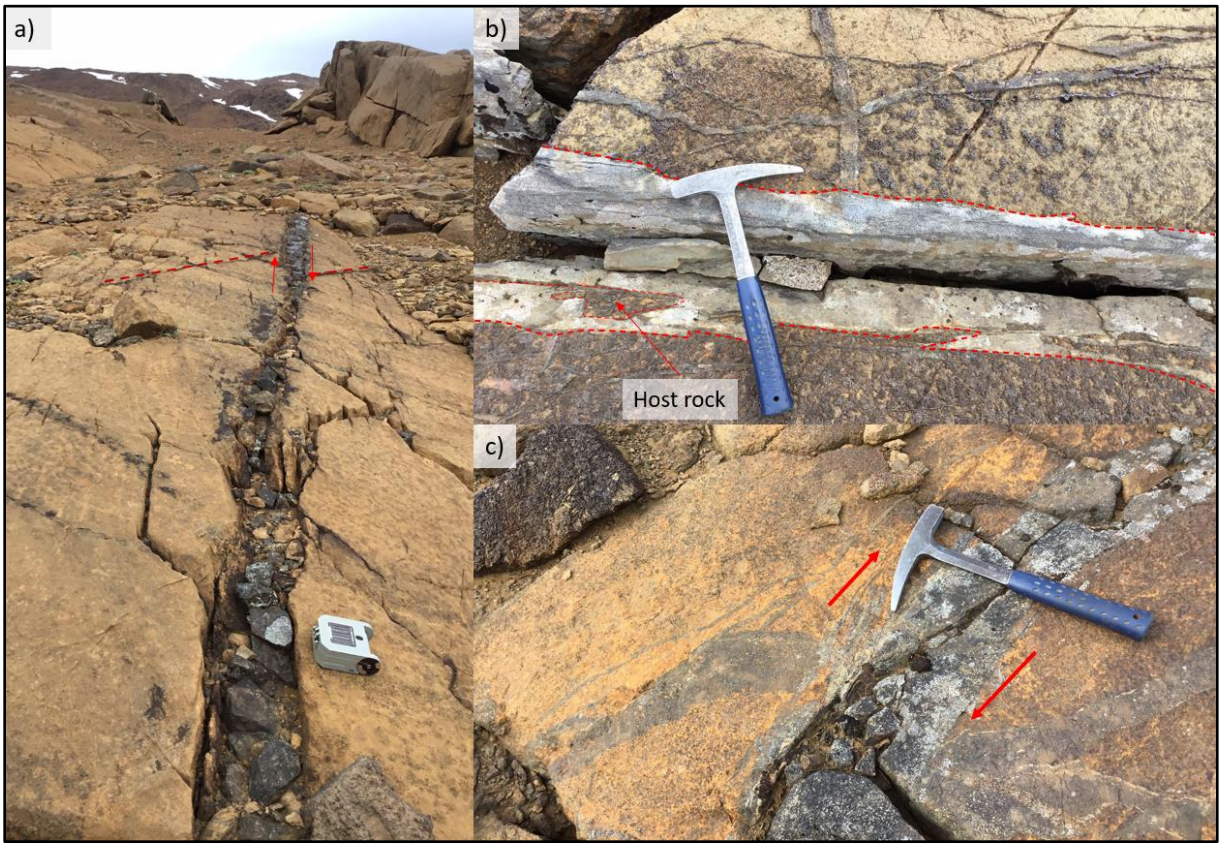

Figure 3.32. ***This figure shows three different localities of the same dyke type. a) This photo shows the hbl gabbro intruding through the LSRD, striking parallel to its orientation. The dyke seen here is ~20 cm wide, and exposed for 40 m. The dyke is straight, and does not deviate much from its strike. The dyke also offsets a few older dykes marked by a red stippled line in a dextral sense indicated by the red arrows. b) This image shows the hbl gabbroic dyke cutting an older lhz dyke. The dyke in this photo has a well developed fabric, with the fabric plane being parallel to the dyke plane. The contact of the dyke is highly irregular with the host rock as indicated by the red stippled lines. Parts of the dyke seems to be dragged and stretched, and infiltrating in irregular protrusions from the dyke into the host rock. The host rock surrounding the dyke, and the part of the host rock included in the dyke (indicated by a red arrow) seems to be slightly more deformed than the surrounding host rock, with some domains being stretched out more than the host rock. Interpreted sense of shear here is dextral. c) Similarly to the dyke in b) this dyke also has a highly irregular contact to the host rock. The dyke is also enveloped by the same orange-yellow material as presented in chapter 3.6. This dyke also offsets an older dyke in a dextral sense of shear. The dyke also has small protrusions of dyke material subparallel to the dyke, infiltrating into the host rock.***

As seen in Figure 3.32 these dykes are wide, homogenous dykes, which sometimes show fabric, and have highly irregular contacts with the host rock, while remaining true to strike for long distances. The dyke does not seem to have a chilled margin, and shows a uniform grain size across the width of the dykes. The dyke is also associated with small black, pseudotachylyte like veins parallel to the dyke itself.

Figure 3.33. ***This figure shows the sampling locality of two different samples from the same dyke type. The dyke is roughly 50 cm across and has an irregular contact with the host rock. The dyke is separated into two segments. The undeformed core labelled "undeformed hbl gabbro", and the deformed contacts to the host rock labelled "sheared dyke". These contacts are outlined by red stippled lines. The contact on the right side of the image also hosts some of the yellow-orange sheared wehrlitic material. The contacts between the sheared dykes, and yellow sheared wehrlite hosts some very dark cm wide zones as well, and the two sheared domains seem to mix and mingle indicating high temperatures, and possibly low viscosities to allow for the ductile mingling. The contact between the undeformed and deformed dyke seems to be strongly localized on the left side, but more gradual on the right side. The core of the dyke is a dark, uniform hornblende rich gabbro norite, with 0,5-1 cm xenocrysts of weathered orange ol and possibly some px. The dyke here is oriented 74°/295***

This dyke type changes appearance from and undeformed, coarser grained dyke rich in xenocrysts, to a more fine-grained, xenocryst free dyke with strong fabric. This can be observed in Figure 3.33 where the core of the dyke is homogenously coarse grained with xenocrystic ol, while the wall rock contacts are more leucocratic, and fine grained. This phenomenon is usually only observed in dykes of this width, and the smaller dykes like the ones seen in Figure 3.32 are usually too deformed to observe the xenocrystic appearance of the dyke.

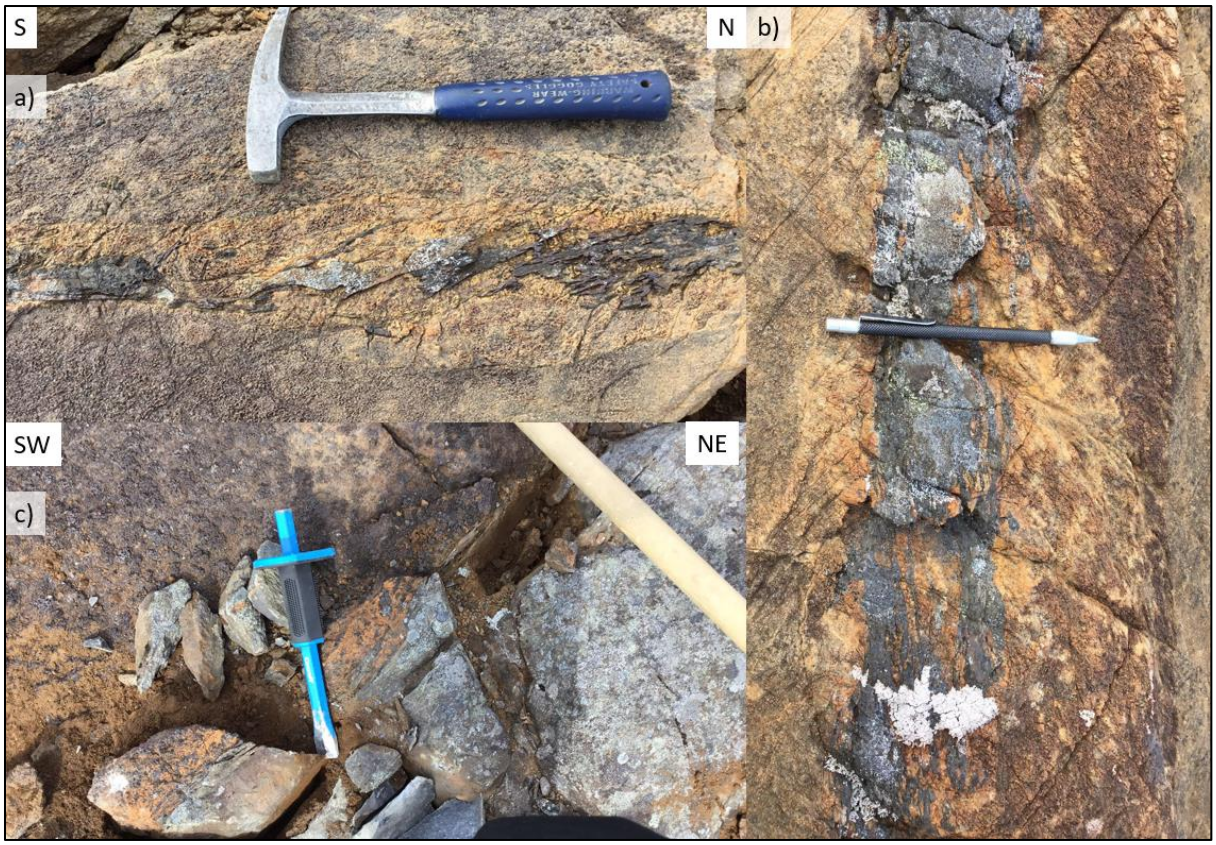

Figure 3.34. ***These three figures also show localities of observed hbl gabbro dykes. The dykes in all three localities are deformed and enveloped by the yellow sheared material. a) The dyke exposed in this locality is strongly deformed, and sheared in a dextral sense. The remainder of the dyke has formed a σ-clast like structure, and the segments of the dyke are imbricated. This indicates high temperature, ductile deformation and dragging, mainly absorbed by the dyke itself. Based on the shape of the clasts and imbrication, it appears as the surface is close to parallel to the orientation of the deformation. The host rock contact is deformed, and the entirety of the dyke is enveloped by the yellow-orange shear zone. b) This dyke is also completely enveloped by the yellow shear zone. The dyke here is not as dragged out as the dyke in a), but this might relate to the orientation of observation. This surface could be close to perpendicular to the orientation of the deformation. c) This photo shows the contact between the dyke and the wehrlite, with a small wedge of dyke material being dragged along the edge of the dyke with a dextral shear sense, into the surrounding yellow material.***

This dyke is unique on the southern plateau of RUC in the sense that it represents one of the youngest dykes, and is the dyke type which is observed to take up the most amount of strain of any dyke type. These dykes are commonly deformed, and enveloped by deformation material in the host rock as seen in Figure 3.32, Figure 3.33 and in Figure 3.34.

3.5.2 Petrographic observations

The samples collected for these dykes were taken both from the well-preserved parts of the dykes, and from the deformed parts of the dykes.

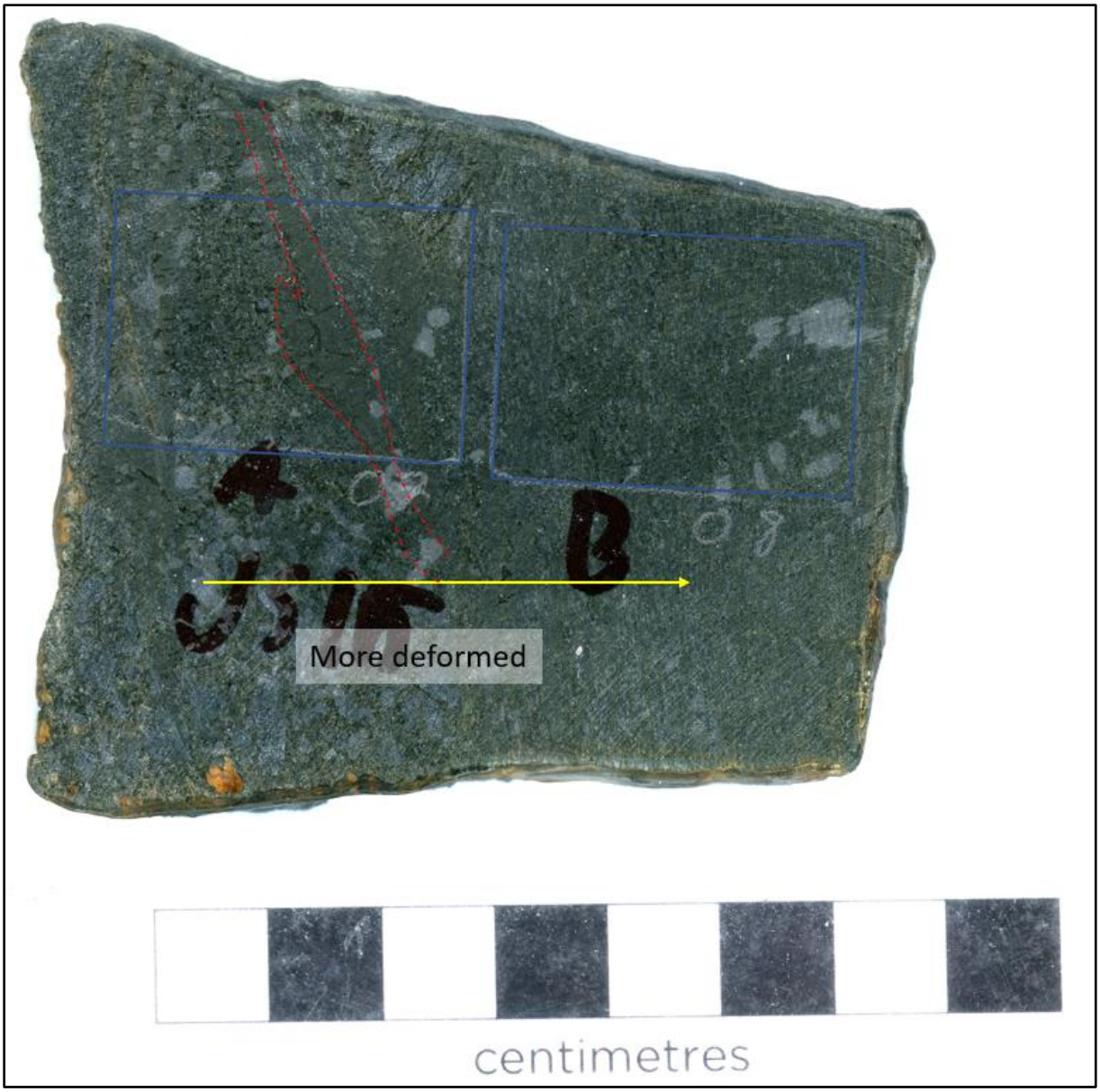

Figure 3.35. ***This is the cut sample from which JS15 A and B were prepared. This sample is collected from the locality seen in Figure 3.33. The left side of the dyke shows the coarser, gabbroic dyke with large phenocrysts of ol. The dyke becomes progressively more deformed towards the right of the sample, as indicated by the yellow arrow. The blue frames indicate where the thin sections prepared from this sample were cut out. The two sides of this sample have also been cut and separated for chemical analysis between the two textures. The dark zone highlighted by the red stippled lines is a form of pseudotachylyte similar to the ones described in Figure 3.32.***

The sample in Figure 3.35 include the contact between the undeformed hbl gabbronorite, and the deformed gabbronorite as seen in Figure 3.33, and provides insight into the deformation and grain size reduction which is observed in the samples. The sample shows distinct changes in fabric, as it progresses from a deformed to an undeformed rock. The thin section sampled from are A in Figure 3.35 can be seen in ppl and xpl in Figure 3.36.

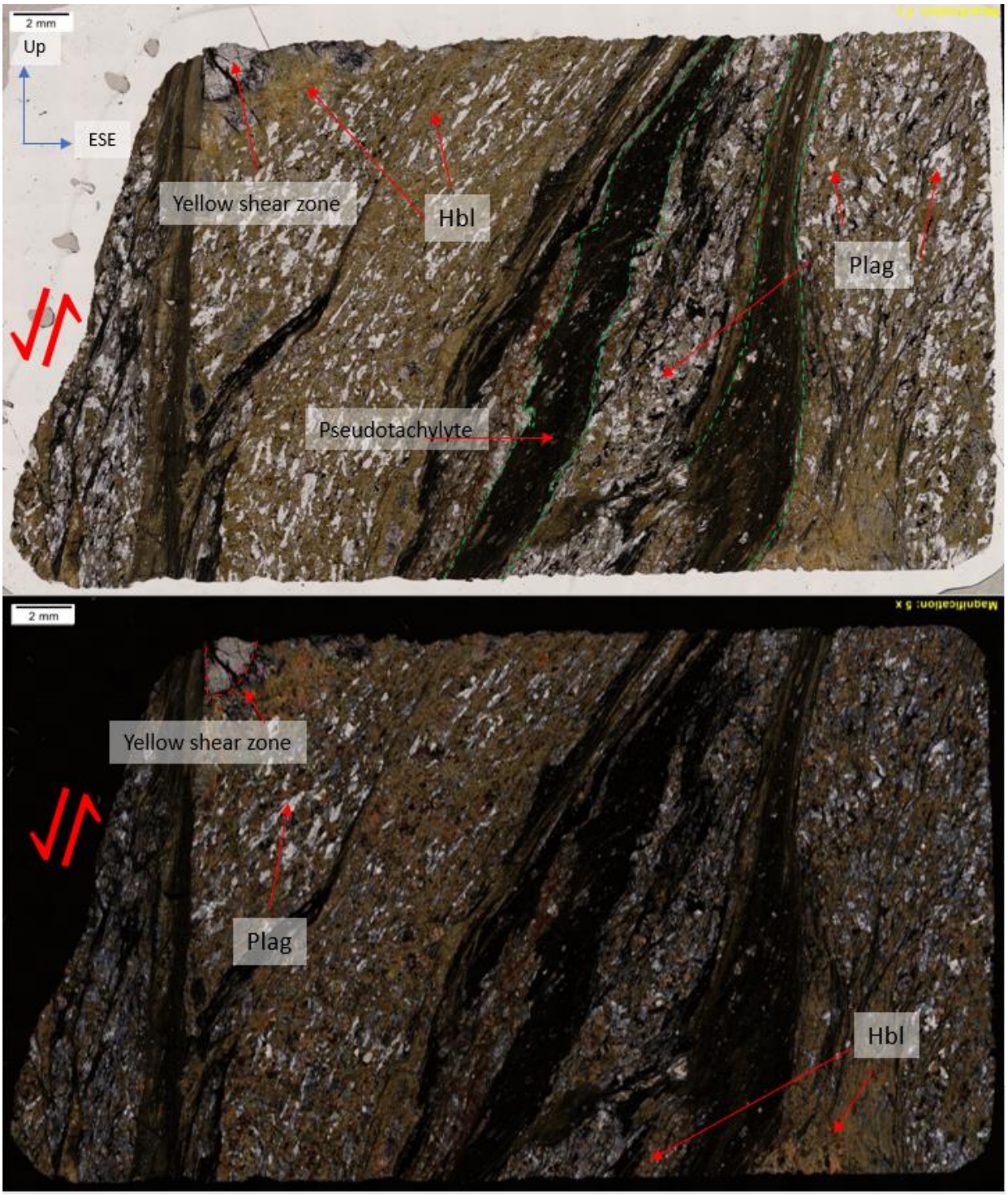

Figure 3.36. ***This image shows the same thin section in ppl (top) and xpl (bottom) of the sample labelled JS15-A. This thin section is prepared from the slab seen in Figure 3.35 from the locality in Figure 3.33. The sample is as seen heavily deformed with dark pseudotachylytes cutting through the sample. This sample mainly consists of coarser plag and hbl, with some finer grained cpx and opx interstitial in the plag and hbl matrix. Based on the dragging and foliation of the hbl and plag domains the shear sense here is interpreted as sinestral to the foliation direction. The pseudotachylytes seem to have accommodated for some of the deformation, as it seems to have formed a mylonite in some areas. The pseudotachylytes in the right portion of the image seems to be mylonitized. The dyke seems to be more hbl rich in the deformed areas, as the portion wedged between the pseudotachylytes is very rich in hbl, while the ends of the thin section seems to be more plag and px rich. Hbl and plag have been indicated by red arrows and text boxes. In the ppl image the two largest pseudotachylytes have been outlined by green stippled lines. There is also a pocket of the yellow shear material usually seen enveloping these types of dykes. These fine grained zones will be described in more detail in chapter 3.6. The thin section has been oriented to its field orientation, indicated by the two blue arrows in the top left corner. Up and ESE is indicated.***

The samples from these dykes show that the dyke has been deformed in a sinestral sense in thin section view based on dragging of features like pseudotachylytes observed on the structures apparent from the thin section. More detailed images of deformation features can be seen in Figure 3.37. With the orientation of the samples in Figure 3.36 this indicates a steep, west dipping normal shear zone, with the western block being down thrown.

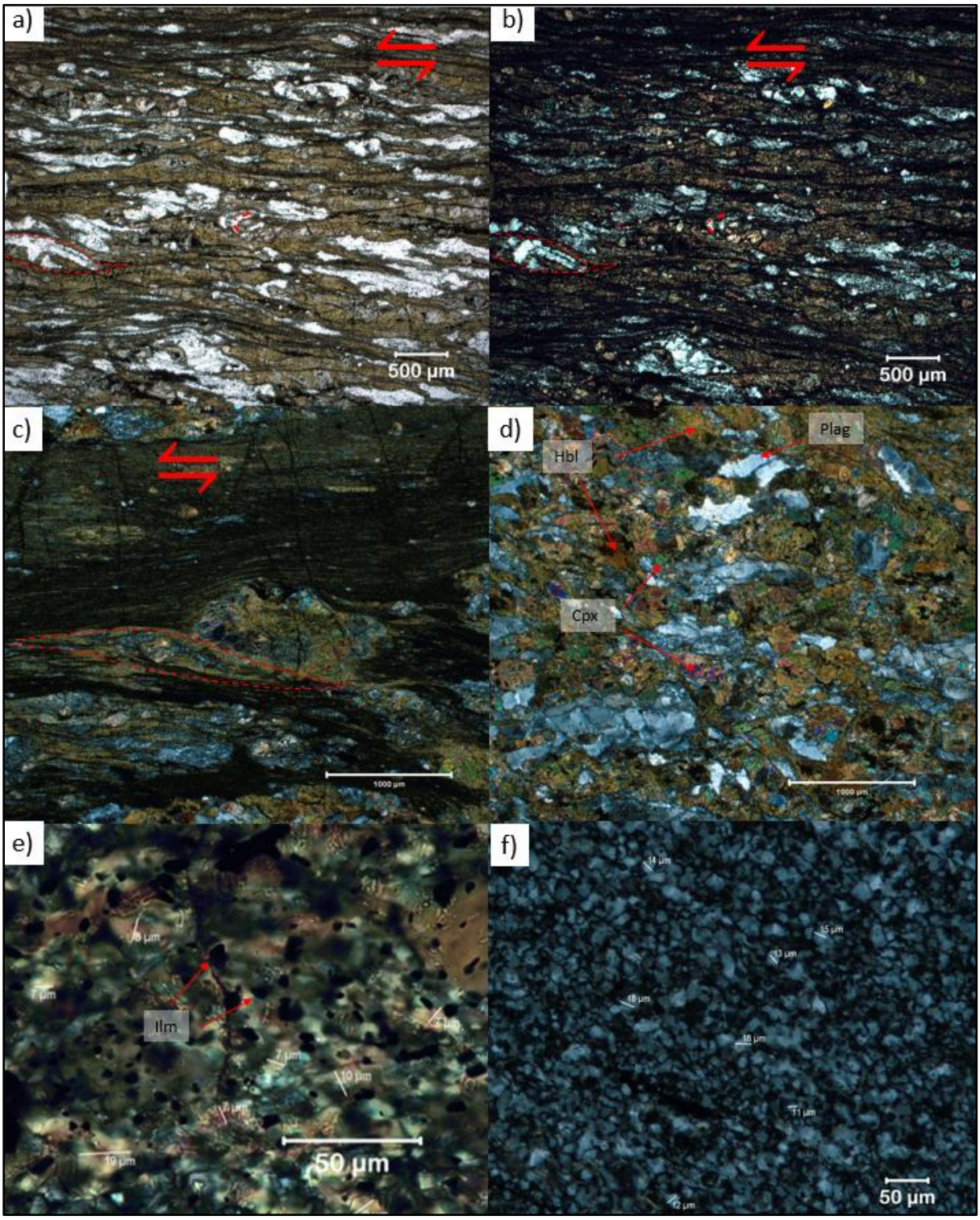

Figure 3.37. ***a) This picture is from a thin section prepared from section B in Figure 3.35. There is a "fish" structure in the left middle of the image marked out by a red stippled line. This fish is dragged in a sinestral way. There is also a small fold***

in a plag grain indicated by a small stippled red line. The dyke itself is strongly foliated, with the foliation of the dyke being parallel to the horizontal of the image. Small dark bands of what resembles the pseudotachylytes in Figure 3.36 cut the dyke parallel to the foliation plane. The brown minerals here are hbl, and the light minerals are mainly plag and some fine grained px. b) This image is the same as the image in a), but this image is taken in xpl. The fish structures and fold structures are much more difficult to see in this image, as the grains are fragmented, and very fine grained. The plag grains are not large uniform plag grains, but rather, new recrystallized, very fine grains. The hbl is also almost completely recrystallized. c) This image is taken from the same dyke type, in an area which has experienced more strain. The hbl is totally recrystallized, and some plag is mixed in with the uniform brown zone. There are two ~1mm clasts being dragged in the shear zone. The left clast has a fish shape and is outlined by red stippled lines, indicating a sinestral shear sense. d) This image is taken from a less deformed dyke of this type. It shows plag grains ~0,5 mm in size, with undulating extinction, indicating the lattice has taken up some strain, but is not dynamically recrystallized as the sample seen in a) or b). The grains show more primary magmatic textures like interlocking grain boundaries and equigranular grain size. The sample also contains some cpx indicated by the red arrows, but is dominated by hbl and plag. e) This picture is taken using a 50X objective with a condenser lens. The picture shows a part of one of the very fine grained shear zones as seen in c). The grain size of the dynamically recrystallised hbl is measured to be ~8 µm. The picture also shows some ilm grains indicated by the red arrows. These are ~5 µm opaque rounded grains which are abundant in these shear zones. These are believed to give the shear zones its dark appearance. f) This picture shows the recrystallized new grains from one of the completely recrystallized plag grains. The average grain size here is measured to be ~14,5 µm. The new grains are granoblastic, with few of the grains showing signs of undulating extinction, indicating these grains are completely recrystallized.

Another dyke sample form this dyke type can be seen in Figure 3.38Figure 3.36. This dyke is related to the dyke type seen in Figure 3.36. The dyke here is more fine grained, so it varies slightly from the other dykes texturally, but mineralogically and chemically this dyke is related to the dyke in the previous figures. The main portion of this dyke has no fabric, and mainly shows magmatic textures and structures.

Figure 3.38. ***This sample is from JS12-1-1-A. The dyke in this image is primarily made of hbl, cpx, opx and plag. The dyke is equigranular, and the grains are subhedral. The notable part of this dyke is the shear zone on the left side of the image. This shear zone texturally resembles the shear zones observed in Figure 3.36 and Figure 3.37 with the shear zone primarily being made of plag and hbl with minor px. The zones has undergone a similar dynamic recrystallization to the previous samples. There is a clear sinestral shear sense, based on deformed and dragged clasts of plag and plag new-grains. The deformed clast is outlined by red stippled lines. There is also a pseudotachylyte cutting through the dyke, which originates from the shear zone. This sample is not oriented, making tectonic interpretation difficult. Based on the orientation of the shear zone and the tachylyte, this could be a Riedel shear, as it is sub parallel to σ_1 in this case. This would help aid in the injection of friction generated melt.***

The dyke in Figure 3.38 shows a change from a ductile deformation zone, to a brittle infiltration of a pseudotachylyte opening a fracture in the dyke and cutting through parts of the rock. Similar textures have been seen in the more deformed thin sections, but these pseudotachylytes (Figure 3.36) are heavily deformed and have been dragged in a ductile manner. The pseudotachylyte in Figure 3.38 has preserved its brittle structures, with kinks and sharp edges. These zones are however now devitrified, and have re-equilibrated to a cryptocrystalline mass, rich in oxides and some silicate minerals.

One of the samples sampled from locality in Figure 3.33 is sampled from the part of the transition from deformed to undeformed dyke. The sample includes an almost monomineralic deformed zone of plag. This sample is interesting because of its deformation textures, but it also represents a significant chemical anomaly, which is described in the next chapter.

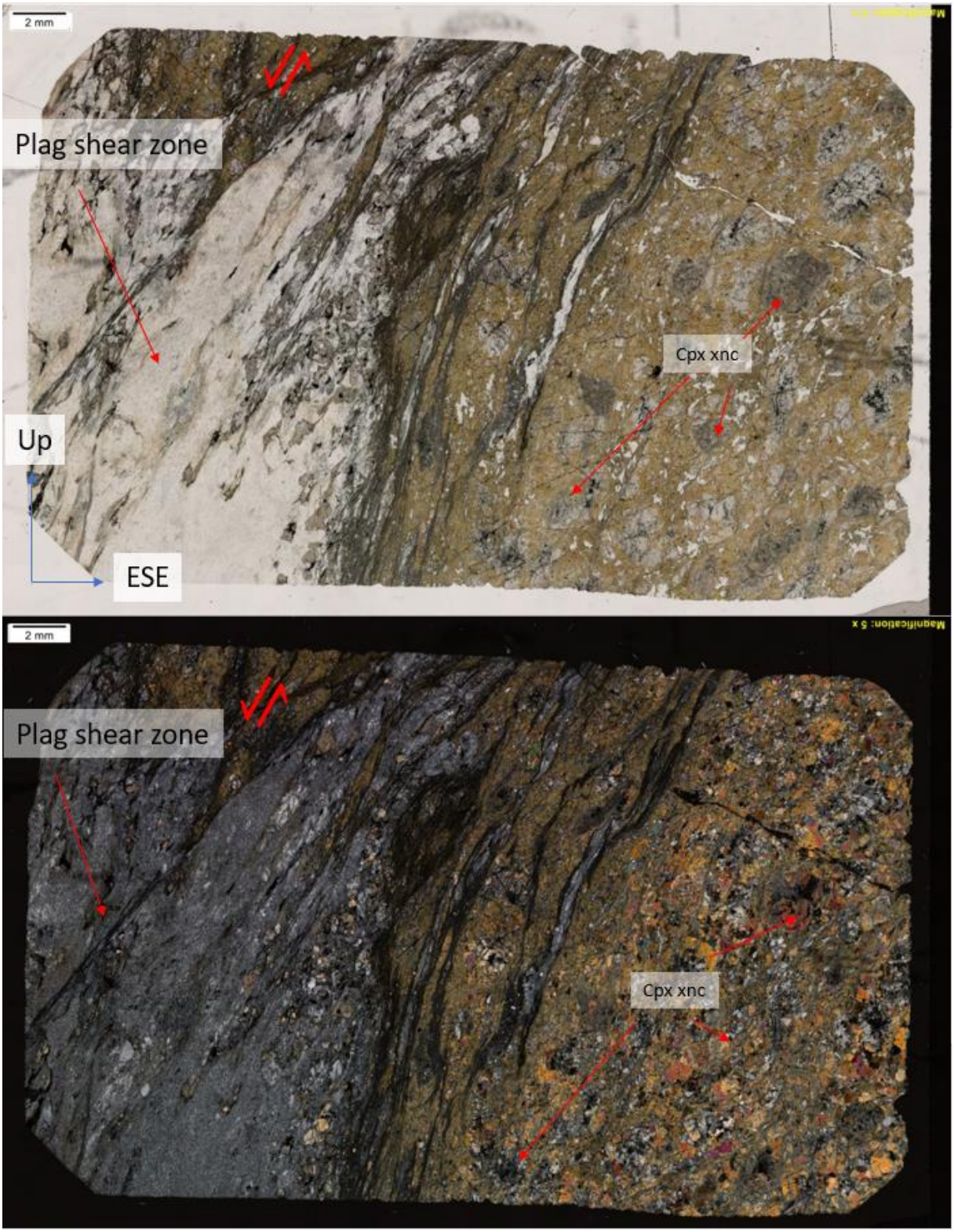

Figure 3.39. ***These scans are from JS_2_12-A. This dyke represents the transition between a plag rich shear zone and the hbl gabbro rich in xenocrysts as is described in further detail in Figure 3.40. The shear zone is almost completely recrystallized and only contains a few old core grains of plag. The rest of the plag has been dynamically recrystallized to new grains. The shear zone does host a few xenoliths of hbl gabbronorite dyke, which are deformed and dragged. The interpreted shear sense in this thin section is dextral, and the thin sections are oriented similar to Figure 3.36, again indicating a steep normal shear zone with the western block being downthrown.***

Another less deformed dyke of this type can be seen in Figure 3.40. This sample is the most hbl rich sample collected in ULS.

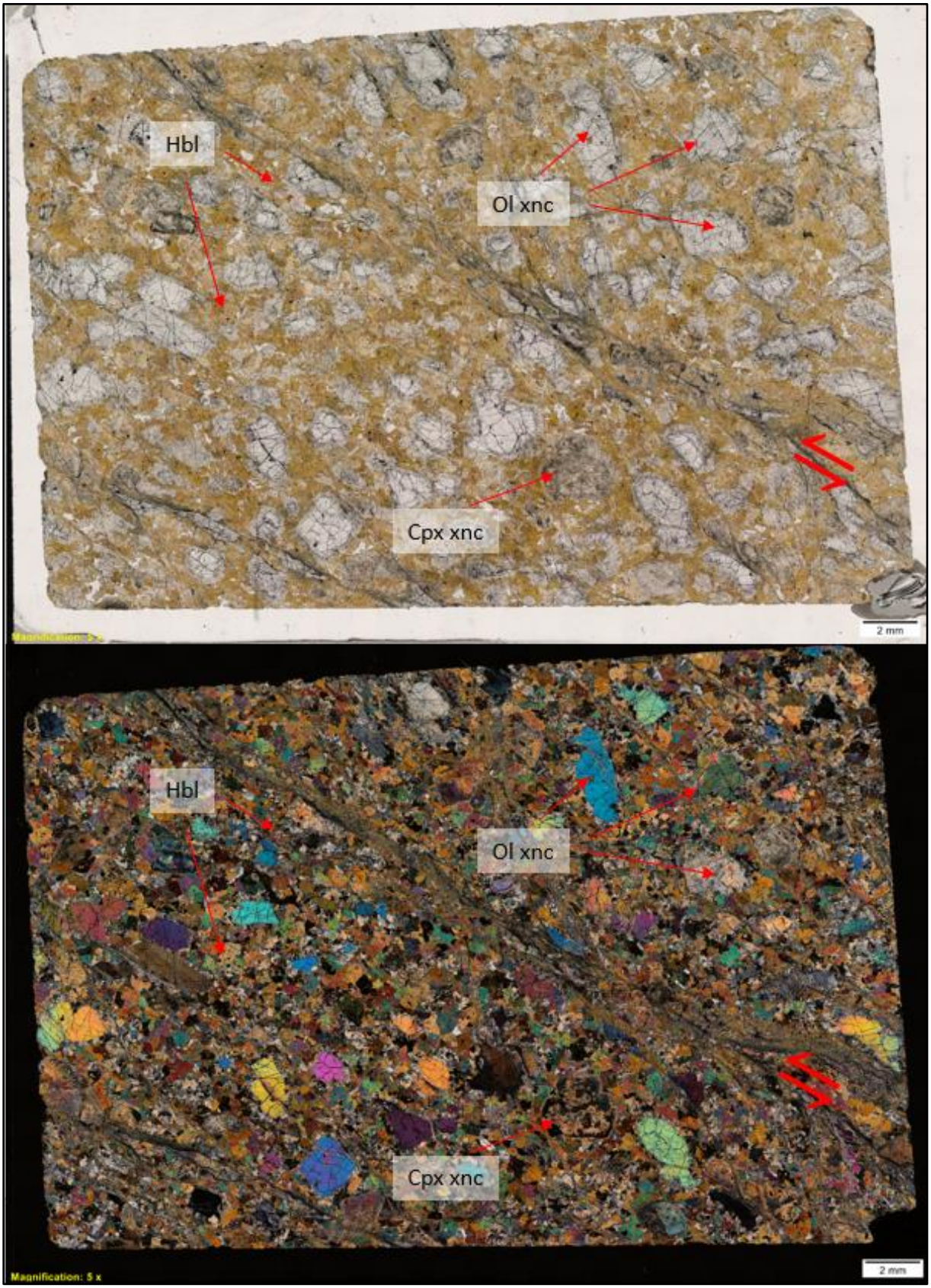

Figure 3.40. ***This figure shows the thin section JS14 prepared form the centre of the dyke in Figure 3.33. The top image is in ppl and the bottom image is in xpl. This dyke is mainly composed of equigranular subhedral hbl, with a high abundance of***

1-2 mm ol and some cpx xenocrysts labelled "Ol xnc" and "Cpx xnc". There is also some interstitial plag in the groundmass which seems to have crystallized together with the hbl. The xenocrysts are all rounded, indicating a re-equilibrium reaction with the hbl rich rock. The xenocryst labelled "Cpx xnc" is being "consumed" by hbl, and is in strong disequilibrium with the surrounding hbl. Most of the pl xenocrysts also have coronas of opx surrounding them. There is a small sinestral shear zone in the thin section which resembles the shear zones observed in other hbl gabbronorites from the intrusion.

The dyke seen in Figure 3.40 is related to the dyke seen in Figure 3.36 as the two samples are collected 15-20 cm from each other. JS14 is the undeformed dyke and JS15 is the deformed dyke. The more leucocratic appearance of JS15 is believed to be related to the small grain size. JS14 is much coarser grained when compared to JS15, as this dyke is not dynamically recrystallized and still has its magmatic grainsize preserved. Some of the ol xenoliths in JS14 show some undulating extinction, probably because of kink banding as a result of stress.

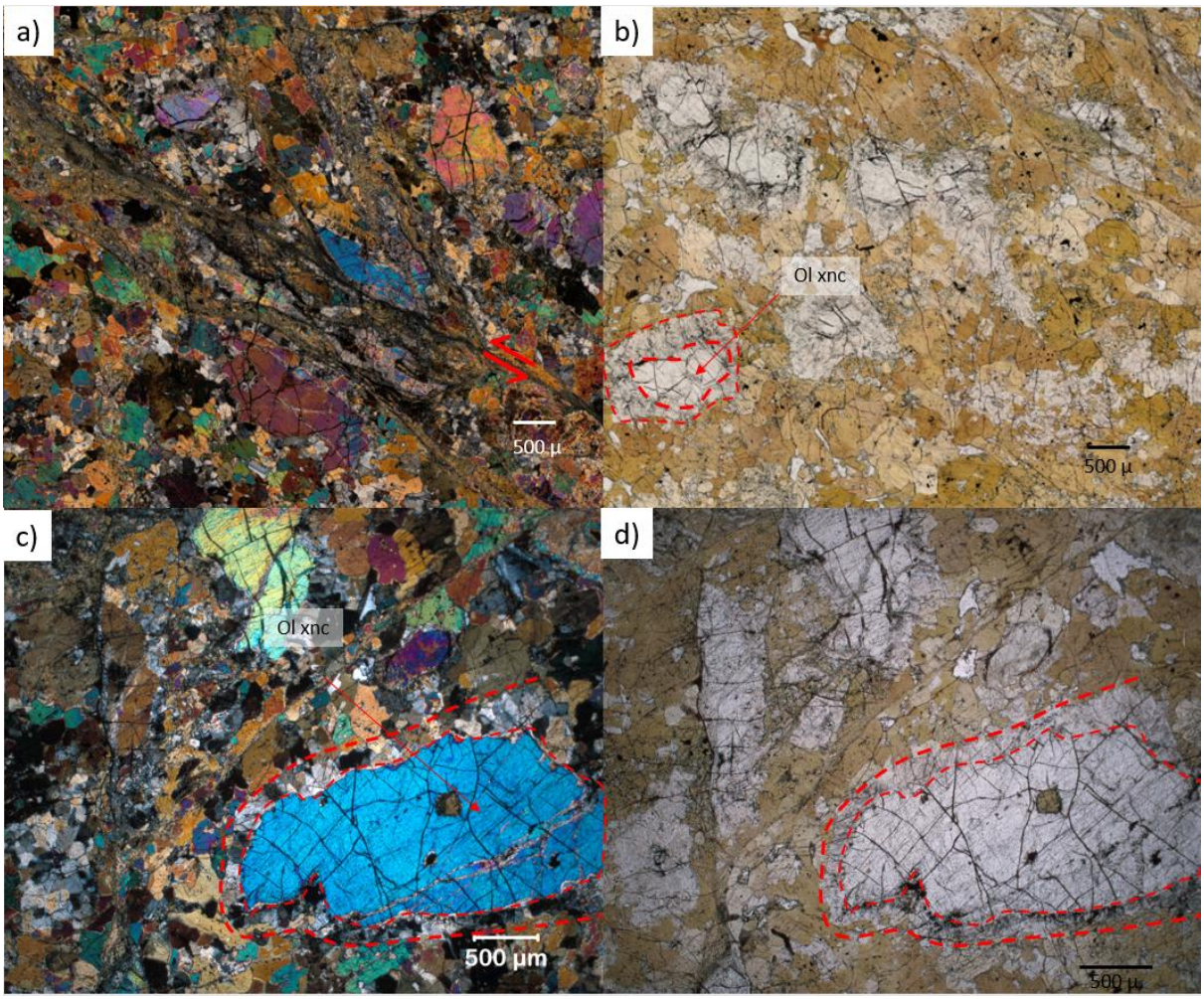

Figure 3.41. ***These images are all from the undeformed hbl rich hbl gabbronorite seen in Figure 3.40. a) This image shows the small sinestral shear zone with dynamically recrystallized hbl. The surrounding grains do not seem to be affected by the deformation in a large degree. Some ol grains may seem to show more variable interference colours, from dark purple to dark blue. b) This image shows one of the ol xenocrysts sitting in the hbl ground mass with a 250 µm wide corona of opx surrounding the grain. The grain and associated corona both have rounded shapes, and sit in a mass of interlocking, equigranular hbl. The corona is outlined by two red stippled lines. c) This image shows a larger 2 mm ol grain with a hbl inclusion in the middle of the grain. The has a 3rd order blue interference colour and is fairly well preserved. The corona is outlined by two red stippled lines. The opx grain forming the corona have grown perpendicular from the surface of the ol grain out towards the ground mass. d) The ol grain in this picture is the same as in image c), but this image is taken with ppl. The hbl inclusion on this grain is more apparent than in the previous picture, as the brown colour of the hbl is in more contrast with the clear ol crystal. The opx surrounding the ol grain is also apparent in its cloudy and dirty grey appearance.***

The XRD results from these dykes are presented in Table 3.17. Although there is some textural variation in these dykes, the mineralogy of the dykes is fairly consistent with a few exceptions.

	JS15-Coarse	JS14	JS08	JS19	JS15-Fine	JS12-3	JS10-1
Fo	4,38	15,03	1,31	2,15	1,71	1,28	1,63
Hbl	41,32	41,98	28,62	39,46	33,75	15,02	28,93
Di	13,46	7,65	19,09	16,94	17,05	26,1	20,23
En	19,96	30,73	16,19	14,98	12	21,12	16,94
Bt	0,92	0,62	0	0,8	1,62	1,19	0
And	16,76	2,56	29,84	21,31	29,59	30,25	27,04
Ilm	3,2	1,43	4,95	4,35	4,28	5,04	5,23

Table 3.17. ***This table shows the XRD results collected for the hbl gabbronorite.***

JS14, the dyke seen in Figure 3.40 and Figure 3.41 and JS15-Coarse, the dyke seen in Figure 3.37 both have hbl contents above 40%, making these two dykes the most hbl rich of this type. The forsterite content is low for most dykes, except for JS14, as the Fo content is mostly attributed to the assimilation of xenocrysts. JS14 also has a very low plag content compared to the other dykes, but is consistent with regard to minerals like Di and En. All sample have a considerable ilm content with the highest being in JS12-3, the sample seen in Figure 3.38 with an ilm content of 5,23%. The ilm in these samples is often accumulated in the shear zones as 5-10 µm sized rounded grains. The ilm can also reside between primary magmatic grains, but overrepresented in the shear zones compared to the concentration in the rest of the rocks.

The amount of Di and En present in the XRD analyses is not as apparent when viewing the samples optically. In terms of the dynamically recrystallized samples, the Di and En is also a part of the fine-grained mass of recrystallized hbl and plag. The coarser samples like JS14, and the undeformed JS15 samples show the coarser opx and cpx present in the primary magmatic suite. These dykes also seem to contain minor bt. Except for JS08 and JS10-1 most dykes have a detectable and observed bt content.

3.5.3 Whole rock geochemistry

The whole rock chemical analyses for the hbl gabbronorite samples are presented in Table 3.18.

	SiO2	Al2O3	FeO	CaO	MgO	Na2O	K2O	Cr2O3	TiO2	MnO	P2O5
JS08-2	45,9	13,1	13,65	11	8,77	2,48	0,42	0,059	2,72	0,19	0,32
JS10-1	46	12,95	13,85	11	9,12	2,45	0,41	0,065	2,72	0,19	0,32
JS12-3	46,7	12,4	13,55	10,9	9,82	2,21	0,29	0,073	2,49	0,19	0,27
JS14-Dyke	45,3	8,06	13,7	7,8	21,3	1,47	0,48	0,126	1,66	0,18	0,19
JS15-Coarse	46,2	11,6	13,1	9,76	13,7	2,33	0,68	0,071	2,52	0,18	0,29
JS15-Fine	46,6	13,8	12,8	10,4	8,88	3,01	0,68	0,039	2,95	0,17	0,37
JS19	44,5	12,85	13,05	10,6	10,45	2,45	0,54	0,063	2,98	0,17	0,35
JS_2_9-Y	45,4	11,95	13,9	10,35	11,4	2,05	0,39	0,097	2,39	0,19	0,26
JS_2_12	53,1	17,95	7,85	7,39	5,7	5,24	0,34	0,023	1,59	0,11	0,39
JS_2_22	45,4	8,21	14,6	7,8	20,6	1,5	0,52	0,125	1,75	0,18	0,2

Table 3.18. ***This table shows the major, and some trace elements for the hbl gabbronorite samples. The sample labels are presented on the left side of the table.***

The chemistry for these samples does not vary much, except for JS_2_12, which is the sample shown in Figure 3.39. This is a sample with a high abundance of dynamically recrystallized plag in a shear zone.

The average SiO_2 content is 46,51 ± 2,4 wt%, and the relatively large S.D is a result of the high SiO_2 value for JS_2_12. Since the plag contribution has given the dyke such high SiO_2 values, the Al_2O_3 values for this dyke is also higher, as plag hosts more Al than many of the other minerals. The average Al_2O_3 content is 12,29 ± 2,8 wt%. The same applies for the Na_2O content, as this sample has a Na content ~2 times higher than other samples.

The other anomaly in chemistry is the high MgO content of JS14, but this is largely explained by the high Fo content seen from the XRD analyses. The average MgO value is 11,97 ± 5,14 wt%. The dykes with high xenocryst contents largely control this.

This dyke type also has a high P_2O_5 content compared to other dykes. The average value for this element is 0,296 ± 0,07 wt%. This is significant as many other dyke types have a P_2O_5 close to the detection limit of the analyses.

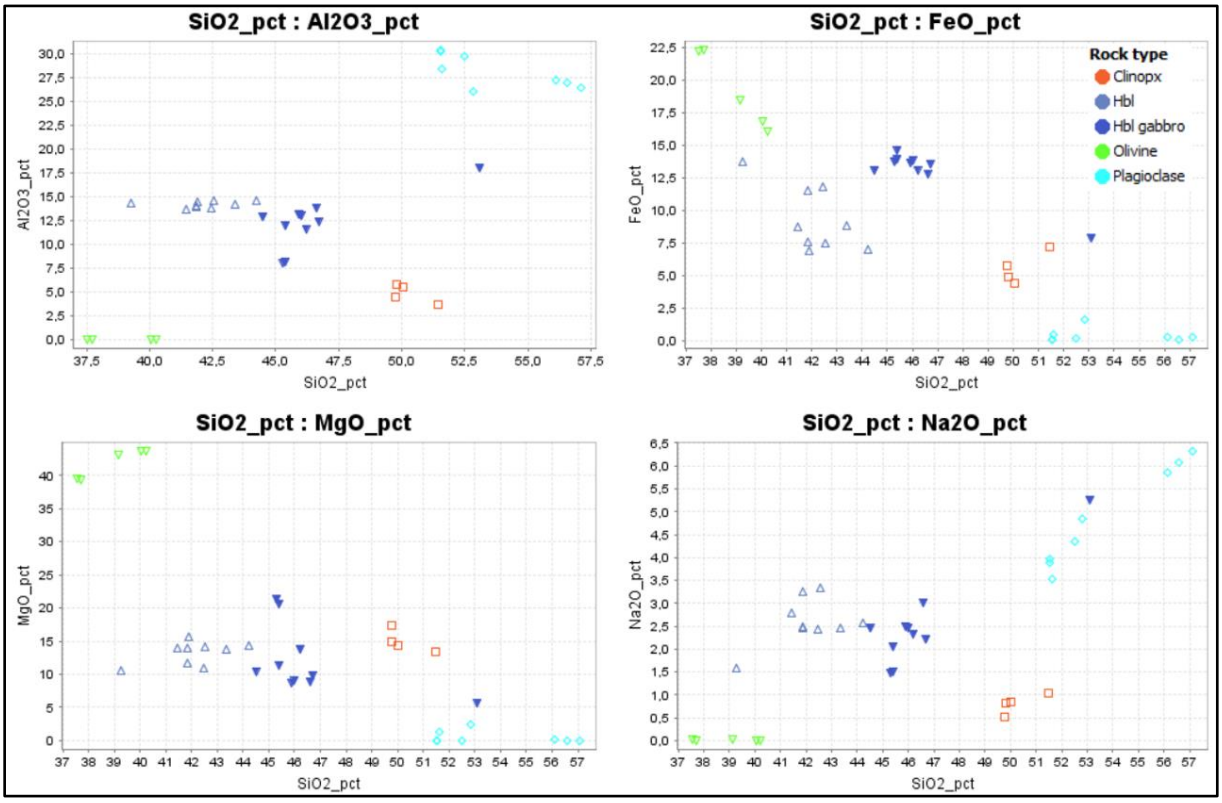

Figure 3.42. ***This figure shows the hbl gabbronorite plotted with SiO_2 against Al, Fe, Mg and Na oxides. The hbl gabbronorite is plotted as solid blue triangles, and these samples are plotted with cpx (open red square), hbl (open blue triangle), plag (open turquoise diamond) and ol (open green triangle). The samples, with the exception of JS_2_12 (outlier) plots closely together. As the chemistry of JS_2_12 contains a large plag rich shear zone, the chemistry o f this sample is more controlled by the shear zone than of the hbl gabbronorite itself. Since the samples plot so closely together it does not seem like this dyke type has undergone extensive fractionation. The Si content is fairly uniform as seen from Table 3.18, and the other elements do not vary much either. The samples all plot closely with hbl, with a slightly more SiO_2 rich signature, making them plot slightly to the left, between hbl, plag and cpx. The samples are predominantly made of hbl, px and plag, meaning the small chemical variations seen in these samples are explained by variations in mineralogy.***

A few of the important major elements are plotted against SiO_2 and are shown in Figure 3.42. The dyke shows a clear clustered trend, with little variation in chemistry across the different samples. Especially in the FeO vs SiO_2 plot, the dyke samples show a tight cluster. As these two elements do not vary much in the sample.

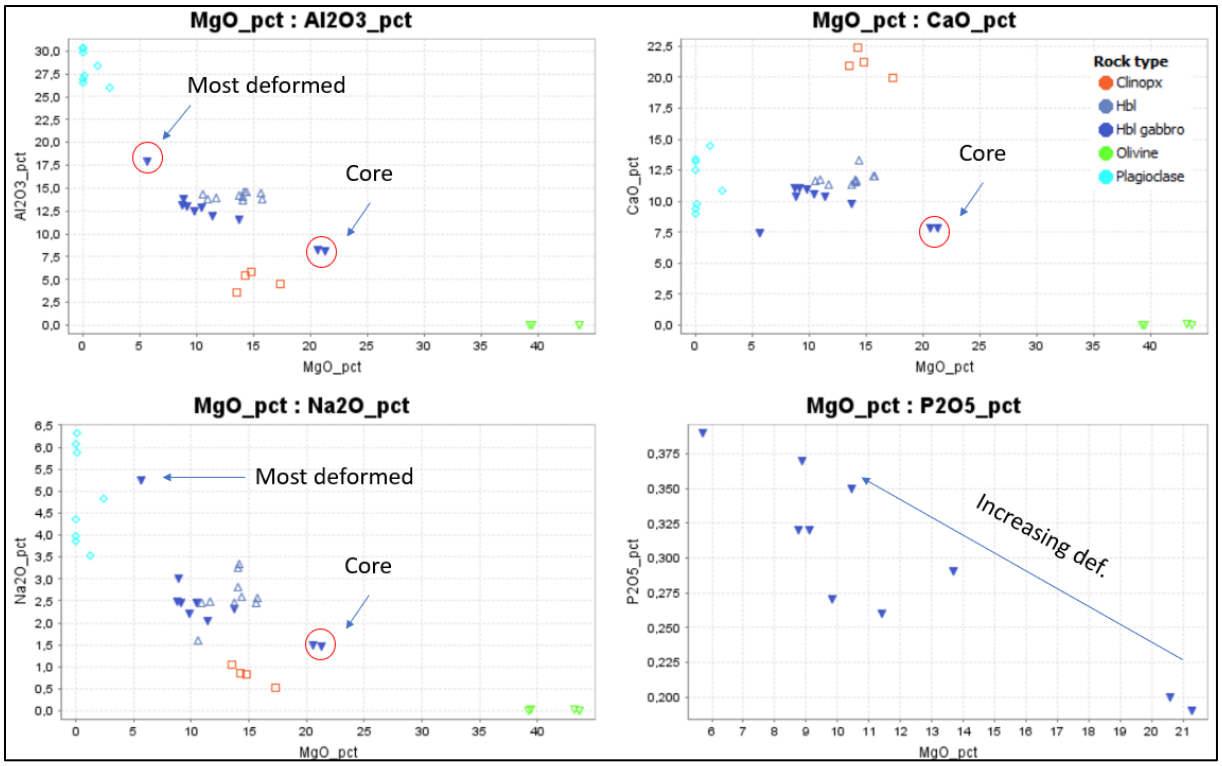

Figure 3.43. ***This figure shows the Al_2O_3, CaO, Na_2O and P_2O_5 content of the hbl gabbronorite plotted against MgO. The Al_2O_3 plot shows the samples plotting next to hbl, with two samples rich in ol xenocrysts plotting closer towards the ol analyses. The two samples with high Mg are JS14 and JS_2_22, both sampled from the core of the dyke in Figure 3.33, and as seen in Figure 3.40 and Figure 3.41 these samples are abundant with ol xenocrysts. These samples are marked with an arrow and red ring labelled "Core". The Ca and Na plot show similar trends. The shear zone dominated JS_2_12 is the sample most depleted in MgO, and in the Na plot is plots together with the plag analyses. The dykes also show a negative correlation between P_2O_5 and MgO, with the most deformed being richer in P. This plot does not include any mineral plots as the P_2O_5 amounts in the minerals were below detection limits for the EPMA.***

As MgO has a wider spread and more variation in these sampled than SiO_2, MgO is able to illustrate small changes in chemistry. The MgO shows ol might have had an effect on fractionation, but the samples plotting closest to ol have assimilated ol xenocrysts. JS_2_12, the deformed plag rich sample also plots closer towards plag in most plots, but this is probably only due to the actual abundance of plag in these samples. The sample has a higher increase in Na, than in Ca, which may indicate the differences in plag chemistry in the shear zone.

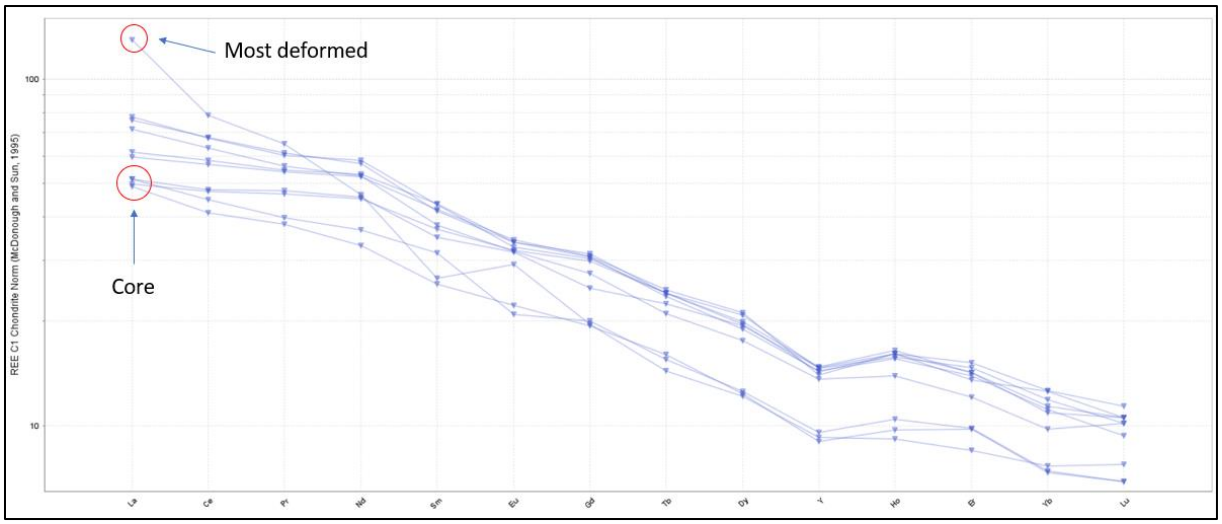

Figure 3.44. ***This graph shows the chondrite normalized REE curves for the hbl gabbronorite dyke from La to Lu, included Y. JS_2_12, the most deformed dyke has the most enriched signature of all the samples, with the largest La/Lu observed in the dataset, and is the only sample with a La value above 100. The most depleted samples of this dyke type are the two samples from the core of the dyke in Figure 3.33, JS14 and JS_2_22. These two samples are labelled "Core" on the graph.***

The samples observed in Figure 3.44 progress from the most depleted being least deformed, and the most enriched being the most deformed. The sample with the highest La value and most enriched LREE signature is JS_2_12, shown in Figure 3.39. This sample has a strong decline from La to Lu, with a positive Eu anomaly. This anomaly is most likely attributed to the high plag content. The curve, despite being the most enriched in LREE ends up being the one of the most depleted samples with respect to HREE. The HREE plot for the deformed sample plots together with the HREE of the two samples from the core of the dyke.

All samples have a characteristic enriched OIB-like signature with a near linear decrease of REE from LREE to HREE. The samples also all have a negative Y anomaly, meaning the samples are depleted in Y relative to the other REE. The samples are also significantly enriched compared to other dykes form ULS, with most La values residing between 50-80 times more enriched than a chondrite, and Lu values residing around 10 times chondrite enrichment.

3.5.4 Mineral chemistry

Some of the samples of this dyke type were analysed using an EPMA. Plag, hbl and cpx were analysed in the thin section JS12-1 shown in Figure 3.38 and in JS14 shown in Figure 3.40. The primary magmatic minerals were analysed as well as some grains in the pseudotachylyte and shear zones.

Plagioclase	Na2O	Al2O3	CaO	K2O	SiO2	Total	An%
JS12	5,74	27,75	9,88	0,22	56,14	100,03	48,77
JS12	5,71	27,72	9,94	0,24	55,61	99,69	49,05
JS12 Pseudotach	6,16	26,53	9,10	0,22	57,27	100,18	44,95
JS12 Shear zone	7,13	25,06	7,11	0,37	59,33	99,38	35,54
JS14	5,49	28,10	10,09	0,07	54,91	99,13	50,38

Table 3.19. ***This table shows EPMA analyses of plag in the hbl gabbronorite dykes. The samples labelled JS12 and JS14 are primary magmatic, undeformed plag, while JS12 Pseudotach and JS12 Shear zone are analyses from the dark pseudotachylyte vein shown and described in Figure 3.38.***

The grains which were analysed transversely were checked for zonation, but there was no significant zonation in any of the grains analysed. There is a significant change in chemistry between the deformed and undeformed plag. The undeformed plag has a consistent Na and Ca content, while the pseudotachylyte and shear zone has a lower An%, making it more albite rich. The dynamically recrystallized plag has an anorthite content of 35,5% and the pseudotachylyte has an anorthite content of 44,95% which is significantly different from the primary magmatic An content. The measurements in the pseudotachylyte were done in 5 different grains, and the values did not vary significantly. An average measurement was the applied to the pseudotachylyte measurements

The calculated plag formulas for this dyke type are

$$(Na_{0,62-0,48}Ca_{0,34-0,49}K_{0-0,01})(Al_{1,32-1,50}Si_{2,66-2,50})O_8$$

Cpx was also analysed, and the results are presented in Table 3.20

Pyroxene	Na2O	MgO	Al2O3	CaO	FeO	TiO2	SiO2	Total	Mg#
JS12	0,91	13,45	3,81	21,42	7,74	0,24	50,49	98,32	0,756
JS12	0,83	13,90	2,67	22,05	7,58	0,27	51,79	99,36	0,766
JS12	0,78	14,14	2,64	21,94	7,49	0,34	51,59	99,15	0,771
JS12 Pstach avg	1,04	13,46	4,25	21,40	7,44	0,37	51,41	99,69	0,763
JS12 Pstach	0,72	14,37	2,12	22,37	6,85	0,13	52,80	99,65	0,789
JS12 Pstach	0,89	13,23	4,14	22,26	7,65	0,46	50,97	99,91	0,755
JS12 Pstach	1,00	13,40	4,18	22,11	7,20	0,49	51,08	99,70	0,768
JS12 Pstach	1,08	12,82	5,97	20,61	8,30	0,78	49,58	99,81	0,734
JS12 Pstach	0,75	14,52	2,01	22,35	6,73	0,13	52,53	99,24	0,794
JS12 Pstach	1,47	12,47	5,68	21,47	6,92	0,33	51,94	100,61	0,763
JS12 Pstach	1,67	11,97	6,79	20,90	6,67	0,33	52,43	101,02	0,762
Corona JS14	0,02	28,86	2,06	0,20	14,09	0,09	53,64	99,37	0,785

Table 3.20. ***This table shown analyses of four cpx grains from JS12, and an analysis of the opx corona surrounding an ol grain from JS14 shown in Figure 3.41 c). All analyses are presented as wt%***

The analysed primary magmatic px grains did not show significant zonation. Representative averages for the grains were therefore analysed. There is a slight variation in Mg# from the primary magmatic cpx to the cpx stabilised in the pseudotachylyte. The pseudotachylyte can be more enriched in Na, Al and Ti compared to the standard JS12 cpx, but the pseudotachylyte analyses show a high degree of variation. The primary magmatic cpx measured is calculated to be $Di_{75,6}$ – $Di_{77,1.}$ The pseudotachylyte varies from $Di_{73,4}$ – $Di_{79,3.}$

The corona in JS14 shows a CaO content of 0,20 wt%, and a Mg# of 0,79. This makes the corona an $En_{0,79}$ corona. It has more relative Mg than the cpx in JS12, but this is due to them being different minerals, and by wt% opx includes more Mg in its lattice.

The calculated primary magmatic cpx formula from this dyke type is

$$(Ca_{0,87-0,88}Na_{0,06-0,07}Fe_{0,05})(Mg_{0,76-0,79}Fe_{0,21-0,24}Al_{o,04-0,07})(Si_{1,90-1,94}Al_{0,06-0,10})O_6$$

The ol analyses from these samples are presented in Table 3.21.

Olivine	MgO	FeO	MnO	NiO	SiO2	Total	Fo%
JS14	39,23	22,30	0,30	0,25	37,70	99,81	0,7582
JS14	39,43	22,28	0,31	0,23	37,68	99,97	0,7593

Table 3.21. ***This table shows the average compositional measurements for two xenocrysts from JS14. The grains did not show any sign of zonation.***

The chemistry of the two grains is near identical, and the grains are calculated to be $Fo_{75,8}$ – $Fo_{75,9}$. The ol analyses show little variation within the dyke type.

The hbl analyses and classifications from this dyke type are presented in Table 3.22

Amphibole	Na2O	MgO	Al2O3	CaO	K2O	Cr2O3	FeO	SiO2	TiO2	Total	Class
JS12 Pst	1,74	10,58	14,86	11,58	2,16	0,1433	13,35	39,52	2,77	98,96	Ti-K-parg
JS12 Pst	1,65	10,57	14,7	11,62	2,09	0,2119	13,33	40,12	2,8	99,40	Ti-K-parg
JS12 Pst	1,61	10,54	14,83	11,62	2,21	0,156	13,49	39,58	2,8	99,03	Ti-K-parg
JS12 Pst	1,66	10,72	14,64	12	2,14	0,2454	13,46	39,62	2,71	99,53	Ti-parg
JS12 Pst	1,54	10,85	14,66	11,39	2,11	0,274	13,36	39,89	2,72	98,97	Ti-K-parg
JS14 Hbl	2,80	13,99	13,74	11,52	0,98	0,09	8,76	41,54	3,44	99,05	Ti-parg

Table 3.22. ***This table shows amphibole analyses form the hbl gabbronorite, as well as classifications based on*** *(Hawthorne, et al., 2012)****. The avg JS14 hornblende is classified as a Ti-rich pargasite, while the hbl analyses from the pseudotachylytes labelled JS12 Pst are classified as a Ti-rich potassic pargasite.***

The hbl analyses form the pseudotachylyte are more consistent than the cpx analyses from the same area. The pseudotachylyte analyses show an enrichment in elements like K and Al. The Cr analyses hover around the LOD, but are below the quantification limit. The pseudotachylyte samples contain some Cr, but at unknown quantities. The JS14 analysis for Cr is below the LOD, and cannot be used to describe the sample.

The calculated formula for primary magmatic hbl is

$$\left(Na_{0,58-0,65}K_{0,16-0,22}\right)\left(Ca_{1,78-1,84}Na_{0,14-0,21}\right)\left(Mg_{2,84-3,20}Fe_{0,92-1,06}\right)$$

$$(Si_{5,96-6,19}Al_{1,81-2,04})O_8(OH_2)$$

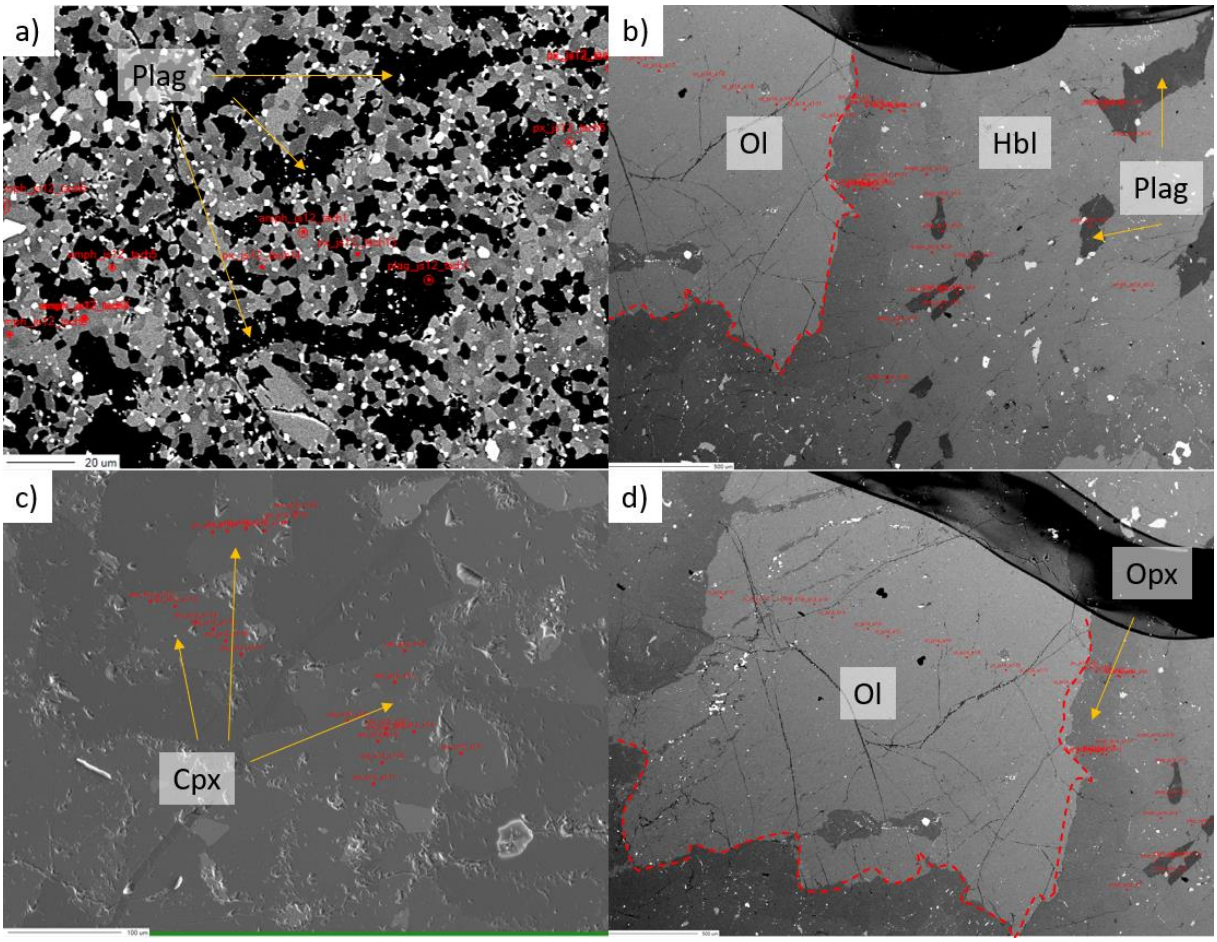

Figure 3.45. ***This figure shows some of the analysed spots presented in the tables above. These are BSE images from the SEM. The red dots represent analysed points. a) This image shows the crystallized groundmass of the pseudotachylyte from JS12. This zone is assumed to once have been glass, but has since been devitrified. The darkest phase here is plag, with the lighter phases being a mix of hbl, opx and cpx. The scale bar here is 20 µm b) This image is from one of the ol xenocrysts in JS14. The dark rim around the bright ol is the opx corona. The small dark elongated grains to the right of the ol grain are plag grains. The scale bar here is 500 µm. c) This image shows analysed cpx grains form JS12. The grains have an interlocking texture with the darker plag grains around. The scale bar here is 100 µm. d) Lastly, this image is the same grain as in image b). This image however shows the traverse through the ol grain. This did not show any zonation. The scale bar here is 500 µm.***

3.6 Olivine dominated shear zones

3.6.1 Field observations

The shear zones described in this chapter can also be seen in many of the field observations from the hbl gabbronorite in *Chapter 3.5.1 Field observations*. The zones enveloping the dykes are what is often referred to as a "yellow shear zone". The hbl gabbro norite is the only dyke on the southern plateau which has this field relation to the shear zones. As seen in Figure 3.32 and Figure 3.34, the most deformed areas of the hbl gabbro norite are associated with the ol rich yellow shear zone, as the shear zone seems to mix and mingle with the deforming dyke.

The zones are however also found without the presence of a gabbro dyke. There are zones found in the wehrlites associated with displacement and deformation as seen very locally in Figure 3.46. The host rock shows a distinct colour change when deformed, as seen in other localities. The scale of displacement is often in the order of cm's to dm's, sometimes up to a meter. It seems here as if the deformation has preferentially occurred in the dunitic material, as it is in this locality only localized to the dunitic material.

Figure 3.46. ***An infiltration of dunitic melt into the wehrlitic host rock. The dunitic material has later accommodated strain, shown by the thin pale yellow zone associated with a significant decrease in grain size. The frame in red is zoomed in to allow for better observation of the strained dunitic material. The contact between the wehrlite and dunite is marked by blue lines, and the yellow, fine grained material is outlined by the burgundy line. Compass for scale.***

The curry yellow to pale yellow deformation zones seem to be consistently associated with deformation, and can displace dykes as seen in Figure 3.47, where two generations of dykes have been displaced. These dykes are not enveloped like the gabbro usually is, but are rather displaces after emplacement. Figure 3.47 c) shows two parallel dykes being cut by the shear zone and being displaced dextrally. Both dykes are dragged and deflected by the shear zone, indicating ductile behaviour.

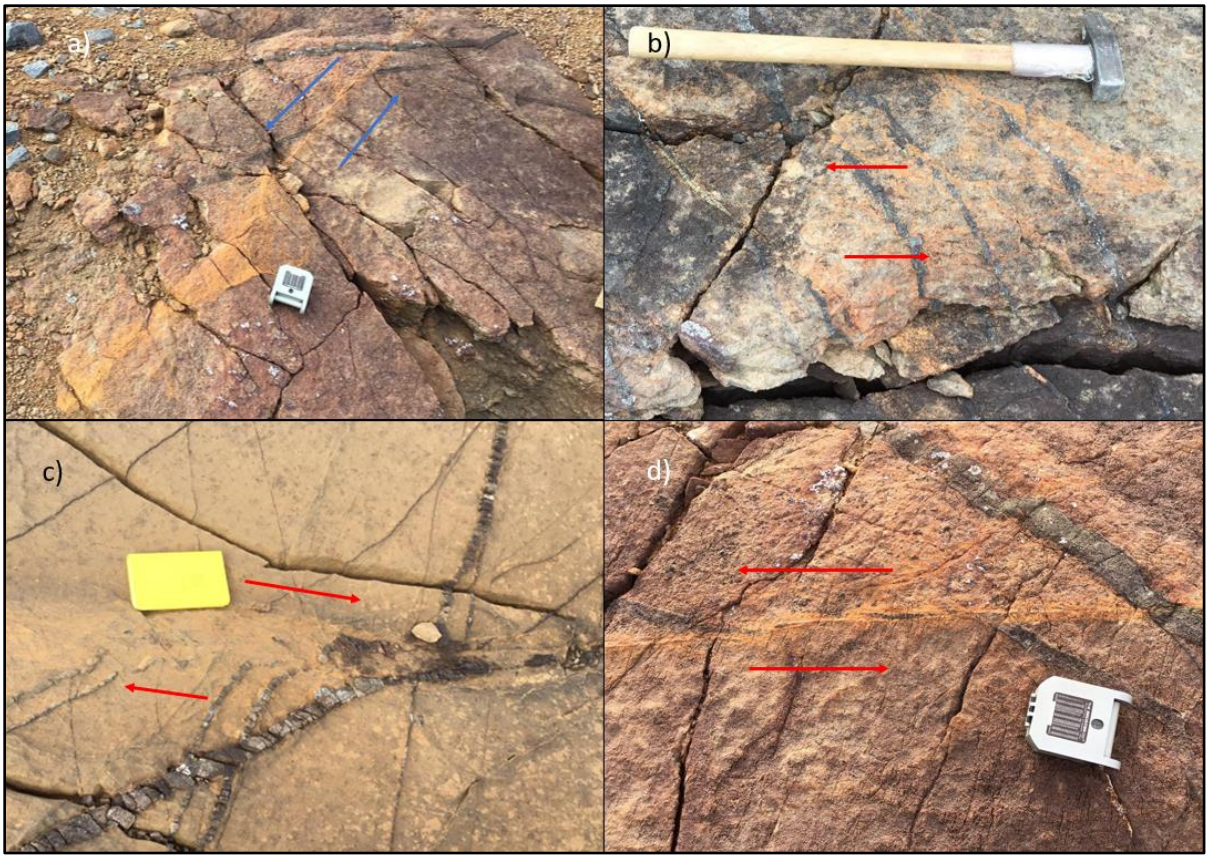

Figure 3.47. **Four images showing observed features related to the shear zones. a) Sinistral deformation in a wehrlitic host rock, older dyke in centre of picture being displaced ~50cm, while younger dyke at the top of the picture is displaced less. Indicates reactivation of deformation zone. Both dykes here are dipping 85/317. The shear zone is ~1 cm wide at the point where the dykes are displaces, but widens out and becomes progressively more diffuse towards the bottom of the image, indicating these zones are more complex than simple shear zones. Compass for scale. b) Shows sinestral micro-faulting in a pyroxenitic dyke. The dyke is being cut by the shear zones, and similarly to a), the shear zone is not a traditional 2D planar shear zone, but a more diffuse shape, spreading out. c) is an image of two old cm thick composite dykes being cut by a younger thicker dyke, where both generations of dykes are sheared and smeared out. The oldest generation seems to be dragging and deflecting along the shear zone. It is unclear exactly which dyke portions are related on either side of the shear zone, as the shear zone has a vertical component in addition to the horizontal component. Based on orientation it looks like the horizontal displacement here is ~25 cm, since the dykes are sub-vertical. d) is a closer look at the shear zone in frame a). Parts of the dyke being displaced is clearly seen in a pocket in the shear zone with displacement being around 20 cm. The deformation here is most likely oblique, with unknown vertical displacement.**

The shear zone also varies a bit in colour. From a pale beige colour, to a more bright orange colour. This is most likely related to serpentinization and later alterations, as the surrounding rock is often more serpentinized where the shear zones are yellow. The shear zones predate the serpentinization, as the shear zones are being cut by serpentinization joints

3.6.2 Petrographic and mineralogical observations

The distribution of the shear zones are random in the host rock, but systematic along some dykes. Because of this, some of the dyke samples taken from the hbl gabbronorite also contain a large amount of the yellow shear zone. One of the hbl gabbronorite samples with an associated shear zone is shown in

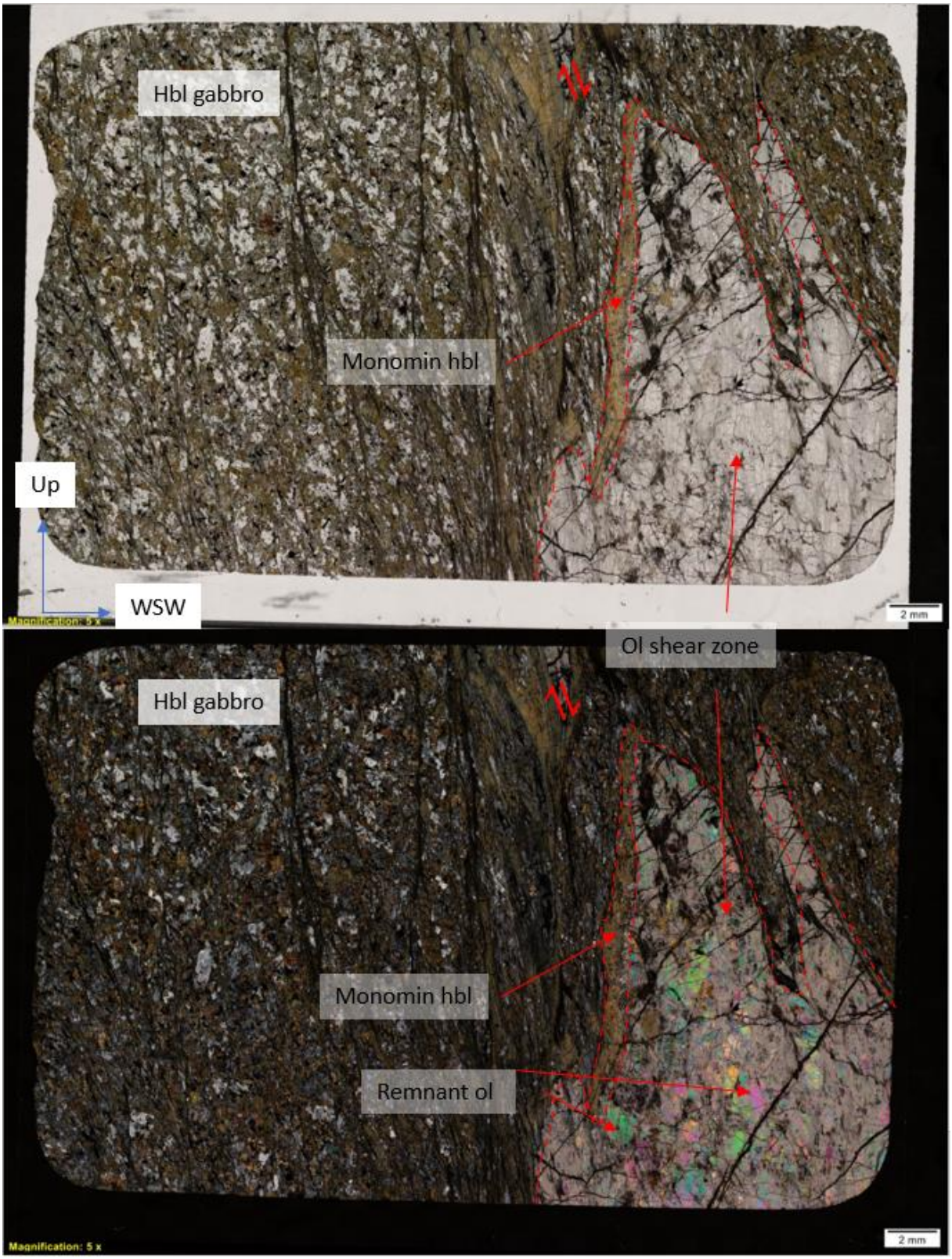

Figure 3.48. ***This image shows the relationship between the hbl gabbronorite and the ol rich shear zones in ppl (top) and xpl (bottom) in thin section JS20-A. The sample is collected from the locality in Figure 3.33. The contact between the two phases is sharp, and looks to be affected by deformation. The ol shear zone (outlined by red stippled line) itself is predominantly made of cryptocrystalline ol, with some remnant ol grains seen with 3rd order green and pink interference colours. These grains are also indicated by a textbox and red arrows. The zone in ppl looks transparent, and has a dusty grey colour in xpl. On both figures, a monomineralic zone of hbl is labelled and indicated by a red stippled line. The hbl rich zone originates from the gabbro, and creates what seems to be a reaction zone between the hbl gabbro and ol sone. The ol grains in the ol rich shear zone are comparatively well preserved, and the original shape of the grains can still be made***

out. The grains are however full of fractures filled with the cryptocrystalline mass. The interpreted shear sense in this thin section is dextral.

The ol rich shear zone seen in Figure 3.48 is isolated as a pocket next to the dyke. This may explain why some of the grains are still preserved, as it seems other similar zones have less preserved remnant grains. The ol rich shear zone does not infiltrate into the surrounding the gabbro, but does seem to have an associated contact reaction with the gabbro consisting of a 1 – 0,2 mm wide zone of fine grained hbl.

The textures in this thin section indicate ductile deformation mechanisms, based on the dragged out gabbro contact and flow like texture of some of the remnant ol grains. The sample is oriented, and orientation arrows are seen in the bottom left corner of the top thin section in Figure 3.48. The dyke shows dextral deformation, based on the dragging of the hbl gabbro into the ol dominated shear zone. Texturally, the gabbro resembles other deformed hbl gabbros described in previous chapters. The interpreted shear sense indicates this dyke is a part of a steep, west dipping normal shear zone.

There are other samples from the dykes from ULS which have similar textures to the thin section JS20-A in Figure 3.48, like the thin section presented in Figure 3.49, JS19-B. This thin section has the same hbl gabbro texture as JS20-A, but JS19-B has a more massive hbl mylonite in the gabbro domain. The ol shear zones are similar, but the shear zone in JS20-A is more protected in a gabbroic pocket, which seems to have preserved more of the remnant ol crystals. The other difference is that JS19-B has some irregular diffuse dark bands in the ol shear zone which are not seen in JS20-A. Overall, the texture of the ol shear zone in JS19-B seems to have accommodated more strain than the ol shear zone in JS20-B.

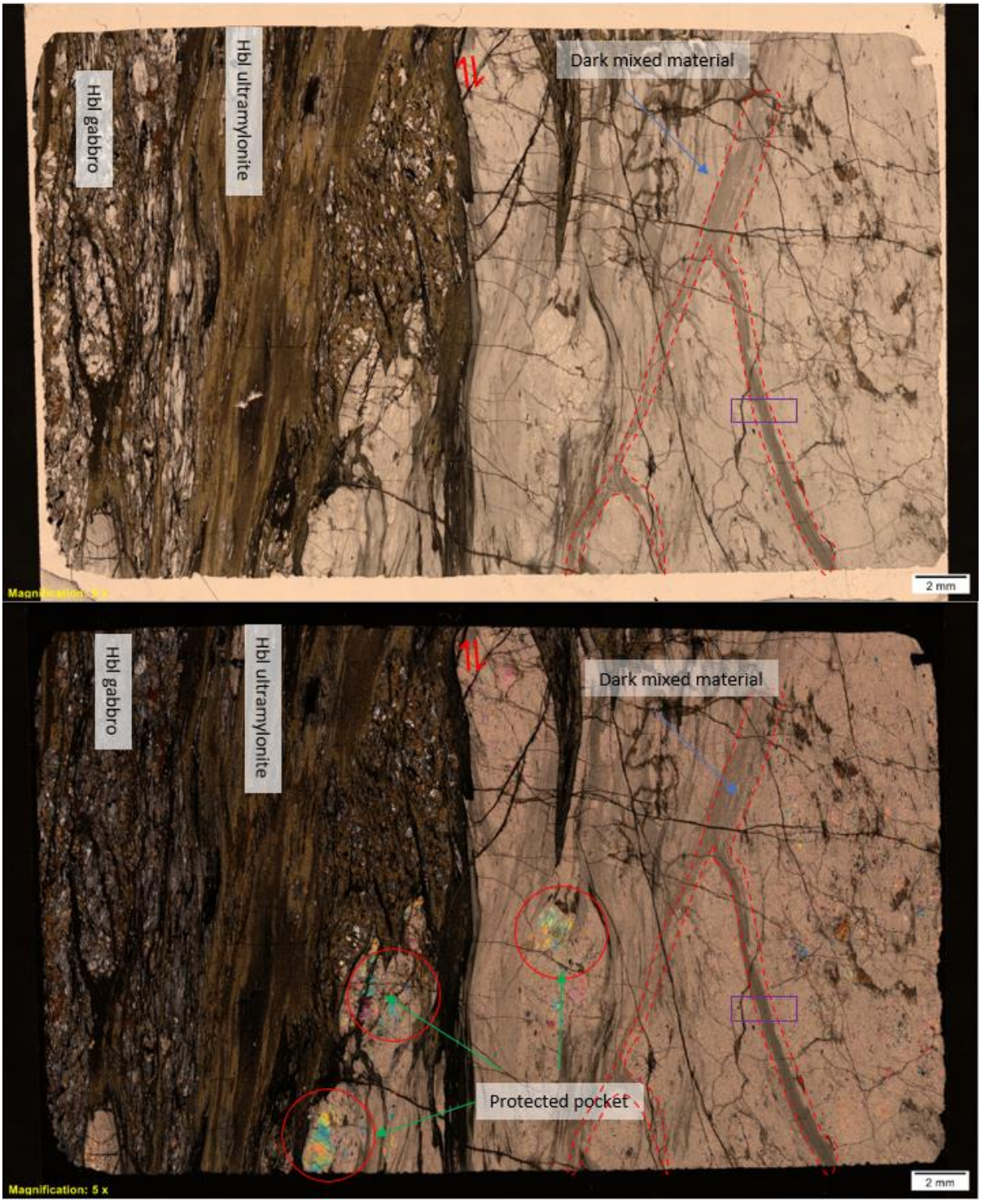

Figure 3.49. ***This figure shows another hbl gabbro sample with the associated ol rich shear material in sample JS19-B. The gabbro transitions from relatively undeformed on the left side, to a hbl rich ultramylonite, labelled "hbl ultramylonite" over to the almost completely recrystallized and fine grained ol rich shear zone. The gabbro is being dragged along in stretched out segments of dynamically recrystallized gabbro (mainly plag and hbl, with some px). There is a similar hbl reaction rim enveloping the gabbro in contact with the ol shear zone. The deformation style and mechanism seen in the gabbro here indicated ductile conditions, and is being dextrally sheared. The sample here is not oriented, so interpreting tectonics is not possible. The ol shear zone seen as the grey domain dominating the right half of the thin section has isolated pockets of remnant grains, while the unprotected and exposed right part almost has total recrystallization. The protected pockets preserve the shape of the remnant grains, as they might have accommodated less strain as they are closer to the gabbro contact. The dark diffuse area labelled "dark mixed material" is too fine grained to optically determine the exact mineralogical composition of. The purple box indicates where the dark diffuse area was analysed using EDS.***

There are very dark, almost black areas in the gabbro which resemble the pseudotachylytes seen in Figure 3.36. These are probably related to the shearing of the dyke, and only reside in the gabbroic part of the thin section. The dark diffuse bands in the ol shear zones however were analysed using EDS in order to determine the chemical composition.

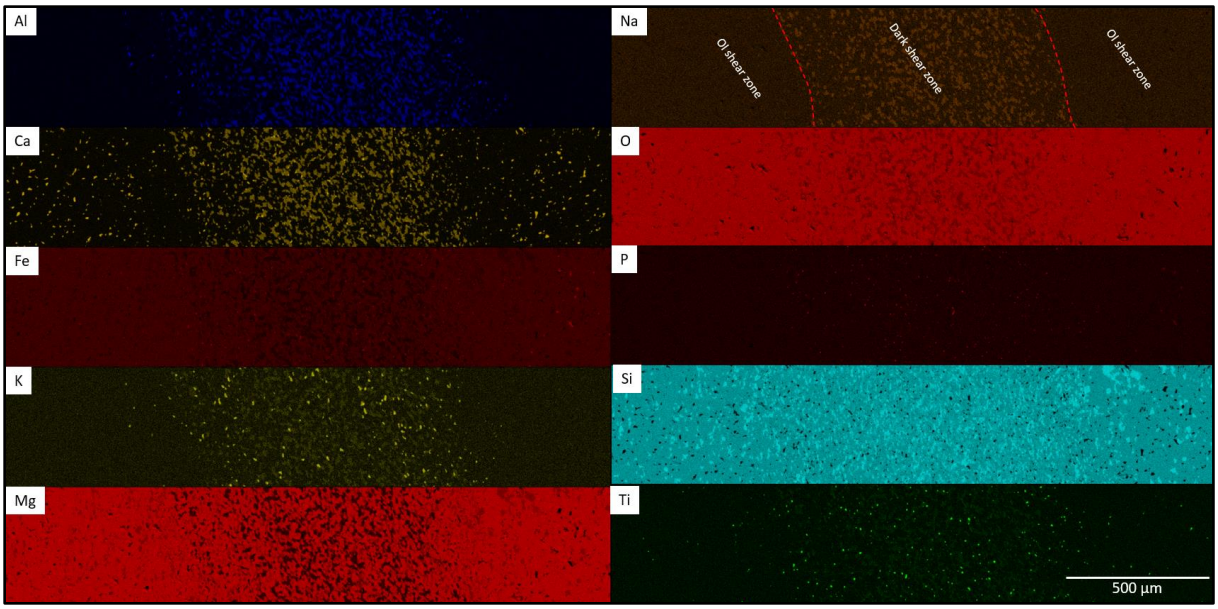

Figure 3.50. ***This image shows 10 different elemental analyses from a stitched EDS map. The mapped area is the purple square shown in Figure 3.49. The scale bar in the bottom right corner is applicable for all the maps. The ol shear zone and dark shear zone is marked out on the Na map, as this map has the most well defined contrast between dark zone and ol zone.***

The analysed dark diffuse area seems to chemically corelate with the chemistry of the hbl gabbro as seen in whole rock analyses in Table 3.18. The core of the zone shows a clear difference in chemistry when compared to the surrounding ol rich zone. The Al and Ca maps show clear trends, being more densely concentrated in the core of the zone. Ca does have some bright spots scattered in the ol zone. These Ca rich grains are most likely cpx.

Na also has an increased concentration in the dark zone. Na is commonly partitioned into plag and some hbl. The K map also shows higher concentrations in the dark zone. This is most likely due to an increase in hbl content in the dark zone, as the plag in the ULS dykes are K-poor. The Ti map also shows a higher concentration in the dark zone, which complies with the increased ilm content observed in the hbl gabbronorite. The zone is also enriched in P, which has been shown in the hbl gabbronorite previously. The small illuminated P rich grains are most likely to be apatite, as this is a common accessory phase in these dykes

The Fe map shows a depletion in the dark zone, meaning the surrounding ol rich material has a higher Fe content than the dark material. Mg and O show similar trends, indicating the dark zone is depleted in particularly ol, but also opx and cpx, as these are carriers of these elements. Minerals like plag also have O in their formula, but the relative proportion of O is lower in some mafic minerals when compared to ultramafic minerals.

The Si map does not seem to vary much in terms of concentration across the map, but individual grains become more visible on the Si map, indicating that the average grain size of the dark zone may be smaller than the ol rich zone around. The qualitative chemistry based in the EDS maps indicate that the dark shear zone is of gabbroic composition.

The fine grained ol rich material is however not only restricted to larger irregular masses of ol. They are also present as small fractures and micro faults in ol crystals as seen in

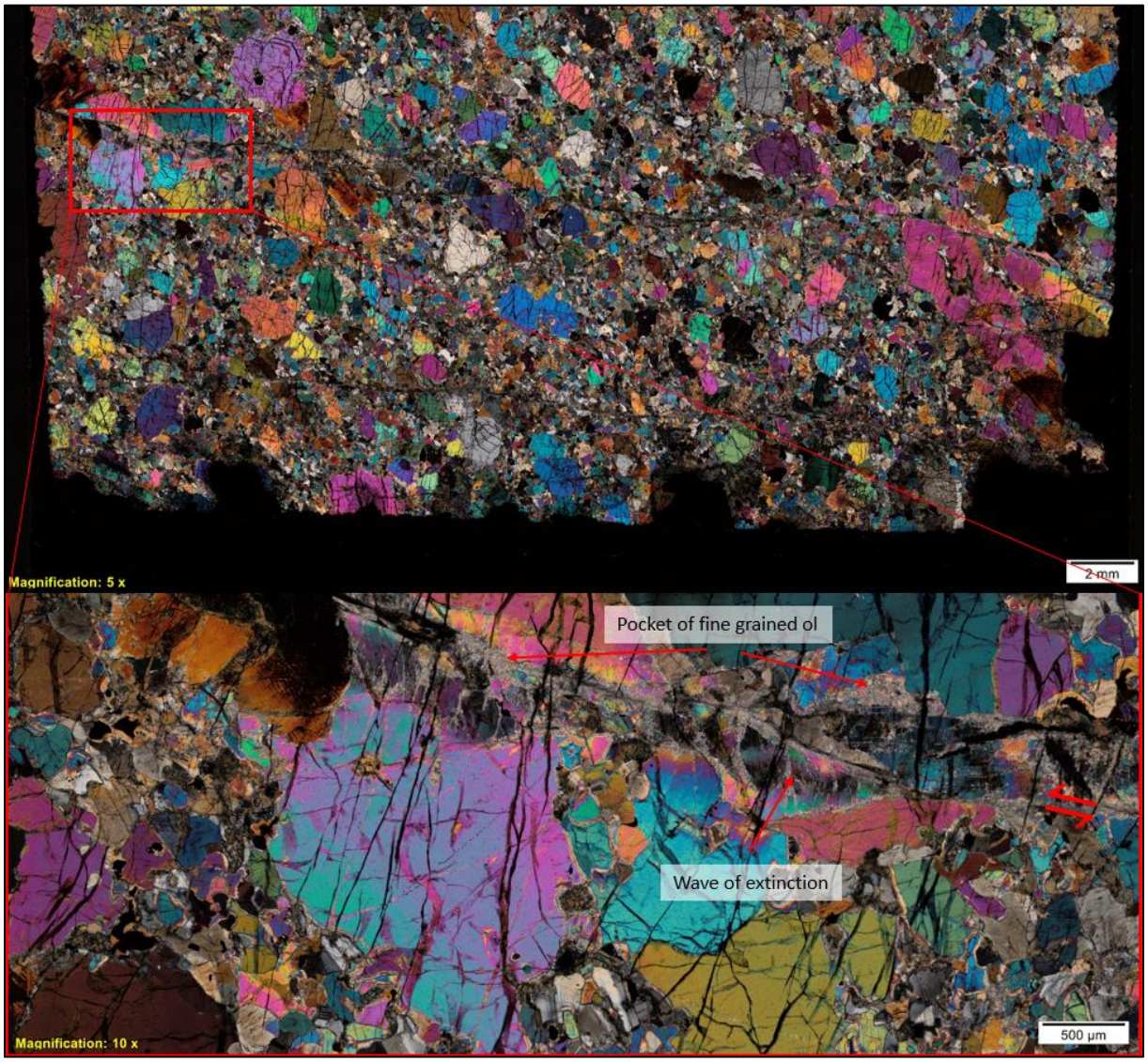

Figure 3.51. ***The thin section shown is JS07, one of the lhz dykes. There is a small sinestral shear zone cutting through the thin section. The bottom image shows a zoomed in view of the red square. An ol grain showing plastic deformation and wavy extinction is indicated by the text box "Wave of extinction". Pockets filled with fine grained ol are also indicated.***

The shear zone in Figure 3.51 shows a ~3mm sinestral displacement, with associated cryptocrystalline ol filling fractures in the surrounding ol grains. This shear zone has less of the highly ductile flow textures of the other zones, but resembles a cataclastic flow. The surrounding grains are highly strained, like the ol with 3rd order green to pink interference colour with the bent domains with a wave of extinction moving through the grain upon stage rotation.

The shear zone is filled with angular fragments of surrounding ol grains, and the fine grained ol material infiltrates into neighbouring grains. The elongated shapes of crystals, and the ductile mechanisms are not present in this shear zone.

These zones can also be seen related to other dykes, but on a much smaller scale than the hbl gabbronorite. Figure 3.52 shows the contact between the host rock and a porphyritic hbl dyke. The dunite is full of fractures filled with the cryptocrystalline aggregate of ol. The fractures seem to be

related to the intrusion of the dyke as the fracture follows the contact of the dyke, and the other off-shoots into the dunite itself seems to protrude and originate from the vein following the dyke.

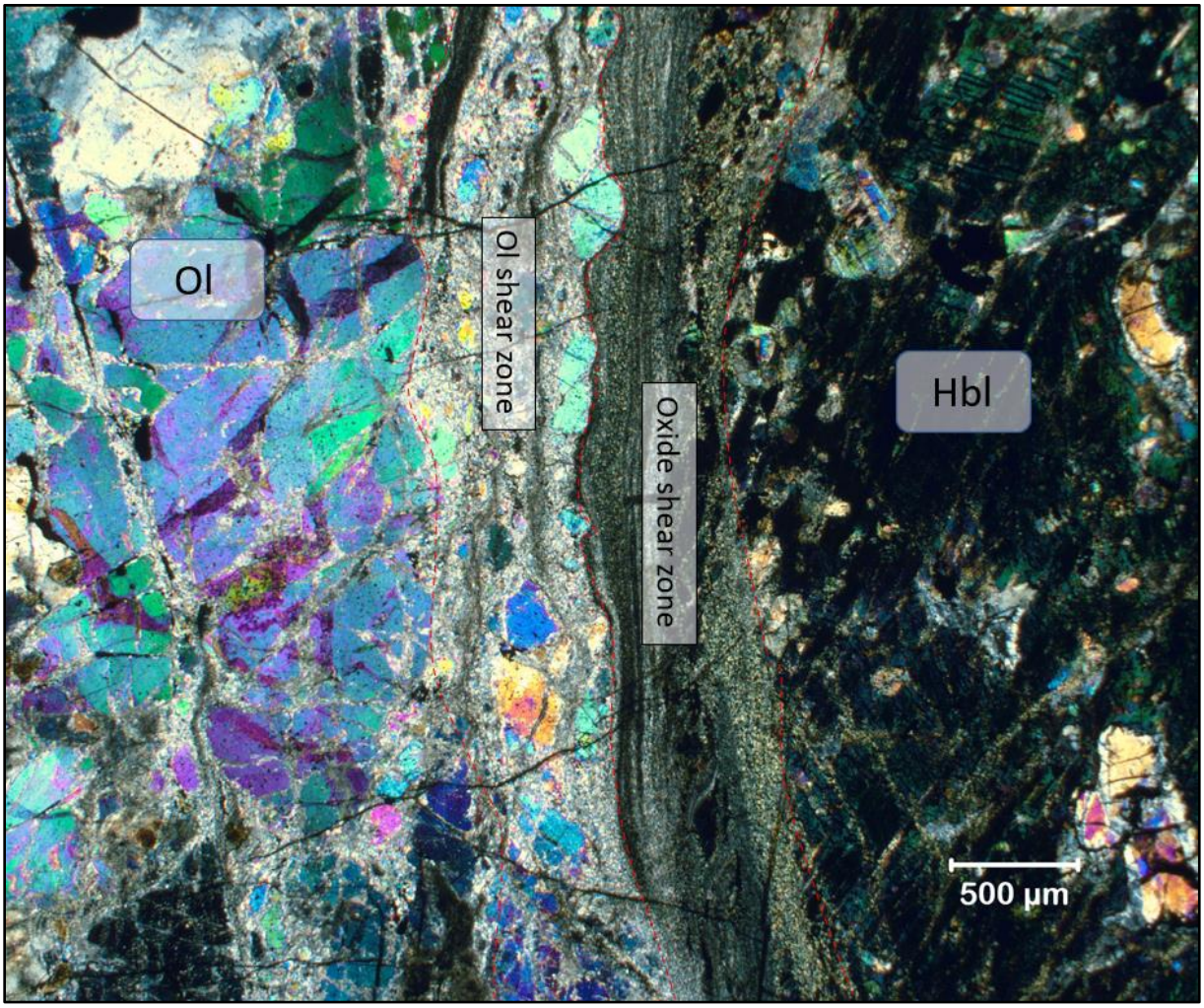

Figure 3.52. ***This figure shows the contact between the hbl phenocrystic dyke to the right, and the olivine dominated host rock to the left. The phenocrystic hbl contains rounded ol and px chadacrysts. A ol rich shear zone is in contact with the host rock, and cryptocrystalline oxide rich mylonite labelled "shear zone" in contact with the hbl phenocryst dyke. 2,5x magnification xpl.***

Along the cryptocrystalline infiltrating vein there is a mylonite in direct contact with the hbl phenocrystic dyke. The mylonite is dominated by cryptocrystalline phases, one of them being an oxide phase, making the mylonite appear dark. Texturally the mylonite seems to comprise material originating from the hbl phenocryst dyke, while the lighter ol rich shear zone seems to originate from the olivine rich host rock.

One of the shear zones associated with the hbl gabbronorite was analysed using XRD. The results from this analysis are presented in Table 3.23

Fo	Hbl	Di	En	Dol
87,73	3,05	2,95	6,12	0,15

Table 3.23. ***This table contains the XRD results from one sample of the fine grained ol shear zones.***

The results in Table 3.23 show that the shear zones are clearly dominated in ol and opx, with some hbl and cpx. There is also a small contribution from the carbonate mineral dolomite.

3.6.3 Whole rock chemistry

The chemical analyses for this lithology are only based on one sample. Therefore, internal variations within the lithology are unknown.

SiO2	Al2O3	FeO	CaO	MgO	Na2O	K2O	Cr2O3	TiO2	MnO	P2O5
39,1	0,64	17,05	0,97	40,2	0,09	0,02	0,048	0,17	0,2	0,03

Table 3.24. ***This table contains the whole rock analyses for the ol rich shear zone.***

The sample is rich in Mg, and has dunitic Mg values. The main elements in this sample is Si, Fe and Mg, which is similar to the chemistry of some of the dunitic samples in Table 3.5.

The trace element plot for this shear zone is presented in Figure 3.53

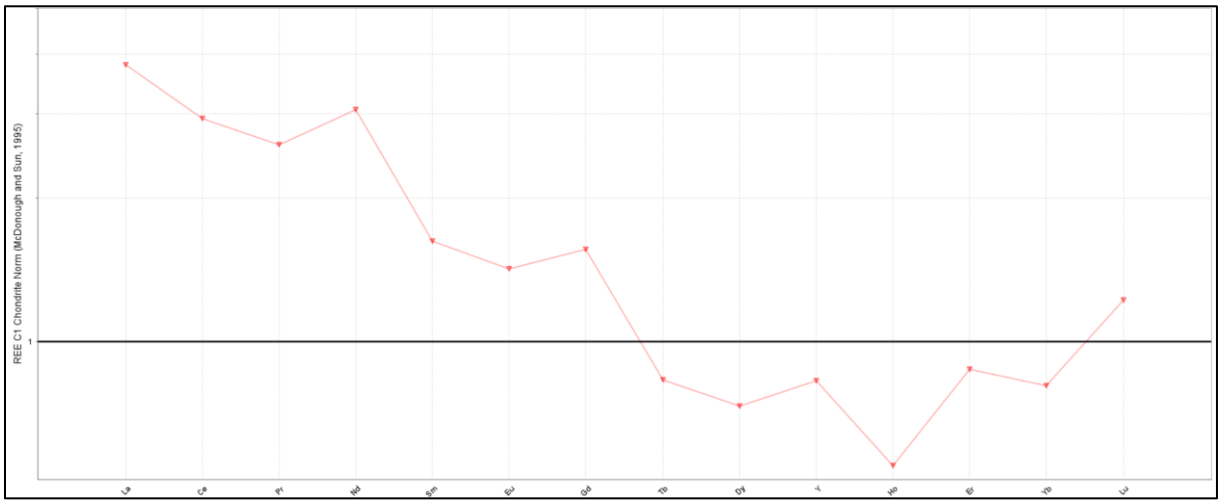

Figure 3.53. ***The graph in this figure shows the chondrite normalized REE plot for the shear zone sample.***

The chondrite normalised REE plot for this sample has the most irregular shape of any REE plot from ULS. The sample is relatively poor in REE with the highest value being La ~3x more enriched than a chondrite. It has irregular peaks for Nd, Gd and also appears to have a positive Y anomaly. This could also be an artifact due to the irregularities found in other elements in this plot.

3.7 Ore forming plagioclase rich phase

3.7.1 Field observations

When sampling the wehrlite on the western hillside a sample was collected with an anomalous plag veinlet in it, which seemed to have associated sulphide mineralization. This sample is labelled JS_2_19-C. The sampling locality can be seen in Figure 3.54.

Figure 3.54. ***Left: This figure shows the sampling locality of JS_2_19-C, a mineralized sample from ULS. The sample is taken from a px rich layer in the wehrlite. Right: The plag veinlet found in the mineralized wehrlite sample is believed to be related to the plag veinlet seen in this image. A raft of gabbro is seen as a dark body in the background. The gabbro body is ~250 m from the locality depicted here.***

The plag veinlet or the associated mineralization was not observed in the field, but found during cutting of the samples. Texturally, the plag veinlet seems to relate to the plag domains described in chapter 3.4.

3.7.2 Petrographic observations

The cut sample with the plag veinlet, as well as frame for the thin section prepared is shown in Figure 3.55.

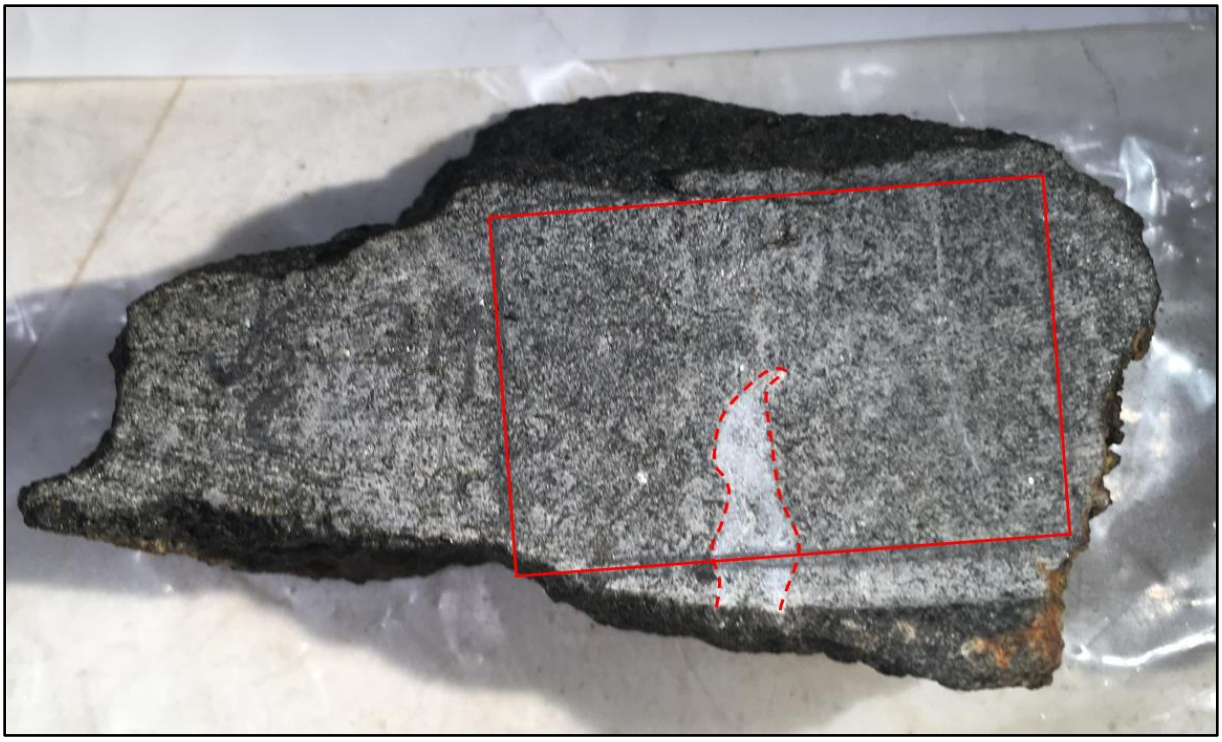

Figure 3.55. ***The picture shows the wehrlite sample from which the JS_2_19-C thin section was prepared. The red frame indicates where the thin section was prepared from, and the red stippled line outlines the plag vein seen in the thin section.***

The sample seen in Figure 3.55 shows the plag vein partially cutting through the wehrlite, and stopping to form a wedge shaped structure. There were also mm sized sulphides in the hand specimen which was the first indication of a potentially mineralizing phase present in this sample. The thin section prepared from the sample is shown in Figure 3.56.

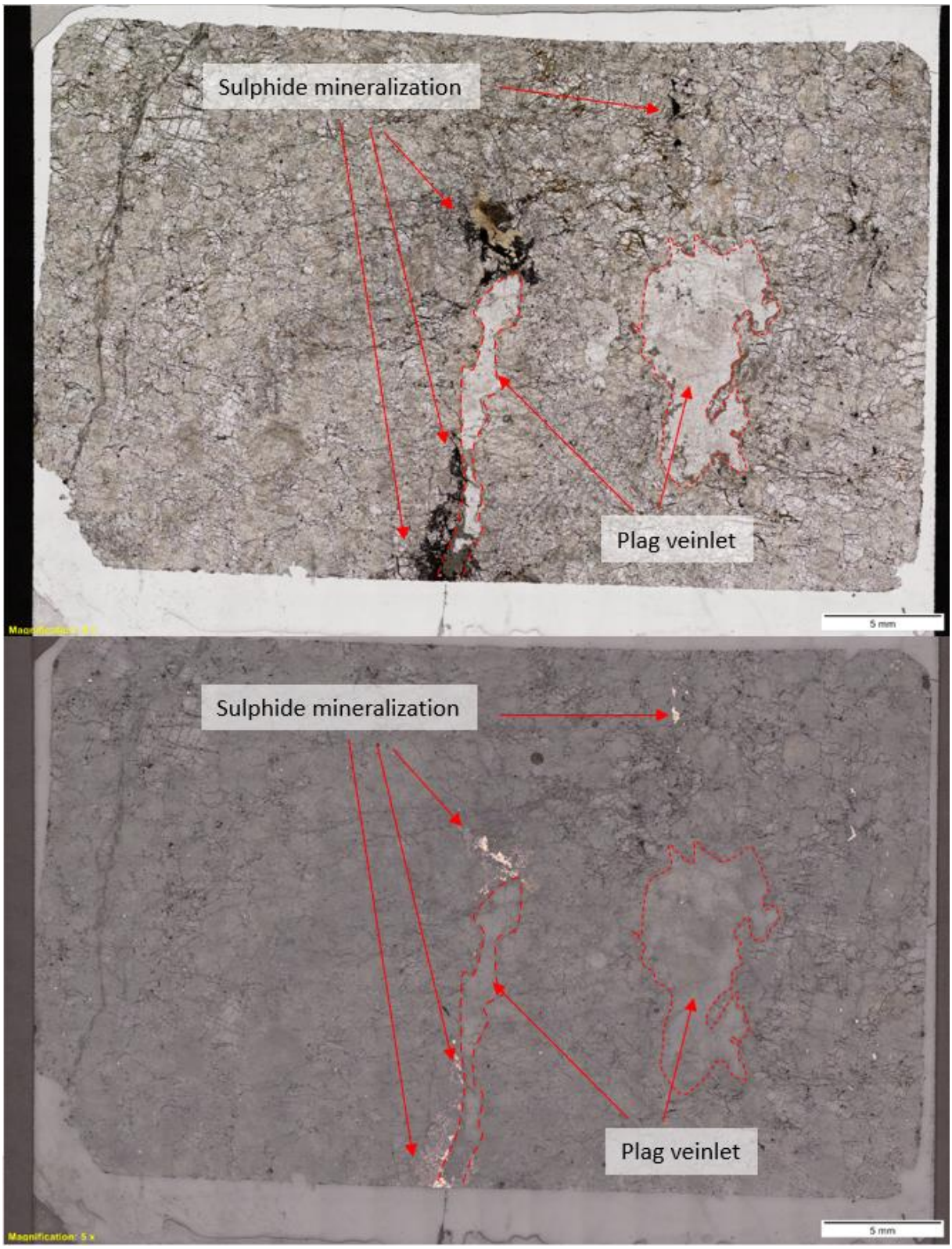

Figure 3.56. ***The two thin section images here are both from JS_2_19-C. The top image is a ppl image, while the bottom image is a reflected light image (rfl). The sulphide mineralization is indicated by red arrows, and the plag veinlets are outlined by red stippled lines.***

The thin section seen in Figure 3.56 shows a pyroxene rich wehrlite, infiltrated by a veinlet of plag rich material. The host rock is seen with an envelope of hbl surrounding the plag veinlet, indicating a reaction between the two phases.

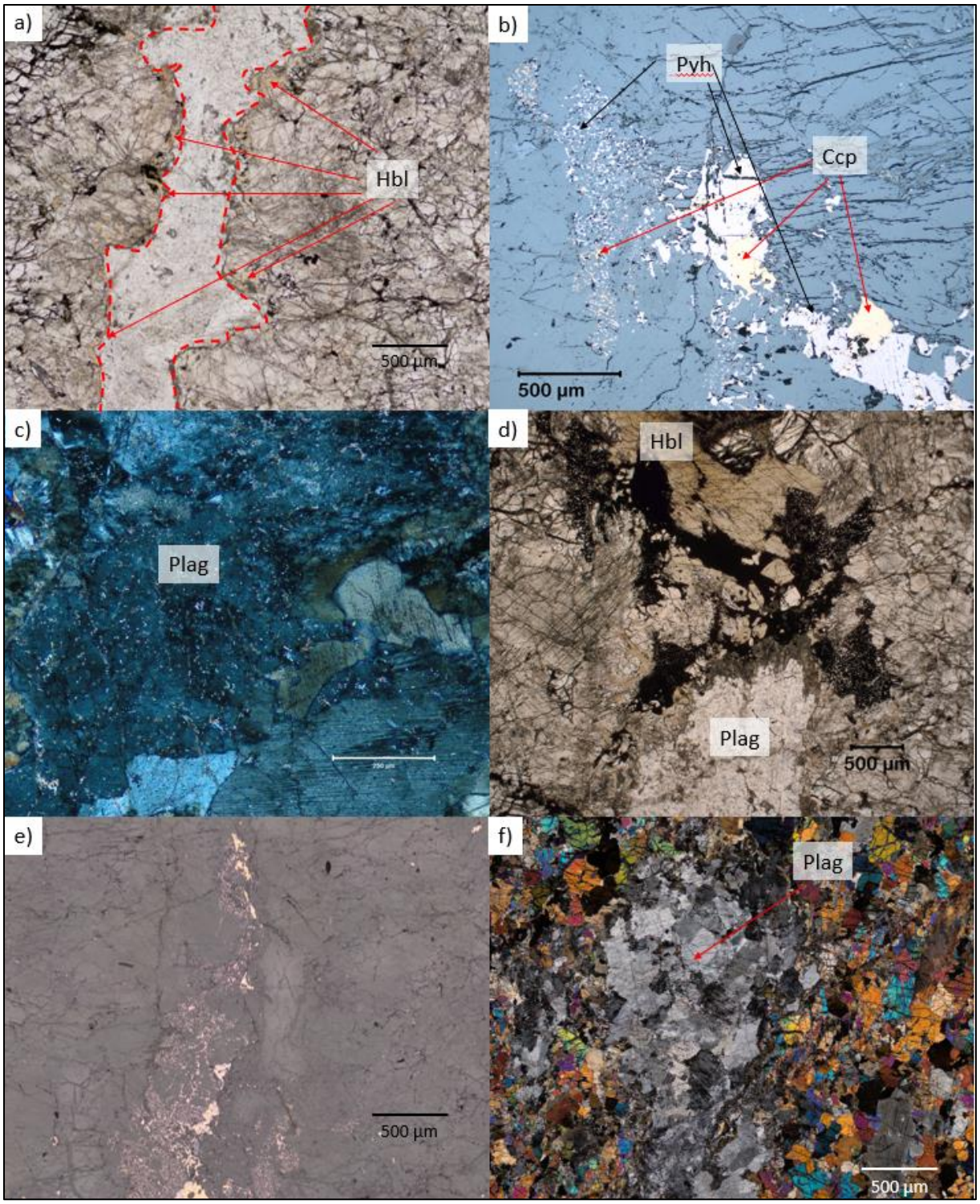

Figure 3.57. ***These six pictures are microscope pictures from JS_2_19-C taken with ppl, rfl and xpl. a) This image shows a segment of the plag veinlet enveloped by a reaction ~50 µm wide rim of hbl. The hbl in the reaction rim has been classified as a pargasite. The hbl grains are seen as small light brown grains originating in the wehrlite, but re-equilibrated with the plag veinlet. b) The zone shown here is the area at the tip of the left veinlet seen in Figure 3.56. It consists of Fe-Ni-Cu-sulphides, which vary from a massive subhedral texture, to a spongy texture which resembles a granophyric texture. There is mixing of pyh and ccp with some pn. The ccp is shown as more yellow coloured grains indicated by red arrows, and the pn has a white-grey appearance indicated by black arrows. c) This picture is from the plag zone itself and is taken with xpl. The plag grains are seen as subhedral 0,5 mm grains rich in inclusions of extremely fine grained ~10 µm grains of carbonates. These carbonates are identified as dolomite grains, and are seen as small bright dots in the larger plag grains. This implies that there is a phase capable of crystalizing carbonates from the melt which formed the plag grains. The plag grains are also rich in fluid inclusions, but are difficult to visualise from microscope pictures. d) This picture is from the same***

zone as image b), at the tip of the plag veinlet. The image shows a large ~2 mm grain of hbl at the very tip of the fracture, which is interlocked with opaque phases. The hbl and opaques seem to have a relation to the infiltrating plag veinlet due to their intermingling textures, and may have formed at the same time, or closely together. e) The bottom left plag veinlet of the thin section in Figure 3.56 also shows similar mineralization textures to what is described in b). The mineralization follows the path of the plag veinlet, and has the similar granophyre like textures. The mineralization seems to envelope the plag rich area. This image is taken using rfl. f) The more massive, isolated plag domain in Figure 3.56 to the right side shows the similar textures to the left plag veinlet, without as much of the associated mineralization. The zone does however have the same hbl envelope, creating a reaction rim between the plag phase and the wehrlitic, pyroxene rich host rock. The surrounding ol and cpx seems to have more iddingsite filled fractures the closer they are to the veinlets, indicative of a potential fluid rich phase present in the plag veinlets.

The pictures in Figure 3.57 show some of the ore forming potential in the plag rich phase. The granophyric texture of intermixed pn, pyh and ccp seem to follow the path of the infiltrating plag. The plag domain is also rich in carbonates, which often sit as small inclusions in the plag, but can also be an interstitial phase, sitting between plag grains. The surrounding ol seems to be more fractured and altered than the ol further away from these veinlets. The alteration is seen as brown iddingsite filled fractures in ol and some opx crystals, sometimes containing small grains of iron oxides.

The mineralizing phase was analysed using a stitched EDS map in order to better separate the granophyric phase. The stitched maps are shown in Figure 3.58.

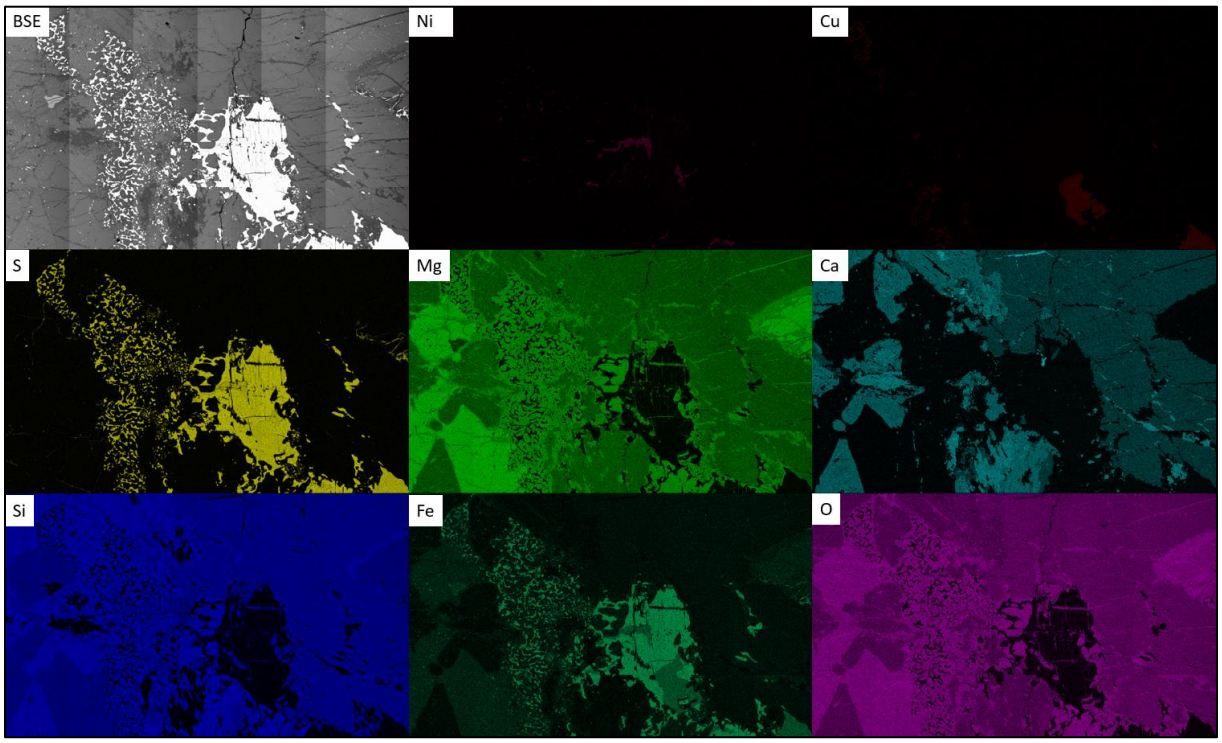

Figure 3.58. ***This figure shows the stitched EDS maps from the mineralizing phase in JS_2_19-C. The first image is a BSE image, with a poorly adjusted beam, causing a very visible stitching effect. The rest of the maps are indicated by which element is mapped in the top left corner.***

The maps shown in Figure 3.58 show the mapped mineralizing phase seen in Figure 3.57 b) and d). The BSE image shows the sulphides as a bright white, massive to granophyric grains. The zone was mapped with elements which would be representative for the phases present. The elements Fe, S, Ni and Cu show higher concentrations in the bright grain, while Mg, Ca, Si and O do not indicate any presence from the maps.

The S map is the best indicator for the grain, as the mineralizing phase is a sulphide phase. The S map is shown in yellow, and shows high concentrations in the grain itself, and very low concentrations in

the surrounding grains. The Fe map also shows high concentrations in the mineralizing phase, as well as some of the surrounding silicate phases. The Cu map and Ni only show concentrations in the mineralizing phase. These maps are however dim as these are both heavy elements which would require higher acceleration voltages in order to obtain a good signal. The Cu rich phase correlates to the phase identified as Ccp optically in Figure 3.57 b).

The Cu map has an inverse relation to the Fe map, meaning the Fe map shows a slight depletion where the Cu map shows an increase in concentration. The sample inverse relationship with Fe applies for the Ni map. The area where Cu shows higher concentrations is a ccp phase, while the phase enriched in Ni is a pn phase.

Based on the results from the Si, Mg, Ca, Fe and O maps it seems the surrounding phases are primarily ol, cpx and hbl. The brightest grains in the Mg map are most likely ol as it has a high relative Mg content, which also correlates with a relatively low Si map. The high Si, high Ca, low Fe, medium Mg grains are probably cpx, while the right most grain showing medium Ca is an amphibole grain.

4 Discussion

4.1 Emplacement and evolution of ULS

Layering of ULS

As seen in chapter 3.2 the ULS of RUC is a modally layered ultramafic intrusion, primarily consisting of layered wehrlite with a varying cpx content. The most cpx rich layers would be classified as cpx rich pyroxenites, and the most cpx poor layers would be classified as dunites. As these variations are interpreted as magmatic variations from the same origin, the host rocks are referred to as wehrlites, as this is the most abundant lithology.

The primary layering shows variation in the px content and textures as well. Some cpx crystals are cm scale eu-subhedtral grains, while the primary rock forming cpx is more-fine grained at mm scale. This may be indicative of some crystal rich magma pulses entering the chamber as described by Charlier et al. (2015), as the coarser crystals may have crystallized in a different part of the chamber, prior to entering the magma chamber which formed ULS. Some of the layers with coarse cpx crystals like the bottom layer seen in Figure 3.3, shows what appears to be settling textures of coarse cpx. The cpx is heavier relative to the melt and would sink to the bottom of the chamber. The layering could then be a result of settling of the cpx crystals in the magma chamber.

In order to get grains of this size, the diffusion rate and nucleation rate of grains must be different from the more fine grained layers of wehrlite, indicating that these coarser crystals may originate from a different part of the magma chamber where nucleation rated were slower, or diffusion rates were higher. Individual crystals can also form at the same time, settling at different rates, which could form the layering. The contacts in ULS are however often too sharp for this to be a realistic cause of the layering, as different settling rates fo crystals would cause more grading contacts over a larger stratigraphic depth.

The layered nature of the cumulates likely started with a magma pulse, rich in Mg and poor in Si. Once the magma pulse starts crystallizing ol making ol a liquidus phase, it fractionates ol out of the melt, making the relative Si content of the melt increase. As cpx has a higher Si/Mg-ratio than ol cpx may start crystallizing once the Si saturation of the magma pulse has reached the liquidus for cpx and the temperature is sufficiently low. This process would form a cyclic layer of an ol rich layer at the bottom and a cpx rich layer above. If new magma replenishments of high Mg melts would enter the chamber and mix with the melt this layering process could produce the pattern seen in ULS.

This process has been described in other layered ultramafic intrusions like the Muskox intrusion (Irvine T. N., 1975), where a cyclic series formed with each new pulse of magma, starting with a bottom layer of dunite, followed by a harzburgite, and ending with an orthopyroxenite layer at the top. This is interpreted as ol being the first liquidus phase of the magma pulse, and opx being the second liquidus phase. This is similar to what is observed in the primary layers of ULS, but happening with ol and cpx rather than opx. Cpx has a lower liquidus temperature than ol and opx (Best, 2003; Gill, 2010; Winter, 2001), and would behave in a similar way to opx in a system like this. The system then starts crystallizing ol, and progresses to a cotectic crystallization between ol and cpx.

The change in the liquidus phase would then mean changing the main cumulate phase as the ol rich layers would have ol as its main cumulate phase, and the more cpx dominated layers would have cpx as the main cumulate phase. This is in accordance with the petrographic observations from the different layers, as sometimes the cpx is the main, large eu-subhedral phase in a thin section, while

other samples show ol as the large eu-subhedral phase, with interstitial fine grained phases like cpx and ol. This crystallization sequence for ULS is also confirmed by Grant et al. (2016).

This means the cpx poor layers found in ULS would represent the start of a magma pulse, and the clinopyroxentic layers representing the end of a crystallization sequence. This process does however not need to go to full completion each time, as a new pulse of Mg rich, silica poor melt could enter the system at any time, restarting the cycle, producing more ol rich layers. This behaviour is indicative of an open chamber system, as fresh magma batches would have to be able to mix with the crystallizing magma to form these layering sequences.

The characteristic layering, which the mapping of ULS was based on was overlooked on the southern plateau of RUC in the geological map by Grant, et al. (2016), probably due to the layering beeing more difficult to see on the plateau. This is due to the layering being sub parallel to the surface of the southern plateau. The new proposed map form this thesis, is that the contact to CS is further north, and the southern plateau is a large surface exposure of ULS.

Chemical evolution of ULS

The cyclic and modal layering of the intrusion indicates a repetition of the same processes, as the intrusion does not show strong chemical variation through the stratigraphic layers. The magma pulses creating the layer does not seem to evolve drastically over time. The individual layers vary relative to mineralogy, but the samples collected from the lower layers of ULS are not significantly different from the samples collected further up in the stratigraphy.

The wehrlite chemistry seen in Table 3.5, Figure 3.14 and Figure 3.15 show that the whole rock chemistry is largely controlled by the cumulus phase present. The samples with high cpx content like JS_2_15.G_3 and JS_2_13_5 are richer in elements like Si, Ca and Al, as these samples can include more of these elements because of their high cpx content. The samples rich in ol often have higher Mg contents and lower Si, as this is directly correlated to the chemistry of the minerals.

Based on the interpretation that ol is the first liquidus phase, and cpx being the second liquidus phase when a new pulse of magma enters the chamber, this would mean the host rock chemistry would be controlled by fractionation between cpx and ol, which from the MgO and SiO_2 plots in Figure 3.14 and Figure 3.15 has happened. The chemical analyses of the different wehrlite samples fall along the fractionation line between measured cpx and ol values from the intrusion.

The sample JS_2_19-C is the stratigraphically highest sample in this data set, meaning it would have in theory crystallized at the latest point compared to the rest of the samples. This sample does however not show much indication of being more fractionated than other samples in terms of major elements, as any fractionation would be overprinted by the continuous replenishments of new batches of magma into the chamber.

The melt forming ULS is assumed to be a fertile melt. This has been described by other authors who have worked with the different magmatic series of RUC. The observed mineral chemistry and whole rock chemistry indicate high Mg values, which are indicative of a fertile melt source. (Winter, 2001; Gill, 2010). The analysed ol in the wehrlites is also Mg rich with measured Fo values of Fo_{81}. The presence of primary magmatic hbl also indicates the presence of a hydrous, volatile phase in the melt forming the minerals. Hbl is a hydrous mineral, and these hydrous phases are often associated with very fertile, juvenile melts.

As the main cumulus phase varies from being ol in the more dunitic layers, to cpx in the wehrlitic and pyroxenitic layers, this also has a large effect on trace element chemistry. This is because high Ca cpx

is a repository for REE^{3+} which can incorporate itself into the M2 site where Ca^{2+} resides. Cpx can also charge balance itself which allows for net charge neutrality. (Gaetani & Grove, 1995) This means a higher cpx content will lead to a more enriched REE signature, as cpx can carry more REE than ol and opx.

The most enriched samples like JS_2_19-C and JS_2_15.G_3 are also enriched in cpx relative to the other samples. JS_2_15.G_3 has a Di content of 69,9%, and JS_2_19-C has a cpx content >60%, based on observations from the thin section prepared from this sample. The most depleted host rock samples are samples like JS_2_6 and JS_2_4, as these samples have cpx contents ~5%, and ol contents form 90-95%. As ol cannot incorporate as much REE in its lattice as cpx, samples rich in ol will subsequently be depleted in REE.

As the new magma pulses contain a concentration of REE the first layers will not preferentially fractionate these into the cumulate phase as REE have partition coefficients < 1 in ol. The REE will therefore preferentially partition in the melt. As this happens the relative REE concentration of the remaining melt phase will increase. As the next cumulate phase which is cpx starts to crystallize from the same magma pulse, the relative REE concentration will in this melt be higher than when ol started to crystallize. As seen in Figure 1.9, the partition coefficient for REE in cpx is < 1 meaning REE will preferentially partition into the melt phase over the solid cpx phase, but REE are is still magnitudes higher than for ol. The trace elements will then partition much more into cpx than in ol.

The hypothesis then is that the uppermost layer will be the most enriched layer in the intrusion with respect to REE and other incompatible elements. This is because of continuous fractionation of phases which REE do not partition into. One of the most enriched sample in the data set for this thesis, is also the stratigraphically highest and would based on this hypothesis should be the most enriched. This sample does also contain high amounts cpx, which would preferentially incorporate REE compared to ol.

JS_2_19-B is one of the most enriched ol rich wehrlite samples with a Fo content of 75,4 % and a Di content of 18,48%. It is sampled form a similar stratigraphic height to JS_2_19-C. This may indicate that it crystallized from a more enriched melt than other similar samples. JS18-has has an ol content of 80,41%, and a Di content of 15,88%, which is comparable to JS_2_19-B. If these samples crystallized form a similar melt they would be expected to have similar REE enrichments because of their similar mineralogy.

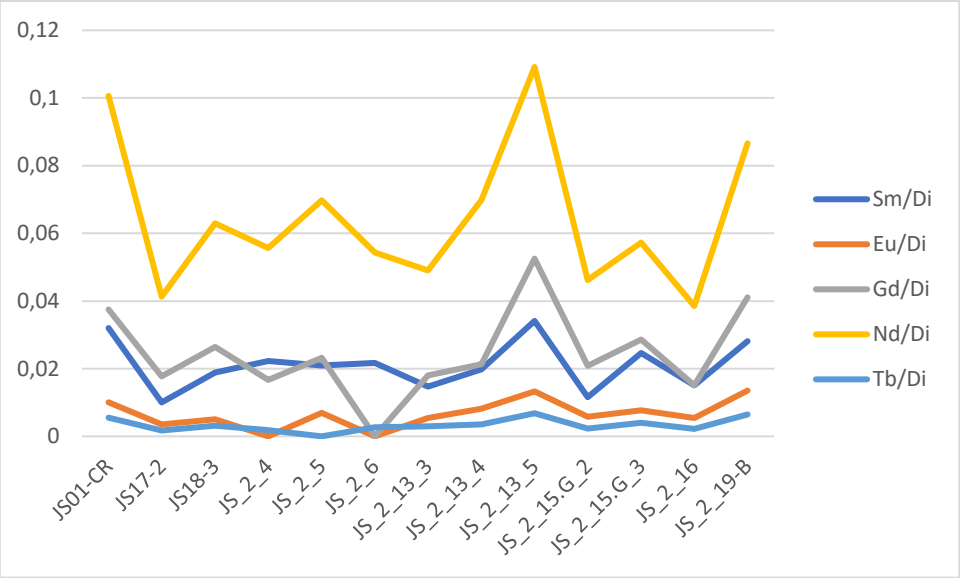

Figure 4.1. ***This graph shows Sm, Eu, Gd, Nd and Tb normalized to the Di content of the wehrlite samples.***

The graph in Figure 4.1 shows five selected REE normalised to the cpx content of the samples. These elements are selected because these are the elements which show the most fractionation in the samples, as seen from Figure 3.16. Cpx has a higher affinity for the MREE to HREE, and a lesser affinity for LREE. The REE contents of each sample has been normalized to the amount of Di based on XRD results in order to check the degree of which cpx controls the REE content of a whole rock analysis.

If the variations and enrichments in REE was strictly controlled and proportional to the cpx content the curved would be expected to not vary. There are three notable spikes in these samples, which show an enrichment in all five Di normalised plots. JS01-CR, JS_2_13_5 and JS_2_19-B. The two first samples, JS01-CR and JS_2_13_5 both have a hbl component in their mineralogy, which may have affected the REE pattern, as some REE are compatible and preferentially partition into hbl over the melt phase. JS_2_19-B however, does not have any observed or measured hbl, and the REE concentration is believed to be mostly controlled by the REE in cpx.

JS_2_19-B may indicate that the upper layers of the intrusion are more enriched in REE, and that the magma forming ULS has had time to fractionate, crystallizing cumulate phases, and letting the residual melt gradually build up a higher concentration in REE over time. If this is the case, this would indicate that the residual melt has not been removed immediately, but rather has had time to mix and mingle with the recharges of magma entering the chamber, without being transported up and away from the partially crystallized cumulates. The lack of laser ablation data for this thesis has made it difficult to determine the exact changes of REE in cpx.

Replacive dunites

The dunitic infiltrations observed cutting the original wehrlitic layering in Figure 3.4 and Figure 3.5 have also been described by Larsen et al. (2018) and Grant et al. (2016). These small scale replacive dunites are believed to relate to the emplacement of CS. The contact between ULS and CS is very diffuse, and difficult to find as it is a gradual change from one magmatic series intruding into another mushy magmatic series. These replacive dunites are interpreted as melt originating form CS, cutting the layering of ULS.

The small scale replacive dunites seen in ULS are of dunitic composition, as they are high in ol and have a cpx content less than 10%. Based on the work of Larsen et al., (2018) it is suggested that these offshoots of melt from CS enter ULS while ULS is comprised of partially crystallized, mushy cumulates. This would mean the cumulate phase would be crystallized, but the interstitial phase would still be liquid. This complies with the observations from the southern plateau of ULS. The shapes of the infiltrating dunitic melts are highly irregular, indicating that ULS was still a hot mush when the replacive dunites infiltrated.

According to the interpretations by Grant et al., (2016), Larsen et al., (2018) and Emblin (1985) melt is thought to have migrated from CS into ULS mainly via channelized flow, but also via porous flow as discussed in chapter 1.3.5 *Melt migration and dyking*. The melt migrating from CS is assumed to have low viscosity because of its low Si content, which inhibits the formation of Si-polymers (Rushmer, 1996). As the melt generated from CS would be in large volumes it would allow the melt to flow through ULS via porous flow. This could be confirmed by mineral chemistry analyses of interstitial ol, but this has not been done for this thesis.

Since the replacive dunites are poor in cpx compared to the wehrlite which they infiltrate the melt is believed to be in chemical disequilibrium with the surrounding wehrlite. The replacive dunites would be undersaturated with respect to Si compared to the wehrlitic cumulates, and therefore assimilate some of the cpx in the wehrlites. The pulses of magma from CS would also be hotter than the cumulates, possibly increasing the temperature sufficiently to initiate melting of cpx.

Field observations from the small scale replacive dunites within ULS show contacts which appear diffuse and gradual over a very short distance. The contacts are not sharp cutting contacts, but rather more undulating contacts which may indicate a reaction between the wehrlite and the replacive dunite. Rafts or xenolith like structures of wehrlitic material are also found in the replacive dunite, where the texture of the surrounding wehrlite is still identifiable but has faded. Rafts like these are shown in Figure 3.4 and Figure 3.5. The contacts here also seem like the replacive dunites have infiltrated into a cumulate mush through channelized flow.

Based on field observations the evidence towards a smaller scale replacive dunite originating from CS and infiltrating into ULS are convincing and has been described in several previous works. (Emblin, 1985; Grant, et al., 2016; Larsen, et al., 2018). The large metre scale replacive dunites however do not seem to relate to the replacive dunites seen in Figure 3.4 and Figure 3.5. These large scale replacive dunites (LSRD) are described as 1-5 metre wide replacive dunitic zones (Grant, et al., 2016), and are characterised by their characteristic orangeish yellow colour.

When the LSRD were investigated in the field, chemically and mineralogically, all samples show strong evidence towards extensive serpentinization. The samples taken from the cores of LSRD had LOI=7,13 ± 3,16 wt%. indicating a high water content compared to the rest of the wehrlitic samples. The XRD results also show high lz contents for some samples. The highest recorded lz content of a sample is 41,80%, from JS17-1, seen in Table 3.4. This sample has had its ol content reduced from ~80% to 40,99%, and its opx content has been reduced from ~3% to 0%. The di content of this sample is 16,95% compared to the surrounding rocks di content of 15,88%. These estimates are based on sample JS18-3, taken from the same magmatic layer, but outside of the serpentinization zone.

Similarly to JS17-1 and JS18-3, the set of samples labelled JS_2_13_(3-5) represent a traverse sampled from the core of a LSRD (3), the margin between the wehrlite and a LSRD (4), and lastly in the wehrlite (5). These samples show a spike in lz content in the core (31,84%), and low lz contents in the margin (0,56%) and in the wehrlite (1,14%). The di content does not seem to be affected by the LSRD as the

core has a di content of 36,71%, the margin has a di content of 25,77%, and the wehrlite has a di content of 29,31%.

The proposed mechanism for the replacive dunites is a process of assimilation of wehrlitic cumulate cpx (Grant, et al., 2016). This is not shown in any of the LSRD found in ULS, as the di content remains unchanged from representative unaltered wehrlite samples. The di contents do not indicate that any di has been consumed or assimilated by the LSRD.

When looking at the chemical plots in Figure 3.14 however, the LSRD seem to contain less SiO_2 than their unaltered counterparts. The samples plot as more SiO_2 depleted than some of the ol analyses. If these were actual infiltration of dunitic melt, ol would most likely affect the chemistry of the samples to a more SiO_2 poor composition, as ol has less SiO_2 than cpx does. When the whole rock chemistry has a lower SiO_2 content than ol itself, it indicates ol is not responsible for this depletion.

The general chemical formula for lizardite is $Mg_3Si_2O_5(OH)_4$ (O'Hanley, 1996), which has a higher Mg/Si molar ratio and total weight ratio than forsterite does. Allen and Seyfried (2003) also state that serpentinizing fluids may become enriched in SiO_2 through the dissolution of pyroxenes. If this process has taken place here this would mean a mobility of SiO_2 away from the system, leaving the samples depleted in SiO_2. These two factors could explain the local depletion in both Si compared to the unaltered samples.

There also seems to be a slight depletion in MgO in the LSRD samples. As the melt forming CS is recorded to have similar Fo contents to ULS, at $Fo_{84,6\text{-}76,1}$ (CS) vs. $Fo_{85,1\text{-}77,4}$ (ULS) a local depletion in MgO would not be expected form dunitic protrusions from CS into ULS. The depletion in Mg may be a result of the serpentinization as Mg in lz may easily be substituted for other elements (O'Hanley, 1996).

Some of the depletion in the serpentinized samples is however attributed to the LOI. This affects the analysis as it "dilutes" the other elements, meaning some of the depletions seen may actually be a reaction, but it may also simply be an artifact of the analysis. If the LOI of a sample is 10%, the remaining elements make up 90% of the sample. This will then affect the magnitude of elemental ratios in the whole rock analysis. Serpentinization reactions can happen without major chemical alterations of the host rock, but will have associated mineralogical changes.

In addition to the apparent serpentinization seen in both XRD, chemistry and in the field, there is a systematic serpentinization joint set which is parallel to the orientation of the LSRD. These joints are shown in Figure 3.9 as a metre scale wall covered with serpentine. This further assists in the interpretation that these zones are mainly a result of a large scale serpentinization network.

It seems as if the LSRD described by Grant et al., (2016) and Larsen et al., (2018) are only related to serpentinization processes rather than emplacement processes from CS. It should however be stated that a primary infiltration, and channelized flow on such a scale could prime the wehrlites and replacive dunites for later alteration and serpentinization. The chemical signature which would be expected from a replacive dunite is unfortunately not seen here.

Px pegmatites

The px pegmatite seen in chapter *3.2 Wehrlites, and host rock features* is a coarse grained px rich pegmatite seen intruding into the wehrlite white it was still a mush. The contacts to the pegmatite are irregular and undulating sometimes even showing individual coarse px crystals decouple from the main px pegmatite bodies, and float around in the wehrlite. These are interpreted as one of the late pulses of melt recharge into the chamber.

Traditional felsic pegmatites usually form through progressive crystallization of anhydrous quarts and feldspar, increasing the residual melts content of incompatible elements and water. The pegmatites then crystallize from this extremely hydrous melt rich in incompatible elements. Pegmatites are then a rich source of REE and other trace elements (Roedder, 1984). This contributes to the assumption that the pegmatites in ULS could be mineralised, as many of the ore forming elements are incompatible in the ultramafic mineral assemblage.

The formation of such pyroxenitic pegmatites has been widely discussed because they are believed to be a part of a mineralizing process. The extremely coarse grained (2-5 cm) opx and cpx in this pegmatite are unlike any other grain size found in the layers of ULS, and the origin of these grains are speculated. Similar coarse pyroxenitic pegmatites are found in the Merensky Unit (MU) in the Bushveld Complex of South Africa. These pegmatites have been studied in relation to their ore forming capabilities and are described and discussed by Cawthorn & Boerst (2005).

The pegmatites found in the MU are described by several authors, but not all provide an explanation to the genesis of these pyroxene pegmatites. Many of the models describing the genesis of these pegmatites involve a late stage, evolved, volatile rich magma produced through fractionation. (Lauder, 1970; Von Grunenwaldt, 1979 ;Vermaak, 1976), but high temperature magmatic processes have also been proposed by other authors (Naldrett et at. 1986; Barnes & Campbell, 1988).

Chemically and texturally the two pegmatites seem to resemble each other. The pegmatites are rich in opx, cpx, with minor ol (Cawthorn & Boerst, 2005). The pegmatite in the MU is associated with chromite mineralization, which is not seen in the pegmatites of ULS. The MU pegmatite is also associated with a significant Cu enrichment, which is observed to a lesser extent in the ULS pegmatite. The pegmatite sample from ULS is the most enriched Cu sample found at 249 ppm Cu, which is much lower than the >1000 ppm found in the Merensky Reef.

The pegmatite may have formed from a stagnant or trapped magma, which crystallized from this trapped melt. If this was the case it seems unlikely that individual grains may have decoupled from the main pegmatite bodies, and the lack of a significantly enriched signature is also an indicator of magma trapping being unlikely. There is however a possibility that as the larger opx grains crystallized form the melt, the residual enriched melt may have remobilized. As the pegmatites were not the focus of this thesis, only one sample was collected, meaning the overall quality and interpretability of the data from this lithology is limited.

Sub solidus, fluid rich processed have been proposed in the formation of such pegmatites, but due to the textures and contacts with the wehrlite in ULS these processes seem unlikely. The emplacement of these pegmatites seem to originate form a primary magmatic process, as fluid rich processes most likely would alter the surrounding wehrlite in a more significant way than what is observed in ULS. The pyroxenite pegmatite found in the MU is also fundamentally different from the pegmatite in ULS in the sense that the MU peg forms a layer in the magmatic sequence, while the ULS peg forms isolated stocks and dyke like infiltrations into a mushy wehrlitic cumulate.

The formation of the pegmatites in the MU is attributed to the addition of superheated magma or a release of pressure caused the supernatant magma to become superheated, allowing for a hiatus of crystallization, resulting in a subsequent crystal ageing in the interface between the superheated magma and the supernatant magma. This mechanism is unlikely to have caused the pegmatites in ULS. Some of the evidence which Cawthorn & Boerst (2005) base their interpretations on are purely textural from thin sections. It is difficult to interpret formation from the ULS pegmatites, as no thin sections were prepared from these samples. More investigation into these pegmatites would therefore be required.

What can be concluded with from the observations and geochemistry however, is that the pegmatites seem to have a primary magmatic origin. Post-magmatic growth of px crystals mentioned as a hypothesis for the MU pegmatites (Lauder, 1970) cannot be excluded without investigating the samples through a microscope, it does however seem unlikely as a mechanism of formation for the coarse grained px. The idea of a fluid rich melt rich in incompatible elements also seems unlikely as the chemical signature of the px pegmatite does not seem to have significantly more enriched signature than other wehrlitic samples. The REE curve does not have a typical enriched linear slope from La-Lu either, which is often seen in enriched samples.

Based on the field observations the pegmatite could have formed via crystallization in a lower part of the magma chamber where the diffusion rates were higher and nucleation rates were lower than higher up towards where the wehrlitic cumulates had formed. This would imply the crystals had already formed and were later transported up through the cumulates of ULS. This process is however unlikely, as the coarse grained pegmatite would then have formed an extremely coarse mush, which is assumed to have poor flow mechanics. For this model to work the wehrlitic cumulates must have been liquid and mushy enough to allow for the infiltration of the coarse mush. This process could explain the isolated coarse px crystals which are sometimes seen “floating” individually in the wehrlitic mush as seen in Figure 3.8 a).

4.2 Lamprophyre relation of porphyritic hbl dyke

The porphyritic hornblende dyke is texturally the most characteristic dyke found in ULS as its abnormally large phenocrysts distinguish it from other dyke types. The hbl phenocrysts are seen as large dark crystals which reside in the dark fine grained ground mass as described in chapter 3.3. They are not abundant, but are observed from the southern plateau up towards the contact to CS, spanning a large horizontal area. These dykes have been referred to as *lamprophyres* in previous works and field descriptions of dykes from Reinfjord, which is a label which often implies a place of origin and a chemical signature. Whether these dykes should be classified as lamprophyres will be investigated.

The dykes themselves are among the most massive found in ULS, and as seen in Figure 3.18 a), the dykes seem to follow more angular paths than neighbouring dykes. This may either indicate that the dykes infiltrated through a more ductile wehrlite allowing them to shape their own path, or it may indicate that the wehrlite was colder, and fracture sets in the wehrlite controlled the path of these dykes. If the temperature were lower, a slightly chilled margin would be expected in the contact between the wall rock and dyke. Such a chilled margin is not observed in this dyke type.

Structures like the ones seen in Figure 3.18 b) also indicate intrusion through a more ductile wehrlite, as inclusions of wall rock in the dyke as well as small protrusions from the dykes are more characteristic of ductile, hotter wall rocks, rather than cold brittle wall rocks. If this was a brittle environment, the dykes would most likely show a sharp, almost linear opening of a fracture, which would be filled with magma. Small pockets of wehrlite protruding and included into the dyke are more easily explained by plastic and ductile emplacement, than by brittle emplacement. This in combination with the lack of a chilled margin indicates emplacement of this dyke type in a hot wehrlite.

The groundmass of these dykes is largely dominated by cpx, opx and ol. The ground mass itself would classify as a websterite, not including the large hbl phenocrysts. As seen in Figure 3.21 the groundmass mainly consists of interlocking grains which crystallized under equilibrium conditions. These dykes also contain a high amount of Fe-Ti oxides (3,34-4,21%), observed as opaque minerals, which attests to the high Fe-Ti content of the melt which formed these dykes. Oxides like these may sometimes be deposited as secondary phases through alteration, but in this case some of the primary silicate minerals occur as inclusions in the ilm phase, indicating a primary magmatic origin for these grains.

The size of hbl phenocrysts vary between localities, with the biggest phenocrysts observed being shown in sample JS21 seen in Figure 3.19 at 1,5 cm. The phenocrysts in JS03 which can be seen in Figure 3.19 are among the smallest found in this dyke type at around 0,5 cm. The phenocrysts in this dyke type all have a rounded, oval shape, which is different from the rhombus or trapezoid shape expected to be seen from a perfect euhedral hbl crystal. Based on this rounded shape the phenocrysts are believed to have been resorbed by the melt which formed the dyke, as these crystals may not have been in equilibrium with the transporting melt.

If the phenocrysts in the dykes were originally all equigranular crystals, this would indicate that the phenocrysts in the dyke from JS03 (small phenocrysts) were suspended in a non-equilibrium melt for longer than the crystals in JS21 (large phenocrysts). If the phenocryst were in disequilibrium with the transporting melt for longer, this could possibly explain the reduction in size found in the phenocrysts. The overall hbl content of JS03 is however higher than JS21, at 29,17% compared to 22,65%. This is mainly attributed to the phenocrysts themselves as there is little hbl in the actual groundmass. This theory is however highly speculative, as the origin of the phenocrysts is unknown, and the original size of the crystals are also unknown.

This dyke type draws significant resemblance to a lithology often referred to as lamprophyres in literature. Rock (1977) describes these rocks as porphyritic dyke rocks, recognisable in the field often containing large porphyroclasts of hbl or bt, and are often the latest product of igneous activity in a region. They are also known to show panidiomorphic textures, hydrous mineralogy, and absent of felsic groundmass, often with an alkaline chemical signature.

There are however differences in the porphyritic hbl dykes from ULS to the lamprophyres described by Rock (1977). The lamprophyres are described to be a lithology enriched in incompatible, and often volatile elements. This is observed to some degree in these dykes, as it is relatively enriched compared to other dykes om similar mineralogy. It shows a noticeable enrichment in REE compared to the lhz and comp dykes, and a similar MREE-HREE to the hbl gabbronorite dykes as seen in Figure 4.2. The hbl gabbronorite does however have a LREE concentration almost a magnitude higher than the phenocrystic hbl dyke. This is likely due to the different mineralogy of the different dykes. JS21 shows a slight increase in Ti over the other dyke types, attributed to the high content of ilm in this sample.

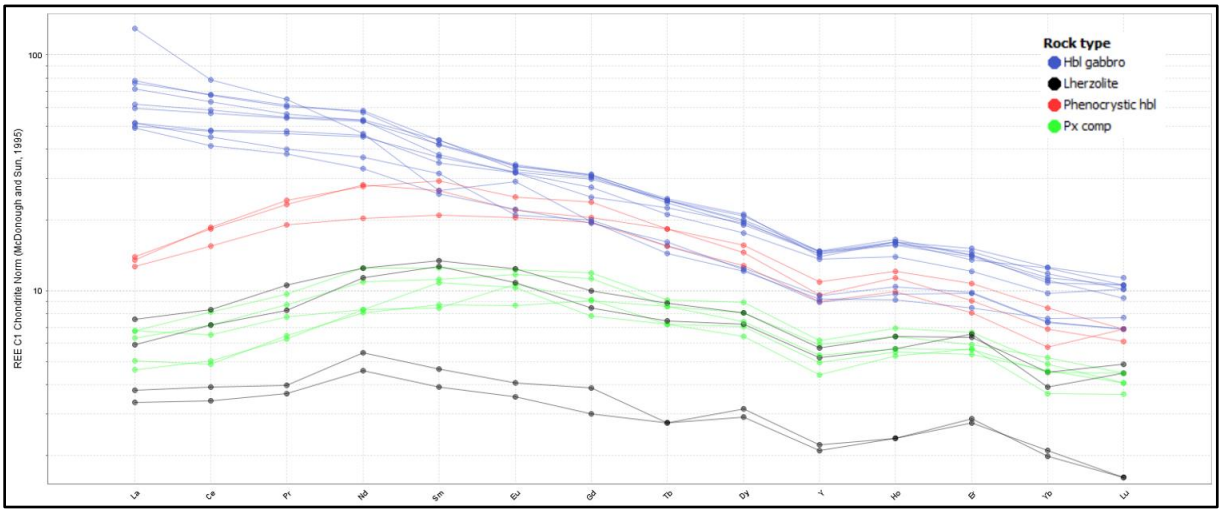

Figure 4.2. ***This graph shows the chondrite normalized enrichment in REE for the four different main dyke types, with the hbl gabbro (blue) as the most enriched, the phenocrystic hbl (red) as the second most enriched, and the comp (green) and lhz dykes (black) being the most depleted.***

Lamprophyre dykes are usually described as alkaline lithologies (Rock, 1977). The porphyritic hbl dykes however plot as subalkaline, with one sample plotting on the border between alkaline and subalkaline as seen in Figure 4.3.

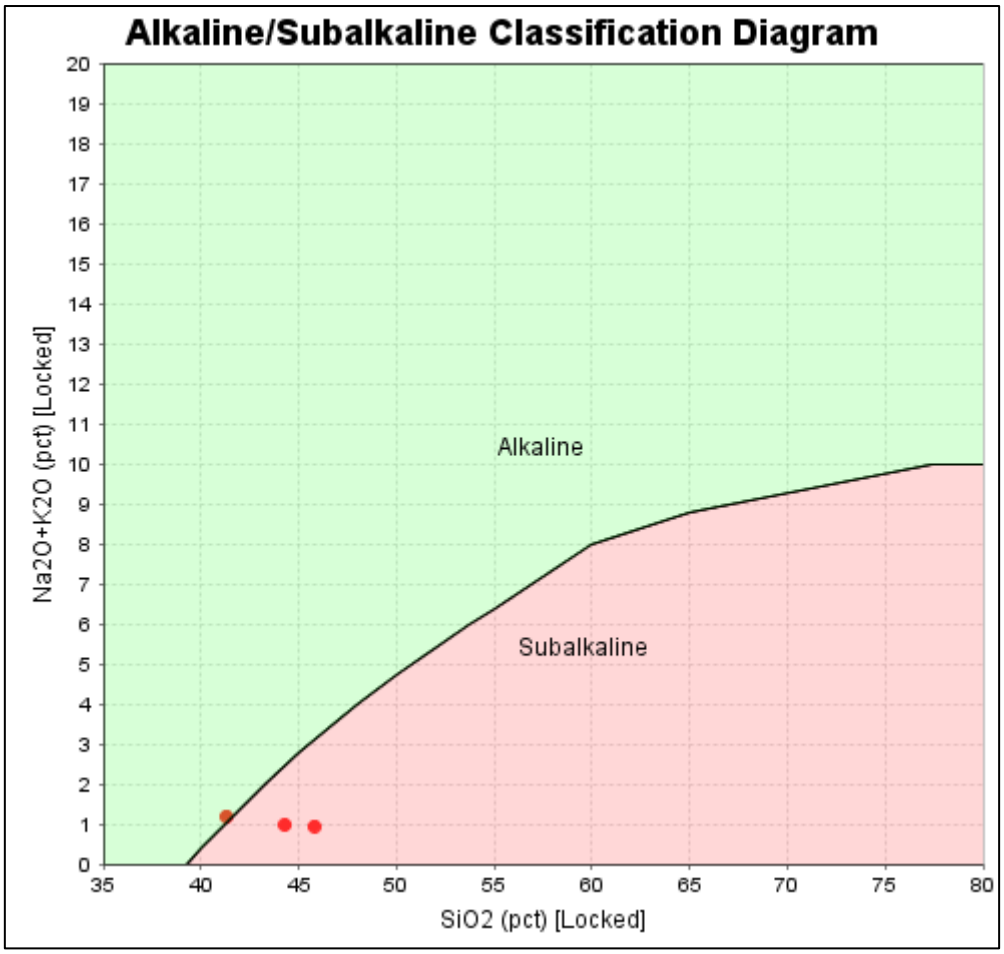

Figure 4.3. ***This alkaline-subalkaline plot is from Irvine and Bargar (1971) where the three phenocrystic hbl samples have been plotted as red dots.***

As the lamprophyres usually represent evolved late pulses of magma, with deep origins they are expected to be enriched in alkali elements as these are often incompatible from the melt source. These trends are however not observed in this setting, which may be due to the relatively close proximity to the melt source compared to other lamprophyre settings. Lamprophyres are not uncommon in felsic intrusions, where they represent a final pulse of magma from the deep chamber. As these dykes are present in a layered ultramafic intrusion, they intrude into a different setting than what is commonly observed.

Gill (2010) describes a lamprophyre as a "porphyritic dyke rock with phenocrysts of solely mafic minerals (usually biotite or amphibole), with feldspars and/or feldspathoids confined to the groundmass". The porphyritic hbl dykes of ULS do not comply with this definition, as the groundmass of the dykes do not contain any feldspathoids, and only one sample contains an accessory amount of plag (0,86%). The SiO_2 content for ultramafic lamprophyres according to Gill (2010) should be <36 wt%, which is lower than the most SiO_2 rich of these dykes.

These dykes seem to fall outside of many models and definitions of lamprophyres, which means the traditional models for lamprophyre formation and emplacement most likely is invalid for this dyke type. Based on the textural and chemical evidence from these dykes, it is believed that the hbl phenocrysts may have nucleated and grown at equilibrium conditions at a stage in the deeper magma chamber where volatile contents were high. The hbl crystals included incompatible elements into their lattice, giving the dyke its characteristic REE curve. As MREE-HREE are compatible in amphibole (Best,

2003) and LREE is incompatible in amphibole, the concave shape of the REE curve indicates that hbl is the main controlling mineral of the REE content of the rock type.

After crystallization of the hbl phenocrysts, the newly formed crystals were transported by a magma pulse, likely from a different part of the chamber because of the dis-equilibrium resorption textures. This magma batch was then transported up through the still hot and ductile-plastic wehrlite of the ULS where they were trapped and crystallized. Getting a temporal relation of this dyke has been difficult as it is only seen cutting a few of the very old pyroxenitic dykes, but has not been observed interacting with the other types described in this thesis. The dyke is however believed to be among the younger dykes based the massive and straight emplacement style, but still older than the hbl gabbronorite.

4.3 Lherzolite dykes and infiltration of plagioclase

Chemistry of the dyke

Based on the chemistry of the ground mass itself and the measured mineral chemistry in this dyke, it seems as if this dyke originated from a primitive pulse of magma. The measured plag is Ca dominated over Na, and the cpx measured has a Di content of ~85% which is relatively Mg rich. It seems from the plots in Figure 3.29 that ol, cpx and plag has the biggest control of the chemistry of theses samples. The dykes, excluding the plag domains are likely to be derived from the same magma chamber as ULS is based on similar REE trends and patterns, and seems to have evolved from the same melt as ULS where cpx and ol has had the main control over fractionation and magma evolution.

Using the same plots from Figure 3.29 it also seems the chemistry is strongly influenced by mixing with the plag domains. This may explain the different trend lines seen in the Ca vs. Mg, and Al vs. Mg plot, where the red stippled lines represent the fractionation trend line controlling the chemistry, and the blue stippled lines represent the mixing contribution from the plag domains. These are two different processes, meaning having two different trend lines is reasonable for the chemistry.

Comparing the REE trends of the lhz and comp dykes to the wehrlites it shows an overall enrichment in REE in the lhz dykes compared to the wehrlites. The trends are similar in all the lithologies. The most enriched lhz sample has a higher hbl content than the most depleted at ~11% compared to ~2,5%. Hbl has been observed to be an important carrier of REE in other dyke types, so the concentrations in these dykes may also be due to the hbl concentration. The lhz dykes show enrichment over dykes with similar Di content, but again, the dyke has a higher hbl content than the wehrlite which most likely causes the enrichment, as the REE curve coincides with the expected concave REE curve of hbl with a peak in the LREE-MREE. (Best, 2003)

These factors indicate that the magma has not come from a particularly enriched or fractionated part of the magma chamber compared to the rocks in ULS, as the contrast in REE enrichments would be expected to be higher when compared to the wehrlites. As the wehrlites are cumulates they are not expected to show strong enrichments in REE, meaning the slightly enriched REE patterns observed in the lhz dykes may be the result of these dykes being trapped, and not had the possibility to fractionate as they crystallized. The lhz dykes and ULS cumulates may therefore have formed from a similar melt. With the main difference being degrees of fractionation, and obviously later infiltrating of plag, which strongly alters the chemistry of the plag rich dykes.

When analysing minerals using EPMA many of the analyses were taken as traverses through grains to check for zonation. Elements which typically indicate zonation like Ca and Na in plag were plotted and showed little to no zonation. A few grains showed what could be interpreted as a Ca rich core with an increase in Na towards the rim, this difference was however only observed in a few grains, and was very subtle when observed. Similarly, Ti, Al, Mg and Fe in cpx were investigated, but showed little to no variation. This indicates that the minerals crystallized under unvarying conditions, as zonation often is an indicator of changing melt chemistry or temperature usually because of a recharge event. (Shcherbakov, Plechov, & Izbekov, 2010)

Emplacement style

The lhz dykes are different from the other types of dykes described from ULS in the sense that they have irregular shapes and contacts, often with conjugate fracture sets and small offshoots. These types

of structures are usually related to more ductile fracture dykes (Weinberg & Regenauer-Lieb, 2010). These conjugate fractures are visible on a cm to metre scale and are even visible on a map scale. These dykes seem to be post-dated by several other dyke typed in ULS, indicating that these dykes are among the earliest dykes formed in ULS.

Ductile fractures which would form these emplacement structures rely on a series of mechanisms which cause microstructural damage. These mechanisms are characterised by crystal plasticity. The first step described by Weinberger and Regenauer-Lieb (2010) is dislocation creep with associated elastic dilation by the dislocation walls. This would create cavities in the wehrlite. As these dislocations accumulate, microstructural dilation starts controlling the process, which depend on anomalies in the lattice of the deforming minerals, shear displacement, or other heterogeneities in the minerals.

Once enough dislocations and dilations have formed this leads to strain localization in shear zones and larger scale dilation than the previous elastic dilation. The larger dilations are caused by microvoid nucleation which grow by creep mechanisms. These voids tend to form in the centre of shear zones, and may over time create more interconnected areas of voids referred to as “void sheets” (Weinberg & Regenauer-Lieb, 2010). Once these void sheets have been established the material between the isolated voids gives in, and void-void connectivity is achieved, which then subsequently can be filled with melt. The voids may however be filled with melt or a hydrous phase prior to void-void connectivity. This would assist in maintaining void dilation.

These ductile fracture mechanisms produce a conjugate structure, and highly irregular tortuous contacts. Often with small mm sized deviates which remerge with the dykes. This is observed in Figure 3.24 b) and to a certain extent in Figure 3.23 d).

Figure 4.4. ***The ductile emplacement textures of the lhz/comp dyke in ULS is shown in this picture. The highly irregular shape of the left composite dyke complies with some of the observations made by Weinberger and Regenauer-Lieb (2010).***

One of the conditions which is required for this type of ductile fracturing to occur is a hot wall rock. In order for these dislocations to move around the mineral via creep, there needs to be sufficient energy in the system in the form of creep. Dislocation creep in ol and px is a high temperature process, ranging

from 800-1050 ^{O}C depending on the pressure and volatile content (Platt, 2015). to This means the wehrlite would still have been hot during intrusion of these dyke types.

This temperature range for dislocation creep in ol and px also complies well with the temperature estimates which were obtained from this dyke type. The intruding magma does not have to be at the same temperature as the rock which it intrudes, but the lack of a chilled margin in these dykes indicate that they were relatively close in temperatures during intrusion.

In Figure 4.4 the comp dyke is seem emplaced in the wehrlite as well as utilizing the path of an earlier emplaced dark but diffuse dyke. These dark dykes are rare in ULS, but can still be seen in some localities. These dykes are more abundant in CS and have been widely described by Orvik et al. (2019). As these dykes represent such a small volume of the dykes in ULS they were not included in the focus of this thesis, but are believed to be the oldest type of dyke as they are diffuse, wehrlitic "ghost dykes" also emplaced via ductile fracturing. These dykes may also have been included in some of the lhz dyke samples, affecting the chemistry and mineralogy to a certain degree.

Infiltration of a plag rich domain

Plag domains and veinlets are only observed on a large scale in this dyke type. Since there are so many dykes on the plateau, and the lhz/comp dyke is the only dyke where this occurs indicates a temporal relationship with the plag veinlets and this dyke type. The plag domains are also seen in the host rock as described in chapter 3.7, but they preferentially seem to follow the path of the lhz dykes.

As described in chapter 3.4, the ground mass of the dykes in the comp dykes seem to chemically and texturally relate to the lhz dykes. Mineralogically there is not much variation between the dykes when excluding the plag. The measured plag in these dykes is exclusively interpreted as a secondary infiltrating phase, and not part of the primary magmatic mineralogy. This assumption is based on the textured found in the plag domains, as the plag appears to mostly form localized bands, sometimes with a SPO, where the long axis of the plag is aligned parallel to the plag veinlet, indicating some sort of flow texture as partially seen in Figure 3.28.

Based on the contact with the surrounding dyke, this infiltration of plag rich material is interpreted to have happened close to the time of emplacement for the dyke itself. The contacts are highly irregular, sometimes following individual grains in the lhz dyke, and a chilled margin is absent. The plag domains seen in Figure 3.26 (top) are very localized, with some plag residing outside of the two main bands of plag rich material. These zones nor the surrounding dyke show any sign of deformation, implying it is not a deformation driven layering, but rather a magmatic separation or division of the phases.

As the magma chamber feeding RUC seems to produce primitive melts (high Mg, low Si), it seems unlikely that these plag rich domains are the result of fractionation processes producing this high Al, Si, Ca melt. Fractionation from this melt would probably not give Ca values as high as the values present in the plag domain, as Ca is highly compatible in cpx (Winter, 2001), which would limit the Ca content if fractionation was the cause of this melt being formed. A Ca content of 12,1 wt% as a result of cpx and ol fractionating out of the melt thus seems unlikely. The chemistry of the veinlets is assumed to closely resemble the actual chemistry of the melt forming the veinlets, as it seems the veinlets are "frozen in place" with little chance to further fractionate during crystallization.

None of the observed plag grains have a euhedral shape, most are sub-anhedral especially in the more diffuse zones. Plag grains in the massive plag zoned show more distinct crystal habits, but still seem to have their shape controlled by the material which they infiltrate into. Plag grains observed in some of

the samples from CS (Orvik, 2019; Grant, et al., 2016; Larsen, et al., 2018) show offitic to sub offitic textures, with large euhedreal plag with twinning. This is not observed in this dyke type, nor any other dyke type in ULS.

Origin of the plag rich domain

Because such an evolved magma forming from fractionation of the magma forming RUC seems unlikely it has been speculated that the melt may have originated from the surrounding Langstrand gabbro. These veinlets have also been recorded by Larsen et al. (2018) as well as Grant et al. (2016), but only mentioned as a feature, rather than discussing its origin. As the veinlets seen in the dykes are assumed to be directly related to the more massive plag veinlet seen in chapter 3.7, it is reasonable to assume they relate form the same source.

Melting of the surrounding Langstrand gabbro in the contact to RUC has been widely recorded (Bennet, 1974; Bennet, Emblin, Robins, & Yeo, 1986; Emblin, 1985; Grant, et al., 2016). Partial melting of a gabbro would create a more felsic, silica rich product than the gabbro it was melted from. The partial melt would be enriched in incompatible elements, especially LREE as these are the least compatible in the mafic system which it was melted from. The curve also follows the expected REE curve for plag, which is expected, as this domain mainly consists of plag.

Partial melting of the gabbro seems more likely to create this intermediate, plag dominated veinlet than fractionation of a high Mg melt which is believed to have formed RUC (Larsen, et al., 2018). The partial melting of the Langstrand gabbronorite is likely to have been so extensive that it may have produced melt volumes high enough to exert a fluid pressure sufficient to infiltrate the adjacent ultramafic rocks. Given this hypothesis and the emplacement textures seen in the dykes they infiltrate, it seems the plag rich veinlets have taken advantage of the already infiltrated lhz dykes.

Once the lhz dykes have intruded into ULS via ductile fracturing, this creates more natural pathways for other melt to infiltrate as it creates a structural weakness plane in the wehrlite. Once this has formed, the plag veinlets followed. It is also important mentioning that the plag veinlets have very different emplacement styles. There is the more diffuse style with interstitial plag grains forming more plag dominated domains in the rock as seen in Figure 3.25 (top), and there is a more monomineralic massive style seen in Figure 3.27. None of the samples nor localities show the exact relationship between the two emplacement styles, but it is believed that the diffuse domains are precursors to the more massive domains.

In some samples, like in the mineralized wehrlite sample, JS_2_19-C seen in Figure 3.56 and Figure 3.57, the plag zone is enveloped by a reaction rim of hbl. Because hbl is a hydrous mineral a hydrous phase would have to be present. The zones also have a dol phase present, which vary from μm sized inclusions in some grains, and up to sub mm sized interstitial grains. These two factors show that the melts have a carbonate and volatile component to them. Kono, et al. (2014) has recorded viscosities in carbonate rich magmas of as low as 2 – 3 magnitudes lower than for basatic melts in the upper mantle making the mobility of these melts 2 – 3 orders of magnitude higher than for basaltic melts. The carbonate content in these veinlets is not particularily high (~10 vol% at the most observed in thin section), but the carbonate content would still make a significant contribution on the mobility of these melts.

As the carbonate melts are extremely mobile comared to other melts at these pressures (Wickham, 1987; Rushmer, 1996; Kono, et al., 2014), it should also be concidered that some of the carbonates

have migrated from the carbonate veinlets through fractional pressing. When the plag starts crystallizing, some carbonate grains have been trapped as inclusions, but carbonate rich melt may have been fractionated out by Rayleigh fractionation (Best, 2003), escaping further up and away from the samples we have preserved. For such a carbonate rich plag melt with a hydrous component, the dihedral angle is also expected to be low, and the mobility high, allowing for easier migration than a silisic melt with low volatile and carbonate content.

The temporal relationship between the plag veinlets and the dykes correlate well with the understanding of the partial melting of the gabbro, combined with ductile behaviour in the wehrlite. If this dyke type showed typical brittle emplacement structures, it would be difficult explaining the origin of the plag domains via partial melting of the surrounding gabbro. The ductile emplacement in the wehrlite indicates a still hot and newly crystallized ULS with lots of residual heat left, which would be capable of both melting the gabbro, and keeping the gabbro partially molten in the marginal zone for a long period of time.

Thermobarometric measurement

To obtain a robust thermobarometric measurement from the intrusion a plagioclase-amphibole thermobarometer was used. This had to be used in one of the dykes with both abundant hbl and plag. As the wehrlite does not have any plag in its primary magmatic assemblage, the analysis had to be performed on a plag bearing dyke. The goal of the thermobarometric measurement was to get an emplacement depth and temperature for the ultramafic cumulates, in order to obtain a measurement as close to the emplacement conditions as possible one of the youngest plag bearing dyke types were selected.

Retrospectively, if the theory of the plag in these dykes being a secondary phase the thermobarometric estimate would be an estimate for the infiltrating of the plag, rather than the emplacement of the dyke. However, as previously discussed, the plag infiltration is believed to have happened shortly after the emplacement of the lhz dykes themselves, making the measurement usable with caution. The grains analysed were checked for zonation to ensure the grains were equilibrized with the neighbouring mineral. The plag and hbl did not show significant zonation from core to rim, and the rim analyses were unvarying for the two mineral phases.

Ridolfi et al. (2009) was used to obtain a temperature estimate for the analysed hbl to later use in the Molina et al. (2015) spreadheet. Ridolfi et al. (2009) uses the aluminum nubers expressed as Al#=($^{[6]}$Al/ Al_T) ≤ 0,21. The calcic amphiboles used in this paper are sampled from basaltic to rhyolitic volcanic products, where the amphiboles varied between tschermakitic paragasite, magnesiohastingsite, and magnesiohornblende. Some of the measured amphiboles in this paper had Al# ≥ 0,21 and were classified as xenoliths. These amphiboles were assumed to be xenolithic amphibole with a crustal or mantle origin.

The amphiboles form JS_2_8 were all classified as xenolithic amphibbole by the Ridolfi et al. (2009) spread sheat, meaning the Al# was too high. Due to the high Al# thermobarometric measurements are less reliable, as this thermobarometer is not calibrated for this. Therfore, a pressure estimate from Molina et al. (2015) was not obtained using the input temperature for these analyses. The analyses form JS07 however, provided better results, although with a relatively large spread in pressure ranges.

With a calculated pressure from the plag and amph pairs from JS07 of 9,42 ± 0,87 kbar, and a temperature of 1037 ± 22 ^{O}C, this equates to an estimated depth of ~32,5 km, with an assumed average

overburden density of 2,9 g/cm^3. This is a rough density estimate partially based on the findings of Pastore et al. (2016). The total thickness of overlaying ultramafic and gabbroic rocks is unknown. If the overburden was only comprised of crustal material and metasediments of lower densities based on the measured values from Pastore et al. (2016) the emplacement depth would then be ~34,1 km. The eplacement depth of ULS is within the estimated range of what was estimated by Larsen et al. (2016), which corresponds to lower continental crust depth.

Based on the calculations, this gives a shallower emplacement depth compared to the previous thermobarometric measurements from Orvik et al. (2019) at 12-14 kbar, but similar temperatures to the measurements from ULS at 1006-1046 ^{O}C. As CS clearly cuts ULS based on field observations, it seems unreasonable that the emplacement depth of ULS is lower than the emplacement depth of CS. Using the same density as was used for ULS, CS has an emplacemen depth of 43,6-50,1 km. This would mean the intrusion sank 10-20 km further down into the mantle post intrusion of ULS. This seems unlikely. Either the depth estimate from CS is too deep, or the depth estimate from ULS is too shallow, as these two depths do not realistically coincide.

As mentioned, the pressure estimate is obtained from analysing a plag-amph pair from one of the later infiltrated plag domains in the lhz. As the lhz dykes themselves show ductile emplacement mechanisms, and the infiltrating plag domains also show ductile emplacement mechanisms, it is assumed that these both intruded through the wehrlite close to the emplacement depth, or at least closer to the crystallizing temperature of the wehrlite. The cooling rate, which is related to the uplift rate of the intrusion is believed to have been slow, meaming the cooling rate of RUC has been slow. Asuming the intrusion has not had an extremely rapid uplift rate, these dykes are believed to closely represent the intrusion depth of ULS, and do at least represent a minimum intrusive depth of ULS.

Ore forming potential

The ore forming potential of these zones is yet to be described in detail in literature, apart from a mention by Grant et al. (2016). This may be due to their unsystematic occurrence, and because they do not form large mineralized zones. Their presence is marked by a few mm sized sulphide grains surrounding the zones. The zone itself as seen in Figure 3.56, and Figure 3.57 b) and e) show a granophyric like texture, which seems to correlate with the infiltration of the plag rich zone. There is no observed sulphide mineralization in the plag rich domain itself, it only seems to reside in the wehrlite.

Along with CO_2, H_2O and halogens, sulphur is considered a volatile. Based on previous observations like the presence of amphibole reaction rims attesting to a H_2O component, and the presence of carbonates attesting to a potential CO_2 component, it also seems these plag rich domains carry a sulphur component based on the reaction rim of sulphide minerals. The halogen presence cannot be commented on as mineral analyses of Cl and F are well below detection limits.

Since some of the most important economic minerals are sulphides, a lot of attention has been turned towards understanding the behaviour of sulphides in magmatic systems. Naldrett (2004) has discussed different mechanisms of how to form an ore deposit. These vary from mixing magmas, changing partial pressures of oxygen and sulphur, to changes in temperature, and much more. In order to understand how the pyh, pn and ccp in JS_2_19-C has formed, the relationship between the plag domain and the wehrlite needs to be studied.

One hypothesis for formation of these sulphide minerals is a process of which the plag domain has started crystallizing and through fractionation the incompatible Cu, Ni, Fe and S has been left in the residual melt, forming the sulphide grains. This does however seem unlikely, as the volume of sulphides is quite substantial compared to the total volume of plag domain in this sample. Other incompatible elements would however, also be expected to be seen in this zone if this was the case. Based on the EDS maps this is not the case. This process would also mean the sulphide phase is in disequilibrium with the mineralogy of the wehrlite.

During the formation of the hbl, a re-equilibrium reaction is believed to have occurred. When the plag domain infiltrated, the hydrous component may have facilitated in lowering solidus temperatures, allowing for effective recrystallization of the surrounding silicate minerals (Best, 2003). A similar process may have happened to the sulphides. Under saturation conditions mafic melts can dissolve more S than felsic melts (Moune, Holtz, & Botcharnikov, 2008). When saturation is reached, liquid immiscibility can occur where a liquid S-Fe phase separates form the silicate melt forming a separate, immiscible liquid. (Naldrett, 2004; Robb, 2005)

The interaction between the silicate melt represented by the plag domain, and the wehrlite could have caused the sulphide from the silicate melt to become an immiscible liquid in combination with the wehrlite. This immiscible liquid would then assimilate most of the chalcophile element available, like the Cu, Fe and Ni naturally residing in the wehrlite and trigger a formation of sulphide minerals. The granophyric texture of the sulphides seen in Figure 3.57 and Figure 3.58 indicates there has most likely been a melt + solid phase, and not simply a sub solidus reaction. The liquid immiscibility theory does include a liquid phase which could form the granophyric like textures. These textures may be the cause of complete melting and rapid crystallization (Barnes et al., 2018).

The largest layered intrusion in the world is the Bushveld Intrusion. This intrusion is known for its immense chromite layers, which is recognised as a world class ore. (Barnes & Campbell, 1988; Cawthorn & Boerst, 2005; Naldrett et al., 1986). The leading theory for formation of the chromite layers in this intrusion is based on the Irvine Model, created by Irvine (1977). The idea of this model involves shifting from cotectic crystallization between ol and chromite, to only crystallizing chromite due to a shift in melt chemistry by assimilation of a more silicate rich phase.

Chromite is a very different mineral from the mineral assemblage seen in the mineralized zones of JS_2_19-C, as it contains different elements, and is an oxide mineral rather than a sulphide. This does put a constraint on the Irvine Model being an explanation for this, as chromite is obviously not the mineralizing phase here. The theory is however that a similar process could occur here. Silicate rich melts, which the plag domain represents could potentially cause a volatile induced melting of parts of the surrounding rock like a peritectic reaction in the sulphide stability field. Similar to the liquid immiscibility theory this theory involves a melt + solid phase capable of producing the granophyric like textures.

The textures of these sulphide minerals are unlike the main sulphide textures found in ULS, as the normal sulphide textures are interstitial grains of pyh-ccp-pn exsolved in grains together. Similar textures to the granophyric like textures have been described by Barnes et al. (2018) from the Eagle deposit in Michigan. The textures here have formed from a massive sulphide melt intruding into an organic rich black shale. The system is therefore very different from what is observed in ULS, but the process of forming these textures may be similar, and therefore be an indicator of how the sulphide minerals formed in ULS.

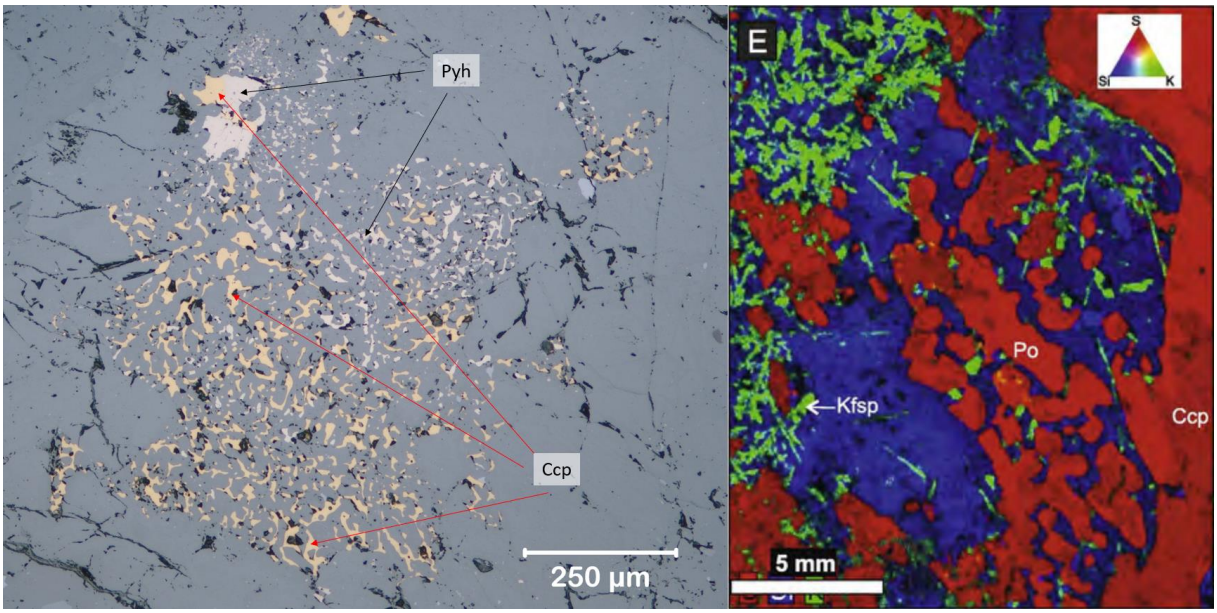

Figure 4.5. ***This figure shows a picture of the granophyric like texture of sulphides from ULS to the left and an EDS map of Si (blue), S (red), and K (green) from the Eagle deposit in Michigan from Barnes et al. (2018). The mineral labelled Po in the right image is pyrrhotite.***

Texturally the pyh from the Eagle deposit resembles some of the ccp and pyh seen in ULS. These are classified as emulsion textures by Barnes et al. (2018). The sulphide melts have intruded into the silicates as a sulphide melt and has crystallized as sulphide minerals. If the same process has occurred in ULS this indicates there has been a total separation of an immiscible sulphide melt as a result of interactions between the plag rich domain and the wehrlite. The sulphide melt has most likely separated from the plag domain in that case, possibly due to fractional crystallization and interaction with the wehrlite.

One of the reason for the intricate mix of different sulphide minerals is because the pyh-ccp-pn mineralization tend to exsolve form a monosulphide solid solution (MSS) (Naldrett, 2004). These form from a single sulphide rich melt, and as the systems cool, and elements are being arranged into a crystal lattice. Some of the minerals cannot mix, and therefore form exsolutions of a Cu rich (ccp), Ni rich (pn) and Fe rich (pyh) sulphide phase.

Separation of an immiscible sulphide melt would have to be further investigated in order to get more robust evidence for. It is likely that the plag domain is carrying higher values of incompatible elements and volatiles as it is believed to originate from large scale partial melting of the Langstrand Gabbro. During the partial melting the incompatible elements would preferentially partition into the melt phase, therefore increasing the incompatible element concentration of the melt, and leaving the solid residue depleted. S and H_2O are incompatible volatiles, and Cu and Ni are incompatible metals (Winter, 2001). Ni is however sensitive to the ol amount in the gabbro, as Ni has higher compatibility in ol.

Since the ore forming potential has not been observed in the dykes it is believed that the ore formed in JS_2_19-C is related to the wedge shape of the plag domain. As seen in Figure 3.56, the mineralization is most concentrated at the tip of the wedge, where the rock/melt ratio would be at its highest. The large mm sized sulphide grain in combination with the emulsion texture behind is believed to be the result of sulphide melt pooling at the tip of the fracture. The dykes themselves rarely show these types of arrest of melt, as they appear to be low channels. This may have inhibited the pooling an accumulation of such immiscible sulphide melts.

The current understanding of ore forming processes in RUC as studied by has been described by several authors (Anker-Rasch 2013; Grant, et al., 2016; Larsen, et al., 2018; Voll, 2019) mostly rely on fracionation models and reef fromation. The previous model is based on the upwards fractionation of magma, until a critical saturation of sulphide is reached, and an immiscible sulphide liquid is formed, which pools on the cumulate floor. The ore forming processes described in the samples from ULS, from the emuslsion textures therefore offers a new ore forming mechanism in RUC. It does not replace the old model, but rather provides a new and different alternative to the ore forming processes.

4.4 Hornblende gabbronorite and associated deformation

Dyke chemistry

Chemically this dyke distinguishes itself from the other dyke types in a few ways. It is a dyke type enriched in typical incompatible elements like Th, U, Pb, Zr and Ti compared to the other dykes, and is the only dyke type with a close to linear negative slope from LREE to HREE. All other dykes have a concave shape with a peak between LREE and MREE and are relatively depleted in incompatible elements. This dyke is also significantly enriched in P compared to the other dykes, which is a common incompatible element. Based on chemical plots of major elements however it is not drastically different from other dyke types. This enrichment can be seen in Figure 4.2 and Figure 4.6.

This dyke type is also the most fractionated and evolved dyke based on the Mg/(Mg+Fe) values. These values are commonly used in mafic and ultramafic rocks, as Mg rich rocks are often more primitive and less evolved than iron rich rocks. This is largely attributed to the difference in melting points in the forsterite-fayalite solid solution as the Mg rich end member, (forsterite) has a higher melting point than the Fe rich end member (fayalite). (Winter, 2001)

Rock type	Avg Mg/(Mg+Fe)
Hbl gabbro	0,46
Lherzolite	0,66
Phenocrystic hbl	0,58
Px comp	0,63
Px dyke	0,66
Wehrlites	0,68

Table 4.1. ***This table shows the calculated Mg/(Mg+Fe) for the major dyke types in ULS.***

Based on the results in Table 4.1 the hbl gabbro is the rock type in ULS with the lowest Mg/(Mg+Fe) ratio at 0,46. The other dyke types are from the 0,58-0,66, with the wehrlites being the highest at 0,68. This indicates that the melt forming the hbl gabbronorite is more Fe rich, and more depleted in Mg compared to the melt which formed the other dyke types, meaning this is a more evolved melt that has undergone more fractionation and evolution. These fractionation processes usually involve pulling compatible elements from the melt into solid cumulates, making the restite enriched in incompatible elements.

As this dyke is more fractionated than the other dykes it is assumed that this dyke represents a late pulse of magma from the underlying magma chamber, making it one of the youngest dyke types of ULS. This is also confirmed by cross cutting relationships as no dykes are observed cutting this dyke type. The second most fractionated dyke using this fractionation parameter is the phenocrystic hbl dyke. These dykes have similar emplacement structures, being more massive than the lhz and comp dykes, also showing straighter, more consistent intrusive paths. These two dykes are yet to be observed cutting each other, but the phenocrystic hbl dyke is believed to be slightly older than the hbl gabbro based on slightly more primitive signature.

Another important aspect of this dyke is the extremely high volatile content in the form of H_2O. Some of the dykes of this type have up to ~42% hbl seen in Table 3.17, indicating that the melt forming these dykes must have had a high water content. According to Deer, Howie, and Zussman (1997) paragasites of similar emplacement temperatures may have water contents around 1,5 % as a conservative estimate. Using this water content in combination with 42% hbl, the melt forming the dykes a water

content of minimum 0,6 wt%. As water is a highly incompatible volatile phase it is likely that most of the water escaped during crystallization, as it is mobile and incompatible.

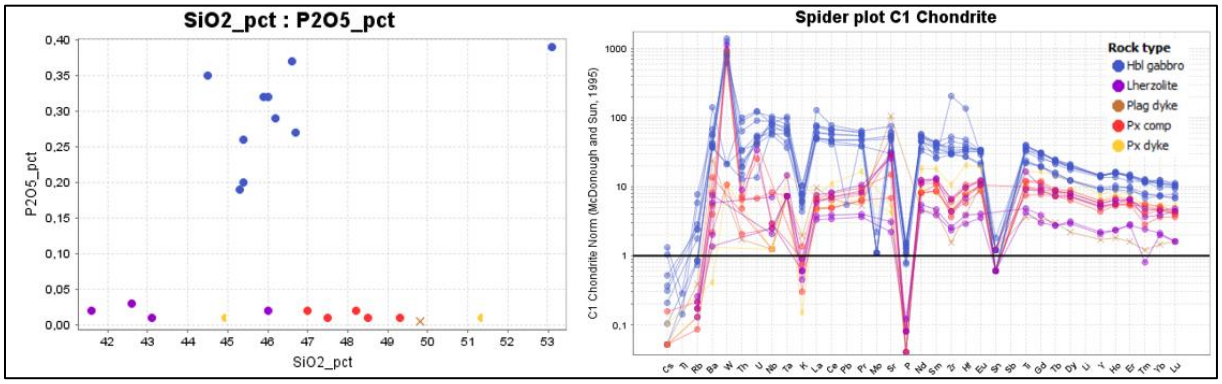

Figure 4.6. ***The left plot shows the P_2O_5 content of the different dyke types plotted against SiO_2. The hbl gabbro is plotted in blue. The right plot shows a spider diagram of the different dykes types normalised to a chondrite.*** *(Sun & McDonough, 1989)*

The hbl gabbronorite is also the dyke most enriched in P, as seen in Figure 4.6. In this dyke type small grains of apatite have been observed, which is most likely to be the source for the high P_2O_5 content found in these dykes. Apatite is a known carrier of REE as apatite as it can incorporate REE into its crystal lattice (Hughes, 2015; Broom-Fendley et al., 2017). This means the high concentration of LREE may be attributed to the apatite content of these dykes. This dyke is significantly enriched in LREE compared to the other dykes with the LREE La concentrations of these dykes being 5-10 times higher than the second most enriched dyke.

Steep, negative REE curves are often associated with evolved magmas (Yoder, 1976; Best, 2003; Gill, 2010) as these elements are incompatible in most minerals. This incompatibility makes the restite more enriched in REE, making more evolved magmas more enriched. The shape of this curve compared to other dyke types may also be a function of the way which these dykes crystallized. The concave shape of the more depleted dykes are sometimes associated with cumulate processes, as the minerals incorporating the LREE are not in the cumulus phase and therefore leave the system. This then makes the linear, negative sloped curves implicitly richer in the restite minerals.

When viewing the plot in Figure 3.44, the dyke labelled “Most deformed” is the most enriched sample from this dyke type. This is also the dyke with the highest P_2O_5 content of these samples. Inversely, the most depleted sample with respect to LREE is JS14 and JS_2_22 labeled “Core” as these samples are taken from the undeformed core of the dyke. These two samples have the lowes P_2O_5 content of the dykes. These observations may indicate that the small apatite content found in these samples are responsible for a quite significant increase in REE compared to the other dykes.

Deformation controlled chemical change related to pseudotachylytes

From the dataset it appears deformation has a slight correlation with P_2O_5 content. If apatite is the main carrier of REE in these dykes it seems unlikely that it would mobilize according to deformation in the rock. Another theory which could explain the increase in REE as a function of deformation is the formation of pseudotachylytes. If the deformation was strong and rapid enough to cause local melting of the rock through frictional heating this could cause melt mobilization of enriched melts to cause the change in REE patterns. These veins of frictional melt throughout the dykes are observed as

pseudotachylytes in some samples. These bands are dark, mainly due to high iml contents, but also contain silicate phases as seen in Figure 3.45.

There has not been any observed apatite grains in these pseudotachylytes, but based on EMPA analyses of grains it seems these grains show a different major element chemistry compared to what are assumed to be their parental grains. These pseudotachylytes were planned to be analysed using LA-ICP-MS at NGU to obtain REE patternt for cpx to compare to host grains in the dykes. Unfortunately, this was not possible due to the closure of NGU in march. Instead of using REE patterns, other elements which fractionate will be observed instead.

Most of the incompatible elements are trace elements in these minerals. The concentrations of these elements are too low, meaning they are below the detection limit of the EPMA. Using detectable elements like K and Na however may give some indication of change. These are both LILE, and would be more likely to partition into the melt phase than elements like Ca or Mg. These observations are based on a few analyses of minerals in the pseudotachylyte, and are therefore a qualitative description rather than a quantitative measurement of changes from dyke to pseudotachylyte.

The analysed plag from the tachylyte shows a sligtly lower An% at 45 compared to the primary magmatic plag at 49 An%. This means the recrystallized plag is more albite rich than the primary magmatic plag in this dyke. In the plag solid solution, the Na component Ab has a lower melting point than the Ca end member An, meaning melting must have happened in the pseudotachylyte. Similarly, the pyroxene analyses show a slight increase in elements like Na and Al in the pseudotachylyte compared to the parental grains.

The pseudotachylytes are more abundant close to the contact of between the wall rock and dyke. The pseudotachylytes are assumed to represent a very small volume of melt, making it extremely enriched in very incompatible elements. These pseudotachylytes can be seen in Figure 3.36, Figure 3.38 and Figure 3.39 as dark bands in the rock. The pseudotachylytes are believed to originate from the hbl and plag dominated shear zones. This relationship is observed in Figure 3.38 where a sinestral hbl plag shear zone seems to be temporally related to the pseudotachylyte.

Based on the kinetics obverved in the shear zone, the path of the pseudotachylyte is interpreted as a Riedle shear-like tensile fracture. The pseudotachylyte alligns parallel to the interpreted σ_1, and the volume expansion and associated fluid pressure related to the volume expansion seems to have induced a tensile fracture allowing for the pseudotachylyte to migrate further from the shear zone into the dyke. The concentration of REE enriched pseudotachylytes would therefore be more concentrated futher towards the contact, and less concetrated towards the core of the dyke. This could explain the increase in REE as a function of deformation. P would behave as a strongly incompatible element in these systems, which would corrolate with the other REE.

Due to the fine grain size of this dyke, the negative REE curve, and the abundance of hydrous minerals it is believed that this dyke represents an evolved pulse of magma, migrating through a cooling ULS, which was trapped, forcing the stagnant magma to crystallize with the chemistry of the magma mostly intact. Texturally the dyke does not appear to be quenched, but is is more fine grained than other dykes on the plateau, indicating a higher contrast in temperature between the wehrlite and dyke.

Deformation and other textures in the hbl gabbronorite

As seen in the field chapter in chapter 3.5 this dyke is the most deformed dyke in ULS. Compared to the lhz dykes which have more irregular orientations of emplacement this dyke does not vary in

emplacement orientation. The dyke can also be seen dragged out and smeared in some localities like the dyke seen in Figure 3.34 a). This dyke shows what appears to be sigmoidal clasts of remnant dyke enveloped by the yellow shear material. The dyke which is assumed to have an original width of ~20 cm based on other dykes of this type has been reduces to a width of only a few cm.

Similar deformation textures are shown in Figure 3.34 b) and c). In figure c) small "fingers" protrude from the dyke into the surrounding yellow shear material. These fingers are believed to be related to both emplacement of the dyke. The highly irregular, almost discontinuous shape of the dyke in figure b) is interpreted to both be emplacement related as well as being later deformed by tectonic forces. Studies done on asymmetrical fabrics related to dyke emplacement may be the explanation to some of the fabrics observed in the hbl gabbronorite.

Correa-Gomes et al. (2001) has described the emplacement structures in dykes with respect to magma flow velocities in combination with wall rock displacement velocities. One of the textures described by Correa-Gomes et al. (2001) is a branching texture related to flow orientation. These branches protrude from the main dyke parallel to the direction of flow in the dyke, and can in some cases indicate direction of magma flow. Based on this interpretation, the magma in this dyke has had a SSW→NNE component of flow. This is however only based on a few observations, and may be an artifact of later deformation. The flow direction is assumed to have a primarily vertical flow direction, with a horizontal contribution as well. This is based on observations where the dyke outcrops in vertical faces like in Figure 3.33 where similar branching structures and asymmetrical fabric is seen on the left side of the dyke.

In Figure 3.32 the dyke is seen offsetting older dyke generations in a dextral sense of movement. This dextral sense complies with the branches observed in Figure 3.34. The offset of surrounding dykes is common during dyke emplacement, as the melt moving through the rock creates a structurally weak discontinuity in the rock during emplacement, capable of absorbing stress and facilitating movement. Like the dykes in the article by Correa-Gomez et al. (2001) there has been wall rock displacement simultaneously as there has been magma flow in this type of dyke found in ULS. This combination of wall rock displacement and magma flow is capable of creating the asymmetrical structures seen in Figure 3.32 and Figure 3.34.

In combination with deformation structures and textures related to the emplacement of the dyke, there is also evidence for post-emplacement deformation of these dykes in the form of deformation fabrics, localized mylonites and foliations observed in thin section. This dyke compared to other dykes on the plateau shows significant deformation related fabric. The minerals deformed are primarily hbl and plag, with some cpx as well. The plag shows core mantle structures with subgrains having a grain size around 14,5 µm. The boundary between core and mantle is diffuse. Some plag grains are completely recrystallized to subgrains, while preserving a shape resembling the original plag grain. This type of subgrain rotation and core mantle structure is commonly observed in deformation around 650-750 ^{O}C in plagioclase. (Vidal et al., 1980; Passchier & Trouw, 2005)

Similar textures are observed in hbl in this rock. Old grains are mostly recrystallized into new grains and subgrains of a grain size between 7-10 µm seen in Figure 3.37 e). As this type of deformation is a plastic deformation mechanism, it is assumed to have occurred around 700 -750 ^{Ó}C (Passchier & Trouw, 2005). Due to a lack of EBSD data from these deformed dykes, obtaining an overview of which slip planes were active in hbl during the deformation is yet to be done. This would have provided information about strain rate and temperatures of deformation, as hbl has several active slip planes across a wide range of strain rates and temperatures.

As seen in Figure 3.36 and Figure 3.37, the areas of recrystallized plag and areas of recrystallized hbl form an interconnected layering, giving the rock its foliation. Some foliation layers are rich in plag, while others are richer in hbl indicating that the two minerals may take up strain in different ways. For the most recrystallized samples, the pseudomorphs of large plag grains and hbl grains seen in ppl are mostly to completely made up of dynamically recrystallized subgrains and new grains, with some grains showing small folds and fish structures indicating shear.

Pseudotachylytes are a common feature observed in these dykes. They appear as dark "veins" cutting through the samples in a way which makes them seem like they fractured their way into the rock. The pseudotachylytes consist of a very fine grained anhedreal aggregate of plag, hbl, cpx, opx and ilm. An EDS image from the core of the pseudotachylyte can be seen in Figure 3.45 a), the grain size observed here is ~5 µm, with some larger grains of assimilated wall rock. Chemically, as previously described seems to be enriched in incompatible elements compared to the surrounding dyke, due to low degrees of melting.

According to Passchier and Trouw (2005) psudotachylytes usually form in massive, dry rocks like gabbros. They are associated with extremlely high strain rates (0,01-1 m/s), often in combination with cataclastic deformation. As a fault slips it may generate sufficient heat to melt the rocks. Studies have indicated that the pseudotachylytes usually from from fine grained cataclastic material, rather than from intact wall rock (Swanson, 1992; Spray, 1995; Ray, 1999). Some of the deformation in these dykes show ductile behaviour, but as Sørensen et al. (2019) have discovered, high strain rates and earth quake nucleation has been identified in Reinfjord.

Formation of pseudotachylytes have been linked to large scale geological processel like superfaults, large landslides and caldera collapses (Legros, Cantagrel, & Devouard, 2000; Spray, 1997). The normal movement in these dykes have alreadt been related to the decline in magmatic activity beneath the intrusion. The pseudotachylytes are therefore also believed to relate to the collapse of the intrusion as a result of termination of magmatic upwelling beneath the ultramafic complex. The intrusion is also significanlty more dense than the surrounding metasediments according to Pastore et al. (2016). This would furter assist in the sinking and downward settling of the ultramafic complex.

The pseudotahylytes are evidence for rapid slip having occurred in these dykes in ULS. Despite the temperatures being high enough for ductile mechanisms to controll the deformation in these dykes, sufficient differential stress and strain rate would be capable of brittle fractures and sliding to occur. Sample JS-12 shown in Figure 3.38 has an injection vein of pseudotachylyte cutting through the sample. This pseudptachylyte seems to originate from the hbl rich shear zone on the left side of the thin section. The frictional heat of the rapid slip is then believed to have initiated local melting of the gabbro, creating an injection vein of pseudotachylyte. Passchier and Trouw mention that pseudotachylytes often morph into mylonites after their formation.

The pseudotachylytes seem to have a relationship with some of the mylonites based on the interaction between pseudotachylyte and shear zones. In sample JS15-A seen in Figure 3.36 the dark bands are interpreted to be pseudotachylytes, but they also appear to have been mylonitized, as there seems to be dragging along these dark bands and some wall rock fragments show sigmoidal clast structures. Since the undeformed pseudotachylytes already have a grain size around 5 µm these zones are most likely weaker than less deformed zones, as the activation energy of grain boundary slip is lower than the activation energy of large intracrystalline plastic deformation (Passchier & Trouw, 2005). This allows for strain localization in these already fine grained pseudotachylytes.

When orienting the samples from the locality in Figure 3.33 it shows that there has been steep normal movement in this locality. This normal movement is similar to the movement observed in the article

from ULS by Sørensen et al. (2019). The movement here is believed to relate to the end of magmatic activity, and the settling on the intrusion into the crust. As the upwards pluming of the chamber reached its end it is believed that an extensional tectonic environment controlled deformation in RUC. This has been documented by several authors working with the intrusion, as the layering of the surrounding Langstrand gabbro is dragged down along the contact to the ultramafic body. (Bennet, 1974; Bennet, Emblin, Robins, & Yeo, 1986; Larsen, et al., 2018)

The mineralogy of the dykes of the hbl gabbronorite is also believed to represent a weakness plane in the intrusion, as plag and amphibole at high temperatures are easily deformed compared to the px and ol rich dykes. The hbl gabbronorite is also a more massive dyke than dykes like the lhz and comp dykes, making them a larger, and possibly more suitable zone to accommodate strain.

Formation of the enveloping yellow shear zones

The formation of the enveloping yellow shear zones is observed to have a strong relationship with both deformation and the hbl gabbronorite. The yellow shear zones are seen offsetting primary magmatic structures, early dykes and late dykes. Based on the cross cutting relationships these shear zones seem to be later than the majority of the magmatic activity, and temporally relate to the hbl gabbronorite, as these two lithologies are often found together. The shear zones are as described found isolated without the presence of a hbl gabbronorite dyke, but as discussed in Sørensen et al. (2019) are related to tectonic slip, and degassing of CO_2, shown by the stabilization of dolomite.

Three main theories have been presented as possible formations of the yellow shear zone envelopes around the hbl gabbronorite.

- Wehrlitic melting induced by heat transfer from hbl gabbronorite emplacement
- Picritic melt movement along hbl gabbronorite
- Fractionation of water and CO_2 out of hbl gabbronorite lowering wehrlite melting point and assisting in deformation

The following hypotheses will be presented in order.

1. *Wehrlitic melting induced by heat transfer form hbl gabbronorite emplacement*

One hypothesis of formation of these yellow shear zones was a partial melting of the surrounding wehrlite via heat transfer from the gabbro to the wehrlite. As the yellow shear zones closely envelope this dyke type, they are assumed to have a genetic relationship. The fine grain size and gradual transition from shear zone to wehrlite were interpreted to be a result of the temperature gradient from the dyke to the wehrlite. The shear zone also has a slight enrichment in LREE compared to other dunitic samples of similar mineralogy based on XRD results. Such a chemical signature could be obtained via local partial melting.

This theory does however not seem likely. Melt temperatures for gabbros are significantly lower than melt temperatures for ultramafic rocks, as Fe-Mg silicates like ol and px melt at higher temperatures than more aluminous silicates such as plag and hydrous silicates like amphiboles. Considering the width of the yellow shear zones it also seems unreasonable that a 15 cm wide dyke would be able to generate a 20 cm wide zone of completely melted wehrlite like the zone seen in Figure 3.34. The difference in melting temperatures combined with the width of the enveloping shear zone does not seem reasonable.

The fine grain size was a proposed result of melting and quenching of the surrounding zone. This hypothesis assumes complete melting of the wehrlite, as the grain size is uniform and extremely fine grained at ~5 µm. The fine grain size also attests to the quenching of this melt since lower crystallization rates would result in a coarser grain size. The temperature gradients from the dyke also seem unlikely in this explanation, as a dyke with an emplacement temperature of ~1000 ^{O}C would not be capable of substantial melting of a wehrlite with a melting temperature ~1300 ^{O}C, only to be rapidly quenched by a still hot wehrlite.

A positive LREE anomaly was also observed in the shear zone sample. This was believed to relate to partial melting and enrichment in the most incompatible elements. Texturally however, small domains of gabbroic melt are seen in the shear zone in Figure 3.50. This small contribution of gabbro is likely the cause of the enrichment in LREE as the hbl gabbronorite is the most LREE enriched dyke type in ULS.

The theory of partial melting of the wehrlite via heat transfer from the emplacement of the hbl gabbronorite does not seem to be the explanation for the enveloping shear zone, as there are too many contradictions with this theory.

2. *Picritic melt migrating along hbl gabbronorite*

Another melt related theory is based on picritic melt moving along the opening of this dyke. Larsen et al. (2018) have estimated the melt forming RUC to be a high Mg melt, called a picritic melt. The melt is using the same pathway as the dyke and is being quenched in place. This theory relies on a late batch of fertile melt derived from the same or at least a similar magma chamber to the melt forming the wehrlites. This theory can explain the temporal relationship between the dyke and the shear zone. This theory is tied to the shear zone having similar chemistry to the dunites and wehrlites of ULS, and may therefore have been formed from the same melt.

The main issue with this theory is the fact that there is a contradiction between melt type and grain size. To obtain this grain size in such a rock, it is believed to have been quenched. If this was the case, that a picritic melt was quenched, the rock should have lower Mg content, and a different Mg# than the surrounding wehrlite. This zone has an Mg# = 0,70 compared to an average in the wehrlites of Mg# = 0,68, with a minimum of 0,64 and a maximum of 0,72. The Mg# of the shear zone therefore falls within the range of the wehrlites, indicating that it is the same as the wehrlites. These factors therefore point towards picritic melt migration being unlikely.

3. *Fractionation of water and CO_2 out of hbl gabbronorite lowering wehrlite melting point and assisting in deformation*

Another theory which may explain the genetic relationship between the hbl gabbronorite dyke and the shear zone is a fractionation of water from the hbl gabbronorite, causing a reaction with the wall rock. The dyke is believed to have had a relatively high water content compared to the other dykes found in ULS based on the abundance of hbl in the dykes. As the dyke crystallized, water is believed to have fractionated out of the dyke, creating a volatile rich, highly mobile, low viscosity melt, which may have interacted with the surrounding wehrlite.

These shear zones have been described by Sørensen et al. (2019) to contain enstatite and dolomite from the reaction 2 Ol + Cpx + 2 CO_2 = Dol + 2 Opx. A similar process is observed in these shear zones, as the zone contains 0,15% dol, seen from XRD. The grain size is too fine to determine mineralogy optically, so the XRD results are used to estimate mineralogy. The shear zone is also abnormally rich in hbl at 3,05% compared to the surrounding wehrlite which is often found lacking hbl. This indicates the presence of a hydrous component.

The presence of both dol and hbl at levels above the levels observed in the wehrlites indicate a CO_2 phase and a hydrous phase must have been present during the formation of these zones. The origin of these two components is likely to be from the hbl gabbronorite as these zones follow the dyke closely. As these components have fractionated out of the crystallizing dyke, they are believed to have been pressed into the surrounding wehrlite causing a reaction which stabilizes these minerals. Volatiles like CO_2 and H_2O are known to lower the melting point of rocks (Best, 2003; Gill, 2010; Winter, 2001), which may have caused partial melting, or at least recrystallization to a degree.

The existence of large xenocrysts of ol like the grains labelled “remnant ol” in Figure 3.48 shows that the matrix ol most likely is derived from wall rock ol. As the melting temperature of the wehrlite is decreased, ol will gradually start to be consumed and melted. The partial preservation of these grains also show that the total amount of strain in these areas has been relatively low, possibly shock deformed, as these grains would be dragged out and non-recognizable as remnant grains if the amount of strain was on a metre scale. The offsetting of other older dykes being cut by this dyke therefore must have happened during emplacement, and before the generation of these zones.

Understanding the origin of these zones often revolves around reactions and infiltrations, but deformation is a significant part of these zones, as they are classified as a shear zone. Water in combination with ol is known to change the rheology of the ol. As there is no EBSD results from these samples, some of the EBSD results form Sørensen et al. (2019) will be used here to interpret the deformation regime found in these zones. Sørensen et al. (2019) found a distinct SPO, but a lacking CPO in these zones. Faul et al. (2011) made a similar discovery to Sørensen et al. (2019) in fine grained ol aggregates. Faul and Sørensen both used the strong SPO but lacking CPO to infer diffusion creep and high strain rates at temperatures <1000 ^{O}C.

The findings by both Faul and Sørensen relate to the enveloping zoned found in the dykes of ULS. Assuming the ultrafine ol rich shear zones in Sørensen et al. (2019) are the same as the zones found here, the same mechanisms are believed to be in place. These ultrafine shear zones are however not only found in the zones which temporally relate to the hbl gabbronorite, although they are most commonly found here. An extremely fine grained zone which strongly resemble the fine grained zones seen in the hbl gabbronorite samples is the zone found in JS07, a lhz dyke sample. This sample can be observed in Figure 3.51.

The ol shear zone found in JS07 shows a resemblence to the zones found enveloping the hbl gabbronorite in the sense that it contains ultra fine ol, which often fills fractures of larger, surrounding ol grains. Notably in this zone, there is an ol grain which shows a characteristic wavy extinction. This wavy extinction is assumed related to the fine grained shear zone, as the shearing is believed to have caused this deformation of the ol grain. In order to obtain this kink banding, high strain rates and shock deformation is believed to have occurred in this sample.

Sørensen et al. (2019) discusses the possibility of seismic activity to be related to the degassing of CO_2 and high strain rates. The shear zone is though to have undegone shock deformation, as some of the ol shows wavy extinction in combination with cm scale displacement and fine grained ol shear zones like seen in Figure 3.51. As this shear zone is in a different dyke type than what is most commonly

observed, it is believed that the same mechanisms are responsible across the dykes, but is most abundant in the hbl gabbronorite.

One possible explanation for the genetic relationship between the hbl gabbronorite and the shear zone is a transfer of volatiles from the crystallizing hbl gabbronorite to the werhlite, causing new minerals to stabilise, partially consuming some of the ol and recrystallizing it. This then led to a softening of the rock in these localities, which then later caused strain localization in these shear zones. This would cause a grain size reduction, as this zone may have been activated and reactivated several times.

The small domains of gabbroic material found in these zones like the ones seen in Figure 3.50 also attest to the ductile, almost melted behaviour of these zones. These domains are believed to relate to the primary emplacement and volatile transfers, as they resemble melt mingling textures. The diffuse transitions and contacts seem like magmatic textures, which may later have been deformed.

Based on the three different theories presented, the 3rd theory seems to be the most likely theory. The genetic relationship with zone is explained by fractionation of volatiles out of the dyke, causing a reaction and partial melting of the wehrlite. The newly crystallized wehrlite then represents a soft, easily deformable zone in ULS, further facilitating strain localization and deformation. The theory also explains the ductile and brittle behaviour of the zones, as the initial partial melting would create ductile structures and textures, and the high strain rate and shock deformation is capable of forming brittle, cataclastic like deformation stuctures, even at high temperatures.

4.5 Proposed melt source

Grant et al. (2016) and Larsen et al. (2018) both have a proposed melt source for the melt forming RUC. Almost all samples analysed from ULS have a negative Y anomaly. Y is an element which has a higher affinity for garnet than most other REE. (Winter, 2001) Some of the wehrlitic samples are enriched in trace elements, with few of the samples having chondrite normalized REE values < 1. In addition to this, primary magmatic hydrous minerals like hbl have been found in the wehrlites, indicating a hydrous component to the melt forming ULS. The intrusive rocks are also rich in Mg, which is common in fertile rocks.

The Y anomaly is often associated with a garnet rich melt source. When the source rock is melted, Y has a higher affinity for garnet than other trace elements. This causes more of the Y to be retained in the source rock compared to other REE. The melt source which has formed ULS is therefore most likely garnet bearing. The overall high REE and trace element content can be attributed to a high cpx content in the source rock. Opx and ol are poor carriers of trace elements, as the crystal lattice is unsuitable for inclusions of such elements. Cpx can have trace elements in the site where Ca resides. The hydrous component could be from metasomatism of the source rock or form a hydrous phase. As both CO_2 and H_2O have been present, metasomatism of the source rock is more probable.

Based on the trace element and whole rock chemistry, it seems that the source rock which was partially melted to form the magma which formed ULS must have been a partially metasomatized garnet bearing lherzolite. This is the same conclusion which was reached by Larsen et al. (2018), Grant et al. (2016) and Orvik et al. (2019).

5 Conclusions

Based on the observations from the layered ultramafic rocks in ULS it seems the wehrlitic, dunitic and clinopyroxenitic layers have been formed in an open magma chamber setting through fractionation of ol, cpx and some opx out of the melt. There is a systematic upward fractionation of incompatible elements as a function of stratigraphy in the intrusion, indicating fresh batches of magma has entered the magma chamber to mingle with fractionated melts richer in trace elements. This also shows that the replenishing magma does not show chemical variation over time. Similar to the findings in previous works from RUC, the melt source proposed for the dykes and layered ultramafic rocks in ULS is a partially metasomatized garnet bearing lherzolite indicating a deep magma source.

The large scale replacive dunites described by Grant et al (2016) and Larsen et al (2018), which were thought to relate to the emplacement of CS seem to be a larger network of serpentinization joints which cut through ULS. Based on the observations here, they do not seem to relate to replacive dunites in any way, but rather late metasomatic alteration.

The px peg found as isolated stocks or dyke like intrusions in ULS are through to have crystallized in a lower part of the magma chamber, to then later be intruded into a mushy ULS. The emplacement of this coarse-grained lithology is thought to represent a recharge event, and one of the latest magmatic processes to happen while ULS was still a cumulate mush.

Using traditional lamprophyre emplacement models for the porphyritic hbl dyke does not seem reasonable in ULS as these dykes fall outside of the definition and often described characteristics of lamprophyres. The feature which these two dyke types have in common is the large phenocrystic hbl. The dyke is therefore believed to represent a late pulse of melt from a chamber which has crystallized large hbl grains, which subsequently were transported to ULS via a non-equilibrium ultramafic dyke.

A ductile fracturing style of emplacement is the proposed emplacement style for the lhz dykes. This emplacement style is similar to some of the dyke types found in CS, and have been described by Orvik et al. (2019). The lhz dykes also show a temporal relationship with the infiltrating plag, likely to originate from the partial melting of the Langstrand gabbro. These plag domains are also shown to have an ore forming potential as they create a free sulphide melt in the interaction with the wehrlite, possibly though a reaction between released volatiles in the plag domain and the elements residing in the wehrlite.

Through EPMA analyse a thermobarometric estimate has also been provided form the lhz dyke, as it contains both hbl and plag. This estimate gives a crystallization temperature and pressure for the infiltration of the plag domain, but gives an indication to a minimum emplacement depth and temperature of ULS. The pressure of 9,42 ± 0,87 kbar, and a temperature of 1037 ± 22 ^{O}C is shallower than the previous estimate by Orvik et al. (2019).

The hbl gabbronorite is the most enriched dyke in ULS. It is believed to represent the youngest dyke type as it has the highest REE concentration, indicating origin from evolved magma. It also has the most fractionated signature using the Mg#-approach. The pseudotachylytes found in the dyke relate to normal movement. This is believed to relate to the collapse, and sinking of the ultramafic intrusion, as the magma pressure beneath the intrusion was lowered at the end of the magmatic activity. This collapse would be able to create strain rates high enough to create pseudotachylytes in the soft and deformable hbl-plag aggregate. Dynamic recrystallization in combination with the generation of pseudotachylytes from fast slip rates are likely the result of the gradual settling of RUC post magmatism.

When investigated, it seems the yellow shear zones enveloping the hbl gabbronorite are the result of a reaction between H_2O, CO_2 and possibly other volatiles fractionated out of the crystallizing dyke. This reaction has created a soft, fine grained aggregate from the wehrlite, partially through the reaction 2 Ol + Cpx + 2 CO_2 = Dol + 2 Opx proposed by Sørensen et al. (2019). This fine grained zone has then experienced further grain size reduction from deformation after the emplacement of the dyke.

6 References

Allen, D. E., & Seyfried, W. E. (2003). Compositional controls on vent fluids from ultramafic-hosted hydrothermal systems at mid-ocean ridges: An experimental study at 400°C, 500 bars. *Geochimica Et Cosmochimica Acta*, ss. 67, 1531-1542.

Anker-Rasch, L. (2013). *Magmatiske malmdannende prosesser i Reinfjord, Seiland magmatiske provins.* Trondheim: NTNU.

Barnes, S. J., & Campbell, I. H. (1988). Role of magmatic fluids in Merensky-type platinum deposits: a discussion. *Geology*, ss. 488-491.

Barnes, S. J., Straude, S., Le Valliant, M., Piña, R., & Lightfoot, P. C. (2018). Sulfide-silicate textures in magmatic Ni-Cu-PGE sulphide ore deposits: Massive, semi-massive and sulfide-matrix breccia ores. *Ore Geology Reviews*. doi:10.1016/j.oregeorev.2018.08.011

Beere, W. (1975, January). A Unifying Theory of the Stability of Penetrating Liquid Phases and Sintering Pores. *Acta Metallurgica*, ss. 131-138.

Bennet, M. C. (1974). The emplacement of a high temperature peridotite in the Seiland Igneous Province of the Norwegian caledonites. *Journal of the Geological Society*, ss. 130, 205-266.

Bennet, M. C., Emblin, S. R., Robins, B., & Yeo, W. J. (1986). High-temperature ultramafic complexes in the North Norway caledonides: I - Regional setting and field relationships. *Norges Geologiske Undersøkelse Bulletin 405*, ss. 1-41.

Best, M. G. (2003). *Igneous and Metamorphic Petrology, Second Edition.* Malden: Blackwell Publishing.

Broom-Fendley, S., Brady, A. E., Wall, F., Gunn, G., & Dawes, W. (2017). REE minerals at the Songwe Hill carbonatite, Malawi: HREE enrichment in late-stage apatite. *Ore Geological Review*, s. 23.

Cawthorn, R. G., & Boerst, K. (2005). Origin of the Pegmatitic Pyroxenite in the Merensky unit, Bushveld Complex, South Africa. *Journal of Petrology*(8), ss. 1509-1530. doi:doi:10.1093/petrology/egl017

Charlier, B., Namur, O., Latypov, R., & Tegner, C. (2015). *Layered Intrusions.* Dordrecht: Springer.

Chenriak, D. J., & Liang, Y. (2012). Ti diffusion in natural pyroxene. *Geochimica et Cosmochimica*, ss. 31-47.

Correra-Gomes, L. C., Souza Filho, C. R., Martins, C. J., & Oliveira, E. P. (2001). Development og symmetrical and asymetrical fabrics in sheet-like igneous bodies: the role of magma flow and wall-rock displacements in theoretical and natural cases. *Journal of Structural Geology*, ss. 1425-1428.

Cox, K. G., Bell, J. D., & Pankhurst, R. J. (1979). *The Interpretation of Igneous Rocks.* London: George Allen & Unwin LTD.

Deer, W. A., Howie, R. A., & Zussman, J. (1997). *Rock-forming minerals, Double-Chain Silicates.* London: The Geological Society.

Emblin, S. R. (1985). The Reinfjord Ultramafic Complex, Seiland Province: Emplacement History and Magma Chamber Model. *Unpublished Ph.D. thesis, Univerity of Bristol*.

Eppelbaum, L., Kutasov, I., & Pilchin, A. (2014). *Applied Geothermics.* Berlin: Springer.

Faul, U. H., Fitz Gerald, J. D., Farla, R. J., Ahlefeldt, R., & Jackson, I. (2011). Dislocation creep of fine-graines olivine. *Journal of Geophysical Research*, s. 116. doi:doi:10.1029/2009JB007174,

Gaetani, G. A., & Grove, T. L. (1995). Partitioning of rare earth elements between clinopyroxene and silicate melt: Crystal-chemical controls. *Geochemica et Cosmochemica Acta*, ss. 1951-1962.

Gill, R. (2010). *Igneous Rocks and Processes, A Practical Guide.* Oxford: Blackwell Publishing.

Goldschmidt, V. M. (1937). The Principles of Distribution of Chemical Elements in Minerals and Rocks. *Journal of the Chemical Society*, ss. 655-673.

Goldstein, J., Newbury, D. E., Echlin, P., Joy, D. C., Romig Jr, A. D., Lyman, C. E., & Fiori, C. (2012). Scanning electron microscopy and X-ray microanalysis: a text for biologists, materials scientists, and geologists. *Springer Science and Business Media*.

Grant, K. J., & Wood, B. J. (2009, December). Experimental study og the incorporation of Li, Sc, Al and other trace elements into olivine. *Elsevier*, ss. 2412-2428.

Grant, T. B., Larsen, R. B., Anker-Rasch, L., Grannes, K. R., Iljina, M., McEnroe, S., . . . Øen, E. (2016). Anatomy of a deep crustal volcanic conduit system; The Reinfjord Ultramafic Complex, Seiland Igneous Province, Northern Norway. *Lithos*, ss. 252-253, 200-215. doi:http://dx.doi.org/10.1016/j.lithos.2016.02.020

Griffin, W. L., Stuart, B. A., O'Neill, C. J., Kirkland, C. L., & O'Reilly, S. Y. (2013). Intrusion and contamination of high-temperature dunitic magma: the Nordre Bumandsfjord pluton, Seiland, Arctic Norway. *Contributions to mineralogy and petrology*, ss. 165, 903-930.

Griffith, A. A. (1920). The phenomena of rupture and flow in solids. *Philos Trans. R. Soc. London*, ss. 221:163-97.

Hawthorne, F. C., Oberti, R., Harlow, G. E., Maresch, W. V., Martin, R. F., Schumacher, J. C., & Welch, M. D. (2012). Nomenclature of the amphibole super group. *American Mineralogist*, ss. 97, 2031-2048.

Higgins, M., & van Breemen, O. (1998). The age of the Sept Iles layered mafic intrusion, Canada: implications for the late Neoproterozoic/Cambrian history of southeastern Canada. *Journal of Geology*, ss. 106, 421-431.

Hughes, J. M. (2015). Presidential adress. The many facets of apatite. *Am Miner 100*, s. 1033.

Irvine, T. N. (1975). Crystallization sequences in the Muskox intrusion and other layered intrusions-II. Origin of chromite layers and similar deposits of other magmatic ores. *Geochemica et Cosmochemica Acta*, ss. 991-1020.

Irvine, T. N. (1977). Origin of chromite layers in the Muskox intrusion, and other stratiform intrusions: A new interpretation. *Geology*, ss. 273-277.

Irvine, T. N., & Bargar, W. R. (1971). A Guide to the Chemical Classification of the Common Volcanic Rocks. *Canadian Journal of Earth Sciences*, ss. 8(5): 523-548. doi:https://doi.org/10.1139/e71-055

Kono, Y., Kenney-Benson, C., Hummer, D., Ohfuji, H., Park, C., Shen, G., . . . Manning, C. .. (2014). Ultralow viscosity of carbonate melts at high pressures. *Nature Communications 5*, s. 5091. doi:10.1038/ncomms6091

Krogh, E. J., & Elvevold, S. (1990). A Precambrian age for an Early Gabbro-Monzonitic Intrusive on the Øksfjord Penninsula, Seiland Igneous Province. ss. pp. 267-273.

Larsen, R. B., Grant, T., Sørensen, B. E., Tegner, C., McEnroe, S., Pastore, S., . . . Michels, A. (2018, November). Portrait of a giant deep-seated magmatic conduit system: The Seiland Igneous Province. *Lithos 296-299, 600-622*.

Lauder, W. R. (1970). Origin of the Merensky Reef. *Nature*, ss. 365-366.

Legros, F., Cantagrel, J. M., & Devouard, B. (2000). Pseudotachylyte at the base of the Arequipa volcanic landslide deposit: implications for emplacement mechanisms|. *Geology*, ss. 108:601–611.

Molina, J. F., Moreno, J. A., Castro, A., Rodriguez, C., & Fershtater, G. B. (2015). Calcic amphibole thermobarometry in metamorphic and igneous rocks: New calibrations based on plagioclase/amphibole Al-Si partitioning and amphibole/liquid Mg partitioning. *Lithos*, ss. 232 286-305.

Moune, S., Holtz, F., & Botcharnikov, R. E. (2008). Sulphur solubility in andesitic to basaltic melts: implications for Hekla volcano. *Contributions to Mineralogy and Petrology*, ss. 157:691–707.

Naldrett, A. J. (2004). *Magmatic Sulphide Deposits: Geology, Geochemistry and Explotation.* Berlin: Springer.

Naldrett, A. J., Gasparrini, E. C., Barnes, S. J., v. G., & Sharpe, M. R. (1986). The Upper Critical Zone of the Bushveld Complex and the origin of Merensky-type ores. *Economic Geology*, ss. 1105-1117.

O'Hanley, D. S. (1996). Serpentinites: records of tectonic and petrological history. *Oxford Monographs on Geology and Geophysics, 34*.

O'Hanley, D. S., Kyser, T. K., & Stauffer, M. (1993). Provenance, deformation, and alteration history of mafic-ultramafic rocks east of Amisk Lake, and the provenance of the mafic and ultramafic Boundary Intrusions, in the Flin Flon Domain, trans-Hudson Orogen. *Lithoprobe Report*, ss. 34, 190-206.

Orvik, A. A., Sørensen, B. E., & Larsen, R. B. (2019). *The dyke swarm in the Reinfjord Ultramafic Complex: A window into the terminal stages forming the Seiland Igneous Province.* Trondheim: NTNU.

Passchier, C. W., & Trouw, R. A. (2005). *Microtectonics.* Berlin Heidelberg: Springer.

Pastore, Z., Fichler, C., & McEnroe, S. (2016). The deep crustal structure of the mafic-ultramafic Seiland Igneous Province of Norway from 3D gravitational modelling and geological implications. *Geophysical Journal International*, ss. 207 (3), 1653-1666.

Platt, J. P. (2015). Rheology of two-phase systems: A microphysical and observational approach. *Journal of Structural Geology 77*, ss. 213-227.

Ray, S. K. (1999). Transformation of cataclastically deformed rocks to pseudotachylyte by pervasion of frictional melt: inferences from clast-size analysis. *Tectonophysics*, ss. 301:283–304.

Reed, S. J. (2005). Electron microprobe analysis and scanning electron microscopy in geology. *Cambridge university press*.

Ridolfi, F., Renzulli, A., & Puerini, M. (2009). Stability and chemical equilibrium of amphibole in calc-alkaline magmas: an overview, new thermobarometric formulations and applications to subduction-related volcanoes. *Contributions to Mineralogy and Petrology*, ss. 160 45-66.

Robb, L. (2005). *Introduction to Ore-Forming Processes.* Malden, USA: Blackwell Publishing.

Roberts, R. J., Corfu, F., Torsvik, T. H., Ashwal, L. D., & Ramsay, D. M. (2006). Short-lived mafic magmatism at 560-570 Ma in the Norwegian Calidonites; U-Pb zircon ages from the Seiland Igneous Province, Northern Norway. *Journal of the Geological Society*, ss. 167, 71-81.

Roberts, R. J., Corfu, F., Torsvik, T. H., Hetherington, C. J., & Ashwal, L. D. (2010). Age of alkaline rocks in the Seiland Igneous Province, Northern Norway. *Journal of Geological Society*, ss. 167, 71-81.

Rock, N. M. (1977). The Nature and Origin of Lamprophyres: Some Definitions, Distinctions and Derivations. *Earth-Science Reviews*, ss. 13, 123-169.

Roedder, E. (1984). Fluid Inclusions, Reviews in Mineralogy. *Mineralogical Society of America*, s. 664.

Rubin, A. M. (1995). Propagation of magma-filled cracks. *Earth Planet Science*, ss. 23:287-336.

Rushmer, T. (1996). Melt segregation in the lower crust: How have expreiments helped us? *Earth and Enviromental Science Transactions of the Royal Society of Edinburgh*, ss. 87(1-2), 73-83. doi:10.1017/S0263593300006490.

Shcherbakov, V., Plechov, P., & Izbekov, P. (2010). Plagioclase zoning as an indicator of magma processes at Bezymianny Volcano, Kamchatka. *Contributions to Mineralogy and Petrology*, ss. 83-99. doi:https://doi.org/10.1007/s00410-010-0584-1

Spera, F. (1984). Carbon dioxide in petrogenesis III: Role of volatiles in the ascent of alkaline magma with special reference to xenolith-bearing mafic lavas. *Contrib. Mineral. Petrol.*, ss. 88:217-32.

Spray, J. G. (1995). Pseudotachylyte controversy: fact or fiction? *Geology*, ss. 23:1119–1122.

Spray, J. G. (1997). Superfaults. *Geology*, ss. 25:579–582.

Suhr, G. (1993). Evaluation of upper mantle microstructures in the Table Mountain massif (Bay of Island ophiolite). *Journal of Structural Geology*, ss. 1273-1292.

Sun, S., & McDonough, W. F. (1989). Chemical and isotopic systems of oceanic basalts: Implications dor mantle compositions and processes. *Geological Society of London*, ss. 313-345. doi:10.1144/GSL.SP.1989.042.01.19

Swanson, M. T. (1992). Fault structure, wear mechanisms and rupture processes in pseudotachylyte generation. *Tectonophysics*, ss. 204: 223-242.

Sørensen, B. E., Grant, T., Ryan, E. J., & Larsen, R. B. (2019, August 2). In situ evidence of earthquakes near the crust mantle boundary initiated by mantle CO2 fluxing and reaction-driven strain softening. *Earth and Planetary Science Letters*, s. 524 115713.

Vermaak, M. J. (1976). The Merensky Reef-thoughts on its enviroment and genesis. *Economic Geology*, ss. 1270-1298.

Vidal, J. K., Kubin, L., Debat, P., & Soula, J. L. (1980). Deformation and dynamic recrystallization of K-feldspar augen in the orthogneiss from Montagne Noir, Occitania. *Lithos*, ss. 13:247-257.

Voll, M. O. (2019). *Deep processes in the Reinfjord Ultramafic Complex, Nord-Troms.* Trondheim: NTNU.

Von Grunenwaldt, G. (1979). A review of some recent concepts of the Bushveld Complex with particular refrence to sulfide mineralization. *Canadian Mineralogist*, ss. 233-256.

Weinberg, R. F., & Regenauer-Lieb, K. (2010). Ducyile fractures and magma migration from source. *Geology 38*, ss. 363-366. doi:https://doi.org/10.1130/G30482.1

Wickham, S. M. (1987, April). The Segregation and Emplacement of Granitic Magmas. *Geological Society, London*, ss. 144, 281-297.

Winter, J. D. (2001). *An Introduction to Igneous and Metamorphic Petrology.* Upper Saddle River, New Jersy: Prentice-Hall Inc.

Yoder, H. S. (1976). *Generation of Basaltic Magmas.* Washington DC: National Academy of Science.

7 Appendix A – Thin section scans

Figure 7.1. ***Thin section JS_2_2 in ppl. Plag rich lhz dyke***

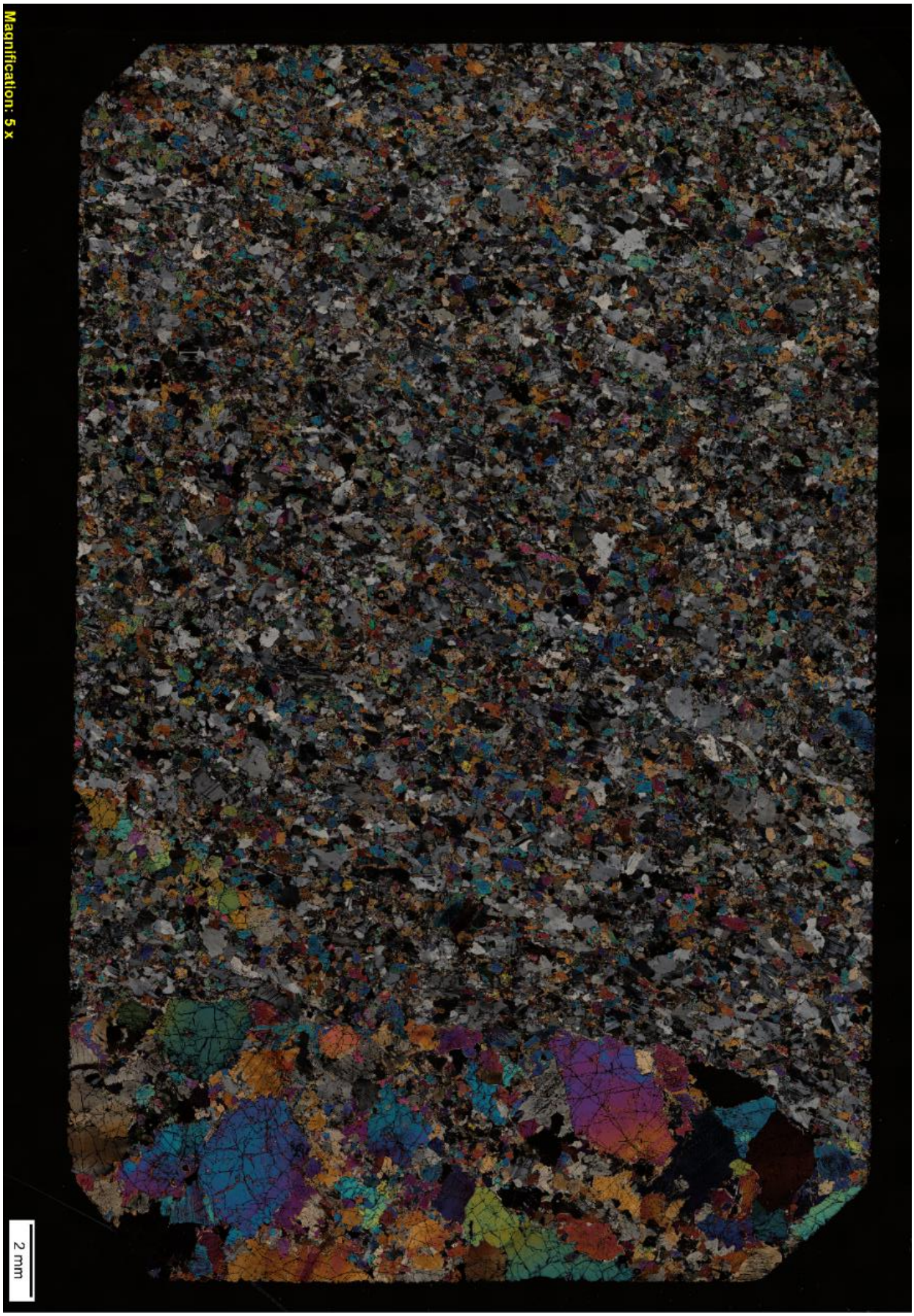

Figure 7.2. ***Thin section JS_2_2 in xpl. Plag rich lhz dyke***

Figure 7.3. ***Thin section JS_2_10 in ppl. Px rich dyke***

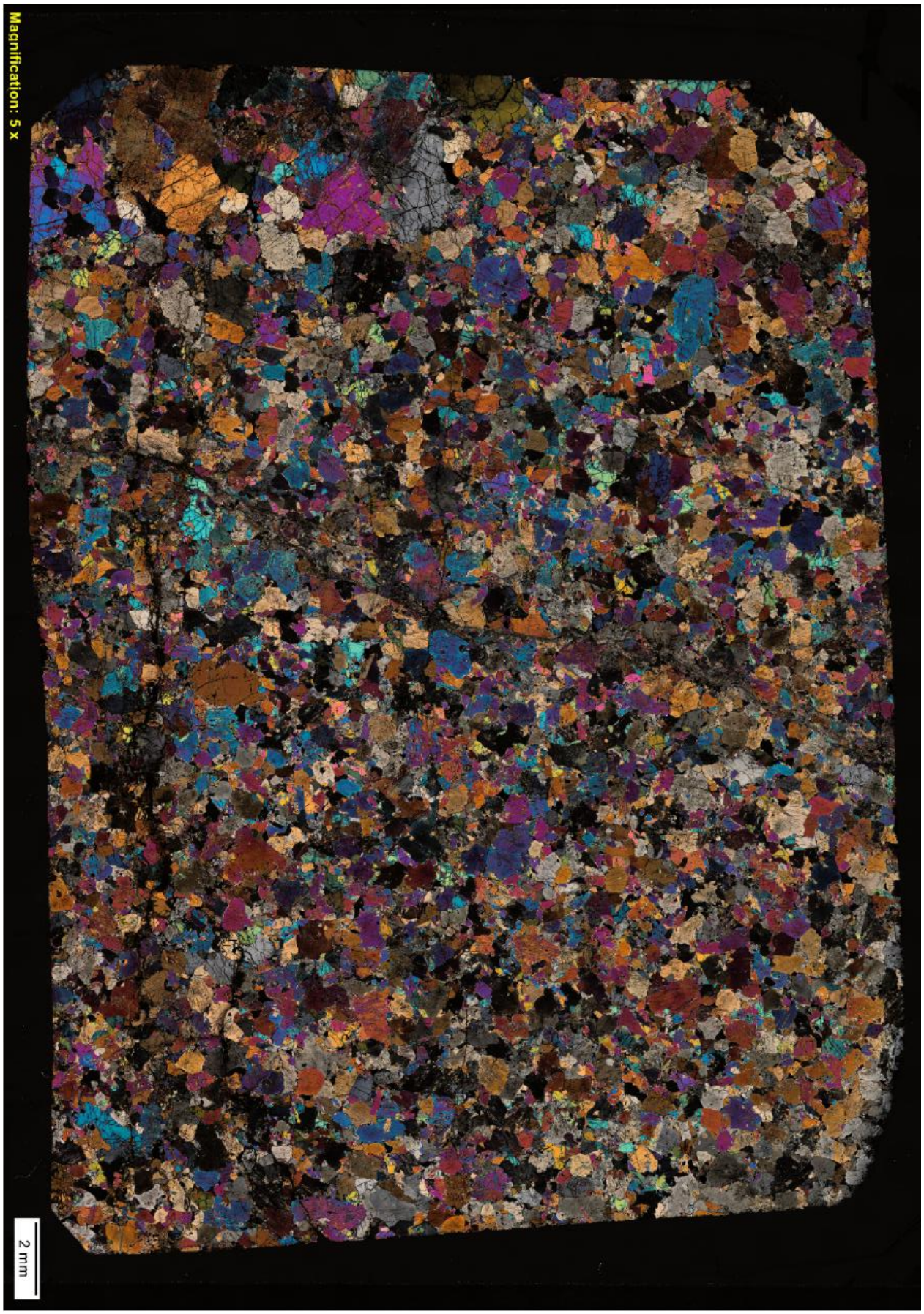

Figure 7.4. ***Thin section JS_2_10 in xpl. Px rich dyke***

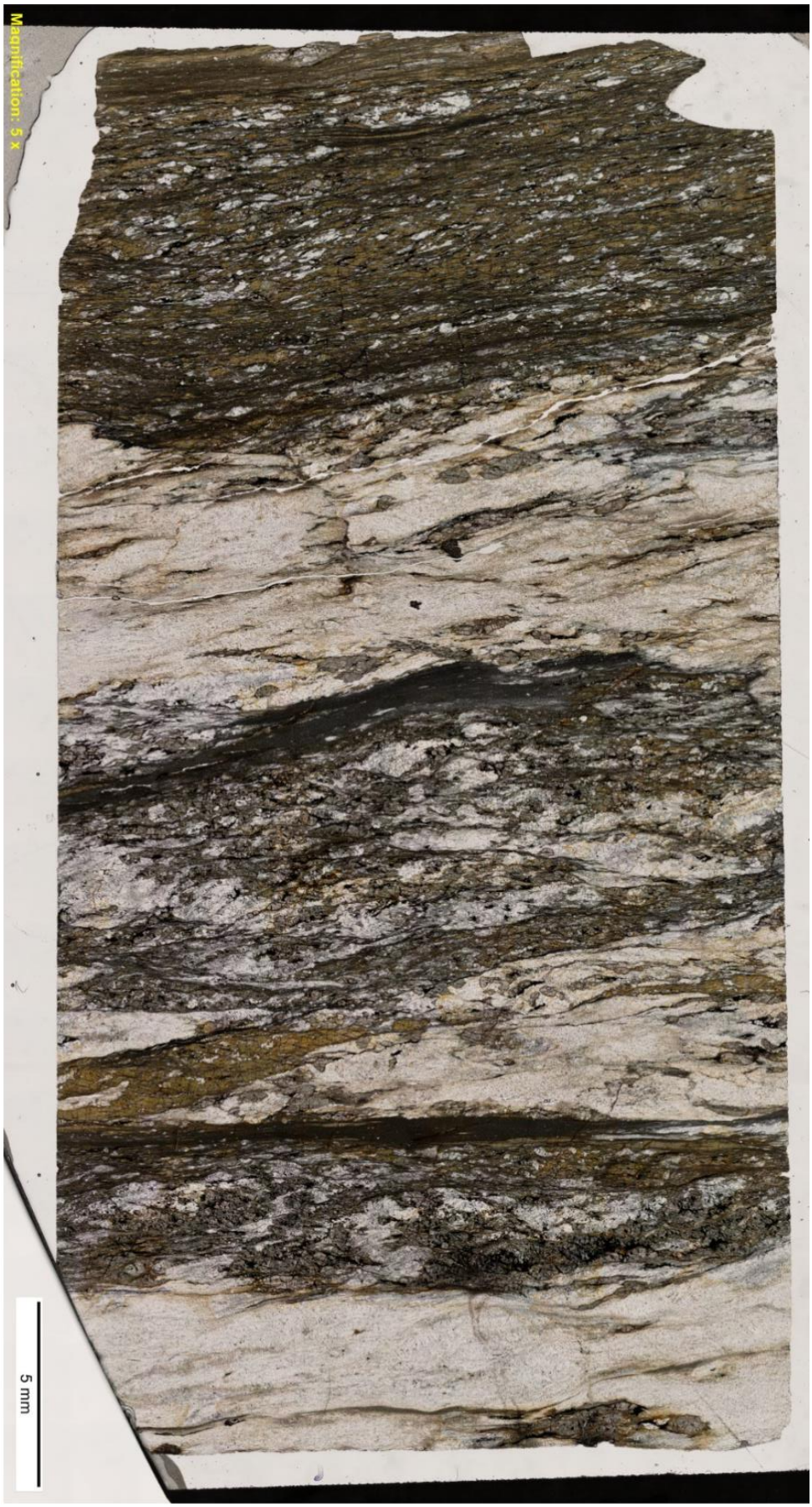

Figure 7.5. ***Thin section JS_2_12-B in ppl. Deformed hbl gabbronorite***

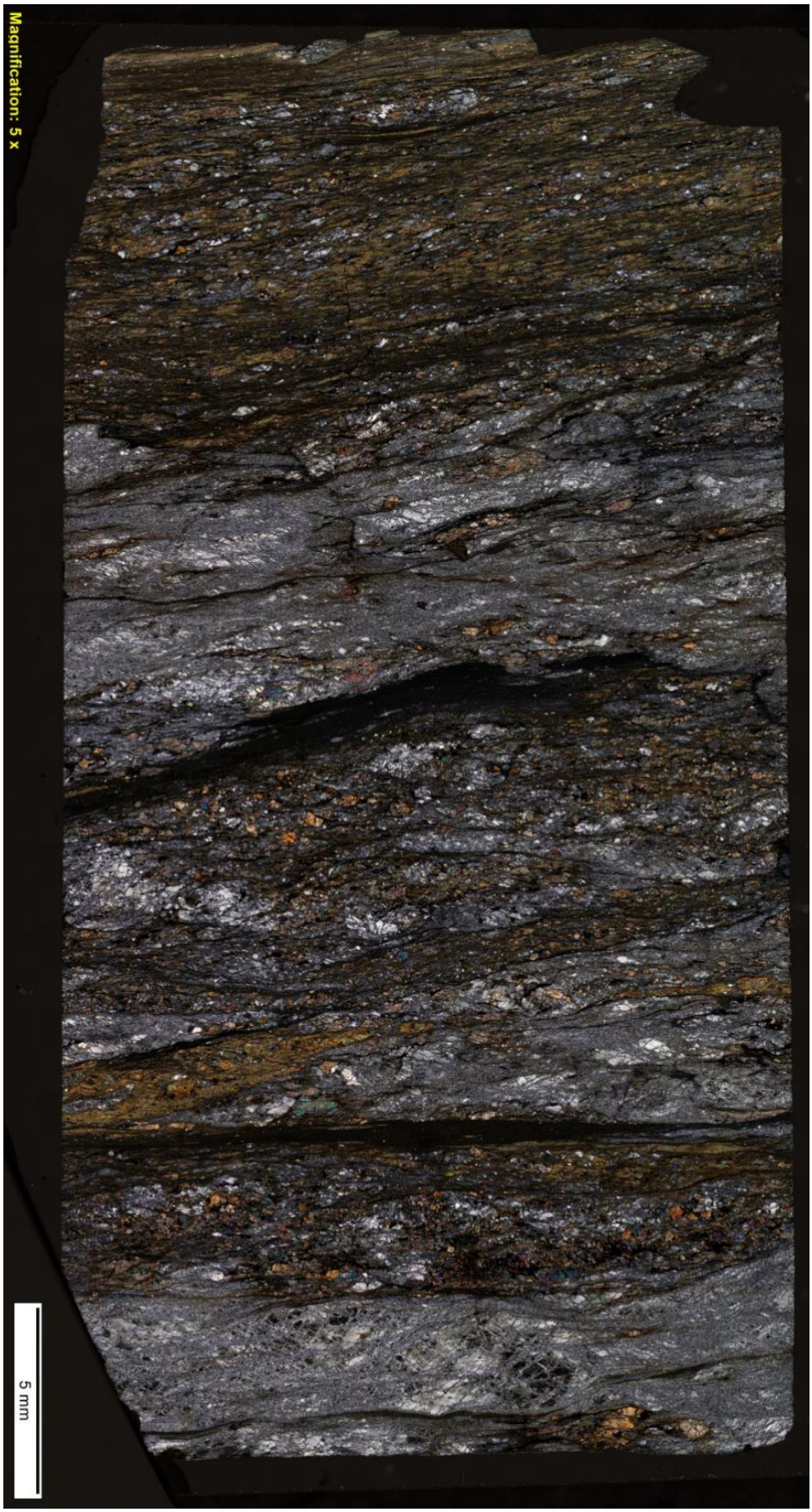

Figure 7.6. ***Thin section JS_2_12-B in xpl. Deformed hbl gabbronorite***

Figure 7.7. ***Thin section JS_2_18 in ppl. Comp dyke with plag domains***

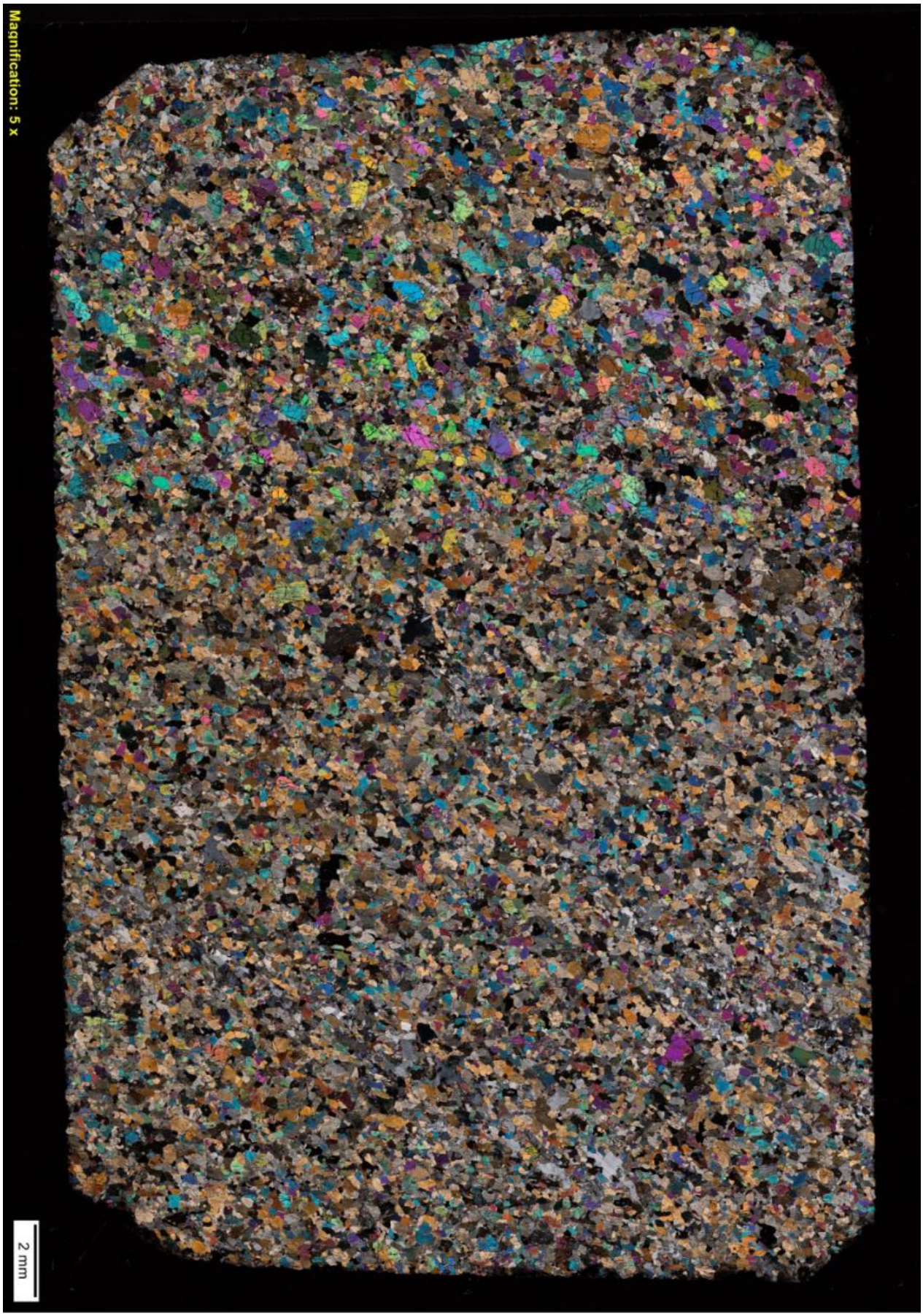

Figure 7.8. ***Thin section JS_2_18 in xpl. Comp dyke with plag domains***

Figure 7.9. ***Thin section JS03-A in ppl. Phenocrystic hbl dyke with wehrlite contact.***

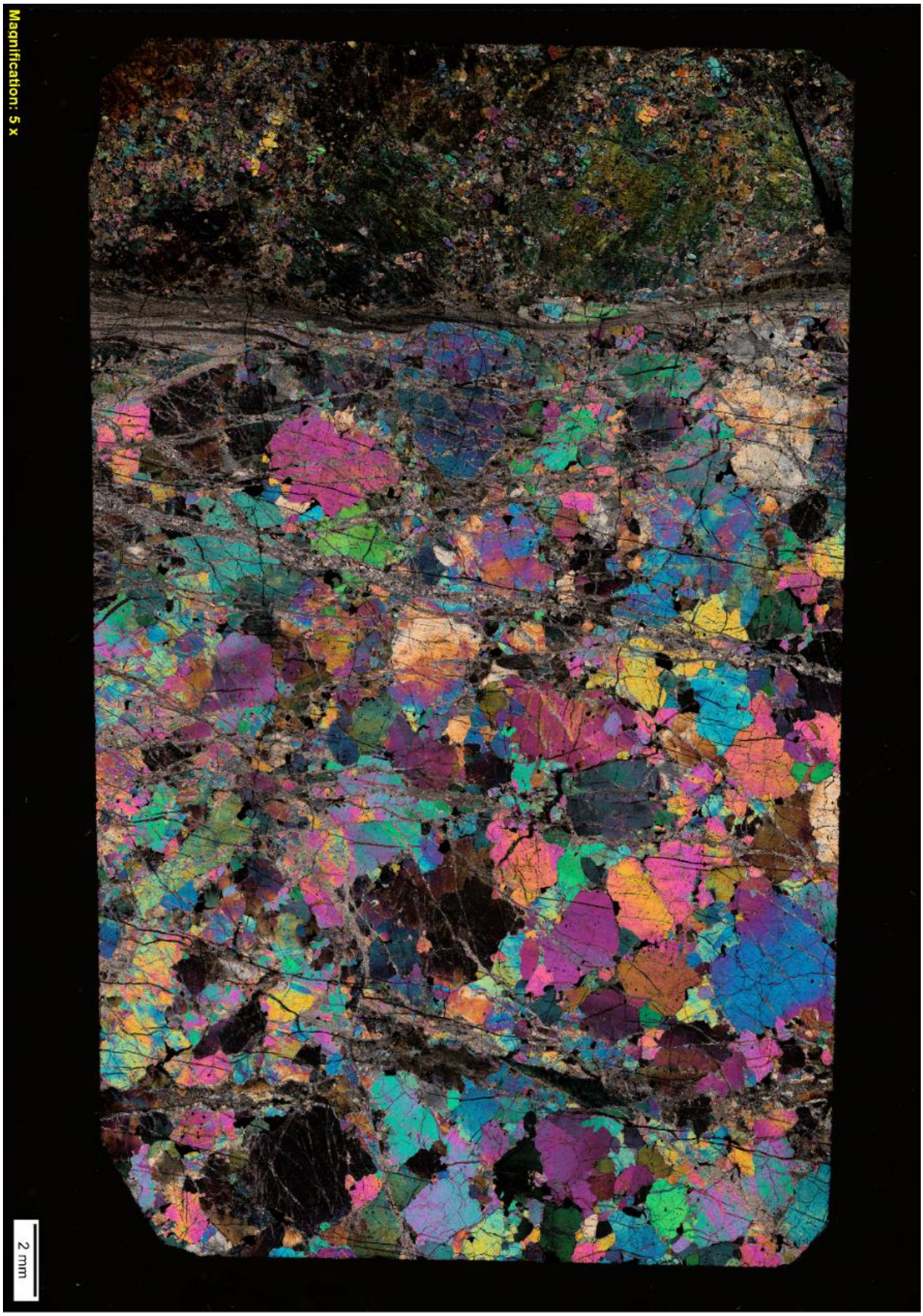

Figure 7.10. ***Thin section JS03-A in xpl. Phenocrystic hbl dyke with wehrlite contact.***

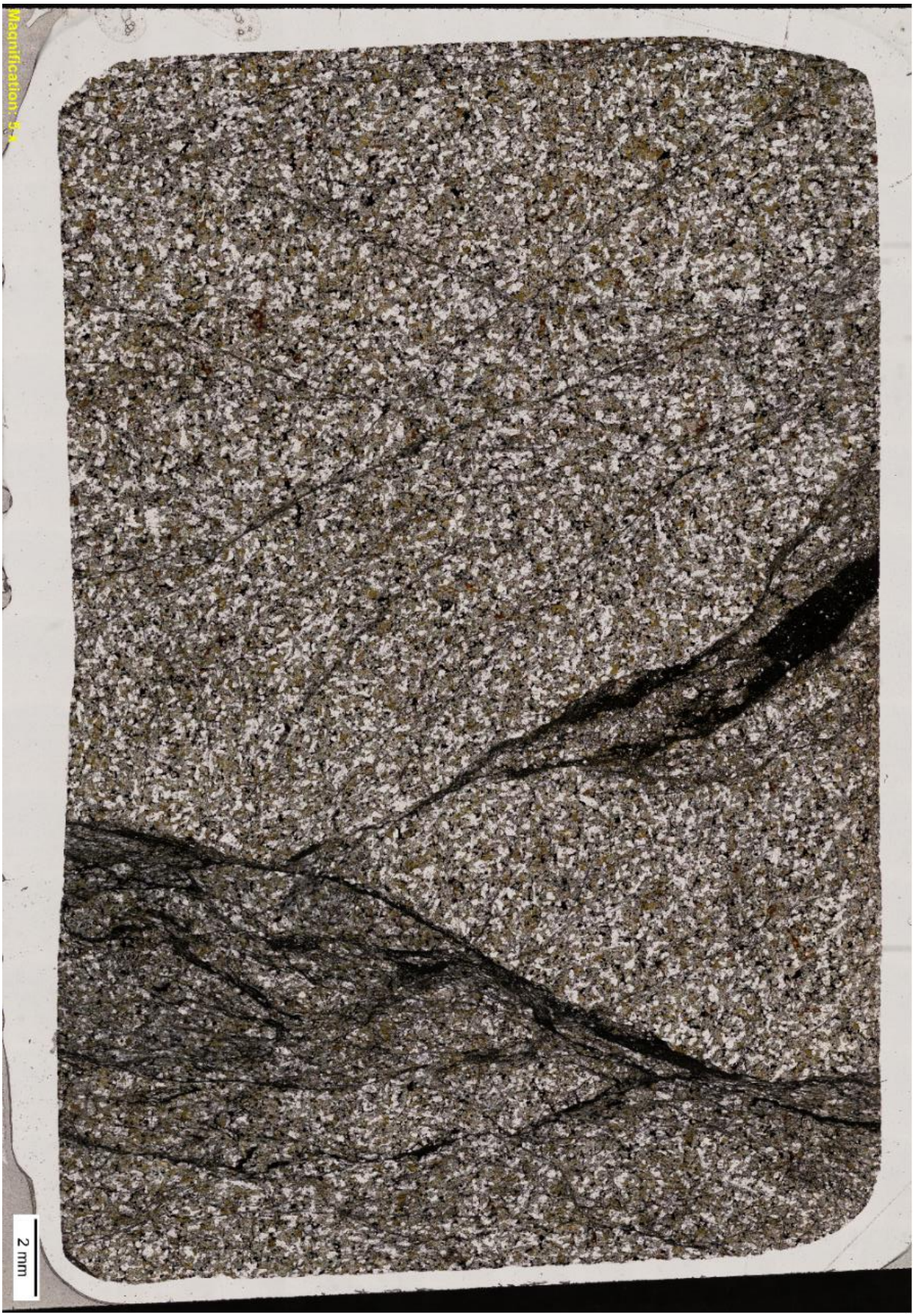

Figure 7.11. ***Thin section JS12-1-1-B in ppl. Hbl gabbronorite with pseudotachylytes.***

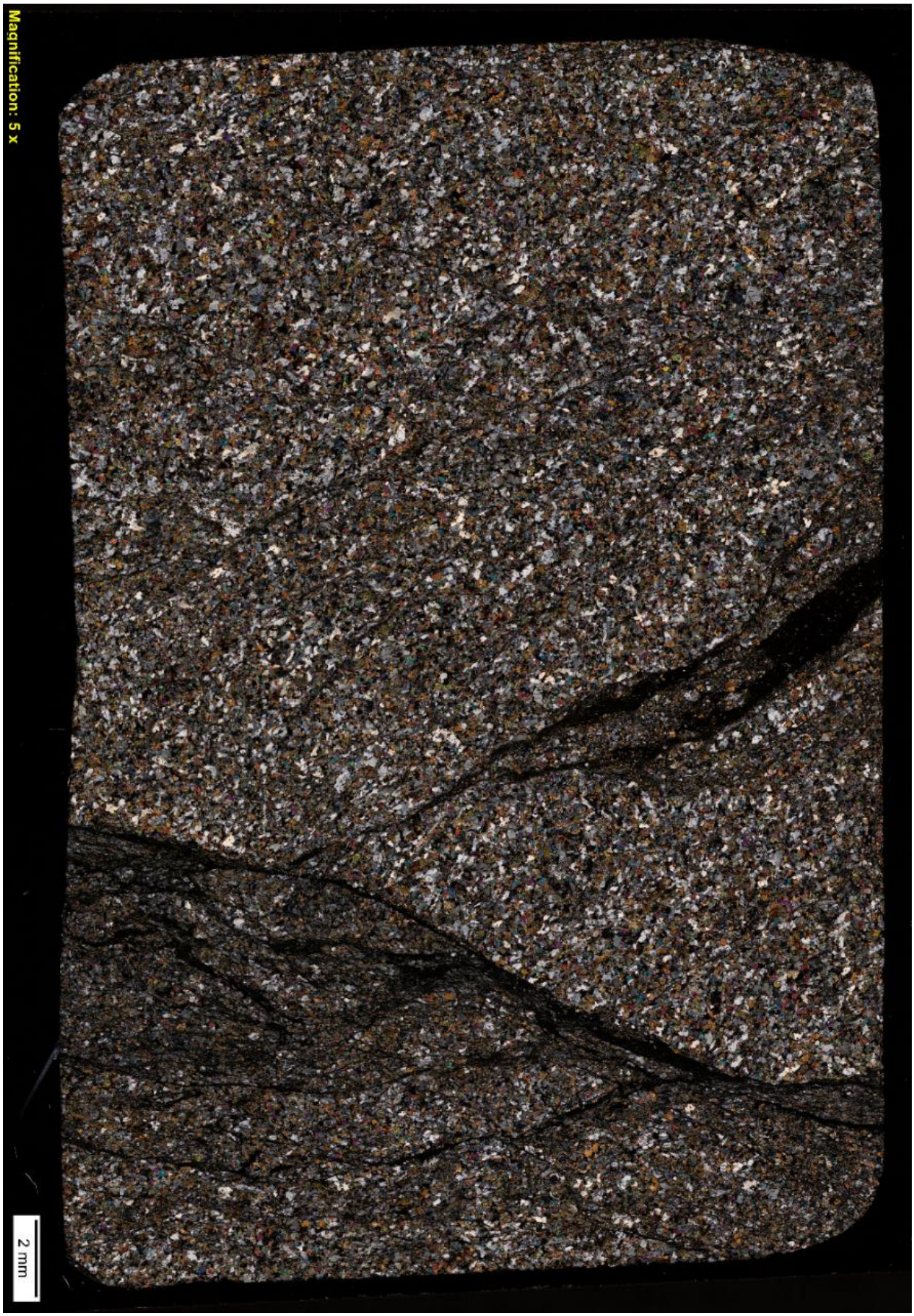

Figure 7.12. ***Thin section JS12-1-1-B in xpl. Hbl gabbronorite with pseudotachylytes.***

Figure 7.13. ***Thin section JS15-B in ppl. Deformed hbl gabbronorite.***

Figure 7.14. ***Thin section JS15-B in xpl. Deformed hbl gabbronorite.***

Figure 7.15. ***Thin section JS19-A in ppl. Deformed hbl gabbronorite with yellow shear material.***

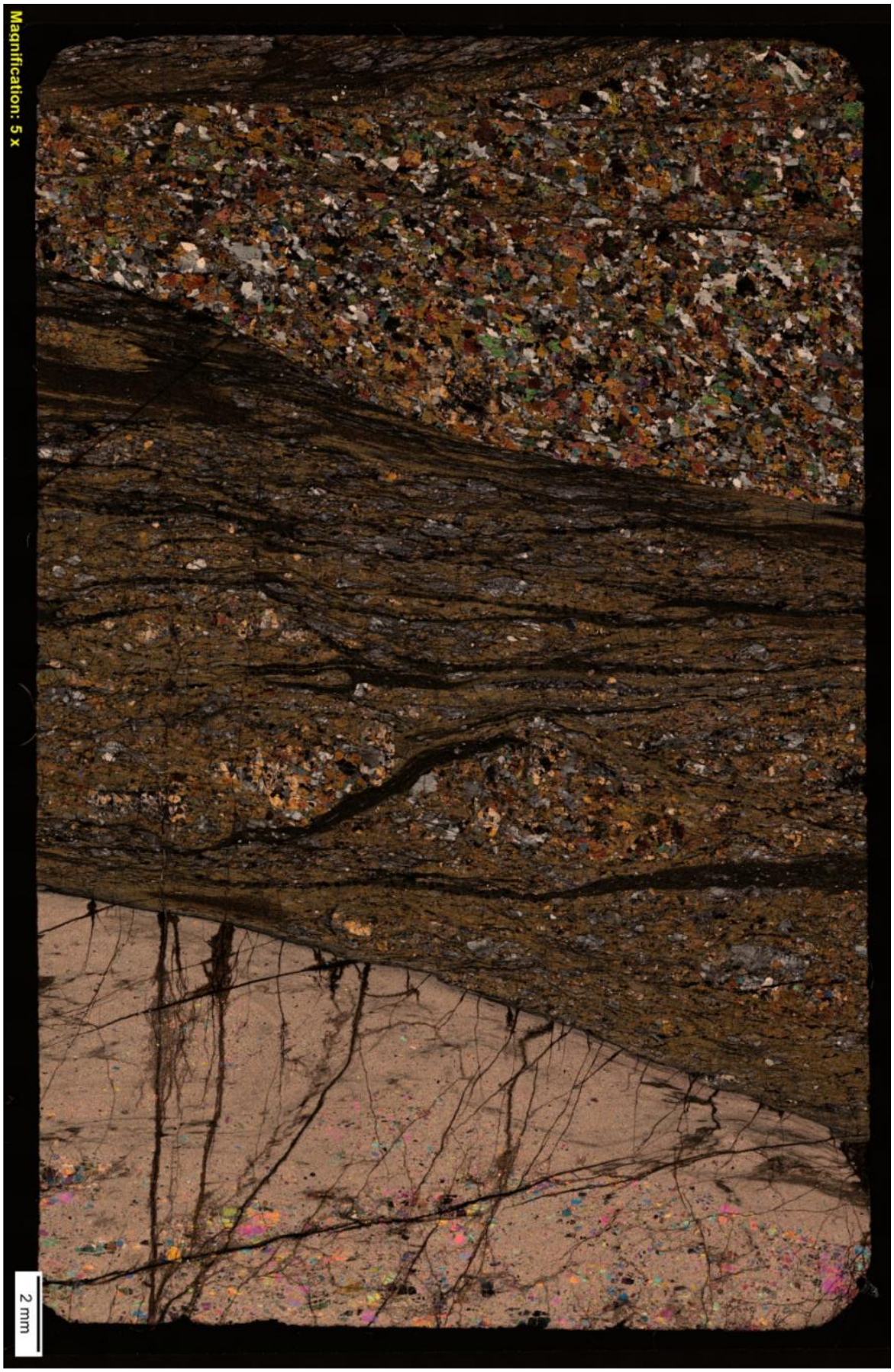

Figure 7.16. ***Thin section JS19-A in xpl. Deformed hbl gabbronorite with yellow shear material.***

8 Appendix B – Rock classification

Ultramafic rock classification

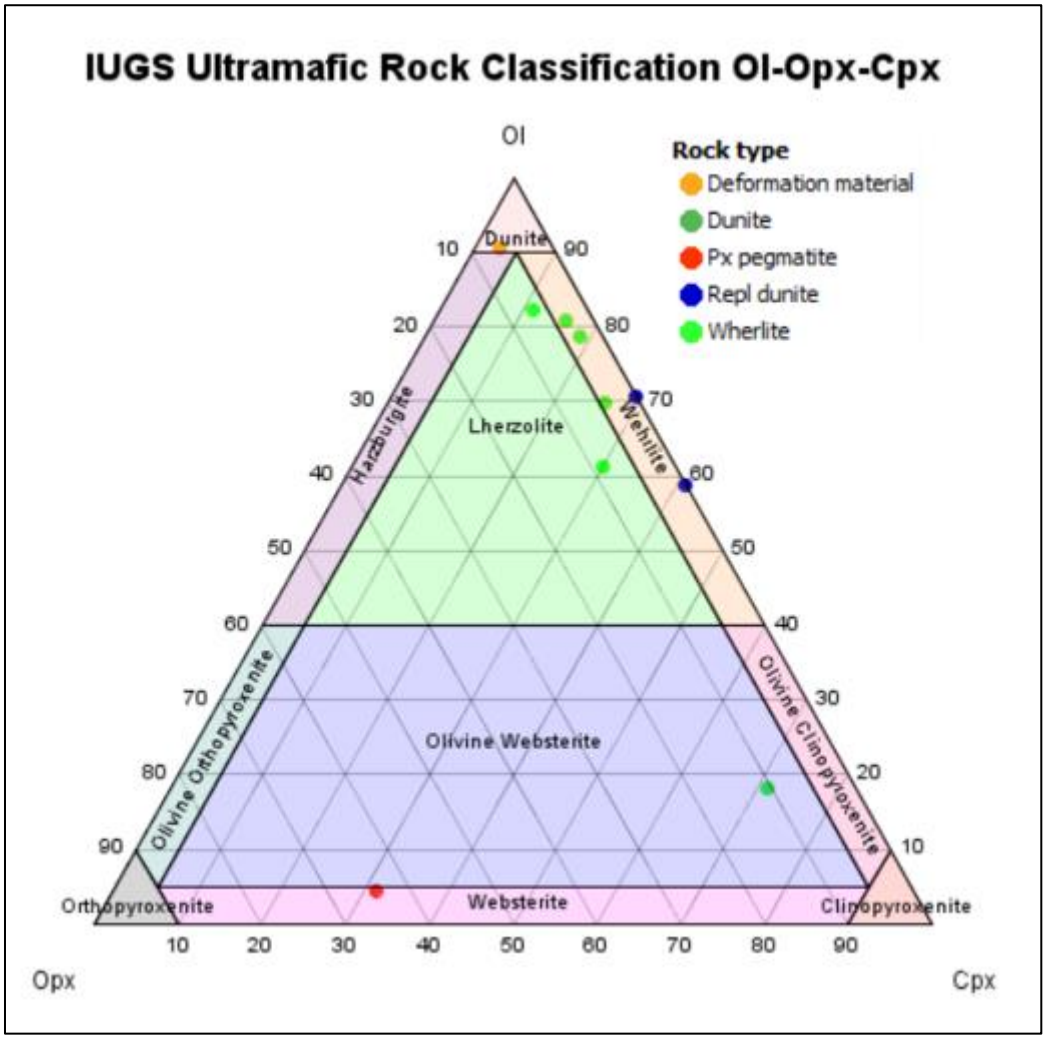

Gabbroic rock classification

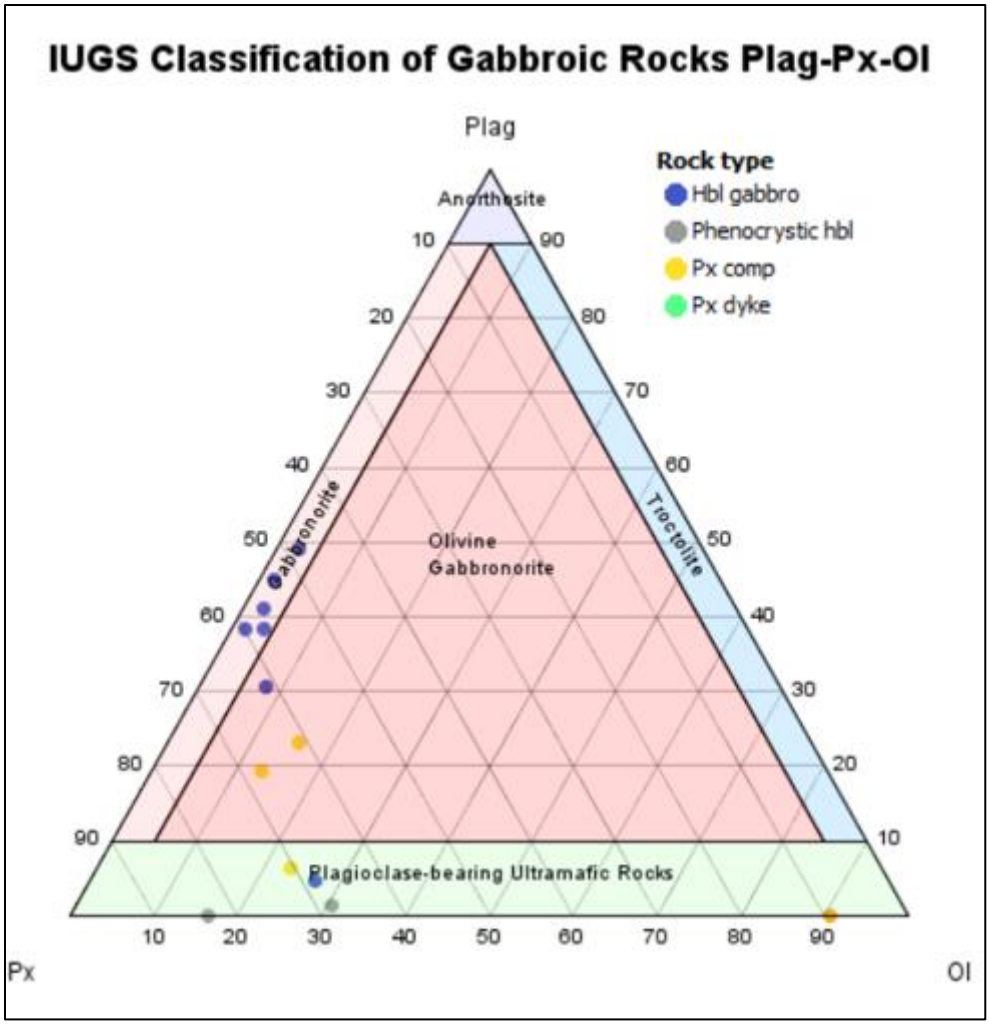

9 Appendix C – Whole rock geochemistry

Major elements

Lables	Rock type	SiO2	Al2O3	FeO	CaO	MgO	Na2O	K2O	Cr2O3	TiO2	MnO	P2O5	SrO	BaO	LOI
JS01-Dyke	Px comp	47	5,81	12,75	10,8	21,6	0,69	0,04	0,188	0,9	0,19	0,02	0,01	<0.01	0,21
JS01-Country Rock	Wherlite	39,6	1,5	16,9	2,27	38	0,15	<0.01	0,298	0,2	0,2	0,01	<0.01	<0.01	-0,44
JS02-3 Most Gabbroic	Px comp	49,3	9,4	11	10,4	18,85	1,18	0,05	0,149	0,73	0,16	0,01	0,03	<0.01	0,4
JS03	Phenocrystic hbl	41,3	7,02	16,25	10,5	19,3	1,05	0,16	0,126	2,59	0,2	0,03	0,03	<0.01	0,04
JS08-2	Hbl gabbro	45,9	13,1	13,65	11	8,77	2,48	0,42	0,059	2,72	0,19	0,32	0,05	0,01	0,38
JS09 Dyke	Lherzolite	42,6	1,51	16,2	6,38	32,2	0,19	0,04	0,347	0,36	0,21	0,03	<0.01	<0.01	-0,23
JS10-1	Hbl gabbro	46	12,95	13,85	11	9,12	2,45	0,41	0,065	2,72	0,19	0,32	0,05	0,01	0,36
JS11-3 Dyke	Px comp	48,2	8,41	10,75	10,1	20,5	1,08	0,06	0,156	0,85	0,16	0,02	0,02	<0.01	0,08
JS12-3	Hbl gabbro	46,7	12,4	13,55	10,9	9,82	2,21	0,29	0,073	2,49	0,19	0,27	0,04	0,01	0,76
JS14-Dyke	Hbl gabbro	45,3	8,06	13,7	7,8	21,3	1,47	0,48	0,126	1,66	0,18	0,19	0,03	0,01	0,23
JS15-Coarse	Hbl gabbro	46,2	11,6	13,1	9,76	13,7	2,33	0,68	0,071	2,52	0,18	0,29	0,04	0,02	0,59
JS15-Fine	Hbl gabbro	46,6	13,8	12,8	10,4	8,88	3,01	0,68	0,039	2,95	0,17	0,37	0,05	0,02	0,62
JS16-3	Px pegmatite	50,3	3,51	13,7	7,47	23,1	0,21	0,01	0,199	0,84	0,22	0,01	<0.01	<0.01	0,06
JS17-2	Repl dunite	37,6	0,48	15,1	2,06	33,5	0,04	<0.01	0,13	0,12	0,18	0,02	<0.01	<0.01	10,3
JS18-3	Wherlite	39,9	0,62	16,25	3,39	37,1	0,06	<0.01	0,162	0,14	0,2	0,01	<0.01	<0.01	0,29
JS19-Dyke	Hbl gabbro	44,5	12,85	13,05	10,6	10,45	2,45	0,54	0,063	2,98	0,17	0,35	0,06	0,02	0,69
JS19-Yellow shear material	Deformation material	39,1	0,64	17,05	0,97	40,2	0,09	0,02	0,048	0,17	0,2	0,03	<0.01	<0.01	-0,33
JS21-2 Hbl Pheno X	Phenocrystic hbl	44,3	5,66	13,7	11	20	0,85	0,14	0,174	3,18	0,18	0,02	0,01	<0.01	0,07
JS07-2	Lherzolite	43,1	6,85	14	8,66	24,7	0,9	0,04	0,146	1,22	0,18	0,01	0,02	<0.01	-0,16

JS09-1	Lherzolite	41,6	1,32	17,1	5,52	33,1	0,18	0,03	0,313	0,31	0,21	0,02	<0.01	<0.01	-0,55
JS_2_2	Px comp	47,5	14,8	8,64	12,4	13,1	2,02	0,09	0,049	0,56	0,12	0,01	0,04	<0.01	0,64
JS_2_4	Dunite	38,7	0,19	17,6	0,67	41,5	0,04	<0.01	0,066	0,04	0,2	0,01	<0.01	<0.01	2,52
JS_2_5	Repl dunite	38,3	0,22	16	0,56	42	0,04	<0.01	0,075	0,04	0,18	0,01	<0.01	<0.01	3,75
JS_2_6	Wherlite	39,5	0,24	17,3	0,5	43,5	0,04	<0.01	0,088	0,04	0,19	0,02	<0.01	<0.01	-0,8
JS_2_8-A	Plag dyke	49,8	24,5	3,03	12,1	4,53	3,94	0,13	0,045	0,27	0,04	<0.01	0,08	0,01	1,61
JS_2_8-B	Lherzolite	46	9,4	10,75	10,9	21,4	1,24	0,06	0,168	0,66	0,14	0,02	0,02	<0.01	0,92
JS_2_9-O	Px dyke	51,3	3,88	10,4	12,9	20,8	0,4	0,01	0,325	0,71	0,18	0,01	<0.01	<0.01	0,3
JS_2_9-Y	Hbl gabbro	45,4	11,95	13,9	10,35	11,4	2,05	0,39	0,097	2,39	0,19	0,26	0,04	0,01	1,44
JS_2_10	Px dyke	44,9	4,37	11,55	14,45	22,5	0,39	<0.01	0,271	1,21	0,16	0,01	<0.01	<0.01	0,45
JS_2_11	Phenocrystic hbl	45,8	6,61	13,25	12,7	19,9	0,88	0,08	0,174	1,28	0,19	0,03	0,01	<0.01	0,22
JS_2_12	Hbl gabbro	53,1	17,95	7,85	7,39	5,7	5,24	0,34	0,023	1,59	0,11	0,39	0,06	0,04	0,7
JS_2_13_3	Repl dunite	38,7	1,15	14,35	3,93	31,8	0,12	<0.01	0,216	0,29	0,17	0,02	<0.01	<0.01	10,1
JS_2_13_4	Wherlite	40,6	1,07	15,8	4,65	35,2	0,15	<0.01	0,246	0,27	0,19	0,01	<0.01	<0.01	2,93
JS_2_13_5	Wherlite	41,6	1,85	15,85	6,78	31	0,22	<0.01	0,228	0,49	0,19	0,02	<0.01	<0.01	-0,19
JS_2_15.G_2	Wherlite	39,9	0,62	16,25	3,3	36,8	0,1	<0.01	0,204	0,13	0,19	0,01	<0.01	<0.01	2,96
JS_2_15.G_3	Wherlite	48	2,76	9,16	15,65	21,8	0,38	<0.01	0,78	0,56	0,15	0,01	<0.01	<0.01	1,24
JS_2_16	Repl dunite	38,7	0,9	14,15	4,27	33,1	0,13	0,01	0,307	0,2	0,17	0,02	<0.01	<0.01	8,59
JS_2_18	Px comp	48,5	4,34	13,05	9	24,3	0,48	0,02	0,237	0,7	0,19	0,01	<0.01	<0.01	0,01
JS_2_19-A	Wherlite	40,3	0,84	20,3	3,29	36,2	0,11	0,01	0,096	0,21	0,22	0,01	<0.01	<0.01	-0,35
JS_2_19-B	Wherlite	40,8	1,03	18,3	4	36,2	0,13	<0.01	0,123	0,27	0,21	0,01	<0.01	<0.01	-0,34
JS_2_19-C	Wherlite	45,1	2,62	13,3	10,8	26,4	0,3	<0.01	0,336	0,68	0,18	0,01	<0.01	<0.01	0,66
JS_2_22	Hbl gabbro	45,4	8,21	14,6	7,8	20,6	1,5	0,52	0,125	1,75	0,18	0,2	0,02	0,01	0,19

Minor and trace elements Ba - Tm

Lables	Rock type	Ba	Ce	Cr	Cs	Dy	Er	Eu	Ga	Gd	Ge	Hf	Ho	La	Lu	Nb	Nd	Pr	Rb	Sm	Sn	Sr	Ta	Tb	Th	Tm
JS01-Dyke	Px comp	9,6	5	1310	<0.01	2,2	1,07	0,69	9	2,37	<5	1,1	0,38	1,6	0,1	2	5,7	0,9	0,4	1,85	1	109,5	0,1	0,33	0,19	0,11
JS01-Country Rock	Wherlite	2,2	1	2100	<0.01	0,39	0,17	0,11	3,4	0,41	<5	0,3	0,07	0,4	0,02	0,4	1,1	0,14	0,2	0,35	<1	26,6	<0.1	0,06	0,1	0,03
JS02-3 Most Gabbroic	Px comp	13	3,1	1020	0,01	1,74	0,86	0,6	11,1	1,83	<5	0,8	0,3	1,1	0,1	<0.2	3,8	0,58	0,3	1,25	<1	211	<0.1	0,26	0,14	0,13
JS03	Phenocrystic hbl	40,7	11,2	850	<0.01	3,59	1,45	1,24	13,2	4,07	<5	2	0,62	3,3	0,15	7,5	12,9	2,16	0,8	3,95	1	213	0,1	0,66	0,22	0,19
JS08-2	Hbl gabbro	103,5	35,7	400	<0.01	5,11	2,35	1,9	20,7	6,23	<5	3,6	0,86	14,6	0,25	18,9	24,3	5,07	2	6,47	1	396	1	0,87	0,56	0,32
JS09 Dyke	Lherzolite	4,9	2,4	2430	<0.01	0,78	0,44	0,23	3,5	0,77	<5	0,4	0,13	0,9	0,04	0,7	2,5	0,37	0,5	0,69	<1	22,4	<0.1	0,1	0,26	0,06
JS10-1	Hbl gabbro	102,5	34,7	420	<0.01	5,2	2,43	1,93	19,8	6,14	<5	3,6	0,88	14,1	0,28	18,4	23,9	5,02	1,7	6,22	1	379	0,8	0,89	0,57	0,3
JS11-3 Dyke	Px comp	19,7	4,4	1110	<0.01	1,98	0,95	0,66	11,1	2,25	<5	1	0,35	1,5	0,11	0,7	5	0,81	0,4	1,66	1	203	<0.1	0,31	0,21	0,14
JS12-3	Hbl gabbro	94,6	29,1	500	0,01	4,82	2,27	1,8	19,5	5,94	<5	3,4	0,88	11,8	0,26	15,6	20,6	4,32	1,9	5,47	1	359	0,6	0,87	0,44	0,29
JS14-Dyke	Hbl gabbro	92,1	27,5	860	0,06	3,08	1,57	1,18	14,2	3,99	<5	2,8	0,57	12,2	0,17	13,6	16,8	3,69	5,5	4,66	1	229	0,5	0,56	0,96	0,2
JS15-Coarse	Hbl gabbro	139	38,8	480	0,2	4,32	1,93	1,79	19,2	5,48	<5	4,3	0,76	17	0,25	21,2	24	5,21	13,5	5,6	2	340	0,9	0,76	1,83	0,29
JS15-Fine	Hbl gabbro	163	41,5	270	0,25	4,91	2,28	1,84	22,9	6,03	<5	4,9	0,9	18,4	0,26	24,8	26,6	5,59	17,8	6,44	1	442	1,3	0,87	2,51	0,3
JS16-3	Px pegmatite	1,5	2,2	1430	<0.01	1,23	0,71	0,36	8,4	1,39	<5	0,7	0,24	0,7	0,09	0,3	2,9	0,43	0,2	0,93	<1	16,2	<0.1	0,21	0,12	0,08
JS17-2	Repl dunite	1,2	0,5	900	<0.01	0,15	0,12	0,06	1,6	0,3	<5	<0.2	0,03	0,2	0,02	<0.2	0,7	0,08	<0.2	0,17	<1	6	<0.1	0,03	0,13	0,01
JS18-3	Wherlite	0,7	0,6	1220	<0.01	0,26	0,15	0,08	1,8	0,42	<5	0,2	0,05	0,3	0,02	<0.2	1	0,13	<0.2	0,3	<1	7,8	<0.1	0,05	0,08	0,02
JS19-Dyke	Hbl gabbro	133	41,6	430	0,04	4,67	2,23	1,9	21,1	6,09	<5	3,9	0,85	18	0,23	23,4	26,1	5,68	4,1	6,17	2	455	1,1	0,85	0,67	0,31
JS19-Yellow shear material	Deformation material	6,1	1,8	310	<0.01	0,18	0,14	0,08	2	0,31	<5	0,3	0,03	0,9	0,03	1,1	1,4	0,24	0,5	0,24	<1	18	<0.1	0,03	0,15	0,01
JS21-2 Hbl Pheno X	Phenocrystic hbl	24,5	11,4	1280	<0.01	3,84	1,72	1,41	12,9	4,73	<5	2,5	0,66	3,2	0,17	8	12,7	2,25	0,8	4,32	1	134	0,4	0,66	0,17	0,24
JS07-2	Lherzolite	14,1	5,1	1070	<0.01	1,99	1,02	0,7	10,6	1,99		1	0,35	1,8	0,12	1,7	5,7	0,98	0,3	1,99	2	187,5	0,2	0,32	<0.05	0,12
JS09-1	Lherzolite	3,3	2,1	2450	<0.01	0,72	0,46	0,2	2,8	0,6		0,3	0,13	0,8	0,04	0,6	2,1	0,34	0,4	0,58	1	16,2	0,1	0,1	<0.05	0,02
JS_2_2	Px comp	32,8	4	360	0,03	1,58	0,91	0,58	15,5	1,56		0,8	0,29	1,6	0,09	0,3	3,8	0,72	0,5	1,6	2	388	0,1	0,26	<0.05	0,07
JS_2_4	Dunite	1,3	0,2	460	<0.01	<0.05	0,07	<0.03	0,8	0,09		<0.2	<0.01	0,2	0,01	<0.2	0,3	0,03	0,3	0,12	1	2,3	0,1	0,01	<0.05	<0.01
JS_2_5	Repl dunite	1	0,4	580	0,01	0,1	0,05	0,03	0,7	0,1		0,2	<0.01	0,2	0,02	0,2	0,3	0,06	0,3	0,09	1	2,3	0,1	<0.01	<0.05	<0.01
JS_2_6	Wherlite	1,4	0,3	650	0,04	<0.05	0,09	<0.03	0,7	<0.05		<0.2	0,02	0,3	0,01	<0.2	0,2	0,04	0,3	0,08	1	2,1	0,1	0,01	<0.05	<0.01
JS_2_8-A	Plag dyke	58,5	4,1	310	0,01	0,55	0,26	0,59	20,2	0,69		0,4	0,1	2,3	0,04	0,3	2,1	0,5	0,9	0,63	2	780	0,1	0,11	0,05	0,03
JS_2_8-B	Lherzolite	18	4,4	1220	<0.01	1,78	1,05	0,61	11,3	1,69		0,7	0,31	1,4	0,11	0,5	5,2	0,77	0,6	1,88	1	222	0,1	0,27	<0.05	0,09

JS_2_9-O	Px dyke	3,2	3,3	2560	0,01	2,14	1,03	0,49	8,3	1,78		0,9	0,42	1,1	0,11	0,3	4	0,64	0,3	1,22	1	30,9	0,1	0,29	<0.05	0,12
JS_2_9-Y	Hbl gabbro	91,4	29,4	720	0,02	4,76	2,17	1,78	19,9	4,95		3,3	0,88	12,2	0,26	16,3	20,8	4,42	2	5,17	3	395	0,9	0,81	0,37	0,28
JS_2_10	Px dyke	1	6,8	2060	0,02	3,03	1,2	1,09	7,7	3,33		2,1	0,5	1,8	0,13	0,3	8,4	1,55	<0.2	2,66	2	38,4	0,2	0,53	<0.05	0,13
JS_2_11	Phenocrystic hbl	20,1	9,5	1240	0,01	3,14	1,29	1,15	10,8	3,87		2	0,54	3	0,17	2	9,3	1,77	1,1	3,09	2	164	0,2	0,56	0,13	0,18
JS_2_12	Hbl gabbro	341	48,1	160	0,1	2,99	1,36	1,64	24,3	3,91		13,9	0,5	30,7	0,19	20	21,2	6,04	5,6	3,94	2	550	1,4	0,52	2,93	0,19
JS_2_13_3	Repl dunite	1,9	1,6	1720	<0.01	0,62	0,28	0,2	2,4	0,66		0,3	0,12	0,8	0,04	0,3	1,8	0,34	0,2	0,54	1	10,7	0,1	0,11	<0.05	0,03
JS_2_13_4	Wherlite	2,7	1,6	1910	0,01	0,56	0,26	0,21	2,5	0,55		0,3	0,11	0,6	0,03	0,3	1,8	0,3	0,3	0,51	1	13,2	0,2	0,09	<0.05	0,03
JS_2_13_5	Wherlite	2,2	2,7	1810	<0.01	1,49	0,63	0,39	4,1	1,54		0,6	0,21	1	0,07	0,3	3,2	0,59	0,2	1	1	18,1	0,1	0,2	0,05	0,06
JS_2_15.G_2	Wherlite	2,1	0,9	1560	0,01	0,36	0,17	0,1	1,4	0,36		0,2	0,05	0,4	0,02	<0.2	0,8	0,18	0,3	0,2	1	7,7	0,1	0,04	<0.05	0,01
JS_2_15.G_3	Wherlite	2,9	3,8	5780	<0.01	1,7	0,66	0,54	5,2	2		0,7	0,3	1,1	0,1	0,4	4	0,75	0,3	1,72	1	34,2	0,1	0,28	<0.05	0,11
JS_2_16	Repl dunite	2,3	1,1	2400	<0.01	0,38	0,15	0,17	2	0,47		0,2	0,08	0,5	0,03	0,2	1,2	0,2	0,2	0,47	1	10,5	0,1	0,07	<0.05	0,03
JS_2_18	Px comp	5,3	3	1800	0,01	1,82	0,9	0,49	7,3	1,81		0,6	0,31	1,2	0,11	0,6	3,7	0,6	0,2	1,29	1	50,2	0,1	0,31	0,06	0,1
JS_2_19-A	Wherlite	1,9	1	670	0,01	0,59	0,19	0,17	1,7	0,52		0,2	0,08	0,4	0,04	<0.2	1	0,2	0,3	0,38	1	7,7	0,1	0,07	<0.05	0,04
JS_2_19-B	Wherlite	0,9	1,4	900	0,01	0,71	0,27	0,25	2,5	0,76		0,3	0,12	0,5	0,04	<0.2	1,6	0,34	0,2	0,52	1	10	0,1	0,12	<0.05	0,03
JS_2_19-C	Wherlite	1,9	3,5	2550	0,02	1,75	0,74	0,62	5	1,74		0,8	0,33	1,1	0,08	0,2	4,2	0,75	0,2	1,3	1	29,4	0,1	0,34	<0.05	0,08
JS_2_22	Hbl gabbro	87,7	25,2	860	0,07	3,03	1,56	1,25	12,9	3,86		2,8	0,53	11,6	0,17	14,2	15,1	3,54	6,6	3,8	2	218	0,8	0,58	0,99	0,17

Minor and trace elements

Lables	Rock type	U	V	W	Y	Yb	Zr	As	Bi	Hg	In	Re	Sb	Se	Te	Tl	Ag	Cd	Co	Cu	Li	Mo	Ni	Pb	Sc	Zn	Au	Pt	Pd	C	S
JS01-Dyke	Px comp	0,05	186	59	9,7	0,79	25	0,1	0,01	0,01	0,006	0,001	<0.05	0,5	0,05	<0.02	<0.5	0,6	92	194	<10	<1	891	<2	34	68	0,004	0,0034	0,003	0,13	0,22
JS01-Country Rock	Wherlite	<0.05	51	61	1,9	0,16	8	0,1	0,01	0,02	0,007	<0.001	<0.05	0,4	0,02	<0.02	<0.5	0,5	158	181	<10	<1	1780	<2	10	98	0,004	0,0024	0,002	0,06	0,09
JS02-3 Most Gabbroic	Px comp	0,32	146	74	7,8	0,74	17	0,1	0,01	0,005	0,005	<0.001	<0.05	0,5	0,04	<0.02	<0.5	0,5	81	137	<10	<1	762	<2	31	63	0,003	0,0019	0,002	0,13	0,12
JS03	Phenocrystic hbl	0,2	276	60	15,1	1,11	55	0,1	0,02	0,015	0,013	0,001	<0.05	0,7	0,02	<0.02	<0.5	0,8	102	116	<10	<1	714	<2	33	85	0,003	0,0017	0,002	0,21	0,45
JS08-2	Hbl gabbro	0,34	270	130	23	1,91	129	<0.1	0,01	0,016	0,021	0,001	<0.05	0,3	<0.01	<0.02	<0.5	0,5	63	79	<10	1	145	<2	29	109	0,002	<0.0005	<0.001	0,14	0,2
JS09 Dyke	Lherzolite	0,25	82	106	3,5	0,34	10	0,1	0,01	<0.005	0,007	<0.001	<0.05	0,4	0,02	<0.02	<0.5	0,5	134	83	<10	<1	1320	<2	19	110	0,006	0,002	0,001	0,13	0,08
JS10-1	Hbl gabbro	0,39	256	57	22	2,03	119	0,1	<0.01	0,013	0,021	0,001	<0.05	0,2	<0.01	<0.02	<0.5	0,8	61	77	<10	1	151	<2	30	111	0,005	<0.0005	<0.001	0,06	0,2
JS11-3 Dyke	Px comp	0,19	169	85	9,3	0,84	23	<0.1	0,01	0,018	0,005	<0.001	<0.05	0,7	0,03	<0.02	<0.5	<0.5	94	130	<10	<1	912	<2	32	57	0,002	0,0019	0,002	0,03	0,18
JS12-3	Hbl gabbro	0,38	258	76	22,4	1,75	114	0,1	0,03	0,018	0,017	0,001	<0.05	1,1	0,02	<0.02	<0.5	0,7	65	116	<10	<1	170	<2	31	103	0,002	<0.0005	<0.001	0,13	0,54
JS14-Dyke	Hbl gabbro	0,41	164	118	15	1,19	114	0,2	0,01	0,008	0,014	<0.001	<0.05	0,4	0,02	<0.02	<0.5	0,7	100	50	<10	1	929	<2	22	106	0,002	0,0008	0,001	0,13	0,13
JS15-Coarse	Hbl gabbro	0,67	243	81	21,4	1,57	174	0,2	0,02	0,016	0,016	0,002	<0.05	0,7	0,03	0,02	<0.5	0,7	76	155	<10	1	486	3	27	82	0,001	<0.0005	<0.001	0,13	0,25
JS15-Fine	Hbl gabbro	0,9	286	69	23,2	1,83	201	0,1	0,02	0,014	0,023	0,002	<0.05	0,6	0,02	0,04	<0.5	0,7	59	271	<10	2	210	<2	28	57	0,002	<0.0005	<0.001	0,13	0,29
JS16-3	Px pegmatite	0,14	202	73	6,7	0,7	15	<0.1	0,03	<0.005	0,005	0,001	<0.05	0,6	0,05	<0.02	<0.5	0,6	89	249	<10	<1	552	<2	41	89	0,003	0,0012	0,002	0,03	0,04
JS17-2	Repl dunite	0,11	25	8	1,2	0,07	2	<0.1	0,02	<0.005	0,01	<0.001	<0.05	0,4	0,05	<0.02	<0.5	0,5	148	119	<10	<1	1850	<2	10	85	0,004	0,0178	0,031	0,1	0,04
JS18-3	Wherlite	0,12	41	50	1,5	0,13	3	0,1	0,02	0,006	0,007	0,002	<0.05	1	0,02	<0.02	<0.5	0,7	159	145	<10	<1	1880	<2	13	94	0,006	0,0263	0,013	0,07	0,09
JS19-Dyke	Hbl gabbro	0,3	276	89	22,6	1,79	145	<0.1	0,02	0,005	0,029	0,001	<0.05	0,9	0,01	<0.02	<0.5	0,7	64	136	<10	1	283	<2	28	89	0,002	0,001	0,001	0,14	0,27
JS19-Yellow shear material	Deformation material	0,12	25	88	1,3	0,13	7	<0.1	0,02	<0.005	0,008	<0.001	<0.05	1	0,03	<0.02	<0.5	0,5	163	45	10	<1	2610	3	7	129	0,002	0,0055	0,008	0,2	0,04
JS21-2 Hbl Pheno X	Phenocrystic hbl	0,08	284	92	17,1	1,36	70	<0.1	0,02	<0.005	0,009	0,001	<0.05	1,4	0,05	<0.02	<0.5	0,8	93	233	<10	<1	902	3	36	67	0,005	0,0044	0,003	0,14	0,24
JS07-2	Lherzolite	<0.05	150	<1	9	0,73	25																				<0.001	<0.005	0,002		
JS09-1	Lherzolite	<0.05	93	<1	3,3	0,32	9																				<0.001	<0.005	0,002		
JS_2_2	Px comp	<0.05	143	<1	6,9	0,59	14																				<0.001	<0.005	0,001		
JS_2_4	Dunite	<0.05	6	1	0,4	0,07	<2																				0,002	<0.005	0,001		
JS_2_5	Repl dunite	<0.05	<5	<1	0,5	0,09	2																				<0.001	<0.005	0,001		
JS_2_6	Wherlite	<0.05	<5	<1	0,4	0,08	<2																				0,002	0,006	0,003		
JS_2_8-A	Plag dyke	<0.05	38	<1	2,7	0,24	6																				0,001	<0.005	0,001		
JS_2_8-B	Lherzolite	<0.05	135	<1	8,2	0,63	17																				0,004	<0.005	0,005		

JS_2_9-O	Px dyke	<0.05	250	<1	9,8	0,85	18																				<0.001	<0.005	0,002		
JS_2_9-Y	Hbl gabbro	0,1	267	<1	23,1	2,02	114																				<0.001	<0.005	<0.001		
JS_2_10	Px dyke	<0.05	247	1	12,1	0,85	41																				0,002	0,005	0,004		
JS_2_11	Phenocrystic hbl	<0.05	236	1	14,2	0,93	47																				<0.001	<0.005	0,001		
JS_2_12	Hbl gabbro	0,93	152	2	14,5	1,23	789																				<0.001	<0.005	0,001		
JS_2_13_3	Repl dunite	<0.05	78	1	3,2	0,24	8																				0,001	<0.005	0,002		
JS_2_13_4	Wherlite	<0.05	92	2	2,9	0,22	8																				<0.001	0,006	0,001		
JS_2_13_5	Wherlite	<0.05	98	1	6,1	0,51	13																				0,001	<0.005	0,004		
JS_2_15.G_2	Wherlite	<0.05	34	1	1,4	0,11	3																				0,001	<0.005	0,001		
JS_2_15.G_3	Wherlite	<0.05	53	2	7,1	0,55	14																				0,001	0,006	0,005		
JS_2_16	Repl dunite	<0.05	70	2	2,1	0,19	5																				<0.001	<0.005	0,002		
JS_2_18	Px comp	<0.05	200	1	8,4	0,73	17																				0,005	0,006	0,005		
JS_2_19-A	Wherlite	<0.05	47	2	2,4	0,24	5																				<0.001	<0.005	0,002		
JS_2_19-B	Wherlite	<0.05	58	2	3,1	0,27	9																				0,001	0,005	0,002		
JS_2_19-C	Wherlite	<0.05	150	2	7,5	0,44	16																				0,001	0,005	0,004		
JS_2_22	Hbl gabbro	0,31	191	2	14,1	1,18	113																				<0.001	<0.005	<0.001		

10 Appendix D – EPMA results

Plag analyses

		Na2O(wt%)	MgO(wt%)	Al2O3(wt%)	CaO(wt%)	TiO2(wt%)	SrO(wt%)	BaO(wt%)	FeO(wt%)	K2O(wt%)	SiO2(wt%)	MnO(Mass%)	Total(Mass%)
4	plag_js12_a1-1	5,84	0,0622	27,63	9,64	0	0,1067	0,0085	0,5083	0,2137	56,23	0,0029	100,2423
5	plag_js12_a1-2	5,94	0,0658	27,71	9,59	0,0225	0,1027	0	0,2661	0,2682	56,12	0	100,0853
6	plag_js12_a1-3	5,72	0,0529	27,58	9,95	0	0	0	0,1433	0,2342	55,74	0,029	99,4494
7	plag_js12_a1-4	5,32	0	28,6	10,62	0	0,0325	0,0046	0,1144	0,1876	54,97	0,001	99,8501
8	plag_js12_a1-5	5,78	0,0154	27,86	9,98	0	0	0	0,172	0,2083	56,16	0	100,1757
9	plag_js12_a1-6	5,82	0	27,55	9,64	0,0052	0	0,0032	0,2033	0,2177	56,78	0	100,2194
10	plag_js12_a1-7	5,8	0,0159	27,72	9,97	0,0152	0,0743	0	0,2685	0,1956	55,72	0	99,7795
11	plag_js12_a1-8	5,57	0	27,77	9,81	0,0167	0,1146	0	0,1752	0,1996	56,33	0,0019	99,988
12	plag_js12_a1-9	5,76	0	27,95	10	0,014	0,0219	0	0,1816	0,2141	56,2	0,0242	100,3658
13	plag_js12_a1-10	5,85	0,0535	27,8	9,97	0,0259	0	0	0,1596	0,2532	56,11	0,0048	100,227
14	plag_js12_a1-11	5,69	0,1418	27,43	9,87	0,1303	0	0,0025	0,3373	0,2335	56,15	0,001	99,9864
15	plag_js12_a1-12	5,78	0	27,61	9,74	0,0036	0,033	0	0,1276	0,2309	56,96	0	100,4851
16	plag_js12_a1-13	5,58	0	27,64	9,86	0	0,1158	0,002	0,1328	0,2234	56,47	0,0281	100,0521
17	plag_js12_a1-14	5,85	0,0092	27,6	9,66	0	0	0	0,1081	0,1938	56,01	0,0222	99,4533
18	plag_js12_a1-15	5,6	0,1909	27,58	9,97	0,0003	0,0783	0,012	0,3249	0,2595	55,82	0,0232	99,8591
19	plag_js12_a1-16	5,7	0	27,77	10,01	0,0033	0,0566	0,0053	0,2074	0,2136	56,23	0,0145	100,2107
20	plag_js12_a1-17	5,79	0	27,9	10	0,0061	0,0557	0,0064	0,1593	0,2487	55,63	0	99,7962
21	plag_js12_a1-18	5,7	0,1447	27,57	9,93	0,01	0,1743	0	0,1978	0,2022	55,11	0,0387	99,0777
22	plag_js12_a1-19	5,75	0	27,76	9,8	0	0,3957	0	0,2937	0,2619	55,24	0,0232	99,5245
23	plag_js12_a1-20	5,61	0,0298	27,81	9,96	0,024	0	0	0,2162	0,1995	56,28	0,0116	100,1411
24	plag_js12_a1-21	5,79	0,0252	27,77	9,79	0,0203	0	0,0376	0,3032	0,198	56,24	0,0068	100,1811
25	plag_js12_a1-22	5,98	0,0026	27,47	9,42	0,024	0,1546	0,0183	0,3617	0,2475	57,25	0,0029	100,9316
26	plag_js12_a1-23	5,05	2,92	23,5	9,36	0,6926	0,0417	0	4,06	0,8233	53,69	0,0491	100,1867
27	plag_js12_a1-24	6,17	0,0835	26,99	8,92	0,031	0,0515	0	0,4383	0,1903	58,07	0	100,9446

28	plag_js12_a1-25	6,14	0,0005	26,75	9	0,0267	0,074	0,0072	0,3681	0,2312	57,65	0	100,2477
29	plag_js12_a1-26	6,11	0,0165	26,9	9,01	0,0276	0,1358	0,0406	0,367	0,2073	57,55	0,0039	100,3687
30	plag_js12_a1-27	6,13	0,0031	27,05	9,17	0,2632	0,1115	0,0662	0,603	0,2535	56,7	0	100,3505
31	plag_js12_a1-28	6,23	0,4071	24,94	9,38	0,2246	0,1065	0	1,0836	0,2134	56,37	0,0454	99,0006
35	plag_js12_a2-1	7,03	0	25,52	7,45	0,0245	0,053	0,0282	0,0312	0,3657	59,47	0,0097	99,9823
36	plag_js12_a2-2	6,65	0,4437	25,67	7,76	0	0,015	0	0,1626	0,3176	58,5	0	99,5189
37	plag_js12_a2-3	6,83	0	26,14	7,88	0	0,0277	0	0,0689	0,3253	58,57	0	99,8419
38	plag_js12_a2-4	7,37	0,6743	24,19	6,6	0,0003	0,1657	0	0,2159	0,4063	59,51	0,0222	99,1547
39	plag_js12_a2-5	7,33	0,3956	24,66	6,63	0,006	0	0	0,1016	0,3789	59,31	0	98,8121
40	plag_js12_a2-6	7,51	0,0067	24,42	6,35	0	0,0311	0,0172	0,0295	0,4339	60,46	0,0009	99,2593
41	plag_js12_a2-7	7,18	0,0067	24,85	7,13	0,0024	0,026	0,0195	0,0384	0,3382	59,5	0	99,0912
42	plag_js12_a3-1	5,84	0	27,6	9,73	0,0057	0,111	0,0202	0,1912	0,1962	56,31	0	100,0043
43	plag_js12_a3-2	5,8	0	27,75	9,78	0,0061	0,0398	0,026	0,109	0,1865	55,85	0	99,5474
44	plag_js12_a3-3	5,67	0	27,34	9,57	0,0112	0,0458	0,0518	0,136	0,6447	56,58	0	100,0495
45	plag_js12_a3-4	5,67	0	27,85	10,06	0,0233	0,0082	0,0192	0,0783	0,1683	56,61	0,0029	100,4902
46	plag_js12_a3-5	5,5	0,0977	27,52	10,05	0,0713	0,0042	0,0174	0,1992	0,1581	55,32	0,0145	98,9524
47	plag_js12_a3-6	5,5	0	27,86	10,16	0,0237	0,0243	0,0081	0,0864	0,1667	55,97	0	99,7992
48	plag_js12_a3-7	5,62	0	27,93	10,22	0,0173	0,0402	0	0,0861	0,1785	55,61	0	99,7021
49	plag_js12_a3-8	5,76	0	27,82	9,98	0	0,06	0	0,1248	0,1772	55,66	0	99,582
50	plag_js12_a3-9	5,89	0,0097	27,58	9,56	0,0295	0,0678	0	0,1464	0,2045	56,59	0,0145	100,0924
51	plag_js12_a3-10	6	0	27,24	9,51	0,0224	0,0571	0,0005	0,1689	0,1739	56,23	0,0116	99,4144
52	plag_js12_a3-11	5,55	0,084	27,78	10,32	0,0183	0,2721	0,0316	0,3055	0,2041	55,4	0,0183	99,9839
53	plag_js12_a3-12	5,53	0,771	26,41	10,89	0	0	0,0102	0,5364	0,1794	53,81	0	98,137
54	plag_js12_a3-13	5,64	1,0034	27,02	9,57	0,0133	0,1249	0,0076	0,5953	0,1683	55,51	0,0058	99,6586
55	plag_js12_a3-14	5,5	0	28,02	10,22	0,0216	0,0554	0	0,1299	0,1762	55,93	0	100,0531
56	plag_js12_a3-15	5,47	0	28,03	10,27	0,014	0	0	0,1013	0,1639	55,7	0,0309	99,7801
57	plag_js12_a3-16	5,65	0,0112	27,9	10,05	0,0094	0,1122	0,032	0,0758	0,1566	56,42	0,0202	100,4374
58	plag_js12_a3-17	5,67	0,0051	27,78	10,06	0,0477	0	0	0,0751	0,1978	55,41	0	99,2457
59	plag_js12_a3-18	5,79	0,0169	27,66	9,82	0,004	0,1339	0,0279	0,0811	0,2124	56,23	0	99,9762
60	plag_js12_a3-19	5,78	0	27,7	9,75	0,0073	0	0	0,0972	0,2025	56,56	0,0212	100,1182

61	plag_js12_a3-20	5,89	0,0031	27,68	9,78	0,0133	0,0196	0	0,1462	0,1795	56,65	0,0202	100,3819
62	plag_js12_a3-21	5,45	0,587	27,36	9,74	0	0,1378	0	0,6035	0,206	55,43	0,0183	99,5326
63	plag_js12_a3-22	5,65	0,0208	27,75	9,94	0,0196	1,66	0	0,0876	0,1671	55,26	0,0115	100,5666
64	plag_js12_a3-23	5,92	0	27,66	9,77	0,0067	0,1025	0,0029	0,1149	0,1759	56,23	0	99,9829
65	plag_js12_a3-24	5,4	1,81	23,98	8,84	0,1119	0	0	1,004	0,2707	52,32	0	93,7366
72	plag_js12_tach1	5,85	0,0119	27,28	9,56	0,0554	0,0649	0,0404	1,086	0,2333	54,92	0,0212	99,1231
73	plag_js14_a1-1	5,52	0,0072	28,26	10,2	0	0,3417	0,0072	0,2996	0,0401	54,24	0,0058	98,9216
74	plag_js14_a1-2	5,53	0,0113	28,19	10,25	0	0,3214	0	0,1853	0,0659	55,24	0	99,7939
75	plag_js14_a1-3	5,87	0,001	27,34	9,15	0,0091	0,2679	0,0209	0,1048	0,1036	55,08	0	97,9473
76	plag_js14_a1-4	5,28	1,0632	25,87	10,94	0,0371	0,3134	0,0014	0,3348	0,1003	52,09	0,027	96,0572
77	plag_js14_a1-5	5,22	0	28,37	10,29	0,0024	0,301	0	0,1153	0,0885	53,65	0	98,0372
78	plag_js14_a1-6	4,54	0,0051	29,57	11,81	0,0061	0,1954	0,0091	0,1116	0,0583	53	0,0058	99,3114
79	plag_js14_a1-7	5,56	0	27,89	9,79	0,0015	0,2869	0	0,0598	0,0618	55,23	0	98,88
80	plag_js14_a1-8	5,85	0,0103	27,39	9,35	0,004	0,3537	0	0,0857	0,1018	55,36	0,001	98,5065
81	plag_js14_a1-9	5,72	0,0103	27,52	9,6	0,0021	0,2466	0,0187	0,1699	0,1077	55,94	0,0145	99,3498
82	plag_js14_a1-10	5,71	0,0118	27,89	9,62	0,0124	0,3085	0,0237	0,1155	0,0814	55,37	0,0184	99,1617
4	area_1_plag_1	6,43	0	26,5	8,79	0,0136			0,077	0,1256	57,16	0,018	99,2021
5	area_1_plag_2	6,28	0,0191	26,51	9,01	0,0155			0,1307	0,1431	57	0	99,1084
6	area_1_plag_3	5,6	3,12	21,63	12,12	0,0089			1,0506	0,1178	48,44	0,0371	92,1278
7	area_1_plag_4	6,16	0,0184	26,86	9,39	0,0311			0,0805	0,1495	56,85	0	99,5395
8	area_1_plag_5	5,96	0	27,06	9,53	0,0026			0,0631	0,1279	56,68	0,0102	99,4622
9	area_1_plag_6	5,32	0	28,17	10,79	0,0662			0,0942	0,0846	54,9	0	99,425
10	area_1_plag_7	5,8	0	27,53	10,08	0,0197			0,03	0,1211	55,87	0	99,4508
11	area_1_plag_8	5,51	0	27,87	10,4	0,004			0,0302	0,1249	55,55	0,0215	99,5474
12	area_1_plag_9	5,62	0	27,65	10,25	0,0042			0,0449	0,1041	55,05	0,0102	98,7539

13	area_1_plag_10	6,46	0	26,24	8,6	0,0216			0,1455	0,1341	57,87	0	99,4712
14	area_1_plag_11	6,24	0	26,73	9,05	0			0,0806	0,1264	57,12	0,0091	99,3871
15	area_1_plag_12	6,25	0	26,76	9,08	0,0327			0,0246	0,1283	56,86	0,0023	99,1496
16	area_1_plag_13	6,04	0	27	9,38	0,0188			0,0617	0,1267	56,39	0	99,0172
17	area_1_plag_14	6,11	0	26,92	9,39	0,0102			0,107	0,1206	56,74	0,0057	99,4035
18	area_1_plag_15	6,09	0	26,83	9,49	0,0129			0,0321	0,1301	56,94	0	99,5506
19	area_1_plag_16	6,11	0	26,73	9,09	0,0276			0,0823	0,1083	56,78	0	98,9403
20	area_1_plag_17	6,7	0	26,17	8,51	0,0026			0,2566	0,1292	57,47	0	99,2418
21	std_ol2	0	52,31	0	0,0083	0,0105			6,57	0,0026	40,76	0,1363	100,2448
22	std_di2	0,0133	18,33	0,048	25,69	0,0853			0,0212	0,0072	55,04	0,0477	99,3151
23	std_ab2	11,46	0	19,66	0,3451	0,0027			0,0139	0,1989	69,11	0,0045	100,8308
24	area_2_plag_1	6,03	0,0019	27,05	9,45	0,0441			0,2278	0,1413	56,68	0,0193	99,6545
25	area_2_plag_2	5,78	0	27,56	10,17	0,0178			0,1742	0,1136	56,13	0,017	99,971
26	area_2_plag_3	6,14	0	26,89	9,37	0,0023			0,1618	0,1389	56,69	0	99,393
27	area_2_plag_4	6,82	0	25,28	7,98	0,0246			0,657	0,1478	57,28	0,0215	98,2109
28	area_2_plag_5	7,25	0	25,2	7,46	0,0386			0,2755	0,1821	59,45	0,0057	99,8619
29	area_2_plag_6	7,02	0,0112	25,44	7,54	0,0307			0,2968	0,1555	59,08	0,0136	99,5878
30	area_2_plag_7	7,22	0,6124	24,32	6,96	0,3306			0,9045	0,1831	58,79	0,0192	99,3632
31	area_2_plag_8	6,65	0	26,24	8,45	0,0156			0,1928	0,1655	57,42	0,0204	99,18
32	area_2_plag_9	5,07	0	28,6	11,33	0,0335			0,1443	0,0979	53,97	0,0068	99,2687
33	area_2_plag_10	5,21	0	28,26	11,11	0,0228			0,0825	0,1037	54,61	0,0091	99,4081
34	area_2_plag_11	6,28	0	26,69	9,1	0,0365			0,1526	0,156	57,43	0,0045	99,8496
35	area_2_plag_12	6,59	0	26,04	8,48	0,0139			0,1562	0,1666	57,57	0	99,0167
36	area_2_plag_13	6,08	0	26,61	9,47	0,0219			0,0575	0,1259	57,13	0	99,4953
37	std_ol3	0,0119	52,39	0	0,0158	0,008			6,45	0,0062	41,21	0,0831	100,5964
38	std_di3	0,0068	18,26	0,0473	25,69	0,0819			0,0726	0,0009	55,26	0,0306	99,4904
39	std_ab3	11,59	0	19,77	0,3722	0,0071			0,0113	0,1756	68,92	0	100,8655
46	area_4_plag_1	6,41	0	26,56	9,02	0,009			0,0821	0,1259	57,16	0	99,3696
47	area_4_plag_2	5,28	2,19	23,65	12,58	0,0479			0,8502	0,1134	49,07	0,0486	93,8301
48	area_4_plag_3	5,09	0,3152	28,16	10,83	0,3069			0,4711	0,4567	53,81	0,0113	99,5066

49	area_4_plag_4	5,94	0	27,24	9,65	0,0118			0,0988	0,1204	56,74	0	99,8177
50	area_4_plag_5	6,02	0	27,1	9,41	0,0285			0,2356	0,1253	56,76	0,0113	99,7141
51	std_ol4	0,1838	52,4	0	0,0069	0,0043			6,43	0	41,09	0,0537	100,6036
52	std_di4	0,0189	18,43	0,0638	25,53	0,1693			0,0319	0,0039	54,96	0,0553	99,3142
53	std_ab4	11,49	0	19,75	0,3807	0			0,0135	0,1913	69,23	0	101,0607
54	07_a_1_plag1	4,61	0	29,19	12,15	0,0752			0,049	0,0274	53,04	0	99,1586
55	07_a_1_plag2	4,56	0	29,66	12,28	0,0622			0,0965	0,0243	52,75	0,0045	99,4375
56	07_a_1_plag3	4,65	0	29,22	12,04	0,0706			0,0382	0,0075	53,18	0,0271	99,2531
57	07_a_1_plag4	4,84	0,0175	29,19	11,8	0,055			0,0198	0,0109	53,67	0,0192	99,6258
58	07_a_1_plag5	4,45	0	29,36	12,19	0,05			0,0561	0,0205	53,24	0	99,3829
59	07_a_1_plag6	4,55	0,0043	29,67	12,41	0,0448			0,1308	0,0334	52,69	0	99,5804
60	07_a_1_plag7	4,49	0	29,47	12,31	0,0888			0,1579	0,0057	52,27	0	98,8437
61	07_a_1_plag8	4,59	0	29,51	12,21	0,0548			0,1123	0,017	52,59	0	99,0841
62	07_a_1_plag9	4,52	0	29,32	12,31	0,0278			0,1208	0,0227	53,07	0	99,403
63	07_a_1_plag10	2,17	0,2921	32,45	16,45	0,0143			0,1011	0,0132	47,1	0	98,6078
64	07_a_1_plag11	2,39	0	32,75	15,99	0,0161			0,1144	0,0068	47,96	0	99,2349
65	07_a_1_plag12	2,49	0	32,56	15,7	0,0223			0,1043	0	48,25	0,009	99,1473
66	07_a_1_plag13	2,76	0	32,1	15,22	0,0363			0,1739	0,0156	49,01	0	99,332
67	07_a_1_plag14	3,09	0	31,8	14,71	0,0084			0,1383	0,0058	49,82	0	99,5808
68	07_a_1_plag15	4,21	0	29,65	12,55	0,05			0,1249	0,0554	51,84	0	98,4803
69	07_a_1_plag16	4,56	0	29,42	12,15	0,0921			0,1205	0,0227	53,06	0,009	99,4343
70	07_a_1_plag17	4,55	0,0132	29,46	12,31	0,0876			0,135	0,0238	52,39	0,0101	98,9797
71	07_a_1_ex1	0,4455	16,67	26,8	12,35	0,051			10,03	0	33,12	0,1497	99,7796
72	07_a_1_ex2	0,7331	15,28	18,57	17,1	0,3703			7	0,0042	40,71	0,1216	100,1326
73	07_a_1_ex3	0,5301	15,95	3,05	23,14	0,0459			4,19	0	52,46	0,0718	99,4514
74	07_a_1_ex4	0,2237	21,13	22,83	5,94	0,0438			12,57	0	36,89	0,1527	99,8795
75	07_a_1_plag18	3,35	0	30,99	14,12	0,0384			0,1492	0,017	50,58	0	99,2596
76	07_a_1_plag19	4,16	0	30,14	12,99	0,0165			0,0758	0,0102	52,07	0	99,4808
77	07_a_1_plag20	2,42	0,0096	32,48	15,88	0,022			0,0812	0,004	48,19	0	99,0868
78	07_a_1_plag21	4,21	0	29,71	12,61	0,0651			0,0147	0,0258	52,47	0	99,1056

79	07_a_1_plag22	3,83	0	30,45	13,46	0,0185			0,0379	0,0086	51,47	0,009	99,2977
80	07_a_1_plag23	4,31	0	29,8	12,68	0,0513			0,0749	0,0157	52,42	0,0181	99,37
81	07_a_1_plag24	4,23	0	29,9	12,78	0,0219			0,0624	0,0173	52,38	0,0282	99,4264
82	07_a_1_plag25	4,5	0,0231	29,5	12,46	0,0251			0,2449	0,0111	52,73	0,0101	99,5146
83	std_ol5	0,0027	52,36	0	0,0105	0,0047			6,56	0	41,14	0,0649	100,5427
84	std_di5	0,04	18,27	0,0596	25,25	0,123			0,0729	0,0093	55,27	0,0577	99,1789
85	std_ab5	11,56	0	19,77	0,3556	0,0107			0,0068	0,1639	69,11	0,0158	100,9928
86	07_a2_plag1	4,42	0,5347	28,53	12,56	0,2274			0,3826	0,0361	51,02	0	97,7341
87	07_a2_plag2	4,57	0,0098	29,53	12,2	0,0443			0,0757	0,0197	53,16	0,0147	99,6345
88	07_a2_plag3	4,38	0,0053	29,63	12,3	0,0865			0,1158	0,0172	52,45	0,0045	98,9977
89	07_a2_plag4	4,4	0	29,89	12,48	0,1303			0,0912	0,0183	52,49	0,0079	99,5077
90	07_a2_plag5	3,73	0,036	30,77	13,82	0,0509			0,1981	0,0264	50,43	0,009	99,0905
91	07_a2_plag6	4,46	0,0158	29,61	12,31	0,1146			0,2097	0,0306	53,17	0,0011	99,9294
92	07_a2_plag7	4,47	0,0091	29,63	12,22	0,0394			0,1563	0,016	53,23	0	99,7775
93	07_a2_plag8	4,41	0,0007	29,72	12,32	0,0388			0,1506	0,0157	52,77	0	99,4308
94	07_a2_plag9	4,7	0,0187	29,49	11,86	0,0194			0,2312	0,0225	53,47	0	99,8152
95	07_a2_plag10	2,51	0	32,7	15,87	0,0405			0,2311	0,0259	48,51	0	99,8908
96	07_a2_plag11	4,4	0,0057	29,87	12,43	0,0259			0,0965	0,0213	52,56	0,0022	99,4617
97	07_a2_plag12	4,48	0,0328	29,9	12,35	0,0393			0,0862	0,0334	52,54	0	99,4701
98	07_a2_plag13	4,5	0,0108	29,78	12,38	0,0724			0,1601	0,0176	52,97	0	99,8969
99	07_a2_plag14	4,37	0	29,63	12,3	0,0522			0,1089	0,0213	53,03	0,0362	99,5486
100	07_a2_plag15	3,64	0,0021	30,86	13,7	0,0581			0,0652	0,0045	50,78	0	99,1099
101	07_a2_plag16	4,47	0	29,76	12,42	0,0407			0,0667	0,0083	53,12	0	99,889
102	07_a2_plag17	4,59	0	29,5	12,21	0,0293			0,0277	0,0067	53,1	0	99,4637
103	07_a2_plag18	4,53	0	29,73	12,34	0,0414			0,0334	0,0079	53,27	0	99,9694
104	07_a2_plag19	4,39	0	29,86	12,48	0,0555			0,0507	0,0134	52,74	0,017	99,6109
105	07_a2_plag20	4,44	0	29,62	12,31	0,037			0,1508	0,0142	52,79	0	99,362
106	07_a2_plag21	4,55	0	29,65	12,36	0,0373			0,2301	0,012	52,37	0	99,2111
107	07_a2_plag22	4,47	0	29,55	12,32	0,0611			0,1161	0,019	53,3	0,0272	99,8785
108	07_a2_plag23	4,66	2,5	24,91	13,69	0,0117			0,6172	0,0271	47,12	0,0418	93,613

109	07_a2_plag24	4,49	0	29,5	12,12	0,0531			0,1977	0,0124	52,74	0,0203	99,1653
110	07_a2_plag25	4,42	0	29,67	12,27	0,0189			0,1339	0,0114	52,5	0,0057	99,07
111	07_a2_plag26	4,04	0	30,2	13	0,0217			0,1014	0	51,67	0	99,0431
112	07_a2_plag27	4,52	0,0191	29,56	12,27	0,0013			0,0961	0,014	52,92	0,0079	99,4134
113	07_a2_plag28	3,33	0	31,27	14,51	0			0,0336	0,0203	50,16	0	99,3239
114	07_a2_plag29	4,7	0,0187	29,29	12,01	0,0423			0,0516	0,0149	53,24	0,026	99,3935
115	07_a2_plag30	4,61	0	29,32	12,04	0,0624			0,0942	0,0114	53,25	0	99,4277
116	07_a2_plag31	5,11	0	28,77	11,36	0,0185			0,1475	0,007	53,88	0,0113	99,321
117	07_a2_plag32	4,5	0,0355	29,62	12,28	0,0176			0,184	0,0299	52,81	0	99,5004
118	07_a2_plag33	4,44	0,0179	29,61	12,3	0,0055			0,1655	0,016	52,6	0,0272	99,1854
119	07_a2_plag34	3,68	0,0736	23,13	21,02	0,0834			0,1707	0,0117	41,61	0,0023	89,7917
120	07_a2_plag35	4,94	0	28,93	11,31	0,0179			0,1323	0,0251	53,01	0,0339	98,4259
121	std_ol5	0,0076	52,97	0	0,0043	0,0257			6,69	0,0033	40,54	0,1045	100,7561
122	std_di5	0,0316	18,46	0,0549	25,78	0,0784			0,0176	0,0003	55,88	0,0409	100,3506
123	std_ab5	11,39	0,0036	19,6	0,2489	0,0158			0,0192	0,1729	69,68	0,0204	101,1726
124	2_8_carb1	0,0086	19,8	0,0048	28,88	0,0169			2,85	0,0004	0,009	0,1991	51,7688
125	2_8_carb2	0,0258	20	0,0013	29,07	0,0041			2,73	0	0,0045	0,1274	51,988
126	2_8_carb3	0,0178	19,9	0	28,91	0			2,73	0,003	0,0196	0,1475	51,7379
127	2_8_carb4	0	19,62	0	28,96	0			2,81	0	0,0526	0,1432	51,6158
128	2_8_carb5	0,0129	19,88	0	28,92	0,0176			2,71	0,0014	0,0196	0,1421	51,7103
129	2_8_carb6	0	19,92	0,002	28,93	0,0043			2,7	0	0,012	0,1634	51,7317
130	2_8_carb7	0	19,85	0	28,94	0,0016			2,73	0	0,0211	0,1633	51,706
131	2_8_carb8	0	19,6	0	28,99	0,0173			2,91	0	0,0301	0,1778	51,7335
132	2_8_a1_plag1	4,33	0	30,1	12,72	0,0415			0,0778	0,0051	52,49	0,0102	99,7746
133	2_8_a1_plag2	3,41	0	31,13	14,2	0			0,0171	0,0104	51,35	0	100,1175
134	2_8_a1_plag3	4,5	0,0169	29,71	12,42	0,0199			0,0435	0,0261	53,25	0	99,9984
135	2_8_a1_plag4	4,48	0	29,95	12,51	0,0252			0,0522	0,0186	53,34	0,0192	100,3952
136	2_8_a1_plag5	2,72	0	32,19	15,39	0,0221			0,0979	0,0261	49,21	0	99,6561
137	2_8_a1_plag6	4,6	0,0145	29,64	12,37	0,0399			0,0673	0,0144	53,54	0	100,2896
138	2_8_a1_plag7	4,4	0	29,87	12,49	0,0292			0,0851	0,012	53,18	0	100,0663

139	2_8_a1_plag8	4,43	0,0135	29,67	12,42	0,0715			0,0267	0,0126	52,79	0,0158	99,4501
140	2_8_a1_plag9	2,21	0	33,1	16,32	0,0242			0,0115	0	48	0	99,6875
141	2_8_a1_plag10	4,07	0	30,41	13,2	0,0207			0,1668	0,013	51,98	0,0238	99,8972
142	2_8_a1_plag11	4,22	0,0003	30,1	12,9	0,0289			0,1338	0,0108	52,49	0,0147	99,8985
143	2_8_a1_plag12	4,2	0,0104	30,01	12,86	0,0513			0,1066	0,0222	52,05	0,0475	99,358
144	2_8_a1_plag13	3,37	0	30,9	14,05	0,0354			0,1097	0,051	50,37	0,0068	98,93
145	2_8_a1_plag14	1,42	6,14	21,64	20,05	0,3192			1,64	0,0058	49,2	0,0565	100,6051
146	2_8_a1_plag15	0,5834	13,01	7,6	23,19	0,6208			3,65	0,0002	50,98	0,1005	100,0521
147	std_ol6	0	52,1	0	0	0			6,49	0	40,99	0,1236	100,1341
148	std_di6	0,0027	18,51	0,0543	25,93	0,089			0,0698	0	55,47	0,0828	100,2422
149	std_ab6	11,52	0	19,07	0,2585	0,0012			0	0,1447	69,51	0	100,5433
150	2_8_a2_plag1	4,04	10,56	16,33	9,9	2,11			7,12	0,8299	47,35	0,0683	98,734
151	2_8_a2_plag2	4,26	9,27	17	9,29	2,28			6,48	0,7223	48,85	0,0426	98,4215
152	2_8_a2_plag3	5,48	5,41	21,06	8,24	1,2128			4,58	0,3998	52,04	0,0326	98,6288
153	2_8_a2_plag4	5,74	5,72	20,94	8,04	1,5133			2,93	0,7551	53,2	0,0237	99,0912
154	2_8_a2_plag5	4,35	0	29,84	12,57	0,0927			0,0403	0,0451	52,91	0,0227	99,8777
155	2_8_a2_plag6	4,44	0,0215	29,81	12,54	0,0331			0,0441	0,0473	53,39	0	100,3303
156	2_8_a2_plag7	4,53	0	29,69	12,29	0,0226			0,0068	0,0506	53,42	0	100,0281
157	2_8_a2_plag8	4,83	0	29,31	11,78	0,045			0,0453	0,0806	53,37	0,0034	99,5141
158	2_8_a2_plag9	4,67	0	29,3	11,94	0,0648			0,0175	0,0678	52,96	0	99,0201
159	2_8_a2_plag10	4,58	0	29,6	12,26	0,0437			0,0204	0,0788	53,12	0,0113	99,7159
160	2_8_a2_plag11	4,55	0	29,52	12,23	0,0572			0,0299	0,0623	53,53	0,0091	99,9885
161	2_8_a2_plag12	4,58	0	29,63	12,33	0,0503			0,0303	0,058	53,51	0	100,2076
162	2_8_a2_plag13	6,86	0	26,17	8,22	0,0263			0,223	0,0976	58,96	0	100,5755

Pyroxene analyses

Point	Comment	Na2O(Mass%)	MgO(Mass%)	Al2O3(Mass%)	CaO(Mass%)	K2O(Mass%)	Cr2O3(Mass%)	FeO(Mass%)	MnO(Mass%)	NiO(Mass%)	TiO2(Mass%)	SiO2(Mass%)	Total(Mass%)
1	std_ol1	0	52,8	0	0,0175	0	0,0177	5,58	0,1188	0,3793	0	41,25	100,1633
2	std_di1	0,0221	18,44	0,0451	25,83	0,0113	0,0199	0,0611	0,0672	0,0296	0,0686	54,84	99,4349
3	std_ab1	11,29	0	20,02	0,402	0,1549	0	0	0	0	0,0197	66,64	98,5266
4	std_grt1	0,0255	4,36	21,01	0,3554	0	0	36,95	0,2104	0	0,0124	36,24	99,1637
5	js_2_10_a1_1	0,4253	14,93	5,97	21,28	0,0084	0,3057	5,37	0,1617	0	1,6304	49,09	99,1715
6	js_2_10_a1_2	0,5814	13,97	6,36	22,97	0	0,3127	4,88	0,1573	0,0311	1,93	48,92	100,1125
7	js_2_10_a1_3	0,4786	13,75	6,33	22,57	0	0,4231	5	0,1351	0,0311	1,87	46,93	97,5179
8	js_2_10_a1_4	0,5136	14,22	6,11	22,59	0,011	0,3725	5,25	0,1539	0	1,74	48,62	99,581
9	js_2_10_a1_5	0,4997	14,84	6,26	21,32	0	0,3622	5,96	0,1805	0,053	1,82	49,02	100,3154
10	js_2_10_a1_6	0,5693	13,79	6,38	22,91	0	0,3649	4,87	0,0931	0	1,86	48,48	99,3173
11	js_2_10_a1_7	0,524	15,14	6,33	20,34	0	0,4019	6,58	0,1925	0,0143	1,79	48,14	99,4527
12	js_2_10_a1_8	0,523	13,9	6,48	22,33	0	0,3933	5,48	0,1229	0,0143	1,84	47,82	98,9035
13	js_2_10_a1_9	0,5349	13,58	6,56	22,94	0	0,4018	5,24	0,1285	0,0134	2	48,31	99,7086
14	js_2_10_a1_10	0,5518	13,71	6,59	22,76	0,0219	0,4434	4,5	0,1485	0,0723	1,95	48,1	98,8479
15	js_2_10_a1_11	0,5781	13,81	6,21	22,88	0	0,4116	5,23	0,1141	0	1,84	48,46	99,5338
16	js_2_10_a1_12	0,5611	13,8	6,18	22,79	0	0,4102	5,02	0,134	0,0269	1,83	48,49	99,2422
17	js_2_10_a1_13	0,5389	13,62	6,12	23,16	0,0111	0,3538	4,66	0,143	0,0252	1,79	49,36	99,782
18	js_2_10_a1_14	0,6002	14,5	6,45	22,57	0	0,3261	4,55	0,1109	0,0252	1,77	48,35	99,2524
19	js_2_10_a1_15	0,4217	14,13	5,93	23,5	0,0034	0,335	4,27	0,1277	0,0118	1,6344	49,12	99,484
20	js_2_10_a1_16	0,5097	14,45	6,44	22,34	0	0,3808	5,05	0,1085	0,0395	1,81	47,84	98,9685
21	js_2_10_a1_17	0,5567	14,06	6,38	22,87	0	0,4495	4,87	0,134	0,0362	1,99	48,45	99,7964
22	js_2_10_a1_18	0,5495	14,33	6,36	22,42	0,0138	0,4251	5,14	0,122	0,0185	2,01	48,2	99,5889
23	js_2_10_a1_19	0,4587	13,87	6,21	22,85	0	0,3579	5,27	0,1152	0,0219	1,83	48,72	99,7037
24	js_2_10_a1_20	0,5231	14,57	6,18	21,29	0	0,381	6,22	0,1228	0	1,94	48,37	99,5969
25	js_2_10_a1_21	0,5511	13,64	6,38	22,89	0	0,3682	5,12	0,143	0,0134	1,95	48,53	99,5857
26	js_2_10_a1_22	0,5532	14,12	6,26	22,33	0	0,4785	5,09	0,1495	0,0294	1,91	48,77	99,6906
27	js_2_10_a1_23	0,5518	13,92	6,19	22,99	0	0,4047	4,68	0,1476	0,016	1,84	49,52	100,2601

28	js_2_10_a1_24	0,4331	14,08	6,68	23,52	0	0,4617	4,36	0,0943	0,0118	1,68	48,17	99,4909
29	js_2_10_a2_1	0,5166	14,63	5,75	23,03	0	0,3134	4,3	0,0699	0,0025	1,5636	48,88	99,056
30	js_2_10_a2_2	0,4873	14,12	5,93	23,32	0	0,3464	3,86	0,1177	0,0328	1,76	48,79	98,7642
31	js_2_10_a2_3	0,4693	14,06	6,06	23,31	0,006	0,3915	4,36	0,1353	0,0093	1,76	47,8	98,3614
32	js_2_10_a2_4	0,4981	14,12	6,17	23,1	0	0,3818	4,32	0,0876	0,0303	1,84	48,65	99,1978
33	js_2_10_a2_5	0,4474	14,38	6,29	22,92	0,0062	0,4325	4,58	0,1143	0	1,69	49,4	100,2604
34	js_2_10_a2_6	0,4028	14,49	5,83	23,38	0,0029	0,315	4,3	0,0998	0,0564	1,4303	49,1	99,4072
35	js_2_10_a2_7	0,4907	14,47	5,9	23,37	0	0,3349	4,31	0,1288	0,0404	1,5342	48,83	99,409
36	js_2_10_a2_8	0,5101	14,1	6,16	23,2	0,0105	0,3118	4,53	0,1199	0	1,78	47,97	98,6923
37	js_2_10_a2_9	0,5673	14,41	6,15	23,05	0,002	0,3932	4,31	0,133	0,0362	1,83	47,86	98,7417
38	js_2_10_a2_10	0,4851	14,46	5,94	23,01	0	0,3954	4,22	0,0655	0	1,6438	48,84	99,0598
39	js_2_10_a2_11	0,4794	14,43	5,99	22,76	0,0013	0,4062	4,36	0,1087	0	1,5407	47,6	97,6763
40	js_2_10_a2_12	0,4308	14,38	6,1	22,92	0,005	0,38	4,55	0,1009	0,0622	1,6022	49,22	99,7511
41	js_2_10_a2_13	0,387	16,35	5,63	19,81	0,0018	0,3206	5,26	0,1475	0	1,5822	49,23	98,7191
42	js_2_10_a2_14	0,4106	15,52	6,22	21,15	0,0019	0,3755	5,36	0,1329	0,0252	1,69	47,53	98,4161
43	js_2_10_a2_15	0,4272	15,75	6,1	20,54	0,0071	0,3896	5,78	0,1583	0,016	1,67	49,29	100,1282
44	js_2_10_a2_16	0,5146	14,75	6,08	22,24	0	0,409	5,05	0,1508	0,0211	1,77	49,03	100,0155
45	js_2_10_a2_17	0,426	16,34	5,78	19,35	0	0,3748	6,31	0,1562	0,0109	1,7	49,82	100,2679
46	js_2_10_a2_18	0,5508	14,43	6,28	22,64	0	0,3994	4,56	0,0942	0,0463	1,93	48,15	99,0807
47	js_2_10_a2_19	0,5014	14,17	5,98	23,27	0,0066	0,397	4,22	0,1387	0,032	1,84	48,83	99,3857
48	js_2_10_a2_20	0,6069	14,4	6,43	22,77	0,0097	0,3848	4,5	0,1208	0,0177	1,84	48,58	99,6599
49	js_2_10_a2_21	0,5528	14,45	6,08	22,92	0,0035	0,4128	4,33	0,1209	0,0311	1,81	48,54	99,2511
50	js_2_10_a2_22	0,5189	15,63	6,2	21,09	0,0083	0,352	5,01	0,1065	0	1,73	49,18	99,8257
51	js_2_10_a2_23	0,5092	14,67	6,13	23,17	0,0037	0,4037	4,3	0,1144	0,0177	1,5944	49,09	100,0031
52	js_2_10_a2_24	0,5589	14,68	6,1	22,8	0,0018	0,4131	4,5	0,0999	0	1,6328	49,12	99,9065
53	js_2_10_a2_25	0,5139	14,27	6,13	23,1	0,0049	0,3429	4,52	0,1365	0,0876	1,83	48,84	99,7758
54	js_2_10_a2_26	0,5232	14,07	6,44	22,94	0,0113	0,4807	4,68	0,1396	0	1,88	48,24	99,4048
55	js_2_10_a2_27	0,5215	14,11	6,1	22,81	0	0,3507	4,73	0,1431	0,0067	1,84	48,87	99,482
56	js_2_10_a2_28	0,5841	14,18	6,2	22,94	0,0086	0,4046	4,7	0,1376	0,0059	1,87	48,4	99,4308
57	js_2_10_a2_29	0,5871	14,27	6,31	22,91	0	0,3591	4,48	0,0732	0,0682	1,8	48,66	99,5176

58	js_2_10_a2_30	0,5423	14,52	5,97	22,8	0	0,3809	4,38	0,1089	0	1,69	49,24	99,6321
59	js_2_10_a2_31	0,5308	14,4	6,41	22,89	0,0007	0,3691	4,45	0,1055	0,0236	1,85	48,63	99,6597
60	js_2_10_a2_32	0,3595	16,61	6	19,45	0	0,4323	5,86	0,1641	0,027	1,5994	49,02	99,5223
61	js_2_10_a3_1	0,4671	14,26	5,91	23,19	0,0078	0,364	4,2	0,1553	0	1,578	49,31	99,4422
62	js_2_10_a3_2	0,4789	16,18	5,89	20,4	0,01	0,3692	5,67	0,1585	0,0303	1,6124	49,2	99,9993
63	js_2_10_a3_3	0,5976	14,32	6,36	23,05	0,0054	0,4155	4,09	0,1055	0,0388	2,02	47,14	98,1428
64	js_2_10_a3_4	0,5805	14,13	6,3	22,89	0,0136	0,3543	4,58	0,131	0,0269	1,93	48,17	99,1063
65	js_2_10_a3_5	0,5873	14,1	6,25	21,98	0,0046	0,4418	5,01	0,1009	0,0034	2	48,16	98,638
66	js_2_10_a3_6	0,4234	16,68	5,35	18,46	0	0,322	7,23	0,1759	0,0388	1,4542	49,68	99,8143
67	js_2_10_a3_7	0,5188	14,36	5,39	22,97	0,0029	0,3809	4,5	0,1189	0	1,4924	49,32	99,0539
68	js_2_10_a3_8	0,5669	14	6,22	22,82	0,0012	0,4262	4,84	0,1233	0,0295	1,88	48,14	99,0471
69	js_2_10_a3_9	0,5782	14,48	6,13	22,98	0	0,4286	4,26	0,189	0,0202	1,88	48,19	99,136
70	js_2_10_a3_10	0,501	16,09	5,89	20,02	0	0,3628	5,76	0,1453	0,0236	1,68	49,01	99,4827
71	js_2_10_a3_11	0,4763	14,97	5,64	23,09	0,0124	0,4077	3,97	0,0912	0	1,4321	49,66	99,7497
76	js_2_10_a4_1	0,3942	15,34	4,64	22,95	0	0,201	4,69	0,1333	0,0481	1,0759	49,95	99,4225
77	js_2_10_a4_2	0,7425	14,71	6,38	22,3	0	0,4367	4,12	0,1234	0,0354	1,78	47,9	98,528
78	js_2_10_a4_3	0,5153	14,23	6,27	23,5	0	0,3156	4,17	0,1244	0,0236	1,78	47,89	98,8189
79	js_2_10_a4_4	0,5262	14,27	6,04	23,54	0,0003	0,3584	3,9	0,0945	0,0489	1,71	49,05	99,5383
80	js_2_10_a4_5	0,387	14,11	6	23,52	0,0186	0,404	4,22	0,0789	0	1,3507	49,42	99,5092
81	js_2_10_a4_6	0,4203	14,75	6,11	23,33	0	0,3716	4,08	0,1056	0	1,4409	49,04	99,6484
82	js_2_10_a4_7	0,4335	14,3	5,93	23,61	0	0,4224	4,14	0,1157	0	1,6129	49,47	100,0345
83	js_2_10_a4_8	0,4892	14,12	6,15	23,32	0,0137	0,4124	4,23	0,1178	0,0262	1,78	48,88	99,5393
84	js_2_10_a4_9	0,4616	14,66	5,66	23,39	0	0,4236	4,38	0,1211	0,0211	1,4916	49,58	100,189
85	js_2_10_a5_1	0,4733	14,59	6,16	23,49	0,0052	0,3891	4,3	0,12	0,059	1,5848	47,61	98,7814
86	js_2_10_a5_2	0,5379	14,33	6,13	23,24	0	0,3449	4,3	0,1244	0,0109	1,91	48,46	99,3881
87	js_2_10_a5_3	0,4064	16,73	6	18,82	0	0,3915	6,22	0,1764	0,0194	1,5283	49,22	99,512
88	js_2_10_a5_4	0,2106	16,74	1,6608	24,15	0	0,1183	3,33	0,1193	0,0448	0,2147	53,59	100,1785
89	js_2_10_a5_5	0,4994	14,05	6,54	22,79	0	0,4346	4,43	0,1255	0,0564	1,91	48,22	99,0559
90	js_2_10_a5_6	0,5277	14,18	6,56	22,95	0,0058	0,3904	4,71	0,1599	0,0253	1,94	48,19	99,6391
91	js_2_10_a5_7	0,4954	13,73	6,69	22,91	0	0,4829	5	0,1299	0,0202	1,97	47,89	99,3184

92	js_2_10_a5_8	0,5702	13,81	6,37	22,95	0,01	0,3772	4,74	0,151	0,0169	1,98	48,52	99,4953
93	js_2_10_a5_9	0,359	17,49	5,43	16,85	0,0097	0,2546	8,42	0,2465	0,0143	1,4095	50,04	100,5236
94	js_2_10_a5_10	0,501	13,78	6,67	22,94	0	0,4408	4,66	0,1388	0,0531	1,97	48,45	99,6037
95	js_2_10_a5_11	0,5724	14,09	6,42	23,01	0	0,33	4,69	0,1655	0,0051	2,05	48,31	99,643
96	js_2_10_a5_12	0,5142	13,9	6,31	23,06	0,0052	0,3594	4,62	0,1111	0,0051	2	48,28	99,165
97	js_2_10_a5_13	0,4416	14,47	6,09	23,36	0,0027	0,3549	4,3	0,1434	0,0202	1,5157	49,07	99,7685
98	js_2_10_a5_14	0,2755	18,11	4,92	18,38	0	0,3458	6,4	0,1608	0	0,9756	50,29	99,8577
99	js_2_10_a5_15	0,4432	14,32	5,8	23,52	0,0028	0,3888	4,47	0,1299	0,0346	1,6066	48,88	99,5959
100	js_2_10_a5_16	0,5038	14,26	5,89	23,39	0	0,3759	4,52	0,1022	0,0042	1,6326	49,05	99,7287
101	js_2_10_a5_17	0,4468	16,07	5,7	19,8	0	0,4032	5,75	0,0998	0,0186	1,77	49,02	99,0784
102	js_2_10_a5_18	0,4905	14,78	6,31	22,43	0	0,3757	4,5	0,1477	0,0236	1,84	48,51	99,4075
103	js_2_10_a6_1	0,4392	14,26	5,84	23,43	0	0,3921	4,41	0,1088	0,0084	1,5267	49,3	99,7152
104	js_2_10_a6_2	0,5213	13,93	6,27	23,19	0,0057	0,4048	4,6	0,1421	0,0623	1,85	48,27	99,2462
105	js_2_10_a6_3	0,4168	13,91	6,29	23,47	0,0062	0,4313	4,42	0,1266	0,0118	1,77	48,74	99,5927
106	js_2_10_a6_4	0,2968	15,71	3,28	23,53	0,0118	0,1457	4,26	0,1023	0	0,6768	51,83	99,8434
107	js_2_10_a6_5	0,3779	14,95	4,52	23,52	0	0,1277	4,18	0,0845	0,0312	0,9799	51,02	99,7912
108	js_2_10_a6_6	0,399	14,67	5,9	22,74	0,0022	0,3348	4,68	0,1433	0,0034	1,5549	48,35	98,7776
109	js_2_10_a6_7	0,4859	13,87	5,94	23,28	0	0,3304	4,11	0,1433	0,0101	1,77	48,44	98,3797
110	js_2_10_a6_8	0,4451	14,51	5,95	23,34	0	0,3269	4,45	0,1267	0,0354	1,5223	49,09	99,7964
111	js_2_10_a6_9	0,5126	14,26	6,29	23,03	0,0041	0,3957	4,36	0,1389	0,0455	1,73	49,09	99,8568
112	js_2_10_a6_10	0,5678	14,37	6,15	22,77	0	0,4226	4,68	0,1287	0,0404	1,73	48,68	99,5395
113	js_2_10_a6_11	0,394	14,56	5,92	23,12	0	0,4347	4,48	0,1167	0,0042	1,5494	49,01	99,589
118	js_2_19_a1_1	0,4846	14,94	4,56	22,46	0	0,5176	4,64	0,1218	0,0216	1,349	50,33	99,4246
119	js_2_19_a1_2	0,1897	23,55	3,37	5,73	0,0002	0,309	12,63	0,2554	0,0775	0,486	52,24	98,8378
120	js_2_19_a1_3	0,5092	16,46	3,73	20,79	0,009	0,3895	5,12	0,1524	0,015	0,7871	48,8	96,7622
121	js_2_19_a1_4	0,6341	14,32	5,4	22,79	0,003	0,4795	4,53	0,1405	0,0275	1,5158	50,06	99,9004
122	js_2_19_a1_5	0,6243	14,46	5,52	22,62	0	0,334	4,72	0,1526	0,0092	1,4707	49,41	99,3208
123	js_2_19_a1_6	0,7247	14,27	6,32	22,8	0,0061	0,3194	4,44	0,1239	0,0333	1,85	48,81	99,6974
124	js_2_19_a1_7	0,665	14,19	6,75	22,87	0,0012	0,3857	4,29	0,0899	0,0424	2	48,14	99,4242
125	js_2_19_a1_8	0,5603	15,69	4,34	22,92	0,0399	0,3918	3,56	0,0747	0,0383	0,8029	51,78	100,1979

126	js_2_19_a1_9	0,6003	15,6	4,28	22,65	0,0407	0,4016	3,47	0,0857	0,0208	0,844	50,8	98,7931
127	js_2_19_a1_10	0,7109	14,27	5,52	22,87	0	0,3791	4,59	0,1163	0,0225	1,4812	50,25	100,21
128	js_2_19_a1_11	0,7611	13,9	6,41	22,26	0,006	0,2498	4,71	0,1315	0,0383	1,8	48,44	98,7067
129	js_2_19_a1_12	0,7006	14,3	6,22	21,99	0,0034	0,2613	4,73	0,1547	0,0283	1,87	48,34	98,5983
130	js_2_19_a1_13	0,6295	14,72	6,44	21,51	0,0062	0,211	4,93	0,1271	0,0266	1,9	48,92	99,4204
131	js_2_19_a1_14	1,0844	14,9	6,8	20,31	0,0046	0,2298	5,38	0,1424	0,0399	1,75	48,34	98,9811
132	js_2_19_a1_15	0,6034	14,94	5,81	22,11	0,0031	0,3191	4,84	0,1129	0,0458	1,436	49,68	99,9003
133	js_2_19_a1_16	0,5701	14,82	5,24	22,82	0,0083	0,4632	4,4	0,1086	0,0208	1,239	50,4	100,09
134	js_2_19_a2_1	0,4457	17,12	4,3	20,28	0	0,5411	5,27	0,1404	0,0092	1,1308	50,82	100,0572
135	js_2_19_a2_2	0,5036	17,25	3,73	19,66	0,0122	0,5685	5,78	0,1938	0,0508	0,9131	50,76	99,422
136	js_2_19_a2_3	0,559	15,53	4,43	20,76	0,0032	0,5849	5,08	0,135	0,03	1,0648	50,95	99,1269
137	js_2_19_a2_4	0,4973	16,18	3,57	21,44	0	0,6424	5,06	0,1622	0,0475	0,9609	50,94	99,5003
138	js_2_19_a2_5	0,4582	18,03	3,39	18,3	0,0139	0,6891	6,6	0,1795	0,0625	1,2665	51,16	100,1497
139	js_2_19_a2_6	0,3336	21,46	2,66	13,51	0	0,4506	8,05	0,1814	0,0375	0,5813	53,43	100,6944
140	js_2_19_a2_7	0,4006	19,23	3,3	17,11	0,0129	0,5012	6,86	0,1818	0,0592	0,8103	52,28	100,746
141	js_2_19_a2_8	0,5277	15,81	3,88	21,62	0,0064	0,6787	4,91	0,1361	0,04	0,9947	49,57	98,1736
142	js_2_19_a2_9	0,3824	18,74	3,7	16,76	0,0023	0,5142	7,31	0,1859	0,0491	0,881	51,55	100,0749
143	js_2_19_a2_10	0,4872	17,17	3,59	19,7	0,0017	0,5747	5,93	0,1687	0,0342	0,953	51,62	100,2295
144	js_2_19_a2_11	0,4827	16	3,64	21,88	0	0,6455	4,71	0,1274	0,045	0,9934	50,91	99,434
145	js_2_19_a2_12	0,4473	15,84	4,83	22,38	0,0184	0,4748	4,22	0,0527	0,0441	1,4095	50,62	100,3368
146	js_2_19_a2_13	0,4529	15,26	4,57	23,74	0,0086	0,6021	3,83	0,0835	0,0292	1,1501	50,26	99,9864
147	js_2_19_a2_14	0,5588	15,24	4,63	22,52	0,0098	0,5649	4,61	0,1021	0,0408	1,2296	48,93	98,436
148	js_2_19_a2_15	0,302	20,07	5,97	13,03	0,0046	2,21	10,02	0,1958	0,0648	0,6512	49,25	101,7684
149	js_2_19_a2_16	0,4796	16,81	4,43	19,59	0,0043	0,8262	5,98	0,1623	0,0242	1,1218	50,51	99,9384
150	js_2_19_a2_17	0,5088	16,9	3,49	19,8	0	0,5924	5,41	0,1338	0,0509	0,8999	51,61	99,3958
151	js_2_19_a2_18	0,4102	18,13	3,56	17,27	0,0041	1,1694	7,22	0,162	0,0259	0,7779	51,01	99,7395
152	js_2_19_a2_19	0,4831	17,1	3,37	20,07	0	0,4686	5,69	0,1526	0,066	0,9171	51,8	100,1174
153	js_2_19_a2_20	0,53	17,25	3,62	19,67	0,0085	0,5214	5,86	0,1449	0,0192	0,9532	52,22	100,7972
154	js_2_19_a2_21	0,5243	15,89	3,51	22,04	0	0,7747	4,64	0,1219	0,02	0,9916	51,02	99,5325
155	js_2_19_a2_22	0,5426	15,37	3,74	22,7	0	0,6789	4,56	0,1484	0,0117	0,9841	51,92	100,6557

156	js_2_19_a2_23	0,4961	16,03	3,9	21,83	0	0,6919	4,89	0,0878	0,0233	1,0792	51,06	100,0883
157	js_2_19_a2_24	0,5344	15,4	3,75	22,47	0,0041	0,5957	4,09	0,0847	0,0359	0,9869	50,75	98,7017
158	js_2_19_a2_25	0,5564	15,19	4,03	22,43	0,0009	0,6881	4,45	0,1263	0,0233	1,0792	51,38	99,9542
159	js_2_19_a2_26	0,5614	15,2	4,15	22,69	0	0,668	4,28	0,1638	0,0359	0,9997	51,05	99,7988
160	js_2_19_a2_27	0,4901	15,95	4,2	21,84	0,0112	0,6249	4,81	0,1274	0,0234	1,1327	51	100,2097
161	js_2_19_a2_28	0,0413	42,89	0	0,0267	0,0028	0,0303	18,66	0,2835	0,2143	0,0495	39,1	101,2984
162	js_2_19_a3_1	0,5318	14,74	4,77	23,16	0	0,5642	4,16	0,123	0,0342	1,3268	50,66	100,07
163	js_2_19_a3_2	0,554	15,39	4,76	22,27	0	0,6109	4,55	0,0956	0,0334	1,3717	50,61	100,2456
164	js_2_19_a3_3	0,5978	14,7	4,89	22,81	0	0,6519	4,26	0,1011	0,0092	1,5122	50,24	99,7722
165	js_2_19_a3_4	0,5931	14,88	4,73	22,82	0,0018	0,6632	4,2	0,1286	0,0359	1,3416	49,74	99,1342
166	js_2_19_a3_5	0,5313	15,41	4,66	22	0,0058	0,607	4,89	0,0923	0,0234	1,3293	50,13	99,6791
167	js_2_19_a3_6	0,5492	15,21	4,69	22,37	0	0,5854	4,29	0,1154	0,0409	1,3945	49,74	98,9854
168	js_2_19_a3_7	0,5458	16,16	4,56	20,61	0,0063	0,49	5,31	0,1735	0,0718	1,2708	51,14	100,3382
169	js_2_19_a3_8	0,6224	14,82	4,68	22,68	0,0003	0,6629	4,67	0,1605	0,0476	1,3002	50,57	100,2139
170	js_2_19_a3_9	0,5871	15,04	4,28	22,98	0	0,5653	4,26	0,1134	0,0092	1,1471	50,53	99,5121
171	js_2_19_a3_10	0,4723	16,02	4,28	21,65	0,0017	0,4884	4,65	0,1023	0,0418	1,1403	50,25	99,0968
172	js_2_19_a3_11	0,4873	16,94	4,56	19,98	0,003	0,6283	5,42	0,0911	0,0184	1,2773	50,62	100,0254
173	js_2_19_a3_12	0,5754	15,28	4,5	22,79	0	0,6456	4,17	0,1264	0,0484	1,2121	50,5	99,8479
174	js_2_19_a3_13	0,2815	22,43	3,45	11,97	0,0048	0,3924	8,69	0,2492	0,0467	0,6975	52	100,2121
175	js_2_19_a3_14	0,5556	15,45	4,26	22,67	0,0124	0,5987	4,19	0,1012	0,0225	1,2233	50,67	99,7537
176	js_2_19_a3_15	0,5962	14,87	4,4	22,85	0,003	0,7255	4,26	0,1483	0,0317	1,1982	50,29	99,3729
177	js_2_19_a3_16	0,2911	24,81	3,6	7,15	0	0,3261	10,45	0,2279	0,0809	0,5965	52,5	100,0325
178	js_2_19_a3_17	0,5534	16,35	4,35	21,04	0	0,4326	4,93	0,1219	0,0518	1,1617	51,1	100,0914
179	js_2_19_a3_18	0,5176	18,12	4,53	18,23	0	0,4283	5,19	0,1581	0,01	1,2054	50,54	98,9294
180	js_2_19_a3_19	0,4619	15,75	4,07	22,03	0	0,3838	4,97	0,1295	0,0559	1,0262	49,29	98,1673
185	js_2_19_a4_1	0,5851	14,76	5,06	23,46	0,0021	0,4542	3,94	0,1295	0,0475	1,3786	50,4	100,217
186	js_2_19_a4_2	0,8588	15,26	5,57	21,96	0	0,2888	4,35	0,1163	0,0716	1,3787	49,29	99,1442
187	js_2_19_a4_3	0,4478	15,2	4,1	23,69	0,0126	0,2121	3,61	0,1341	0,0208	1,0859	51,16	99,6733
188	js_2_19_a4_4	0,6713	14,16	6,37	22,62	0	0,2986	4,62	0,1548	0,0108	1,77	48,8	99,4755
189	js_2_19_a4_5	0,7115	14,43	6,27	22,39	0	0,3134	4,59	0,111	0	1,74	48,73	99,2859

190	js_2_19_a4_6	0,7359	14,08	6,61	22,65	0	0,2877	4,47	0,0769	0,0217	2	48,18	99,1122
191	js_2_19_a4_7	0,6691	14,39	6,54	22,8	0,0114	0,3411	4,36	0,1505	0	1,85	48,13	99,2421
192	js_2_19_a4_8	0,5171	15,19	5,69	22,65	0	0,4849	4,54	0,1187	0,0134	1,1562	49,54	99,9003
193	js_2_19_a4_9	0,118	43,23	0	0,0062	0	0	18,4	0,2698	0,2154	0,0297	39,03	101,2991
194	js_2_19_a4_10	0	43,47	0	0,0046	0	0	18,12	0,2535	0,2052	0,0276	39,41	101,4909
195	js_2_19_a4_11	0	43,09	0	0,3126	0,0016	0	18,49	0,2418	0,2004	0,0106	39,08	101,427
196	js_2_19_a4_12	0,5352	14,68	5,78	23,25	0,0023	0,387	3,94	0,0957	0,0325	1,71	49,19	99,6027
197	js_2_19_a4_13	0,8033	16,49	6,14	19,34	0	0,2927	5,52	0,136	0,0458	1,7	49,3	99,7678
198	js_2_19_a4_14	0,5861	15,07	5,79	21,95	0	0,3842	4,85	0,123	0,0117	1,74	49,14	99,645
199	js_2_19_a4_15	0,7612	15,23	6,17	21,03	0,0104	0,2918	5,28	0,0824	0,0275	1,666	49,46	100,0093
200	js_2_19_a4_16	0,7414	14,2	6,1	22,43	0,0066	0,2859	4,7	0,0989	0,0058	1,68	48,79	99,0386
201	js_2_19_a4_17	0,5436	14,73	4,72	23,32	0	0,3037	4,56	0,1219	0,0509	1,2263	50,53	100,1064
202	js_2_19_a4_18	0,634	14,1	6,29	23,09	0	0,4059	4,25	0,1429	0,0417	1,82	48,91	99,6845
203	js_2_19_a4_19	0,8369	15,74	5,42	21,84	0	0,3252	3,93	0,0638	0,0142	1,0766	49,64	98,8867
4	cpx_js12_a1-2	0	22,25	1,2016	1,1949	0	0,0286	23,12	0,5946	0,015	0,0299	50,52	98,9546
5	cpx_js12_a1-3	0,0163	22,38	1,4362	0,2652	0	0,0151	24,06	0,5335	0	0,0475	52,12	100,8738
6	cpx_js12_a1-4	0,0193	22,19	1,4949	0,2449	0,0017	0,0135	23,76	0,5298	0,0251	0,0401	51,6	99,9193
7	cpx_js12_a1-5	0,0207	21,91	2,1	0,6005	0	0,003	23,41	0,5402	0,0426	0,0414	50,42	99,0884
8	cpx_js12_a1-6	0,8224	13,82	3,25	21,35	0	0,0339	8,36	0,1846	0,0488	0,2432	50,73	98,8429
9	cpx_js12_a1-7	0,9921	13,07	4,37	21,48	0	0,0794	7,11	0,2027	0	0,2447	50,24	97,7889
10	cpx_js12_a1-8	0	21,9	1,7813	0,2534	0,0026	0	23,8	0,5427	0	0,044	51,72	100,044
11	cpx_js12_a1-9	0	22,25	1,6198	0,2245	0,0011	0,0165	23,82	0,5378	0,0351	0,039	51,3	99,8438
12	cpx_js12_a1-10	0,0011	22,4	1,5486	0,2546	0	0	23,4	0,5518	0,0134	0,0667	51,76	99,9962
13	cpx_js12_a1-11	0	22,31	1,8103	0,235	0,0016	0,0466	24,07	0,5415	0,0025	0,0726	51,54	100,6301
14	cpx_js12_a1-12	0,9249	13,75	3,07	21,97	0,0038	0,06	7,43	0,2129	0,0118	0,2556	51,81	99,499
15	cpx_js12_a1-13	0,8398	13,87	2,66	22,05	0,0089	0,0243	7,76	0,1673	0,0194	0,197	51,86	99,4567
16	cpx_js12_a1-14	0,8203	14,05	2,54	22,25	0,0046	0,073	7,33	0,1807	0,0008	0,1771	51,48	98,9065
17	cpx_js12_a1-15	0,7383	13,96	2,46	22,11	0,0068	0,0568	7,62	0,2096	0	0,3529	51,9	99,4144
18	cpx_js12_a1-16	0,7438	13,81	2,62	21,95	0	0,0858	7,81	0,2149	0	0,335	51,78	99,3495
19	cpx_js12_a1-17	0,8971	13,97	2,68	21,99	0	0,013	7,55	0,2206	0,0135	0,2859	51,9	99,5201

20	cpx_js12_a1-18	0,7694	14,05	2,55	22,07	0,0119	0,0308	7,34	0,2029	0,0059	0,3552	51,98	99,3661
21	cpx_js12_a1-19	0,8028	14,19	2,41	22,02	0	0,0454	7,46	0,2285	0	0,3735	52	99,5302
22	cpx_js12_a1-20	0,7304	14,32	2,65	21,61	0,0086	0,0551	7,6	0,1774	0	0,2951	51,28	98,7266
23	cpx_js12_a1-21	0,8003	14,01	2,93	22,04	0	0	7,57	0,194	0,0051	0,3218	51,09	98,9612
24	cpx_js12_a1-22	0,0425	21,76	1,94	0,2788	0,0058	0,0197	22,7	0,5136	0,031	0,0431	51,37	98,7045
25	cpx_js12_a1-23	4,25	6,07	21,34	6,9	0,1445	0,0016	6,61	0,1465	0	0,0239	53,92	99,4065
32	px_js12_tach1	0,892	13,7	3,5	21,53	0,0126	0,0504	7,21	0,1689	0,0431	0,3528	50,96	98,4198
33	px_js12_tach2	0,7177	14,37	2,12	22,37	0,0109	0,0619	6,85	0,1958	0,0169	0,1332	52,8	99,6464
34	px_js12_tach3	0,8882	13,23	4,14	22,26	0,0163	0,1023	7,65	0,1966	0	0,4569	50,97	99,9103
35	px_js12_tach4	0,9975	13,4	4,18	22,11	0,0056	0,0586	7,2	0,1801	0	0,4862	51,08	99,698
36	px_js12_tach5	1,3013	12,09	9,82	16,45	1,23	0,1602	10,68	0,1566	0,0067	1,6427	42,72	96,2575
37	px_js12_tach6	0,9197	14,64	3,86	19	0,0223	0,0903	9,47	0,1563	0,005	0,3266	50,37	98,8602
38	px_js12_tach7	2	10,43	8,52	18,24	0,0638	0,1151	7,43	0,1843	0,0211	0,2575	48,91	96,1718
39	px_js12_tach8	0,8122	12,51	3,47	20,71	0,041	0,1148	8,8	0,2082	0	3,05	48,81	98,5262
40	px_js12_tach9	0,9187	13,1	4,46	21,15	0,0142	0,0487	7,44	0,1544	0,0211	0,5701	48,37	96,2472
41	px_js12_tach10	1,0814	12,82	5,97	20,61	0,3884	0,0908	8,3	0,1632	0,0219	0,78	49,58	99,8057
42	px_js12_tach11	0,9139	12,71	3,88	21,88	0,0142	0,0925	8,01	0,1821	0	1,4115	48,86	97,9542
43	px_js12_tach12	0,7517	14,52	2,01	22,35	0	0,0799	6,73	0,1436	0,0008	0,1269	52,53	99,2429
44	px_js12_tach13	1,47	12,47	5,68	21,47	0,0234	0,0911	6,92	0,219	0	0,329	51,94	100,6125
45	px_js12_tach14	1,67	11,97	6,79	20,9	0,0174	0,0733	6,67	0,1692	0	0,3324	52,43	101,0223
61	px_js14_a1-1	0	29,61	0,9107	0,12	0,0022	0	13,83	0,363	0,0723	0,042	54,26	99,2102
62	px_js14_a1-2	0,0114	28,6	2,29	0,2855	0	0,0961	13,89	0,3165	0,0374	0,1282	52,43	98,0851
63	px_js14_a1-3	0	29,08	2,33	0,1838	0	0,0284	14,15	0,3264	0,0179	0,0936	54,12	100,3301
64	px_js14_a1-4	0,0442	28,61	2,1	0,1896	0	0,0597	14,55	0,3526	0	0,0963	53,89	99,8924
65	px_js14_a1-5	0,0098	28,48	2,33	0,2796	0	0,0786	14,68	0,3228	0,0493	0,0618	53,6	99,8919
66	px_js14_a1-6	0,0189	28,06	2,21	0,298	0,0068	0,055	14,29	0,3548	0,0093	0,1572	53,84	99,3
67	px_js14_a1-7	0	28,76	2,37	0,1613	0	0,0504	13,92	0,3339	0,0527	0,0944	53,22	98,9627
68	px_js14_a1-8	0	29,09	2,1	0,1767	0	0,0205	13,65	0,2899	0,0425	0,1485	53,93	99,4481
69	px_js14_a1-9	0	29,34	2,2	0,1364	0	0,0457	13,68	0,3145	0,0213	0,0777	54,21	100,0256
70	px_js14_a1-10	0,0317	29,69	1,2242	0,1696	0	0,0031	13,79	0,3197	0,0195	0,0316	54,12	99,3994

71	px_js14_a1-11	0,0838	28,62	2,27	0,2213	0	0,066	14,3	0,3658	0,0374	0,0996	53,12	99,1839
72	px_js14_a1-12	0,0429	28,4	2,37	0,2355	0	0,0518	14,33	0,3216	0,0331	0,1014	52,88	98,7663
66	07_a2_amp4	0,7597	14,78	4,66	22,82	0,0013	0,3236	3,9	0,1206	0	1,153	50,32	98,8632
67	07_a2_amp5	0,9578	13,99	6,01	22,3	0,0037	0,3993	4,23	0,1171	0	1,85	49,89	99,7479
68	07_a2_amp6	0,7393	14,23	5,86	21,8	0,0077	0,3881	5,09	0,1282	0	1,96	48,83	99,05
69	07_a2_amp7	0,6592	14,59	4,69	22,45	0,0088	0,3556	4,96	0,1384	0,0197	1,0246	50,65	99,5614
70	07_a2_amp8	0,7668	14,49	4,86	22,41	0	0,3164	4,41	0,1667	0,0086	1,1781	50,48	99,0901
71	07_a2_amp9	0,7784	14,12	5,32	22,7	0,0075	0,4037	4,73	0,1114	0,0197	1,4934	50,06	99,7488
72	07_a2_amp10	0,8202	13,99	5,81	22,92	0,0041	0,4243	4,16	0,161	0	1,72	49,14	99,1496
73	07_a2_amp11	0,7017	15,41	3,83	22,99	0,0061	0,1642	4,19	0,1364	0,0428	0,76	51,77	100,0012
87	07_a2_amp25	1,0772	14,37	6,5	22,03	0	0,3736	4,07	0,1236	0,0102	0,9669	49,86	99,3941
88	07_a2_amp26	0,7582	14,79	5,77	20,99	0	0,4579	5,35	0,1279	0	1,5984	49,76	99,6441
89	07_a2_amp27	0,9487	14,03	5,85	22,46	0	0,3889	4,11	0,0956	0,0171	1,75	49,14	98,8427
90	07_a2_amp28	0,9133	14,04	5,49	22,71	0	0,3594	4,26	0,1474	0	1,5047	49,62	99,0448
91	07_a2_amp29	0,8285	14,84	5,45	22,21	0,0006	0,2619	4,13	0,089	0	0,7438	50,91	99,4663
92	07_a2_amp30	0,8093	14,33	5,78	22,4	0	0,4249	4,38	0,1113	0,0461	1,6085	49,95	99,85
93	07_a2_amp31	0,8941	14,17	5,66	22,24	0,0054	0,3776	4,26	0,1126	0,0154	1,5286	50,03	99,2949
94	07_a2_amp32	0,8802	13,96	5,86	22,05	0,0108	0,3604	4,66	0,1146	0,0375	1,93	49,6	99,4672
95	07_a2_amp33	1,1118	13,9	5,46	22,44	0,0041	0,4005	4,11	0,081	0,0384	1,1553	50,51	99,2159
96	07_a2_amp34	0,9929	13,88	5,82	22,55	0,0008	0,371	4,07	0,1384	0,0026	1,4976	50,02	99,3527
97	07_a2_amp35	1,0598	13,64	5,74	22,42	0,0067	0,3953	4,24	0,1135	0,0051	1,4126	50,52	99,6213
98	07_a2_amp36	0,7787	14,01	5,28	22,85	0	0,3124	4,49	0,1338	0	1,4689	50,12	99,4473
99	07_a2_amp37	0,8032	14,04	5,66	22,35	0,0073	0,4328	4,55	0,1202	0,0068	1,5401	49,4	98,9341
100	07_a2_amp38	0,7501	14,07	5,45	22,3	0,0083	0,4029	4,91	0,1506	0,0409	1,5249	50,18	99,8133
105	2_8_a1_amp1	0,6799	14,07	5,58	22,87	0	0,4394	4,53	0,1011	0,0222	1,3267	49,32	98,9393
110	2_8_a1_amp6	0,6189	14,27	5,46	23,32	0,0019	0,3986	4,02	0,0899	0,0511	1,2964	50,39	99,9168
111	2_8_a1_amp7	2,41	16,01	13,28	12,11	0,1868	0,2043	6,4	0,1018	0,0359	1,1995	45,05	96,9883
112	2_8_a1_amp8	0,6766	14,07	5,51	22,86	0	0,4278	4,65	0,1291	0,0196	1,5439	49,4	99,2901
113	2_8_a1_amp9	0,7167	14,17	5,66	22,62	0,0032	0,491	4,34	0,1259	0	1,6312	49,92	99,7387
117	2_8_a1_amp13	0,5361	15,56	2,62	23,3	0,0055	0,2454	3,88	0,0754	0,0436	0,3469	53,18	99,7999

118	2_8_a1_amp14	0,6652	13,91	5,46	22,76	0,01	0,4295	4,4	0,1471	0,0239	1,74	49,63	99,1852
119	2_8_a1_amp15	0,7004	14,29	5,33	22,52	0	0,4411	4,65	0,1629	0	1,5101	49,84	99,4445
120	2_8_a1_amp16	0,5528	17,1	4,88	16,86	0	0,3708	7,86	0,1746	0,035	1,4051	50,15	99,3923
121	2_8_a1_amp17	0,709	14,91	4,12	22,58	0,0008	0,3848	4,54	0,119	0,0179	1,0738	51,09	99,5881

Olivine analyses

Comment	Na2O(wt%)	MgO(wt%)	Al2O3(wt%)	CaO(wt%)	K2O(wt%)	Cr2O3(wt%)	FeO(wt%)	MnO(wt%)	NiO(wt%)	TiO2(wt%)	SiO2(wt%)	Total(wt%)
area_3_ol_1	0	43,67	0,0003	0	0	0,0376	15,73	0,1916	0,4423	0,0071	40,13	100,2089
area_3_ol_2	0	43,62	0	0,0045	0	0	16,01	0,2037	0,3876	0,0126	40,07	100,3084
area_3_ol_3	0	43,35	0	0,0262	0	0,0063	16,41	0,1937	0,3868	0	40,32	100,693
area_3_ol_4	0,0146	43,9	0	0	0	0	16,05	0,2136	0,4328	0	39,91	100,521
area_3_ol_5	0	43,32	0,0139	0,0092	0,0027	0	15,89	0,2313	0,4181	0,0063	40,6	100,4915
area_3_ol_6	0	43,97	0,0003	0,0071	0	0	16,29	0,2135	0,3457	0,0212	40,37	101,2178
2_8_ol1	0	43,75	0	0	0,0074	0	16,71	0,2519	0,3177	0,0059	40,31	101,3529
2_8_ol2	0	43,46	0	0	0	0	16,91	0,2019	0,2861	0,0173	39,43	100,3053
2_8_ol3	0,0154	43,54	0	0	0	0,0094	16,98	0,2329	0,2544	0,0018	40,37	101,4039
2_8_ol4	0,0095	43,67	0,0027	0	0,0006	0,0251	16,55	0,2062	0,2859	0,0119	40,13	100,8919
ol_js14_a1-1	0	39,5	0	0	0,0062	0,0015	22,61	0,3213	0,2598	0,0027	37,79	100,4915
ol_js14_a1-2	0,0115	39,09	0	0	0	0,0076	22,41	0,2801	0,2373	0,0235	38,07	100,13
ol_js14_a1-3	0,0234	39,28	0	0	0	0	22,83	0,3575	0,1944	0,017	37,39	100,0923
ol_js14_a1-4	0	39,27	0	0	0	0	22,39	0,2901	0,2559	0,0089	37,67	99,8849
ol_js14_a1-5	0,0168	39,25	0	0	0	0,0136	22,65	0,2923	0,2476	0,019	38,05	100,5393
ol_js14_a1-6	0	39,69	0	0,001	0	0,0045	22,11	0,2752	0,2554	0,0164	37,24	99,5925
ol_js14_a1-7	0	39,14	0	0	0	0,0015	21,8	0,2772	0,2755	0,0029	37,31	98,8071
ol_js14_a1-8	0	39,23	0,0006	0	0,0058	0,0395	22,19	0,2664	0,2663	0,0139	37,43	99,4425
ol_js14_a1-9	0,0231	39,1	0	0	0	0	22,23	0,3154	0,2663	0,0243	38,07	100,0291
ol_js14_a1-10	0	38,95	0	0	0,0021	0	22,11	0,2884	0,2454	0,0192	37,86	99,4751
ol_js14_a1-11	0	39,08	0	0	0	0	22,08	0,3244	0,2293	0	37,95	99,6637
ol_js14_a1-12	0,0246	39,21	0	0	0	0,0045	22,2	0,3178	0,2554	0,0059	37,6	99,6182
ol_js14_a2-1	0,0055	39,36	0	0,0021	0,0107	0	21,27	0,2545	0,2259	0,0329	37,27	98,4316
ol_js14_a2-2	0	39,68	0	0	0	0,0182	22,46	0,2837	0,1895	0,0133	37,56	100,2047
ol_js14_a2-3	0	39,35	0	0	0	0	22,04	0,324	0,2189	0,0128	37,69	99,6357
ol_js14_a2-4	0,0864	39,62	0	0	0,0036	0	22,15	0,2824	0,234	0,0185	37,16	99,5549
ol_js14_a2-5	0	39,38	0,0062	0,0065	0,0035	0,0106	22,35	0,2892	0,2443	0,0096	37,89	100,1899

ol_js14_a2-6	0	39,59	0	0	0,0009	0	22,17	0,3153	0,2669	0	37,97	100,3131
ol_js14_a2-7	0,141	39,6	0	0	0	0	22,41	0,3021	0,2122	0,0024	37,85	100,5177
ol_js14_a2-8	0,013	39,76	0	0	0	0	22,22	0,2933	0,2231	0,0258	36,05	98,5852
ol_js14_a2-9	0,0359	39,22	0	0	0	0	22,37	0,3447	0,1978	0,0132	38,22	100,4016
ol_js14_a2-10	0	39,49	0	0	0	0	22,02	0,2947	0,1946	0,0088	37,98	99,9881
ol_js14_a2-11	0,0407	39,16	0	0	0	0,0303	22,66	0,3989	0,2314	0	37,48	100,0013
ol_js14_a2-12	0	39,43	0,009	0	0	0,0121	21,99	0,3035	0,2595	0,0119	37,78	99,796
ol_js14_a2-13	0	39,48	0	0	0	0,0076	22,53	0,3153	0,2308	0	36,75	99,3137
ol_js14_a2-14	0	39,57	0	0,0055	0	0,0137	22,27	0,2598	0,2461	0,0202	37,54	99,9253
ol_js14_a2-15	0	38,99	0	0,0018	0	0	22,25	0,3239	0,2416	0,0214	37,93	99,7587
js_2_19_a2_28	0,0413	42,89	0	0,0267	0,0028	0,0303	18,66	0,2835	0,2143	0,0495	39,1	101,2984
js_2_19_a4_9	0,118	43,23	0	0,0062	0	0	18,4	0,2698	0,2154	0,0297	39,03	101,2991
js_2_19_a4_10	0	43,47	0	0,0046	0	0	18,12	0,2535	0,2052	0,0276	39,41	101,4909
js_2_19_a4_11	0	43,09	0	0,3126	0,0016	0	18,49	0,2418	0,2004	0,0106	39,08	101,427

Hornblende analyses

Point	Comment	SiO2(wt%)	Al2O3(wt%)	FeO(wt%)	CaO(wt%)	MgO(wt%)	Na2O(wt%)	K2O(wt%)	Cr2O3(wt%)	TiO2(wt%)	MnO(wt%)	ZnO(wt%)	Cl(wt%)	H(wt%)	Total(Mass%)
1	kaer1	40,9	12,9	11,66	11,37	12,63	2,47	0,9402	0	5,42	0,1706	0,024	0,0223	2	100,5071
2	Area1_amp1	42,03	13,89	11,33	11,16	11,8	2,48	1,25	0,0146	2,9	0,1258	0,0671	0,0601	2	99,1265
3	Area1_amp2	41,86	14,49	11,4	11,47	11,43	2,5	1,34	0,0911	2,84	0,1203	0,0336	0,0611	2	99,6516
4	Area1_amp3	41,48	14,03	11,66	11,49	11,59	2,5	1,26	0,0552	2,97	0,1011	0	0,052	2	99,1883
5	Area1_amp4	42,57	13,69	11,74	11,3	11,83	2,51	1,22	0,047	3,1	0,1178	0,0024	0,058	2	100,1852
6	Area1_amp5	41,42	14,25	11,88	11,15	11,38	2,5	1,26	0,0698	2,98	0,0842	0,0227	0,0527	2	99,0494
7	Area1_amp6	42,95	13,94	11,69	11,15	11,72	2,41	1,32	0,1136	2,83	0,0786	0,012	0,0492	2	100,2634
8	Area1_amp7	41,56	14,1	11,68	11,25	11,52	2,54	1,28	0,0876	3,13	0,1424	0,0514	0,0594	2	99,4008
9	Area1_amp8	40,91	14,5	11,74	11,32	11,11	2,48	1,39	0,0421	3,08	0,1245	0	0,0586	2	98,7715
10	Area1_amp9	41,58	14,13	11,5	11,42	11,72	2,48	1,29	0,052	2,84	0,1516	0	0,0552	2	99,2368
11	Area1_amp10	42,24	13,19	11,17	11,26	11,95	2,53	1,21	0,0747	3,22	0,1133	0,0215	0,0464	2	99,0473
12	Area1_amp11	42,34	13,6	11,43	11,41	11,83	2,46	1,36	0,0584	3,31	0,0976	0,0885	0,0489	2	100,0368
13	Area1_amp12	41,83	13,91	11,51	11,49	11,49	2,43	1,5	0,0732	3,31	0,1034	0	0,0625	2	99,7125
14	Area1_amp13	42	14,03	11,27	11,42	11,65	2,42	1,44	0,0211	3,15	0,0954	0,0168	0,0657	2	99,5884
15	Area1_amp14	42,43	13,39	11,47	11,33	12,17	2,49	1,26	0,0991	3,02	0,0842	0	0,0452	2	99,8048
16	Area1_amp15	41,24	13,82	11,55	11,53	11,77	2,49	1,25	0,1138	3,14	0,1618	0,0131	0,0668	2	99,197
17	Area1_amp16	41,79	14,16	11,56	11,36	11,63	2,5	1,28	0,0941	3,06	0,1077	0,0383	0,0609	2	99,665
18	Area1_amp17	41,24	13,92	11,38	11,79	11,88	2,42	1,35	0,0488	2,82	0,128	0,0299	0,0489	2	99,0582
19	std_kaer2	40,61	12,88	11,46	11,35	12,84	2,51	0,975	0,0405	5,4	0,1792	0,0035	0,0295	2	100,2999
20	Area_2_amp_1	42,27	13,13	12,37	11,39	11,57	2,43	1,36	0,0696	3,13	0,1041	0,0968	0,0548	2	100,0078
21	Area_2_amp_2	42,03	13,28	12,39	11,36	11,34	2,46	1,39	0,0615	3,31	0,1053	0	0,0671	2	99,7939
22	Area_2_amp_3	41,08	14,64	12,36	11,53	11,01	2,32	1,63	0,0259	2,86	0,1154	0,0347	0,0656	2	99,711
23	Area_2_amp_4	40,39	16,34	12,32	11,14	10,48	2,26	1,69	0,0713	2,44	0,1323	0,0227	0,0727	2	99,407
24	Area_2_amp_5	44,75	17,02	9,9	10,54	8,89	3,13	1,31	0,0473	2,35	0,0922	0,0372	0,047	2	100,1686
25	Area_2_amp_6	42,01	14,03	11,8	11,45	11,43	2,35	1,58	0,0973	3,17	0,0785	0,0299	0,0616	2	100,0873
26	Area_2_amp_7	45,92	11,81	10,19	13,75	10,99	2,41	0,9949	0,0816	1,87	0,1203	0,0706	0,0286	2	100,2729
27	Area_3_amp_1	41,1	13,43	12,68	11,12	11,07	2,52	1,36	0,0275	3,29	0,1063	0	0,052	2	98,7558

28	Area_3_amp_2	44,26	10,93	11,25	13,84	11,62	2,16	1,0272	0,0147	2,46	0,1314	0	0,0358	2	99,7291
29	Area_3_amp_3	40,78	13,18	12,47	11,44	11,14	2,42	1,27	0,055	3,35	0,1422	0	0,0455	2	98,2927
31	Area_3_amp_5	34,02	12,43	10,66	14,44	11,18	2,33	1,0864	0,0049	2,21	0,1571	0	0,0313	2	90,5497
36	kaer3	40,19	13,05	11,8	11,38	12,63	2,52	0,9745	0,0065	5,43	0,1737	0	0,0152	2	100,1724
37	07_a1_amp1	41,73	14,88	7,51	12	14,43	3,44	0,3069	0,0886	3,06	0,0225	0	0,0035	2	99,5264
38	07_a1_amp2	42,38	13,82	7,85	11,78	14,49	3,35	0,4115	0,203	3,48	0,0831	0,018	0,006	2	99,9213
39	07_a1_amp3	41,89	13,56	7,69	11,7	14,17	3,3	0,5538	0,3013	3,91	0,0944	0	0,0085	2	99,2653
40	07_a1_amp4	41,66	13,8	7,75	11,71	13,73	3,38	0,454	0,3621	4,37	0,082	0,0072	0	2	99,3738
41	07_a1_amp5	42	13,52	7,7	11,71	13,76	3,22	0,6053	0,3459	4,47	0,0371	0	0,009	2	99,4005
42	07_a1_amp6	41,28	14,59	7,8	11,76	13,47	3,41	0,3684	0,3328	4,43	0,0596	0	0,0018	2	99,5643
43	07_a1_amp7	41,48	14,88	7,59	11,77	13,48	3,43	0,3501	0,2363	3,89	0,0552	0,036	0,0101	2	99,2574
44	07_a1_amp8	41,92	13,97	7,71	11,7	14,09	3,14	0,72	0,3655	4,23	0,0585	0,036	0,0123	2	100,0029
45	07_a1_amp9	41,8	13,89	7,74	11,72	14,3	3,19	0,6939	0,4702	4,04	0,0798	0	0,0075	2	100,0145
46	07_a1_amp10	41,23	13,88	7,69	11,73	14,19	3,08	0,7686	0,4068	4,24	0,1069	0,0503	0,009	2	99,4202
47	07_a1_amp11	41,27	13,48	8,09	11,71	14,02	3,13	0,7322	0,4651	4,7	0,0977	0,0347	0,001	2	99,8292
48	07_a1_amp12	41,6	13,74	7,49	11,75	14,26	3,1	0,7689	0,5001	4,16	0,0888	0	0,006	2	99,5691
49	07_a1_amp13	41,68	13,97	7,6	11,76	14,14	3,1	0,7287	0,4163	4,36	0,0753	0,049	0	2	99,9229
51	07_a1_amp15	41,68	13,31	7,73	11,85	14	3,14	0,6695	0,4619	4,97	0,0708	0	0,002	2	99,9706
52	07_a1_amp16	42,26	13,68	7,37	11,72	14,37	3,29	0,7269	0,4623	4,06	0,0888	0,0334	0,0035	2	100,0778
53	07_a1_amp17	42,22	14,32	7,33	11,67	14,56	3,21	0,7586	0,487	3,5	0,0809	0,0671	0,0045	2	100,2783
54	07_a1_amp18	42,01	13,63	7,53	11,67	14,02	3,21	0,7247	0,4653	4,28	0,0921	0,0167	0,0013	2	99,6989
55	07_a1_amp19	41,75	14,02	7,72	11,78	13,8	3,11	0,8051	0,5131	4,17	0,0641	0,0264	0,0118	2	99,827
56	07_a1_amp20	41,78	13,94	7,96	11,8	14,04	3,18	0,7168	0,5351	4,4	0,0842	0,0215	0,0065	2	100,5394
57	07_a1_amp21	41,66	13,91	7,73	11,83	13,71	3,19	0,7391	0,4455	4,47	0,0303	0	0,0098	2	99,8265
58	07_a1_amp22	42,13	14,97	7,51	11,61	13,69	3,44	0,4477	0,2294	3,95	0,073	0,0695	0,006	2	100,1872
59	07_a1_amp23	42,24	15,49	6,74	11,72	14,18	3,54	0,2705	0,2416	2,75	0,0811	0	0	2	99,309
60	07_a1_amp24	42,09	14,76	7,48	11,65	14,03	3,43	0,3999	0,3362	3,7	0,0731	0,0084	0	2	100,0116
61	07_a1_amp25	42,82	13,99	7,21	11,7	14,04	3,33	0,5796	0,4896	4,23	0,1035	0	0,0058	2	100,5354
62	kaer4	39,99	13,04	11,7	11,35	12,58	2,48	0,9792	0	5,62	0,1654	0,0334	0,0221	2	99,9601
63	07_a2_amp1	42,78	17,14	6,99	11,45	14,79	3,59	0,2137	0,0575	1,1184	0,1183	0	0,0091	2	100,2905

64	07_a2_amp2	42,12	17,45	7,05	11,5	14,42	3,68	0,2271	0,0526	0,9092	0,0935	0,0216	0	2	99,5798
65	07_a2_amp3	42,34	17,21	7,16	11,45	14,78	3,68	0,2123	0,0624	0,9815	0,1228	0	0,0013	2	100,0596
74	07_a2_amp12	42,52	13,69	7,57	11,7	14,25	3,26	0,6256	0,3802	4,04	0,0831	0	0	2	100,1643
75	07_a2_amp13	42,07	13,54	7,99	11,68	13,82	3,17	0,6366	0,3123	4,44	0,0774	0	0,0023	2	99,8421
76	07_a2_amp14	42,88	14,31	7,46	11,54	14,16	3,42	0,4066	0,2439	3,48	0,0528	0	0,001	2	100,0082
77	07_a2_amp15	42,71	14,9	7,37	11,56	14,38	3,46	0,3845	0,1588	3,02	0,0988	0	0,0028	2	100,104
78	07_a2_amp16	43,13	13,71	7,42	11,69	14,39	3,26	0,57	0,3963	4,04	0,0618	0,0383	0,0055	2	100,7487
79	07_a2_amp17	42,07	14,6	7,69	11,64	13,54	3,44	0,3724	0,2894	4,12	0,0707	0,0143	0	2	99,8998
80	07_a2_amp18	42,29	14,09	7,86	11,72	13,44	3,17	0,7111	0,3692	4,28	0,102	0	0	2	100,0622
81	07_a2_amp19	42,23	14,24	7,77	11,63	13,79	3,16	0,7402	0,4772	3,91	0,0964	0,0418	0,0033	2	100,129
82	07_a2_amp20	42,64	13,94	7,64	11,67	14,06	3,17	0,7044	0,4139	4,07	0,0617	0	0,0093	2	100,428
83	07_a2_amp21	42,4	14,08	7,76	11,71	13,86	3,14	0,7829	0,5069	3,76	0,1065	0	0,0033	2	100,166
84	07_a2_amp22	42,39	14,06	7,45	11,7	14,11	3,12	0,7435	0,4516	3,62	0,074	0,0286	0,0108	2	99,7961
85	07_a2_amp23	42,27	13,59	7,78	11,76	14,04	3,15	0,6943	0,3502	4,49	0,0808	0	0,001	2	100,267
86	07_a2_amp24	42,21	14,21	7,25	11,81	14,37	3,23	0,5663	0,3521	3,93	0,0707	0	0,0078	2	100,0608
101	07_a2_amp39	42,93	14,13	7,15	11,7	14,32	3,49	0,2943	0,3509	3,42	0,0517	0	0,001	2	99,8773
102	07_a2_amp40	43,24	14,34	7,23	11,56	14,25	3,44	0,3694	0,2786	3,54	0,082	0,0324	0,0096	2	100,4448
103	07_a2_amp41	43,05	15,02	7,23	11,57	14,01	3,48	0,3233	0,3273	3,47	0,1245	0,0634	0,0088	2	100,7269
104	kaer5	40,17	12,95	11,73	11,28	12,61	2,53	0,9449	0,0258	5,43	0,1649	0,0475	0,0328	2	99,9176
106	2_8_a1_amp2	43,76	18,26	6,81	12,87	13,43	2,66	0,1758	0,0951	0,7293	0,0663	0,0539	0,0056	2	101,0051
107	2_8_a1_amp3	42,69	16,84	7,05	12,07	14,46	2,9	0,2712	0,1851	1,86	0,0416	0,0108	0,0053	2	100,4559
108	2_8_a1_amp4	42,61	15,95	7,1	11,99	14,42	2,83	0,3656	0,2801	2,19	0,1134	0	0,0055	2	99,8735
109	2_8_a1_amp5	42,95	15,24	7,47	12,04	14,48	2,8	0,5897	0,3619	2,55	0,0943	0,0048	0,0063	2	100,6572
114	2_8_a1_amp10	47,44	10,52	6,22	16,53	14,78	1,88	0,1211	0,173	1,0814	0,0867	0	0,0045	2	100,9018
115	2_8_a1_amp11	45,87	11,87	6,91	14,86	14,53	2,33	0,1756	0,3334	1,73	0,0776	0,0073	0,0068	2	100,7744
116	2_8_a1_amp12	44,14	13,59	7,78	12,82	14,34	2,68	0,2281	0,3894	2,03	0,1168	0	0	2	100,2077
121	2_8_a1_amp17	52,39	4,13	4,57	22,59	14,96	0,7121	0,0008	0,3869	1,0787	0,1197	0,0431	0	2	102,9993
122	kaer6	39,88	12,95	11,45	11,36	12,77	2,45	0,9752	0,021	5,48	0,1725	0,051	0,0206	2	99,6032
123	2_8_a2_amp1	44,66	14,05	9,06	11,37	14,43	2,31	0,8422	0,0472	1,2958	0,1019	0,1481	0,0023	2	100,3731
124	2_8_a2_amp2	43,5	13,84	8,81	11,55	13,82	2,48	1,1149	0,2688	3,13	0,0728	0,0345	0,0138	2	100,7253

125	2_8_a2_amp3	43,52	13,71	8,68	11,37	13,65	2,32	0,9644	0,4284	2,48	0,0515	0	0,0055	2	99,2114
126	2_8_a2_amp4	43,56	14,1	8,39	11,4	13,66	2,37	1,0183	0,4142	2,59	0,084	0	0,0108	2	99,6443
127	2_8_a2_amp5	42,71	15,17	8,19	10,8	13,79	2,86	0,8488	0,4421	3,15	0,0941	0	0,0115	2	100,1058
128	2_8_a2_amp6	43,38	14,18	8,71	11,4	13,61	2,54	1,0163	0,3585	2,82	0,121	0	0,0093	2	100,1947
129	2_8_a2_amp7	43,09	14,06	8,52	12	13,8	2,35	1,151	0,4124	2,7	0,0582	0,0847	0,0183	2	100,2676
130	2_8_a2_amp8	42,13	14,75	8,06	11,55	13,53	2,37	1,1137	0,3347	3,81	0,0381	0,0143	0,0048	2	99,7347
131	2_8_a2_amp9	42,63	14,32	8,82	11,91	13,32	2,4	1,1378	0,3728	3,16	0,0694	0,0226	0,0137	2	100,2394
132	2_8_a2_amp10	42,94	13,93	8,74	11,78	13,8	2,34	1,1563	0,3695	2,81	0,1018	0	0,0218	2	100,0167
133	2_8_a2_amp11	42,46	14,01	8,83	11,61	13,6	2,34	1,0576	0,4246	3,97	0,0906	0,0108	0,0272	2	100,4836
134	2_8_a2_amp12	43,84	13,2	8,64	11,61	13,86	2,47	0,9327	0,2444	3,03	0,0873	0,0203	0,0165	2	100,0084
135	2_8_a2_amp13	43,8	13,13	9,01	11,6	13,87	2,35	0,9743	0,3186	2,82	0,1152	0,0178	0,0155	2	100,0683
136	2_8_a2_amp14	42,41	14,3	9,24	11,58	13,37	2,54	0,921	0,2207	2,85	0,0726	0	0,013	2	99,5914
137	2_8_a2_amp15	44	14,53	8,62	11,67	14,3	2,24	1,0483	0,0896	1,0787	0,0684	0,0322	0	2	99,7439
138	2_8_a2_amp16	43,16	13,71	10,21	9,77	14,21	2,44	0,7919	0,0956	3,61	0,1028	0,0942	0,009	2	100,2598
139	2_8_a2_amp17	44,32	13,82	8,51	10,99	14,61	2,53	0,7573	0,044	2,15	0,0852	0,0084	0,0058	2	99,864
140	2_8_a2_amp18	43,05	14,41	9,81	11,11	12,95	2,54	0,9978	0,013	3,3	0,0614	0,0358	0,014	2	100,3406
141	2_8_a2_amp19	44,76	15,55	9,35	10,98	12,11	2,97	0,9469	0,0244	2,89	0,0459	0	0,004	2	101,6534
142	kaer7	40,94	13,01	11,48	11,41	12,67	2,44	0,9877	0,0177	5,48	0,2249	0,0094	0,0253	2	100,695

11 Appendix E – XRD results

Sample	Rock type	Fo	Hbl	Di	En	Bt	Lz	And	Dol	Spl	Ilm
JS11-03 Dyke	Comp dyke	13,46	14,83	26,63	25,38	0	0	19,7	0	0	0
JS02-3 Gabbro	Comp dyke	12,03	7,42	28,59	33,53	0	0	17,86	0	0	0,57
JS09	Lherzolite dyke	61,35	2,86	24,96	10,83	0	0	0	0	0	0
JS07	Lherzolite dyke	40,95	11,09	26,7	11,09			10,16			
JS09	Lherzolite dyke	63,68	2,4	23,48	9,93			0,51			
JS_2_18	Comp dyke	18,28	5,71	32,49	41,6		1,92				
JS15 Coarse	Hbl gabbronorite	4,38	41,32	13,46	19,96	0,92	0	16,76	0	0	3,2
JS14	Hbl gabbronorite	15,03	41,98	7,65	30,73	0,62	0	2,56	0	0	1,43
JS08	Hbl gabbronorite	1,31	28,62	19,09	16,19	0	0	29,84	0	0	4,95
JS19	Hbl gabbronorite	2,15	39,46	16,94	14,98	0,8	0	21,31	0	0	4,35
JS15-comp fine grained	Hbl gabbronorite	1,71	33,75	17,05	12	1,62	0	29,59	0	0	4,28
JS12-3	Hbl gabbronorite	1,28	15,02	26,1	21,12	1,19	0	30,25	0	0	5,04
JS10-1	Hbl gabbronorite	1,63	28,93	20,23	16,94	0	0	27,04	0	0	5,23
JS03	Porphyr hbl	19,68	29,17	28,81	15,21	1,01	0	0,86	0	1,92	3,34
JS21 Hbl pheno X	Porphyr hbl	11,98	22,65	33,78	27,39	0	0	0	0	0	4,21
JS01 DYKE	Comp dyke	21,35	6,92	38,34	26,87	0	0	5,92	0	0	0,6
JS16-3	Pyroxenite peg	4,22	3,1	29,42	60,38	0	0	0	0	0	2,89
JS19-3 Yellow shear mat	Shear zone	87,73	3,05	2,95	6,12	0	0	0	0,15	0	0
JS17-2	Repl dunite	40,99	0,26	16,95	0	0	41,8	0	0	0	0
JS18-3	Wherlite	80,41	0	15,88	3,23	0	0,48	0	0	0	0
JS_2_4	Wherlite	89		5,39	0,001		5,61				
JS01-Country rock	Wherlite	79,66	1,99	10,93	6,18	0,93	0,31	0	0	0	0
JS_2_5	Wherlite	94,47		4,3	0,001		1,22				
JS_2_6	Repl dunite	96,32		3,68	0,001						
JS_2_13_3	Repl dunite	31,45		36,71	0,001		31,84				
JS_2_13_4	Wherlite	69,46		25,77	4,2		0,56				

JS_2_13_5	Wherlite	59,6	1,5	29,31	8,45		1,14				
JS_2_15.G_2	Wherlite	73,49		17,3	2,46		6,75				
JS_2_15.G_3	Wherlite	17,76	1,7	69,85	10,46		0,24				
JS_2_16	Wherlite	44,6		31,15	0,001		24,26				
JS_2_19-B	Wherlite	75,4		18,48	0,001		2,82				
JS_2_9-O	Unknown		4,88	51,12	44						
JS_2_9-Y	Hbl gabbronorite		23,32	24,16	26,99	1,25		24,28			
JS_2_10	Unknown	28,67	3,41	61,4	6,52						

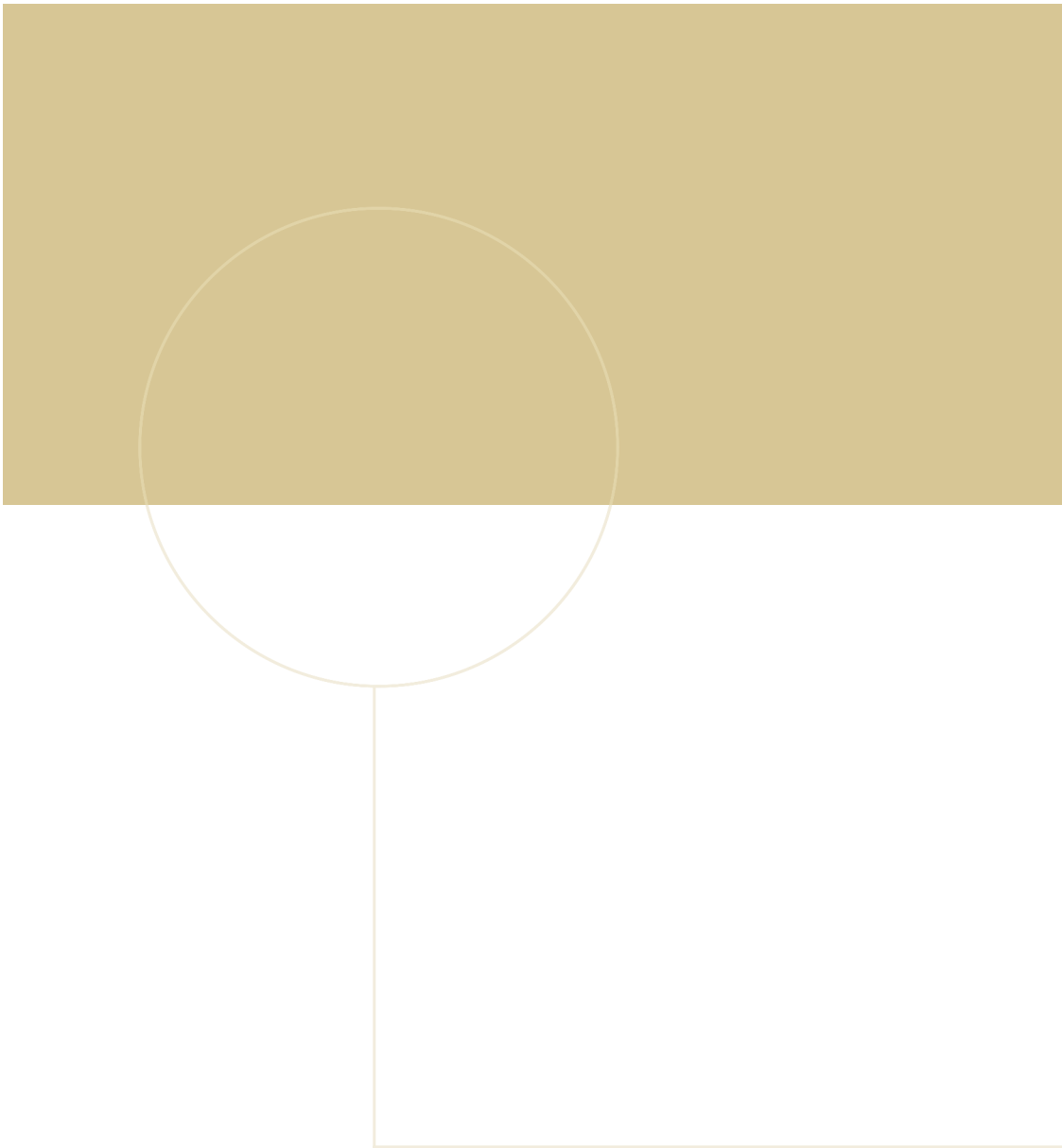

NTNU

Norwegian University of
Science and Technology